NANYANG TECHNOLOGICAL UNIVERSITY

Application of Sand-rubber Mixtures to Mitigate Vibration and Ground Shock

Chew Jia Han

School of Civil and Environmental Engineering

2018

Application of Sand-rubber Mixtures to Mitigate Vibration and Ground Shock

Chew Jia Han

School of Civil and Environmental Engineering

A thesis submitted to

Nanyang Technological University

in fulfilment of the requirements for the degree of

Doctor of Philosophy

2018

Table of Contents

Abstract

With the rapid increase in population density in urban cities, it is inevitable that vibrations levels due to myriad of reasons will be higher. Coupled with increased risk of terrorism, there is a need to mitigate ground vibrations caused by man-made ground shock from possible acts of terrorism. One of the most effective ways of reducing ground vibration caused by man-made activities is to introduce a seismic wave barrier between the source and the area of interest. Besides hardening an underground structure, it is possible to use a seismic wave barrier to mitigate ground shock pressure on the structure. The objective of this research is to study the responses of sand-rubber mixtures (SRM) as a seismic wave barrier to vibration and ground shock. Characterisation of SRM using laboratory tests were performed. Two separate series of small-scale field tests were performed. The first series involves using SRMs and open trench as seismic wave barrier against surface waves complemented with numerical simulations using LS-DYNA. Dimensionless amplitude ratio (Ar) contour plots were developed for use as a preliminary guide in implementation of seismic wave barrier on site. The second series involves using SRM to protect underground structure against ground shock caused by buried explosions. The field tests were modelled in LS-DYNA. The finite element model in LS-DYNA was verified to be able to correctly simulate underground explosions. The finite element model was able to replicate the field test results. In additions, the effect of density ratio between soil and structure on the peak incident pressure was examined through numerical modelling.

Acknowledgement

Sometimes the right path is not the easiest one. It is not just the knowledge that I have gain in this PhD journey, but the lifelong skills of problem solving, be it in research or daily life. This journey could not have happened if not for the guidance and support provided by my supervisor. No amount of words can express my heartfelt gratitude to A/P Leong Eng Choon.

Next, I would like to give thanks to the technical staff from Geotechnics Laboratory and Construction Technology Laboratory, particularly Mr Eugene Tan Hiap Guan, Mr Phua Kok Soon and Mr Vincent Heng for their technical and administrative support.

I would also like to thank my fellow colleagues and final year students whom I have work with. Making this journey a less painful one. I am also grateful to Nanyang Technological University for providing me the research scholarship.

I am forever grateful to my parents and family members for the support given to me. Last but not least, I would like to thank my wife, Eileen, who have let a listening ear to my complains and being the reason for me to stay in the fight.

List of Figures

List of Tables

List of Symbols

A, B, and C	Linear coefficient for JWL eqauation of state
A’	Experimentally determined factor from Lee at al. (2009)
a’, b’ and c’	Half major, minor axis length of the ellipsoid
$\bar{a}_1$, $\bar{a}_2$ and $\bar{a}_3$	Coefficient for equation 3.5
a'_0	Peak acceleration
a_0, a_1 and a_2	Constants for equation 5.1
AR	Amplitude reduction
B_R	curve fitting constant
B_f	Residual strength factor
b	Experimentally determined b-exponent Lee at al. (2009)
b_1 and b_2	Coefficient for equation 3.6
C_0, C_1, C_2, C_3, C_4, C_5 and C_6	Constants for linear polynomial equation of state
C_v	Specify heat capacity at constant volume
C_p	Specify heat capacity at constant pressure
c	seismic velocity
c’	Effective cohesive force
CN	Coordination number
d	Depth of the seismic wave barrier
d'_c	Apparent crater depth
d_c	True crater depth
D	Normalised with d with λ_R
D_c	Diameter of crater or camouflet
D_{min}	Minimal diameter of particle
D_{max}	Maximum diameter of particle
D_{s50}	Mean diameter of sand
D_{r50}	Mean diameter of rubber
E_0	Detonation energy per unit volume
E	Young’s modulus
e	Void ratio
e_{max}	Maximum void ratio
e_{min}	Minimum void ratio
f’	Unit less couple factor
f	Frequency
f_e	Frequencies corresponding to the bounds of the frequency range
f_s	Function of mean total strain
f_{in}	Input excitation frequency
f_r	Strength reduction factor
G	Shear stiffness
G_{max}	Small-strain shear stiffness
g	Gravitational force
i & i’	Ratio between wave velocities for solution suggested by Viktorov (1967)
I_0	Impulse
I_1	First invariant of the Cauchy stress
IR	Impedance ratio
J_2	Second invariant of the stress deviator

l	Length of seismic barrier
L	Normalised length of seismic barrier
L_{tt}	Tip-to-tip distance of the bender element
K	Bulk modulus
K_L	Loading bulk modulus
K_{uL}	unloading bulk modulus
M_{ru}	Rubber chips content in percent
P	Pressure
P_0	Peak pressure
P_{atm}	Atmospheric pressure
$P(f)$	Ordinate of the power spectrum
P_{cut}	Pressure cutoff
Δt	Wave travel time
t	Time
T	Temperature
V	Relative volume
V_c	Current volume
v_0	Original volume of the detonation products
V_0	Peak particle velocity
V_P	P wave velocity
V_s	S wave velocity
$V_{s,o}$	V_s of the specimens with 0% rubber chips
V_m	Von Mises yield function
V_r	Rayleigh wave velocity
$V(t)$	Velocity at time t
ΔV_c	Fall-back volume
ν	Poisson's ratio
r	Distances away from source
R_1, R_2, and ω	Nonlinear coefficients for JWL equation of state
R	Ratio between d and r
R_c	Depth of buried charge
sr	Size ratio between sand and rubber chips
w	Seismic wave barrier width
W	Weight of the explosive
x	Distance in the x-direction
X	Dimensionless distance in x-direction
y	Distance in the y-direction
Y	Dimensionless distance in y-direction
Y_e	Yield function
Y_s	Deviatoric part represented by the paraboloid
Y_p	Volumetric part represented by a plane normal to the hydrostatic axis
Y_{DP}	Drucker-Prager yield function
z	Distance in the z-direction
α' and k	Constants for equation 5.4
L'	Length of area of interest
B'	Breath of area of interest
ε_1	Axial strain
ε_3	Radial strain
ε_v	Volumetric strain

ρc	Acoustic impedances
ρ_o	Mass density
ρ	Density
ξ	Damping ratio
$\xi_{soil,100}$	Damping ration of soil at 100 kPa confining pressure
φ and κ	Graduation of the SRM (uniform or well-graded)
λ	Wave length
λ_R	Rayleigh Wave length
σ'_m	effective confining pressure
σ_a, σ_b, σ_c, σ_d and σ_e	Stresses for Equations 2,13 to equation 2.16
σ_1	Major principal stress
σ_3	Minor principal stress
σ_y	yield stress
τ	Shear stress
ϕ'	Effective friction angle of sand
π	Mathematical constant (3.14159)
ω_n	Natural radian frequency
ω	Cyclic frequency
μ	Volumetric parameter
γ	Ratio of the specify heat capacities of constant pressure and constant volume

Chapter 1 Introduction

1.1 Background

In a land-scarce country such as Singapore, it is inevitable that infrastructure has to be constructed in close proximity or underground to accommodate the rapidly growing population. Close proximity between activities (e.g, construction, transportation) and residential areas would potentially cause discomfort or even harm to the occupants. It becomes even more challenging with current threats of act of terror on the rise. Hence, methods which can effectively reduce shock and vibration are gravely needed. While the most effective way of reducing vibration caused by man-made activities is to introduce a seismic wave barrier between the source and the area of interest, there is more than one approach to mitigate ground shock caused by buried explosion. Approaches to mitigate ground shock can be generally classified into: (i) rigid barriers like reinforced concrete wall; and (ii) barriers with different acoustic impedances. Rigid barriers are the conventional form of hardening underground structures against ground shock, but there is a trade-off between increasing the strength of the boundary walls of the underground structure and cost. A more promising approach is to use seismic wave barriers with different acoustic impedance.

Studies on using seismic wave barrier to mitigate ground vibrations have been reported by researchers as early as 1968. One of the earliest seismic wave barriers was probably the open trench suggested by Woods (1968, 1974). Woods (1968) made use of an air gap (open trench) as barrier to damp out vibrations. Woods (1974) later suggested that a row of cylindrical piles may produce the same effect. Similar concept was investigated by Beskos et al. (1986), Aviles and Sanchez-Sesma (1988) and

Kobielak et al. (2007). However, using an open trench or a row of cylindrical piles is not suitable for underground structures. Furthermore, the voids may be filled with groundwater which will negate the attenuating effects of the barrier. Instead of air, others have made use of low acoustic impedance materials like expanded polystyrene (geofoam), polyester and styrofoam to damp out the stress waves. Fondaw (1993), Horvath (1995), Wang et al. (2009), Murillo et al. (2009) and, Alzawi and El Nagger (2011) investigated the use of geofoam as a seismic wave barrier both experimentally and numerically. However, at large depths, the capability of the geofoam is reduced. Harzarika (2006) studied geofoam as a seismic wave barrier numerically and suggested that at large strains, the strain-hardening behaviour of the geofoam reduces its effectiveness against blast wave.

Studies on seismic wave barrier against shock wave have also been reported. The materials used by researchers are not only restricted to single material, but also fibrous and composite materials such as carbon and glass fibre-reinforced polymeric composites. Schimizze et al. (2013) tested different deformable materials sandwiched between foam while Zhou et al. (2012) used face sheets with a cellular solid core. Such composite materials form part of the underground structure and is considered as a structural approach to modify the underground structure.

An alternative approach is to modify the properties of the soils surrounding the underground structures by mixing the soils with low acoustic impedance materials. An example of low acoustic impedance materials is rubber chips. The performance of such a soil mixture is dependent on the mix proportion and the properties of the low acoustic impedance material used. The main advantage of such soil mixtures is that they rearrange under stress wave loading to dissipate the energy. While the use of

sand-rubber mixtures (SRM) as a seismic wave barrier against earthquake has been investigated numerically by Tsang et al. (2012), Tsang (2008), Xu (2010), Hazarika et al. (2008) and Uchimura et al. (2007), no systematic study has been performed to investigate the SRM as seismic wave barrier against vibration caused by man-made activities and ground shock. There are many factors affecting the properties of SRM, hence characterisation of SRM is critical. To date, limited data on the dynamic properties of SRM is available in the literature. Filling knowledge gaps in the literature on SRM can contribute to better understanding of the material. Using SRM as a seismic wave barrier will also solve the environmental problem of disposing used rubber tyres.

1.2 Objective of Research

The objective of this research is to study the responses of SRM as a seismic wave barrier to surface wave and ground shock through field tests and numerical modelling.

1.3 Scope of Research

Effectiveness of SRM as a seismic wave barrier against surface wave and ground shock is investigated. Before field tests were performed, the properties of SRM were characterised in the laboratory. Effects such as rubber chips content, confining pressure and particle size ratio between sand and rubber were investigated. The characterisation of SRM in the laboratory focuses mainly on its dynamic properties, particularly wave velocities and damping ratios.

Small-scale field test to investigate the effectiveness of SRM barrier against surface wave was performed. The small-scale field tests include two types of SRM and an open trench. The field tests were used to calibrate the numerical model (LS-DYNA).

A parametric study was then performed to investigate the effects of soil properties and barrier dimensions.

Small-scale blast field tests involving two buried concrete targets (one with and one without SRM barrier) were conducted. The field tests were modelled numerically in LS-DYNA. Before modelling the field tests, parametric study was conducted to verify the ability of LS-DYNA to model buried explosions including crater and camouflet formations.

1.4 Organisation of Thesis

The thesis is organised into six chapters

Chapter 1 provides background of the problem, the objective and scope of the research.

Chapter 2 reviews the basics of wave propagation in soils, the sources and crater and camouflet formations as a result of underground explosions. Dynamic properties tests performed on SRM by other researchers were examined. Factors that affect the properties of SRM such as different stress conditions, particle size composition and rubber content are discussed. Past research on the materials used for seismic wave barrier to mitigate different types of vibrations (ground vibrations, earthquake and ground shock) are studied. The chapter ends with identification of research gaps.

Chapter 3 focuses mainly determination of static and dynamic properties of SRM. Fabrication of the bender/extender element and methodology of the experimental setup are presented. Methods on identification of arrival time of P and S wave and methods on data processing to obtain damping ratio are described. Effects of rubber

content in SRM, effective confining pressure and differences in particle size ratio between rubber and sand particles on material properties such as friction angle, wave velocity and damping ratio are studied and discussed. Results obtained from the laboratory tests are then compared with data from the literature.

Chapter 4 first describes the small-scale field tests to investigate SRM as a seismic wave barrier. The test site and the equipment that were used for the field test. Before commencement of the field test, site investigations were performed using non-invasive methods such as the continuous surface wave (CSW) test and drop hammer test. Results obtained from the small-scale field tests involving two SRMs and an open trench as seismic wave barrier were analysed and discussed. Following which, numerical simulations using LS-DYNA to simulate the small-scale field test were performed and the numerical model was verified with literature data. Parametric studies involving various barrier dimensions were then performed and dimensionless amplitude ratio contour plots were created. The use of the dimensionless amplitude ratio contour plots was demonstrated using case studies to illustrate how preliminary design of a seismic wave barrier can be made to achieve desired amplitude reduction for a project.

Chapter 5 presents the small-scale blast tests. It begins with description of the site, sensors used, design and fabrication of the reinforced concrete structures, preparation of the SRM barrier, and layout of small-scale blast tests. The results obtained are plotted and discussed. Material models from the LS-DYNA material library which were used to simulate the different component of the small-scale blast test were presented. Before simulating the small-scale field test, the finite element model was first verified. Soil properties to replicate the peak pressure plots for soil in TM5-855-1

(1986) were calibrated. The ability of the finite element model to simulate underground explosion leading to the formation of crater and camouflet was also investigated as amount of energy transmitted to the ground is dependent on the containment of the explosion. Further studies on material impedance, and density ratio of structure and soil were carried out with the finite element model for the small-scale field test.

Chapter six concludes this study. The significance and contribution of the study are highlighted. In addition, recommendations for future research are also presented.

Chapter 2 Literature review

2.1 Wave Propagation in Soils

Wave propagation in soil medium can be a result of natural occurrences such as earthquakes or man-made activities such as blast, traffic, railway and machinery. Waves coming from these sources generally composed of body and surface waves. Body waves comprising compression (P) and shear (S) waves are known to propagate radially outwards from the source in a hemispherical wave front. Surface wave, on the other hand, is composed of Rayleigh, Love and Lamb waves which are known to travel radially outwards from the source along a cylindrical wave front and stay mainly at the surface with their amplitude decreasing with depth (Richart et al. 1970). Among the different types of waves, P wave is known to have the highest velocity followed by S wave and surface wave. The P waves (shown in Figure 2.1a) induce movement of the particles in the direction of wave propagation and has the ability to transmit through all types of medium reflects the medium's bulk modulus (K). The S waves (shown in Figure 2.1b) vibrate the soil particles perpendicular to their direction of propagation and reflects the medium's shear stiffness (G). Equations 2.1 and 2.2 show the relationship between bulk modulus (K), shear stiffness (G), P-wave velocity and S-wave velocity derived from theory of elasticity.

$$V_p = \sqrt{\frac{K + {}^4/_3\, G}{\rho}} \tag{2.1}$$

$$V_s = \sqrt{\frac{G}{\rho}} \tag{2.2}$$

where V_p is the P-wave velocity, V_s is the S-wave velocity, K is the bulk modulus, G is the shear modulus and ρ is the density of the soil. Rayleigh-wave velocity V_R can be deduced from V_p and V_s component of the wave with the condition that free boundary conditions are imposed on the general equation for wave propagation in a linear elastic medium. This solution can be obtained using Helmholtz decomposition with the assumption that a surface wave decays quickly with depth (Richart et al. 1970). For the plane strain case, Rayleigh wave's solution can only be found if characteristic Equation 2.3 can be fulfilled by the surface wave propagating velocities.

$$i^6 - 8i^4 + (24 - 16i'^2).i^2 + 16.(i'^2 - 1) = 0 \quad (2.3)$$

where $i = V_R/V_s$ and $i' = V_s/V_p$. The relationship between V_p, V_s and V_R as function of Poisson's ratio are shown in Figure 2.2. Viktorov (1967) suggested an approximate solution for Equation 2.3. The approximate solution is:

$$i = \frac{0.87 + 1.12\upsilon}{1 + \upsilon} \quad (2.4)$$

where υ is the Poisson's ratio. As shown in Figure 2.2, V_s is very close to V_R. As a result, the range of variation in the ratio between V_R and V_s , i, is given by:

$$0.87 \leq i \leq 0.96 \quad (2.5)$$

where υ ranges from 0 to 0.5.

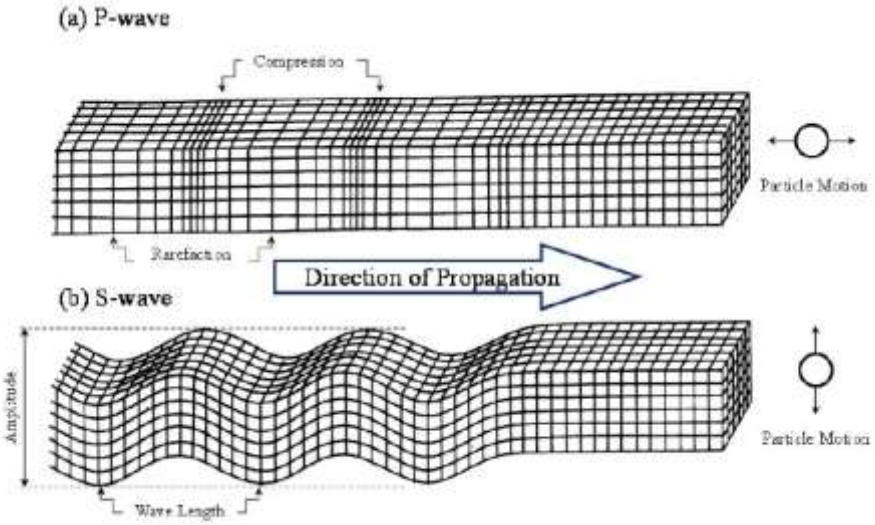

Figure 2.1 Propagation of P and S wave (Modified from

http://www.astro.uwo.ca/~jlandstr/planets/webfigs/earth/images/waves.gif)

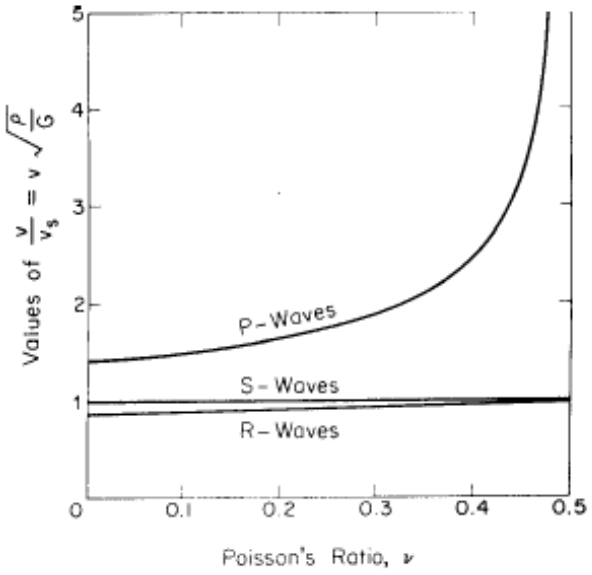

Figure 2.2 Relationship between Poisson's ratio V_p, V_s and V_R in linear elastic homogenous half space (from Richart, 1962)

2.1.1 Ground vibration by man-made sources

Ground vibrations caused by cars, machinery and trains may cause disturbance to people, affect sensitive equipment and damage structures. The vibration level is dependent on the soil condition and the operating conditions of the source. Murillo et al. (2009) presented a plot of displacement versus frequency (Figure 2.3) for different source types (car, bus and environmental noise) and the potential discomfort or damage it can cause. The data presented in Figure 2.3 are obtained from standard DIN 4150 (1999) and Caicedo (2007). From Figure 2.3, it is suggested that the frequency range of vibration caused by these sources are within 0 to 100 Hz. Miller and Pursey (1955) investigated the distribution of energy content present in ground vibration generated by a vertical oscillating disk. They concluded that 67% of the total energy passing through the medium comprises of Rayleigh wave while, S wave accounts for 26% and P wave accounts for only 7%. This suggested the importance of obtaining Rayleigh wave velocity and wavelength when dealing with problems caused by surface vibration.

2.1.2 Ground shock from explosives

The investigation of ground shock parameters was first made by Rankine (1870) and Hugoniot (1887) for explosions in air and then explosions in the ground. Explosion near the surface or underground will cause both surface wave (Rayleigh wave) and body waves (P-wave and S-wave) as illustrated in Figure 2.4. It is known that P and S waves dominate at close distances for buried explosion and Rayleigh wave dominates for surface explosion (Smith and Hetherington, 1994). Due to the slower rate of decay

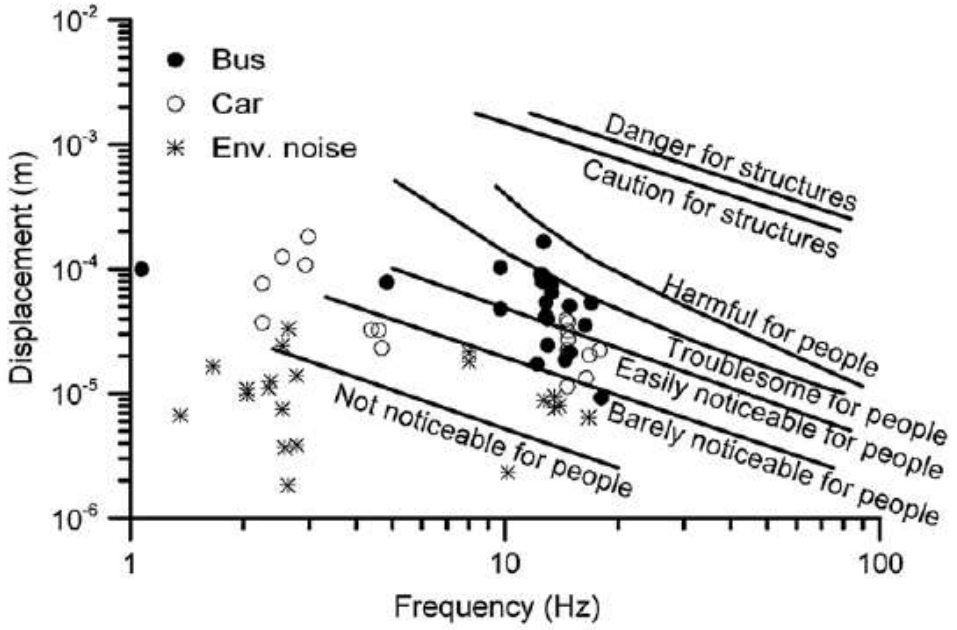

Figure 2.3 Comparison between traffic measurements in Bogota (Colombia) and DIN 4150 (1999) thresholds (from Murillo et al. 2009).

for Rayleigh waves with distance; Rayleigh waves also dominate at large distances from the explosion for buried explosions (Smith and Hetherington, 1994).

Explosion in air is characterised by a violent release of energy in a gaseous medium causing a sudden increase in pressure. The pressure disturbance, known as the blast wave, is characterized by an almost instantaneous rise from ambient pressure to a peak incident pressure and then followed by a negative phase duration characterised by a pressure below the ambient pressure at detonation (i.e suction effect) as shown in Figure 2.5. The negative phase is usually less important in design than the positive phase.

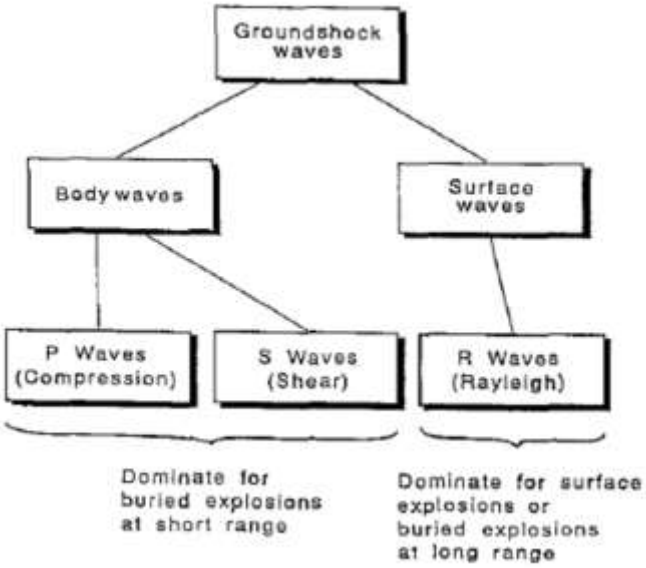

Figure 2.4 Categorisation of ground shock (from Smith and Hetherington, 1994).

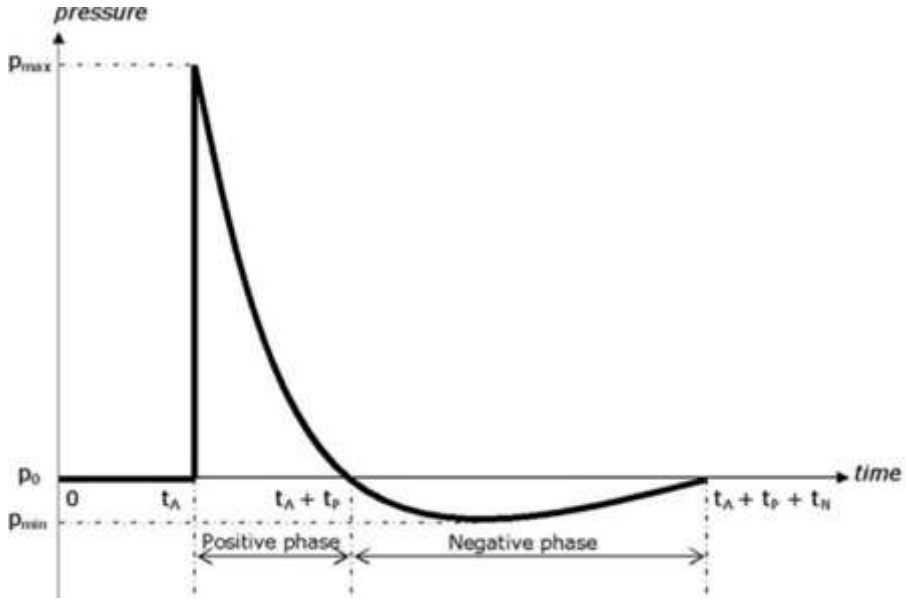

Figure 2.5 Blast wave pressure time profiles (from Smith and Hetherington, 1994).

Reliable ground shock parameters can be obtained from full-scale tests or small-scale tests complemented by numerical analyses. However, field explosion tests are expensive, time-consuming and difficult to conduct in land-scarce Singapore. With

the advancement in finite element software such as LS-DYNA, numerical experiments can be conducted to investigate the effects of ground shock on underground structures. However, numerical models need to be calibrated with test results to ensure that the correct phenomenon is captured. A database of field explosion tests that have been performed over a period of 30 years, between 1950 and 1980 (Drake and Little, 1983), have been compiled in TM 5-855-1 (1986). The TM 5-855-1 (1986) presents the correlations between the peak pressure, peak velocity, peak acceleration, peak displacement and impulse in soils with scaled distance as shown below:

Peak pressure:
$$P_o = f.(\rho c).160.(\frac{r}{w^{1/3}})^{-n} \quad (2.6)$$

Peak velocity:
$$V_{o} = f.160.(\frac{r}{w^{1/3}})^{-n} \quad (2.7)$$

Peak aceleration:
$$a_o w^{1/3} = f.50.c(\frac{r}{w^{1/3}})^{(-n-1)} \quad (2.8)$$

Peak displacement:
$$\frac{d_o}{w^{1/3}} = f.500.\frac{1}{c}.(\frac{r}{w^{1/3}})^{(-n+1)} \quad (2.9)$$

Impulse:
$$\frac{I_o}{w^{1/3}} = f.\rho_o.1.1.(\frac{r}{w^{1/3}})^{(-n+1)} \quad (2.10)$$

where P_0 is the peak pressure in psi, V_o is the peak particle velocity in fps, a_o is the peak acceleration, I_o is the impulse in lb-sec/in^2, do is the peak displacement in ft, f' is the unit less couple factor, ρc is the acoustic impedances in psi/fps, r is the distance to the detonation in ft, w is the weight of the explosive in lb, n is the attenuation coefficient, c is the seismic velocity in fps and ρ_o is the mass density in lb-sec^2/ft^4.

The correlations presented in TM 5-855-1 (1986) could be treated as averaged test data that captured the phenomenon of buried explosions in the ground.

Equations 2.6 through 2.10 from TM 5-855-1 (1986) are dimensionally inconsistent and care must be exercised to convert from imperial units to SI units. Therefore, modification and improvement to the plots from TM 5-855-1 (1986) were made by Leong et al. (2006) who re-plotted the peak pressure plots from TM 5-855-1 (1986) into a dimensionless plot. Peak pressures in underwater explosion from Coles (1965) and air blast were incorporated into the plot for better understanding. The dimensionless plot is shown in Figure 2.6.

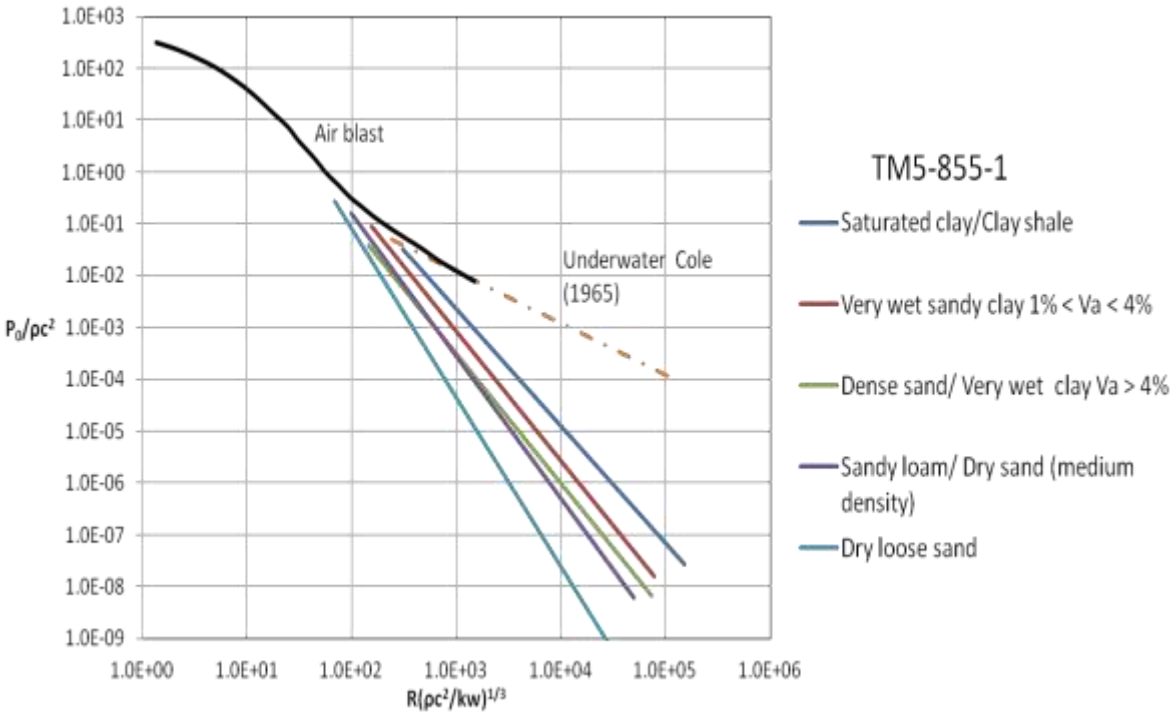

Figure 2.6 Relationship of peak pressures with scaled distance using dimensionless parameters (modified from Leong et al. 2006)

2.2 Explosives, Effects of Charge Coupling and Cratering

Explosives are chemical compounds or mixtures which are able to have a rapid reaction to produce gaseous products at significantly high pressure and temperature (Dobratz et al, 1985). For the initiation of an explosion, certain condition has to be present such as adequate shock and heat so that the chemical component in the high explosive can react efficiently (ISEE, 2000). A primer which is an explosive charge that contains the initiating device is used to ensure that the entire explosive are expended and the direction of the blast is as intended. Explosives have density ranging from about 600 kg/m^3 to 1700 kg/m^3 and have a detonation velocity ranging from 1520 m/s to 7620 m/s. For common explosives, the potential energy ranges from 152,440 joules to as much as six times of this amount (Taiquideen, 1982; Anand, 2007).

There are generally two types of explosive reactions, they are deflagration and detonation (ISEE, 2000). Deflagration is the accelerated burning of the explosive at a velocity less than the sonic velocity of the unreacted explosive. For detonation, the reaction proceeds at a speed faster than the speed of sound in the unreacted explosive. When this reaction occurs, surface and body waves are produced which changes the state of the explosive so that exothermic reaction is formed at a desired detonation velocity (Smith and Hertherrington, 1994).

When an explosion occurs underground, the depth at which the detonation occurs becomes important as it will decide how much energy is transmitted into the ground. This effect can be accounted for using the coupling factor f'. A coupling factor f' of unity implies that the explosive energy is fully contained within the soil. Figure 2.7, a

plot of coupling factor versus scaled depth of burst, shows that both weight of the charge and the depth to which the charge penetrates have a part to play in determining the coupling factor f'. When the explosive is buried at a shallow depth, the soil is unable to contain the explosive gas and thus the soil breaks up and forms a crater. Due to this escape of energy, the energy that travels through the soil medium will be reduced. On the other hand, if the energy from the explosion was insufficient to cause a break-up of the soil, the energy will be contained in the soil, forming a camouflet.

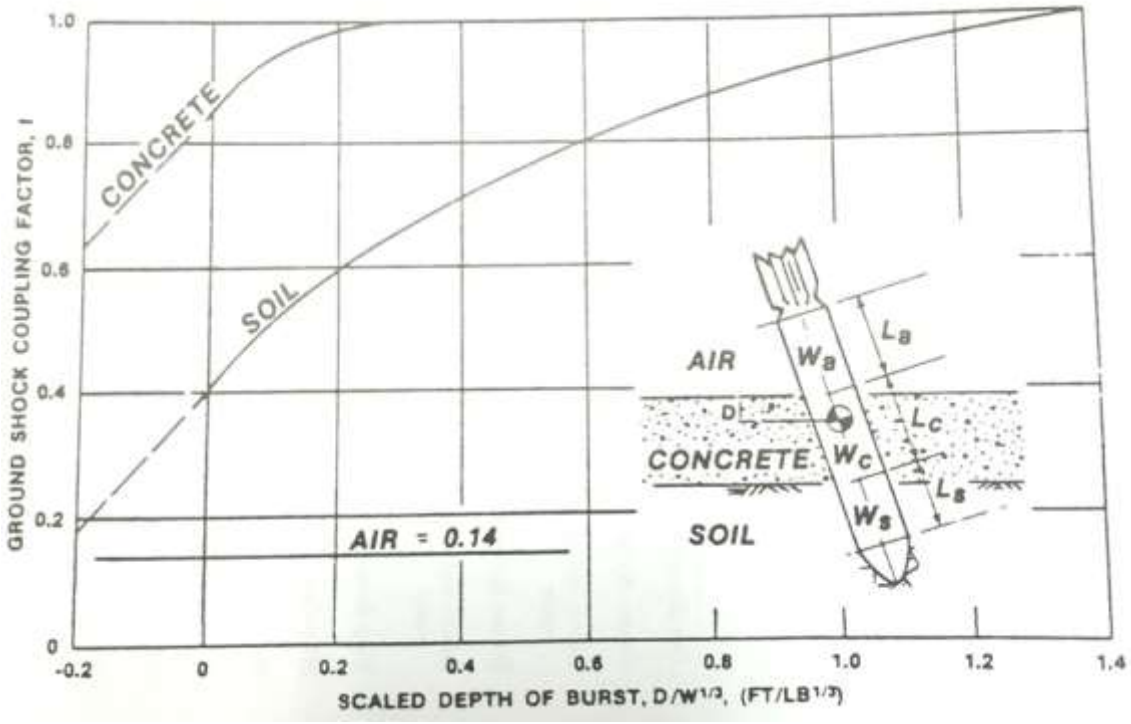

Figure 2.7 Dependence of coupling factor on scaled depth (from TM 5-855-1, 1986)

The visible hole resulting from an explosion is generally referred to as apparent crater. True crater, on the other hand, is the true hole resulting from the explosion but is masked by the soil and debris that fall back into the true crater creating an apparent crater. Figure 2.8 shows a crater profile from TM 5-855-1 (1986). From Figure 2.8a, the rupture region is a region of the soil which has been disturbed severely by the

explosion. Plastic zone, which is the larger region of lesser disturbance, surrounds the rupture zone. On the surface, the rupture and plastic zones form a region of surface displacement or up thrust. Up thrust of the soil can be caused by both partially and fully-contained explosion. Ejecta are the materials thrown out of the crater by the explosion forming the crater lip.

a)

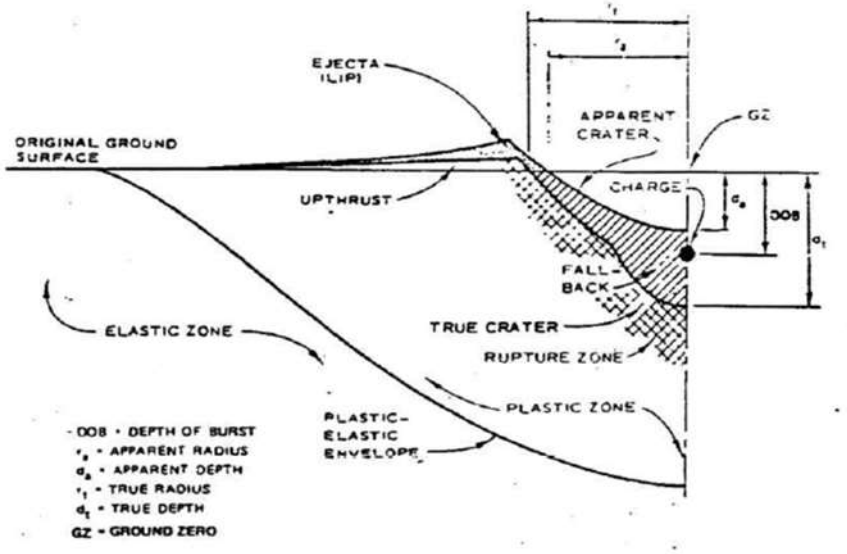

b)

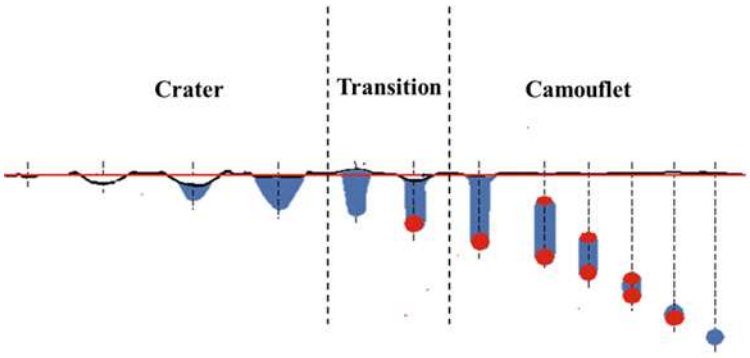

Figure 2.8 a) Half crater profile taken about the centre line of explosion (from TM 5-855-1, 1986) b) Crater formation as a function of depth of burial

Formation of crater has been studied by various researchers using both field experiments and numerical simulations. In the 1960s and 1970s, numerous full-scale explosion tests using charge weights ranging from a few tonnes to few kilotonnes have been carried out and some of the data were compiled in Schoutens (1979). In recent years, field tests to study crater formation due to surface blast have also been carried out in view of the growing threat of terrorism and scarcity of surface blast data (Busch et al. 2015, Moorthy et al. 2015, Ambrosini et al. 2002, Groto et al. 2001).

Ambrosini and Lucioni (2006), Wang and Lu (2003), Wang (2001), Wang et al. (2016) and Nian et al. (2013), Ambrosini et al. (2002) and Fiserova (2006) studied crater formation using numerical simulations with software such as LS-DYNA and Autodyn. While Wang and Lu (2003), Wang (2001), Wang et al. (2016) and Nian et al. (2013) performed studies for a single soil type, Ambrosini et al. (2002) and Fiserova (2006) varied soil types. Ambrosini et al. (2002) and Fiserova (2006) concluded that the significant changes in crater dimensions are a result of the change in soil's shear strength parameters (friction angle and cohesion) and other soil parameters such as density, bulk modulus and Poisson's ratio have little effect on the crater dimensions. They also concluded that numerical simulations are unable to simulate thrown material falling back into the crater. Ambrosini and Luccioni (2006) attributed Autodyn's inability to simulate fall back of thrown materials to the use of Euler formulation with a continuum model. Charwick et al. (1964) performed a numerical study on formation of camouflet caused by explosions at a great depth in different soil types. Charwick et al. (1964) results also suggest that the dimensions of the camouflet depended largely on the soil's shear strength parameters.

TM5-855-1 (1986) gives a plot of empirical apparent crater curves for various soil types. The plot contains both the ordinate (diameter and depth) and abscissa (depth of buried charge) using scaled distance $R_c/W^{1/3}$, where R_c is the depth in ft and W is the weight of the buried charge in lb as shown in Figure 2.9. The trend of the curves can be explained using explosion energy and law of physics. Increase in depth of buried charge will result in an increase in crater size until it reaches the optimum depth (crest of the curve). Any further increase in depth of the buried charge results in the energy from the explosion becoming insufficient to throw the material beyond the edge of the crater and results in more material falling back into the crater and decreases the crater dimensions. The apparent crater dimensions will decrease till full containment of the explosion is reached. From Figure 2.9, clay forms the upper bound of the curves and sand forms the lower bound of the curves with mixed soil sandwiched in between the two soil types. TM5-855-1 (1986) does not provide any information on depth of charge leading to a camouflet formation. As the depth of buried charge increases, a camouflet is formed (Figure 2.8b). Collapsing of camouflet may occur leading to a depression in the ground surface (Bull and Woodford, 1998).

2.3 Characterisation of Sand-Rubber Mixtures

Sand-rubber mixtures (SRM) is a type of binary mixtures which comprises of sand and rubber-chips. The rubber-chips which are used in the mixtures come mainly from post-consumer type of rubber such as tyres.

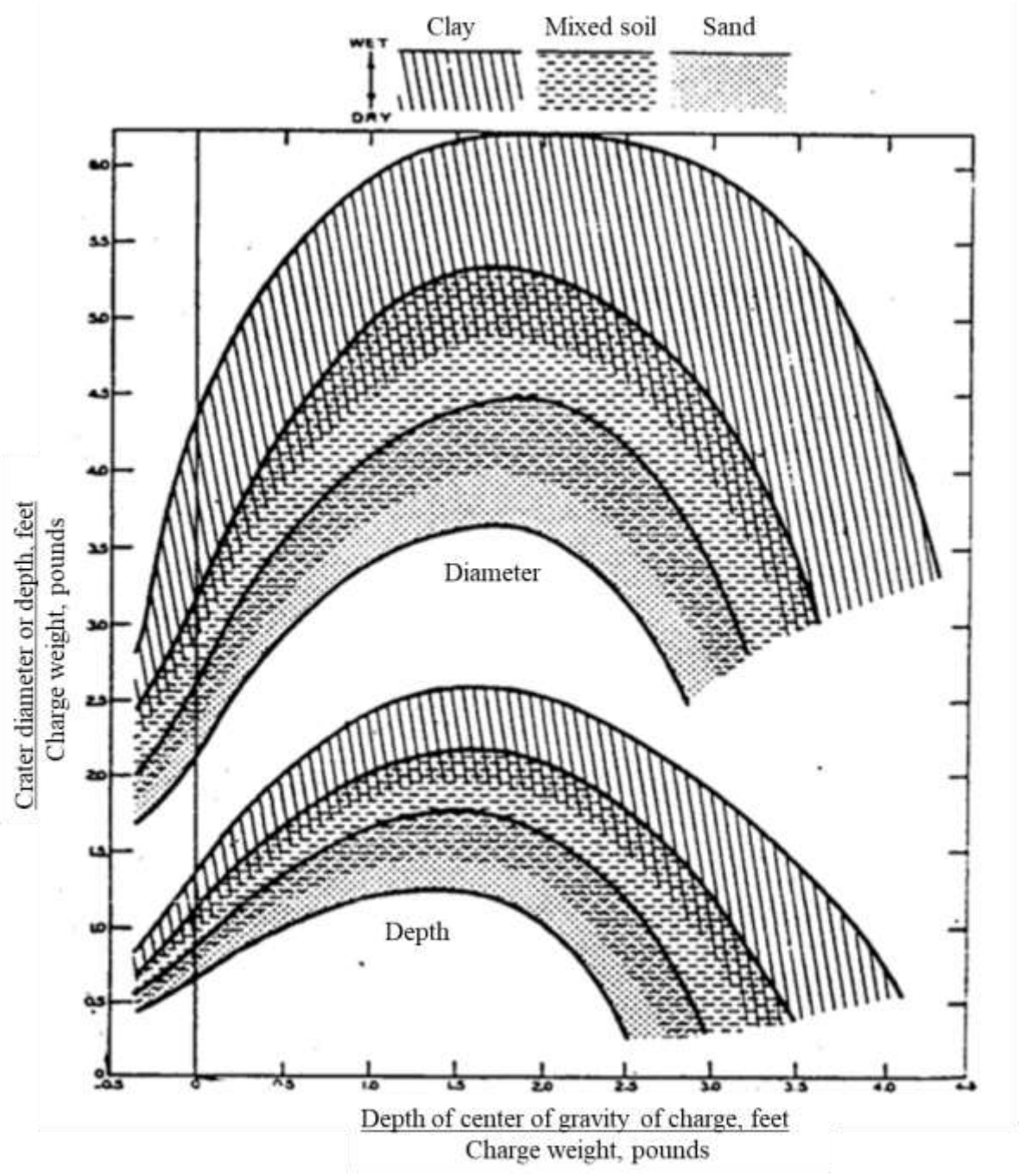

Figure 2.9 Field test crater diameter plotted on TM5-855-1 crater curves

These waste tyres are non-degradable and due to its shape and compaction resistance requires a large amount of space in landfill or stockpiling. To reuse the waste rubber tyres as a constructions material, the waste rubber tyres first undergo a process of removal of steel and tire cord. Following which, the rubber tyres are sent to granulator

or cracker mill to reduce the rubber tyres to rubber chips. Usage of waste tyre rubber chips as a construction material is attractive due to the availability and low cost of the waste tyres and at the same time, it helps to combat the disposal problem of waste rubber tyres. The use of SRM as backfills and construction materials has proven satisfactory in civil engineering projects (Humphrey and Manion 1992, Bosscher et al. 1997, Foose et al. 1996, Zornberg et al. 2004a and 2004b, Humphrey et al. 1993).

Tsang (2008), Senatakis et al. (2009), Pitilakis et al. (2015), Hazarika et al. (2007,2008) and Uchimura et al. (2007) have proposed the use of SRM to reduce vibrations caused by earthquakes. However, to date only numerical simulation and scaled modelling in a controlled laboratory environment have been performed. The suitability of SRM for such applications depends on the physical characteristics of the sand and the rubber chips, size ratio of sand and rubber chips, mix proportions, effective confining pressure and dry density. To better understand the effects of different particles sizes in SRM, mix proportions and effective confining pressure, the properties of the SRM must be studied in the laboratory. The following section will review laboratory experiments (wave propagation test and shear tests) performed by other researchers to date. Factors affecting the properties of SRM such as wave velocities, small strain shear modulus, damping ratio and friction angle will be reviewed in the following section.

2.3.1 Dynamic properties

Wave propagation and resonant column tests which are categorized under advanced geotechnical laboratory testing methods allows wave velocities, stiffness and damping ratio to be obtained. In the wave propagation test, piezoelectric materials are used to

transmit and receive P and S waves due to its ability to convert mechanical energy into electrical signals. Table 2.1 summarises the tests performed by researchers on SRM.

Table 2.1 Summary of the wave propagation test done on SRM

s/n	Reference	Rubber content (%)	Laboratory apparatus	Objective of test
1	Feng and sutter (2000)	14, 28, 56 & 100	Resonant column device	S wave velocities and damping ratio
2	Pamukcu and Akbulut (2006)	0, 5, 7.5, 10, 12.5 & 15	Resonant column device	S wave velocities and damping ratio
3	Kim and Santamarina (2008)	30 & 50	Odeometer modified with bender element	S wave velocities and damping ratio
4	Anastasiadis et al. (2009)	0, 5, 10, 15, 25 & 35	Resonant column device	S wave velocities and damping ratio
5	Lee et al. (2009)	0, 20, 40, 50, 60, 80 & 100	Odeometer modified with bender element	S wave velocities
6	Senetakis et al. (2012)	0, 5, 10, 15, 25 & 35	Resonant column device	S wave velocities and damping ratio
7	Cheng (2015)	0, 15, 30, 50, 70 & 100	Modified triaxial cell with bender/extender element	P & S wave velocities and damping ratio

2.3.1.1 P and S wave

The propagation of P and S waves through the particles depends on the contact conditions between particles for transmission. Inter-particle contact law (Hertz's law) has a strong influence on the wave propagation velocity. Hertz's law states that the

stiffness of an inter-particle contact depends on the normal force between the two particles. To properly illustrate Hertz's law, a simple illustration is shown in Figure 2.10.

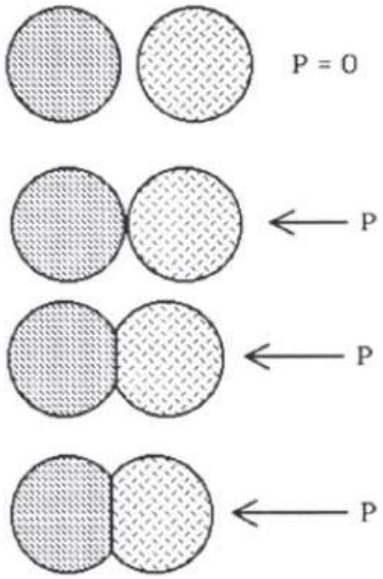

Figure 2.10 Hertz's contact theory (from Liu and Nagel, 1992)

As shown in Figure 2.10, in the absence of external pressure applied to the particles, the particles do not come into contact. As a result, no transmission of wave occurs. However, with the increase in application of external pressure, the particles come into contact and distort which result in higher wave velocity.

P and S wave can also be affected by size ratio (sr) which is a ratio of two different material particle size or two particle sizes of the same material in a mixture. Although Wiacek (2016) studies is not based on SRM, Wiacek (2016)'s investigation on effects of size ratio sr on the geometric parameters such as coordination number (CN) of granular binary mixtures can provide a good insight of effects of sr in SRM. The coordination number (CN), or number of contact points per particle, is an important

parameter in describing the geometrical arrangement of particles in a packing and is widely used in the evaluation of structural properties related to the connectivity between particles. Figure 2.11 shows the average CN plotted against different fines content for sr of 0.4 and 0.8. Size ratio, sr, which is defined by D_{min}/D_{max}. Figure 2.12 illustrates the different particle interactions in a binary mixture which can explain Figure 2.11. General trend in Figure 2.11 shows that with the addition of fines results in a change in the CN. Figures 2.11a, c and d show that when sr is big, which implies that the size difference between the small and the big particles are big, yield a higher CN value is obtained for all fines content.

CN for all inter-particle contact cases presented in Figure 2.11 is tabulated and presented in Table 2.2. From Table 2.2, it is evident that small particles generally have more contact points compare to bigger particles and CN increase with increment in fine content ratio. These observations suggested that the behaviour of the binary mixtures with small sr can be dominated by the properties of the smaller particles. These observations are supported by studied performed Muir Wood and Kumar (2000). Muir Wood and Kumar (2000) studied on binary mixtures comprising of Kaolin clay and coarse sand using fall cone test and one-dimensional compression using an odeometer apparatus with different Kaolin clay content. Muir Wood and Kumar (2000) concluded that mechanical response due to presence of the sand (bigger particle) has no influence on the behaviour of the clay matrix (smaller particle) until the sand content reaches about 65% by mass of soil mineral. From the above observation, it is suggested that SRM with a $D_{s50}/D_{r50} < 1$ will have result in an higher velocities in comparison with SRM with a $D_{s50}/D_{r50} > 1$.

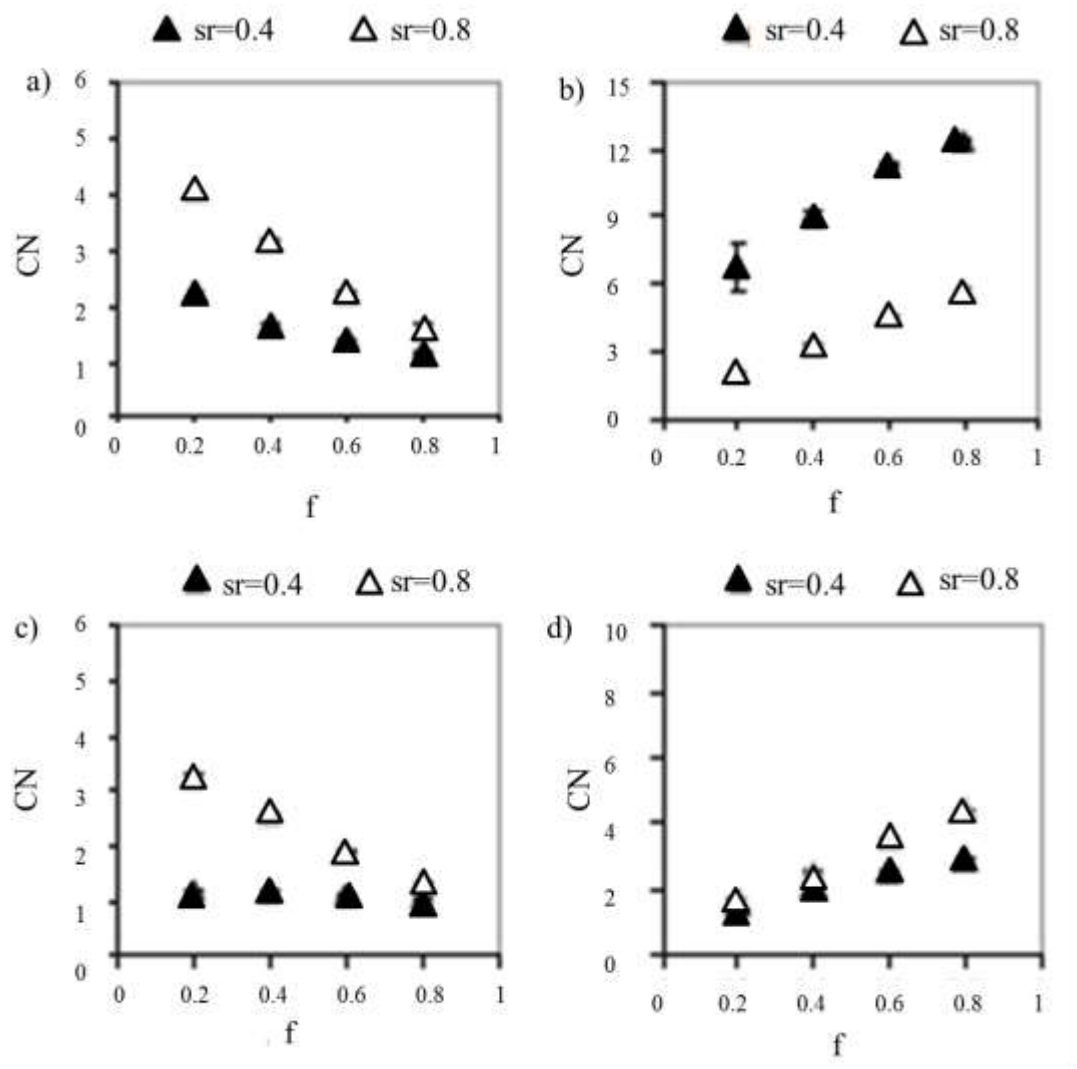

Figure 2.11 Coordination number versus fines ratio between a) large particles b) large and small particles c) small and large particles and d) small particles (modified from Wiacek, 2016)

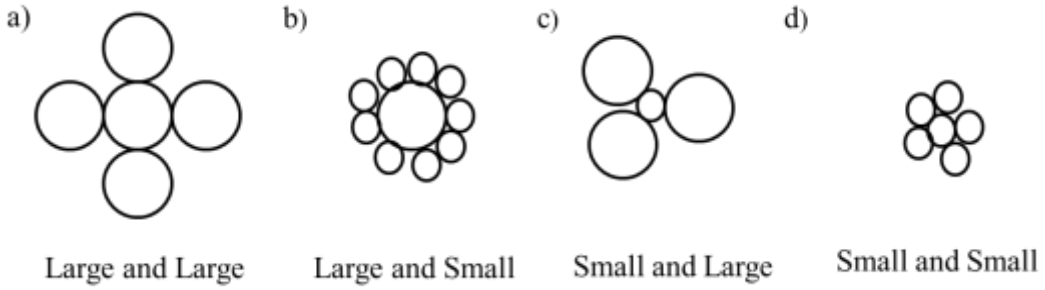

Figure 2.12 Illustration on of particle interactions to explain Figure 2.11

Table 2.2 CN in small and big particle

	sr 0.4		sr 0.8	
f	Small particles	Large particles	Small particles	Large particles
0.2	8	3	4	7
0.4	11	2.5	5	5.5
0.6	13	2	8	4
0.8	15	2	10	3

2.3.1.2 Small-strain stiffness (G_{max}) and damping ratio

Lee at al. (2009) suggested that small-strain shear stiffness G_{max} is governed by both inter-particle contacts and inter-particle coordination. Consequently, Lee et al. (2009) reported that the effective stress governing the shear stiffness G_{max} of uncemented particulate materials when capillary effects are negligible can be predicted by the semi-empirical power relation as follows:

$$G_{max} = \rho V_s^2 = A(\sigma_m'/kPa)^b \quad (2.11)$$

where σ_m' is mean effective stress, A is an experimentally determined factor which is the value of G_{max} at 1 kPa and b is the experimentally determined b-exponent, V_s is shear wave velocity and ρ is the density of the material. Equation 2.11 will allow the transition mixture (from rubber-like behaviour at low confining pressure to sand-like behaviour at high confining pressure) to be identified. As shown in Figure 2.13, Lee et al. (2009) concluded that the SRM transits from sand-like to rubber-like behaviour at rubber content of 50 to 60% depending on the sr between the sand and rubber particles.

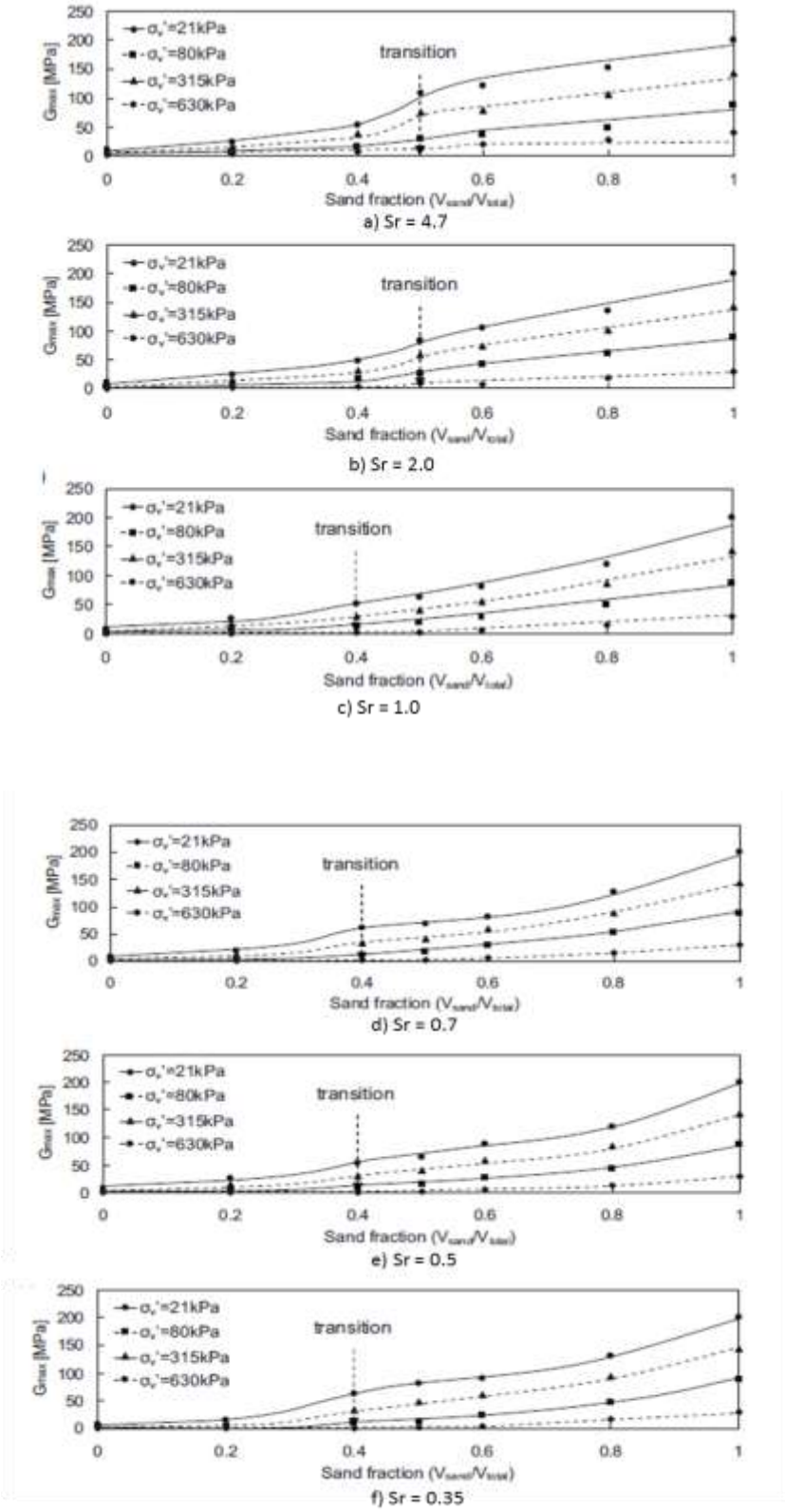

Figure 2.13 G_{max} versus Sand faction at different effective confining pressure from Lee et al. 2009

Observations by Lee at al. (2009) on transition mixture is in good agreement with Simpson and Evan (2014) who reported the transition behaviour of sand and kaolin clay mixtures in fall cone and odeometer tests. Transition threshold is defined as a small change in mixture ratio which results in a significant change in behaviour or response trend to some perturbation. In soil mechanics, percolation theory, which is use to describe liquid or fines passing through a coarser medium, has been used to describe the behaviour of a binary system as the mixture ratio of coarse to fine particles changes (Peters and Berney, 2009). Transition threshold is synonymous with the critical fines content and demarcates a transition from a state where all coarse particles are touching each other (coarse percolated) and fine particles are confined to the interstitials of the coarse particles to a state where clay begins displacing sand particles (coarse and fine particles) (Simpson and Evans, 2014). The transition from coarse and fine percolation to only fine percolation behaviour occurs at the percolation threshold of coarse material in the fines matrix. This fines content is not well known, but the percolation threshold (sand-like to clay-like) estimation by Peters and Berney (2009) corresponds to a fines content range of about 40 – 60%.

Anastasiasdis et al. (2012) measured S-wave velocity and damping ratio of SRM using resonant column and proposed the following empirical equation for small-strain damping.

$$\xi = \xi_{soil,100} \bullet \varphi \bullet (\psi \bullet R + 1) \bullet (\sigma'_m)^{\kappa} \qquad (2.12)$$

where $\xi_{soil,100}$ is the damping ratio at 100 kPa, φ and κ are determined by the gradation of the SRM (uniform or well-graded), ψ is determined by the size ratio. R is the rubber content present in the SRM in % and σ'_m is the effective confining pressure in kPa. The values proposed for the factors are shown in Table 2.3.

Table 2.3 Constants use for empirical Equation 2.12

Parameters	Anastasiasdis et al. (2012)
ψ (D_{s50} << D_{r50})	0.1004
ψ (D_{s50} >> D_{r50})	0.3683
$\xi_{soil,100}$	0.58%
φ	1.750
κ	-0.12

Equation 2.12 is based on the damping ratio of SRM with different sr and rubber contents as shown in Figure 2.14. The tests were performed for SRM with rubber content up till 35%. This suggests that Equation 2.12 may be limited to low rubber content SRM.

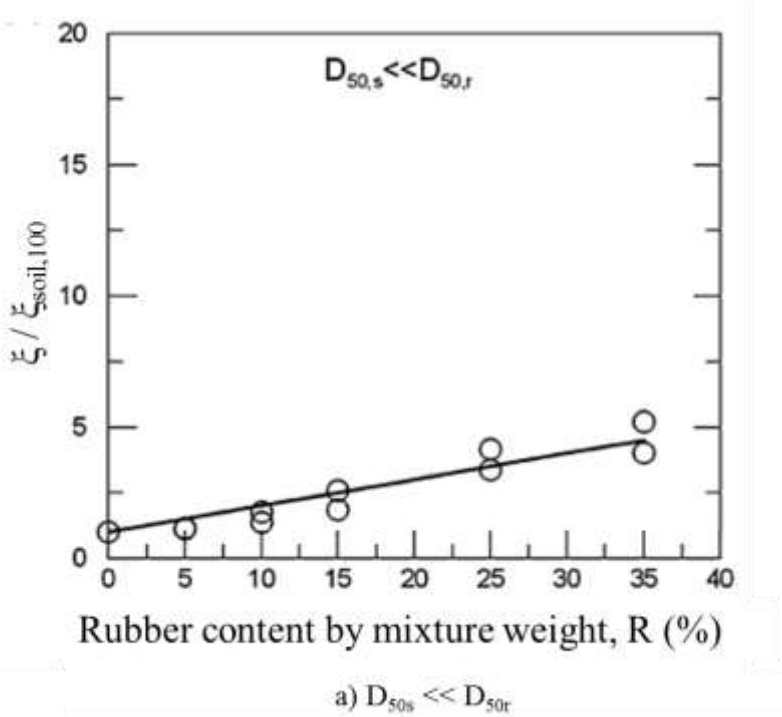

a) D_{50s} << D_{50r}

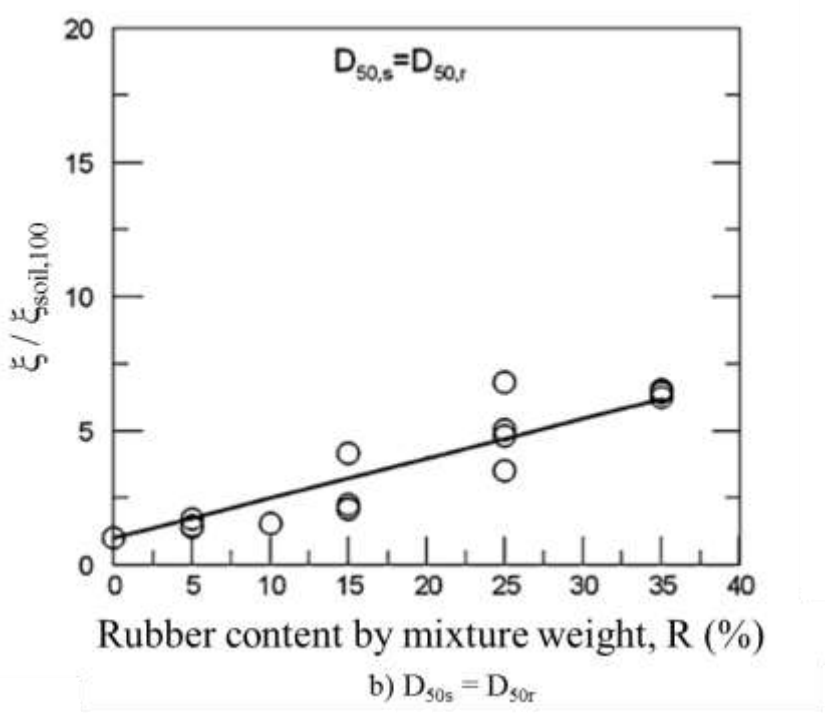

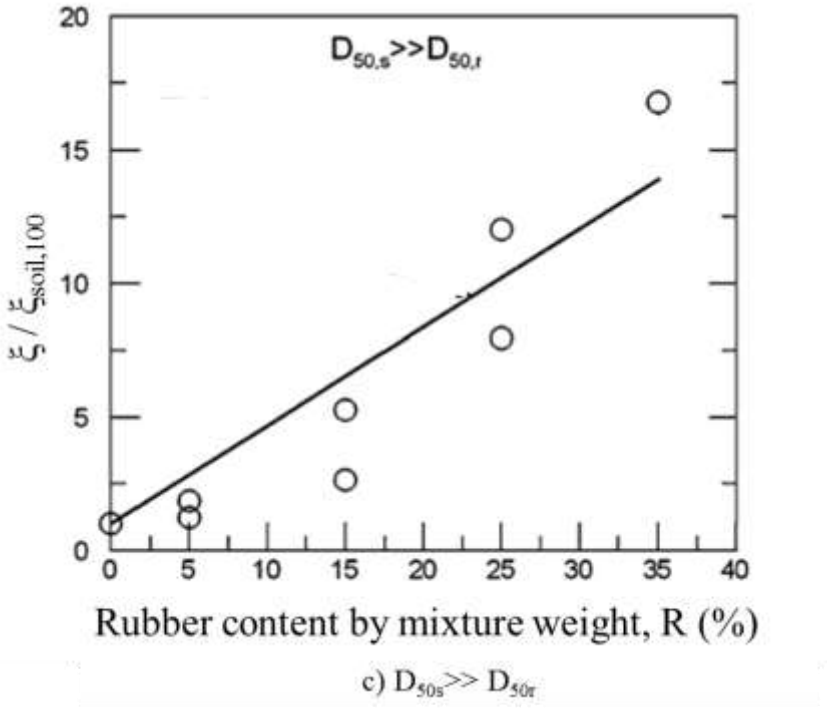

Figure 2.14 Small-strain damping ratio for SRM with different rubber contents at confining pressure of 100 kPa (modified from Anastasiasdis et al. 2012)

Generally, it has been observed that small-strain stiffness decreases and damping ratio increases as rubber content increases. However, the observation on the effect of sr on small-strain stiffness by Lee et al. (2009) differs from the observations of Anastasiadis et al. (2012) and Senetakis et al. (2012). Lee et al. (2009) observed in the study that small-strain shear stiffness G_{max} decreases with increasing sr till sr approaches unity (i.e. $D_{s50} = D_{r50}$), and then increases with increasing sr ($D_{s50} > D_{r50}$), giving a saddle shape to the trend. Anastasiadis et al. (2012) and Senetakis et al. (2012) on the other hand observed a general increase in V_s and G_{max} and decrease in damping ratio with increasing sr.

2.3.1.3 Friction angle

Shear strength tests to characterise SRM were performed as well. Mavroulidou et al. (2009), Cabalar (2011) and Singh and Vinot (2011) used direct shear test and Balachowski and Gotteland (2007), Youwai and Bergado (2003) used triaxial test to obtain the friction angle for SRM. Mechanical properties of shredded rubber chips and strips were also investigated. Wu et al. (1997) and Edil et al. (1994) performed shearing test on rubber tyre chips (diameter ranging from 2 to 38 mm) using a triaxial apparatus and found that friction angle of rubber chip ranges from 45^0 to 60^0. Ahmed (1993), Masad et al. (1996), Bressette (1984), Lee et al. (1999) and Mavroulidou et al. (2009) performed similar tests and found the friction angle to range from 18^0 to 25^0. These differences in the friction angle may be the result of differences in shapes and sizes of the rubber chips used for the SRM. Youwai and Bergado (2003), Zornberg et al. (2004) and Bergado et al. (2005) studied the effects of shape and size of the rubber chips used for the SRM and concluded that higher shear strength can be obtained with

elongated rubber shreds. Table 2.4 summaries the shear strength test performed by researchers.

Table 2.4 Shear strength tests done on SRM

s/n	Reference	Rubber content (%)	Laboratory apparatus	Observations
1	Mavroulidou et al. (2009)	0, 10, 20, 30, 40, 50 & 100	Direct shear test	• Shear strength deceases with increasing rubber content. • Minor differences in shear strength due with varying sr.
2	Cabalar (2011)	0, 5, 10, 20, 50	Direct shear test	• The increase in the percent of rubber contents in SRM lightly decreased the friction angle
3	Balachowski and Gotteland (2007)	0, 14.2, 15.2, 23, 30 & 100	Triaxial test	• Shear strength of SRM is dependent on rubber content. • Randomly distributed tyre chips/shreds have 3 to 5 times lower shear strength than horizontally oriented chips.
4	Christ and park (2010)	(Frozen SRM) 0, 10, 15, 20 & 30	Triaxial test	• All SRM were tested in frozen condition • The increase in the percent of rubber contents in SRM decreased the friction angle
5	Cetin et al. (2006)	Clay rubber mixture 0, 10, 20, 30, 40, 50 & 100	Triaxial test	• Higher confining pressure resulted in higher shear strength • The permeabilities increase as the normal pressure decreases and the rubber content increases
6	Singh and Vinot	Cohesive	Triaxial	• Compacted fine-grain

	(2011)	silty soil rubber mixture 10, 20, 30, 40 & 50	test	soil mixed with rubber chips can increase the shear strength. • Factors that the strength is dependent on are confining stress, rubber content and size ratio
7	Youwai and Begardo (2003)	0, 10, 20, 30, 40, 50 & 100	Triaxial test	• The increase in the percent of rubber contents in SRM decreases in shear strength. • Deformation of SRM is significantly reduced in SRM with less than 70% rubber content

2.4 Seismic Wave Barrier

The seismic wave barrier works on the principle of acoustic impedance. When a stress wave meets a material of different acoustic impedance (wave barrier), part of the stress wave will be reflected and part of the stress wave will be transmitted through the dissimilar material (Achenbach 1973, Rossmanith and Fourney 1982, Bulson 2002, Wang et al. 2006). A stress wave of magnitude σ_a arriving at the interface as shown in Figure 2.15a between material 1, with material properties of ρ_1 and E_1, and material 2, with material properties of ρ_2 and E_2, will result in transmitted and reflected stress waves, σ_b and σ_c, respectively, where σ is the pressure, ρ is the density and E is the Young's modulus of the material.

The stress equilibrium condition at the interface is (Smith and Hetherington, 1994):

$$\sigma_a + \sigma_c = \sigma_b \tag{2.13}$$

According to the compatibility condition, the velocity of the particle to the left must have the same velocity as the particle to the right (Smith and Hetherington, 1994); i.e.,

$$\frac{\sigma_a}{\sqrt{E_1\rho_1}} - \frac{\sigma_c}{\sqrt{E_1\rho_1}} = \frac{\sigma_b}{\sqrt{E_2\rho_2}} \tag{2.14}$$

and σ_b and σ_c can be obtained by solving Equations 2.13 and 2.14 simultaneously. The ratio of the transmitted stress σ_b to the incident stress σ_a is:

$$\frac{\sigma_b}{\sigma_a} = 2\left(\frac{\sqrt{E_2\rho_2}}{\sqrt{E_1\rho_1} + \sqrt{E_2\rho_2}}\right) \tag{2.15}$$

The above can be applied to the cases of soil-barrier-soil and soil-barrier-structure as shown in Figure 2.15b. Hence, the ratio between the transmitted stress σ_d (through material 2) to the incident stress σ_a is:

$$\frac{\sigma_d}{\sigma_a} = 4\left(\frac{\sqrt{E_2\rho_2}}{\sqrt{E_1\rho_1} + \sqrt{E_2\rho_2}}\right)\left(\frac{\sqrt{E_3\rho_3}}{\sqrt{E_2\rho_2} + \sqrt{E_3\rho_3}}\right) \tag{2.16}$$

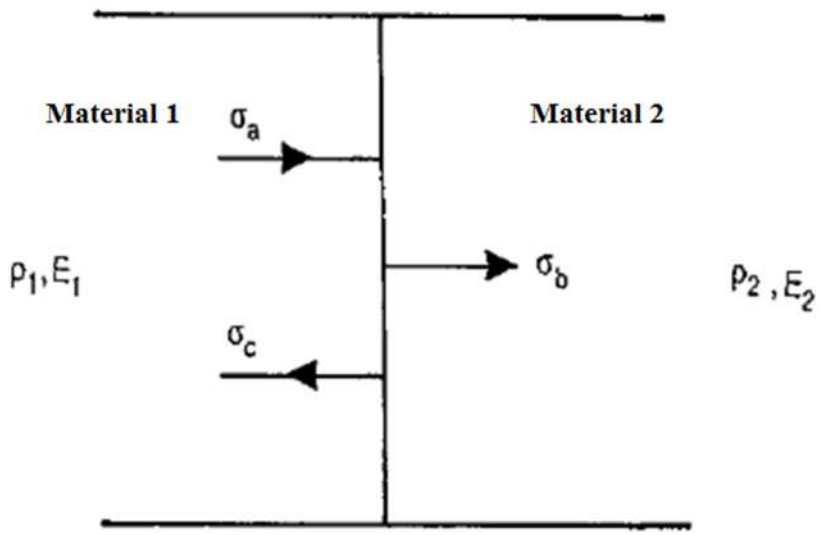

a) Transmission and reflection at the interface between two different materials

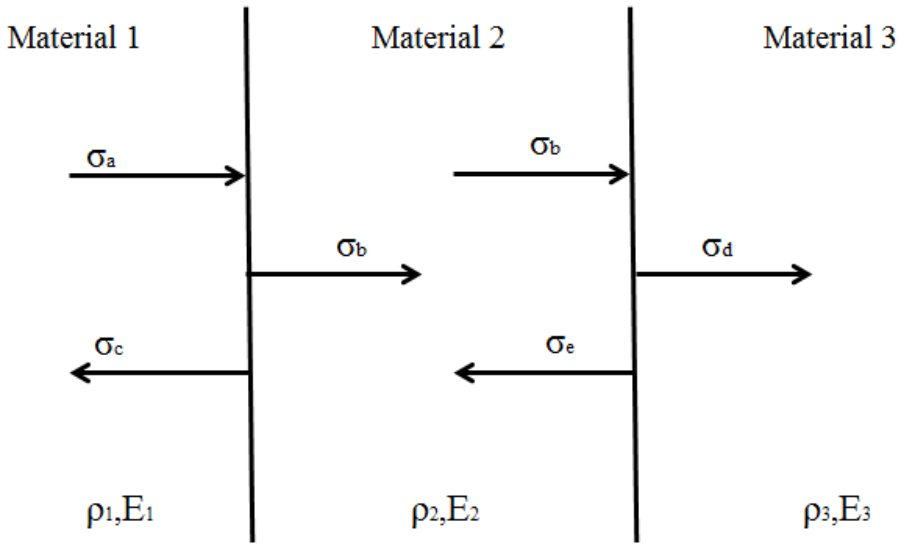

b) Transmission and reflection at the interface between three different materials

Figure 2.15 Transmission and reflection at the interface between different materials (modified from Smith and Hetherington, 1994)

2.4.1 Wave barrier for mitigation of ground vibrations

It is known that ground vibrations from machinery, traffic, rail and explosion at large distances are predominantly near the ground surface in the form of Rayleigh waves (Miller and Pursey, 1955; Smith and Hetherington, 1994). Rayleigh waves have a

lower amplitude attenuation characteristic than body waves. Thus, effectiveness in mitigation of ground vibrations relies in reducing the amplitude of propagating Rayleigh waves. One common mitigation measure is to place a vertical barrier in the path of the propagating Rayleigh waves. Woods (1968) divided the use of seismic wave barrier for reduction of vibrations into active and passive isolation systems. Active isolation system involves placing barriers around the source whereas passive isolation system involves placing the barrier at the structure that needs to be protected. Active and passive isolation systems using open trench are illustrated in Figures 2.16a and b, respectively.

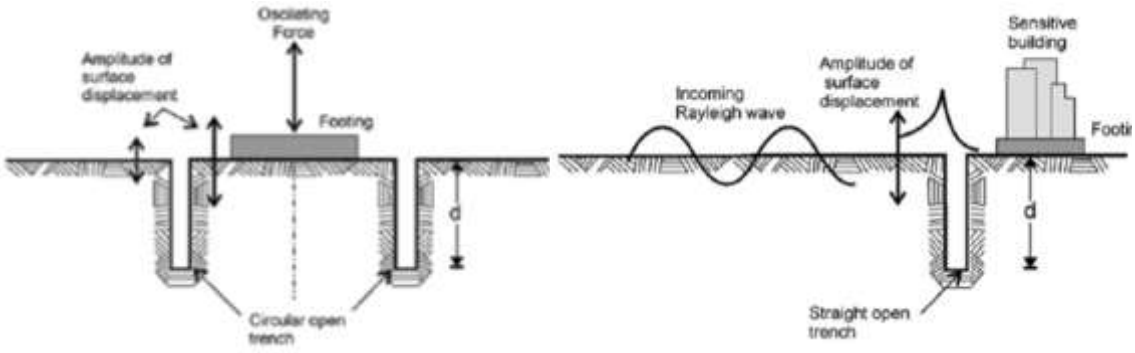

(a) Circular open trench surrounding vibrating footing (active)

(b) Straight open trench to protect sensitive installations (passive)

Figure 2.16 Schematic diagrams for vibration isolation systems (from Woods, 1968)

Dolling (1965) first proposed the use of normalised dimensions and amplitude ratio (Ar) in investigating the isolation effect. Since then, normalised dimensions play an important role when investigating efficiency of isolation system due to induced vibrations. Woods (1968) suggested that a seismic wave barrier is effective if the Ar is below 0.25. As shown in Figure 2.17, width w, depth d and length l of the barrier as well as the distance r away from the source are the main geometrical parameters

considered when designing an isolation system. For an open trench, depth d, width w and distance between source and open trench r can be normalized with λ_R, where λ_R is Rayleigh wavelength.

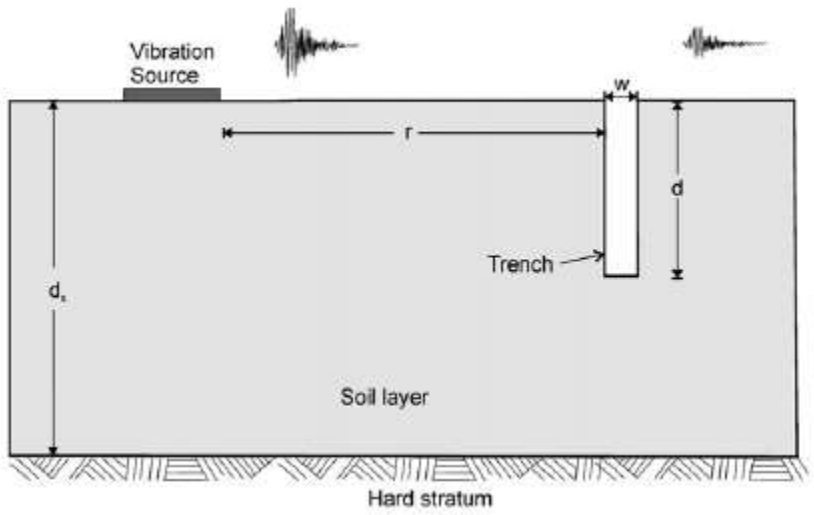

Figure 2.17 Geometry of the isolation system (from Murrillo et al., 2009)

Numerous researchers had studied the mitigating effect of seismic wave barriers using various materials or rows of piles. Materials that have been used includes concrete and geofoam. Materials that have been used as seismic wave barrier includes geofoam, water or slurries and air cushions. Table 2.5 shows a summary of the tests conducted using different materials by various researchers.

From the observation and results in Table 2.5, researchers have achieved variable success in the use of seismic wave barrier. Reasons could be due to differences in the environment under which the tests were conducted (e.g. Murrillo et al., (2009) used the centrifuge while Alzawi and Nagger (2011) and Celebi et al. (2009) conducted their experiment in an open field) and differences in soil conditions which can attribute to the differences in findings. The materials used as the barrier has also

contributed to the differences. Alzawi and Nagger (2011) concluded that an open trench is more effective than a geofoam barrier. Ahmad and Al-Hussaini (1991) concluded that both open trench and concrete barrier are effective but open trench is more effective in reducing the amplitude of incoming vibrations. This strongly suggest that material impedance plays a vital role. Although open trench has been proven to be the most effective seismic wave barrier, open trench is not practical especially in populated areas and is limited to shallow depth due to stability and ingress of rain water. From Table 2.5, effective normalized depth D ranges from 0.6 to 1.0 for active isolation system and ranges from 1.3 to 1.5 for passive isolation system. Woods (1968) and Haupt (1981) found that barrier width has minimal effect on the Ar while Celebi et al. (2009) and Ahmad and Al-Hussaini (1991) found that barrier width posted a limited effect on the Ar and is on barrier material.

Table 2.5 Summary of tests on isolation against surface vibration

s/n	Author	Trench material	Observations and results
1	Barkan (1962)	Open trench and sheet piles	• Ar decreases with increases in trench depth and length of trench • Ar decreases with increase in source frequency • Ar increases with increase in distance away from the trench
2	Woods (1968)	Open trench	• Effective for $d/\lambda_R \geq 0.6$ for active isolation • Effective for $d/\lambda_R \geq 1.3$ for passive isolation • Minimal effect of trench width
3	Dolling (1970)	Bentonite slurry barrier	• Barrier effective for $d/\lambda_R \geq 0.8$
4	Haupt (1981)	Open trench, rows of boreholes and stiff infill trench	• Barrier effective for $d/\lambda_R \geq 1$ • Trench width is unimportant

5	May and Bolt (1982)	Open trench	• Trench effective for $d/\lambda_R \geq 0.6$ for active isolation
6	Besko et al. (1985)	Open and infilled trench	• Trench effective for $d/\lambda_R \geq 0.6$ for active isolation
7	Ahmad and Al-Hussaini (1991)	Open trench and concrete barrier	• Concrete barrier effective for $d/\lambda_R \geq 1.5$ for passive isolation • Open trench effective for $d/\lambda_R \geq 1$ for passive isolation
8	Massarch (2005)	Gas cushion barrier	• Barrier effective for $d/\lambda_R \geq 0.6$
9	Murrillo et al. (2009)	Geofoam barrier	• Effective for $d/\lambda_R \geq 1.5$ • Effective width for $w/\lambda_R \geq 0.25$ • Distance away from source $r/\lambda_R \geq 0.5$
10	Tsai and Chang (2009)	Open trench	• Effective for $d/\lambda_R \geq 1.5$
11	Celebi et al. (2009) & Firat et al. (2010)	Open trench and concrete barrier	• Open trench and concrete barrier effective for $d/\lambda_R \geq 0.64$
12	Alzawi and Nagger (2011)	Open trench and Geofoam barrier	• Effective for $d/\lambda_R \geq 0.6$
13	Turan et al. (2013)	Inclined secant micro-pile walls	• Increase of d/λ_R from 0.5 to 2 shows reduction of Ar by 45%, however, no Ar below 0.25 for vertical vibration

2.4.2 Seismic wave barrier for mitigation of earthquakes

Similar to surface wave, seismic isolation using seismic wave barrier can also be employed in mitigating vibrations from earthquakes. The use of seismic wave barrier to mitigate vibration due to earthquakes using either numerical simulation or model test using a shaking table showed different degrees of success. A summary of the work done is presented in Table 2.6. The major advantage of using model test over prototype test is that it is less expensive, less time consuming and can be done in a

controlled environment (Shehadeh, 2015). However, model test has to be scaled using the law of similitude for it to correctly represent the prototype condition.

Table 2.6 Summary of tests on isolation against earthquake loadings

s/n	Author	Barrier material	Observations and results
1	Inglis et al. (1996)	Geofoam	• Numerical simulation • 50% in reduction of lateral loads
2	Bathrust et al. (2007)	Geofoam	• Model test using shaking table • Geofoam can effectively reduce the induced dynamic vibration
3	Hazarika et al. (2008)	Rubber-soil mixtures	• Model test using shaking table • Depending on the location of the sensors, reduction of displacement can go up to 85%
4	Uchimura et al. (2008)	Rubber-soil mixtures (Rubber contents of 15, 30 and 40%)	• Model test using shaking table • Rubber-sand mixtures have high liquefaction resistance
5	Xu (2010)	Rubber-soil mixtures (Rubber content of 75%)	• Numerical simulation • Reduction of magnitude of vibrations ranging of 30% to 70% depending on the location of the building • Results are influenced by the thickness of the soil-rubber mixtures and the width of the building
6	Tsang et al. (2013)	Rubber-soil mixtures (Rubber content of 75%)	• Numerical simulation • Reduction of acceleration caused by earthquake loadings ranging from 60% to 90% depending on the direction of the load
7	Pitilakis et al. (2015)	Rubber-sand mixtures (Rubber content of 30%)	• Numerical simulation • A average reduction ranging from 30 to 40% on the base shear forces, maximum bending moments and maximum inter-storey structure

2.4.3 Seismic wave barrier for mitigation of ground shock

It is well known that blasting caused by explosion could potentially damage a structure in the path of the blast wave propagation. Studies on using different materials as seismic wave barrier has been investigated both numerically and experimentally. Beside concrete and geofoam, materials used include liquids, fibrous and composite materials such as carbon and glass fibre-reinforced polymeric composites. Table 2.7 summarises the work done on using seismic wave barrier to mitigate against ground shock from blasting. While some materials were found to be effective in reducing incoming incident pressure, their use may not be practical for protection of underground structures. Use of materials such as water, glycerin and aerogel poses a challenge for protection of underground structure. Schimizze et al. (2012), Homae et al. (2007) and Allen et al. (2004) concluded that density of the material contributes significantly to the reduction of peak pressure caused by explosion.

Table 2.7 Summary of Tests on isolation against ground shock

s/n	Author	Barrier material	Observations and results
1	Davis (1994)	• Geofoam • Reinforced concrete wall • Walled open trench	• Experiment conducted using centrifuge • It was concluded that barriers of low acoustic impedance materials (polystyrene and open trench) were highly effective in attenuating the propagating stress waves and reducing the magnitude of shock loading on structures.
2	Wang et al. (2006)	• Geofoam	• Numerical simulation • Use of geofoam effectively reduces the pressure • Length of the geofoam block used plays a more significant role over thickness in reduction of pressure

			• Multiple geofoam blocks should be used to improve the capability of the geofoam block in reduction of pressure
3	Kobielak et al. (2006)	• A series of PVC pipes	• Field experiment • It was observed that as the distance between the explosive source and the structure increases, the effectiveness of the pipes in reducing the pressure is increased. • It was also found that as the charge weight and detonation depth increases, the acceleration experienced by the structure increases.
4	Wang et al. (2009)	• Open trench • Concrete • Water • Geofoam	• Numerical simulation based on the centrifuge experiment done by Davis (1994) • Open trench is the most effective. • Reduction of pressure ranges from 18 to 30% dependent on the density of the geofoam used. • Concrete trench shows the least reduction in pressure (15%)
5	Schimizze et al. (2012)	• Water • Glycerin • Aerogel • CAB-O-SIL • Glass beads • Expanding foam • Tuff	• Experiment using shock tube • Results showed that acoustic impedance and the density of the material play an important role in its ability to mitigate the blast wave and materials with a lower density tend to perform better.
6	Zhou et al. (2013)	• Cellular solid	• Numerical simulation • Result shows a reduction of 80% in pressure
7	Pichandi et al. (2013)	• Glass fibre-reinforced polymer • Carbon fibre-reinforced polymer • Steel fibre • Aramid	• Experiment using shock tube • Results showed that the utilization of fibrous and composite materials as retrofits of existing structures can significantly increase the blast protection by reducing fragmentation and debris

		• Hybrid textile	
8	De et al. (2013)	• Geofoam • Concrete	• Numerical simulation • Both material have shown reduction pressure

2.4.4 Summary on Seismic Wave Barriers

Davis (1994), Wang et al. (2006) and De et al. (2013) had investigated the use of low impedance materials such as geofoam, water, open or in-filled trench as seismic wave barriers both experimentally and numerically. Although open trench proved to be very effective in mitigating incoming vibrations or ground shock, it is impractical due to stability and implementation issues. Stability of open trench becomes more pronounced with increase in trench depth and there in the possibility of water ingress.

Geofoam has become popular in recent years as an effective seismic wave barrier (Alzawi and Nagger 2011, Murrillo et al. 2009, Xu 2009, Wang et al. 2009, Davis 1994, Bathrust et al. 2007). However, the exceptional performance of geofoam is due to its lightweight property (approximately one per cent of the weight of the soil and 10 per cent of the weight of light-weight fill). There are several disadvantages in using geofoam as a seismic barrier material:

1. Geofoam are rigid and may encounter problem in shaping and effectively filling up small gaps between soil and structure.
2. Physical properties of geofoam provided by the manufacturer shows that low density geofoams have compressive resistance of 40 kPa at 10% strain which suggest that the geofoam's performance at greater depth might not be as effective as it can perform at shallow depth.

3. Geofoam subjected to explosions may be shattered (Skews et al. 1993, Britan et al. ,1992, 2012, 2013 and Sugiyama et al. 2014). Britan et al. (1992, 2011) suggested particle-laden foam to overcome the shattering of geofoam caused by the blast wave. Particle-laden foam is essentially conventional geofoam with the addition of a mixture of coal fly ash particles to 5% fire-fighting surfactant in tap water (Britan et al. 2009). However, doing so will potentially increase the weight and density of the geofoam. Which may reduce its effectiveness in reducing peak pressure caused by explosion (Schimizze et al. 2012, Homae et al. 2008 and Allen et al. 2003). The efficiency of the particle-laden foam in reducing peak pressure has yet to be investigated.
4. Reduction in pressure by low acoustic impedance material like polystyrene or geofoam subjected to large amplitude vibrations such as earthquake or underground explosions, is due to its compressive-inclusion property (i.e., the inherent strength of the geofoam is mobilized through the yielding of the ground) rather than damping (Hovarth, 1994; 1995). This would mean that geofoam might potentially be ineffective and fails as a seismic barrier when subjected to large peak overpressure.

2.5 Research gaps

The use of SRM as a seismic wave barrier to mitigate vibration from surface waves and ground shock has not been fully investigated. To date, only a handful of researchers (Anastasiadis et al. 2012, Senetakis et al. 2012, Kim and Santamarina 2008, Lee et al. 2010, Feng and sutter 2000, Pamukcu and Akbulut 2006, Cheng 2015) investigated the wave propagation properties of SRM with limited range of rubber content. Damping or relative size ratio were not investigated. Thus, there is a

need to study the wave propagation properties of SRM besides shear strength properties. This set of data will contribute to the understanding of SRM for application in dynamic problems.

From the literature, the use of SRM as seismic wave barriers against earthquake loadings were investigated by Xu (2009), Tsang et al. (2007), Senetakis et al. (2009), Hazarika et al. (2007, 2008) and Uchimura et al. (2007) experimentally in the laboratory or/and and numerically only. Field experiments to investigate the use of SRM as seismic wave barrier under blast loading and surface wave vibration are scarce. It is known that earthquake loading, blast loading and surface wave vibration behave differently due to the wave's content and the loading magnitude. When blast loads hits the surface of a structure, the loads are transmitted to other parts of the structure. On the other hand, earthquake loadings cause inertia loading effects on the entire structure. Therefore, in the case of blast loadings, each part of the structure is subjected to rapid moving shock and should be designed to resist blast loadings. Blast loadings exert pressure much greater than earthquake loadings (Prasad, 2011). Excessive vibration (mainly surface wave) as a result of human activities cannot be over looked as it may cause discomfort or even harm to people. In view of these differences in the type of loading, the use of SRM as seismic wave barriers against blast loads and surface wave vibration should be investigated.

It is also rare to find the literature where both field experiments and numerical modelling are performed a t the same time especially for blast loadings. To effectively simulate the small-scale field test for underground explosion, numerical simulation must be able to simulate the responses of elastic (far-field) and plastic (near-field) zones correctly. Hence, the numerical model needs to be verified. Thus, combinations

of laboratory, field experiments and numerical modelling is important to provide a greater understanding of SRM as a seismic wave barrier.

Chapter 3 Characterisation of Sand-rubber Mixtures

3.1 Introduction

Sand-rubber mixtures (SRM) are highly variable and are dependent on the characteristics as well as the mix proportion of the sand and rubber contents. It is important to characterise the SRM in order to understand the factors contributing to its performance as a seismic wave barrier. Basic material properties tests such as minimum and maximum dry densities, specify gravity and grain size distribution were performed. Shearing and wave propagation test were carried out using a triaxial cell modified with bender elements on different sand and rubber mix proportions at different effective confining pressures.

3.2 Materials

The materials used for the study were construction sand and rubber chips from used rubber tyres. Figure 3.1 shows the grain size distribution of the sand and rubber chips. The rubber chips were produced by grounding used rubber tyres in cracker mills. Two sizes of rubber chips were used. Coarse rubber chips were those passing through sieve size of 2.36 mm and retained on sieve size of 1.18 mm while fine rubber chips were those passing through sieve size of 0.6 mm and retained on sieve size of 0.3 mm. Two types of SRM were studied: one with the coarse rubber chips and the other with fine rubber chips. Figure 3.2 shows the sand and rubber chips used for this study. Table 3.1 shows the properties of the sand and rubber chips. As the specimens prepared have a diameter of 50 mm; the maximum particle size should not be more than one-sixth of the specimen diameter as stated in ASTM D4767-11 (2011). A total of four

sizes of sand were used. Sand with Ds_{50} of 3.6, 1.8, 0.9 and 0.45 mm were those passing sieve sizes of 4.65, 2.36, 1.18 and 0.6 mm and retained on sieve sizes of 2.36, 1.18, 0.6 and 0.3 mm, respectively. Table 3.2 summarises the mix proportions and the size ratios used for the study. Each specimen was named according to size ratio, rubber content and confining pressure. For example, a specimen denoted as sr8-R50-CP200 has size ratio (sr) of 8, rubber content (R) of 50% by volume and subjected to an effective confining pressure (CP) of 200 kPa.

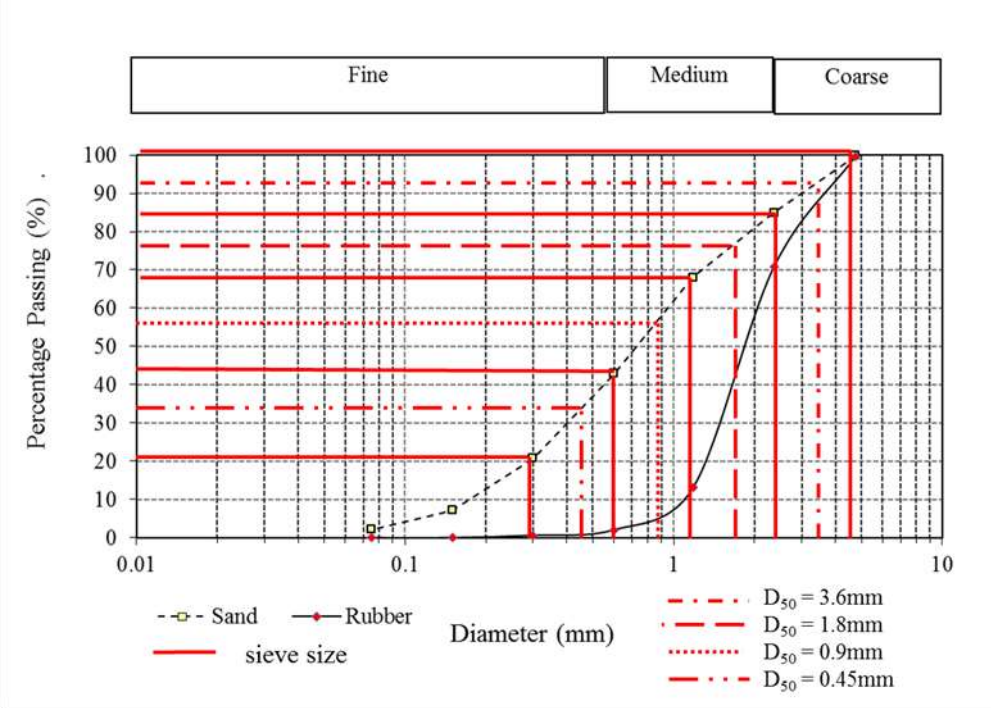

Figure 3.1 Grain size distributions of rubber chips and sand

Figure 3.2 Materials used for the study

Table 3.1 Material properties

	Sand	Rubber chips
Specify gravity	2.7	1.47
Min. dry density (g/cm^3)	1.31	0.36
Max. dry density (g/cm^3)	1.77	0.51
Max. void ratio	1.06	3.09
Min. void vatio	0.53	1.86

Table 3.2 SRM specimens

Series	Size ratio (sr) (D_{s50}/D_{r50})	Sand mean size D_{s50} (mm)	Rubber chip mean size D_{r50} (mm)	Sand	SRM 30% (R30)	SRM 50% (R50)	SRM 70% (R70)	Rubber
sr8	8	3.6	0.45	-	√	√	√	-
sr4	4	1.8	0.45	-	√	√	√	-
sr2	2	0.9	0.45	√	√	√	√	√
sr0.5	0.5	0.9	1.77	√	√	√	√	√
sr0.25	0.25	0.45	1.77	-	√	√	√	-

3.3 Fabrication of Bender Element

The triaxial cell used was modified to include bender elements from Piezo Systems Inc. USA. The top and bottom platens were fitted with a Y (T220-A4-303Y) and X (T220-A4-303X) pole bender elements, respectively. The bender element protrudes about 5 mm from the face of the platen. The fabrication of the bender elements are as follows:

1. Bender element of dimensions of 0.51 mm (thickness) by 8 mm (width) by 12.7 mm (length) was cut from the original piece (0.51 mm by 12.7 mm by 31.5 mm) using a sharp cutter.
2. A sharp cutter is used to mark out about 4 mm lengthwise as demarcation for the piezo-ceramic material to be filed down to exposed the metal shim at the centre using sand-paper.
3. A multi-meter is used to check the resistance and capacitance of the bender element. The multi-meter should reflect an open circuit at all times. Capacitance between the metal shim and ceramic layer on both sides is about two times the capacitance between ceramic layer and ceramic layer.
4. Three wires (red, black and white) are then soldered onto the three bender element layers using conductive soldering flux. The red and black wires are soldered to the ceramic and the white wire is soldered to the centre metal shim.
5. The resistance and capacitance of the bender element are checked after the soldering of each wire to ensure no shorting of the bender element. In the event of the bender element being shorted, alcohol is used to clean off the conductive soldering flux.

6. A thin layer of Teflon tape was used to wrap the red, black and white wire with the bender element. Aluminium tape is then used to wrap the bender element. The grounding wire was then soldered to the aluminium tape to provide electrical shielding from interference such as crosstalk. The bender element is then wrapped with another layer of Teflon tape.
7. The bender element is then slotted into an acrylic casing fabricated to house the bender element. The bender element is then sealed using a slow setting epoxy and left to set for two days.

In order for the bender element to transmit and receive different waves, connection is done according to Table 3.3 and Figure 3.3 as described in Leong et al. (2009).

Table 3.3 Wiring configuration of bender elements (from Cheng, 2015)

Wave Type	X-Poled (Top)	Y- Poled (Bottom)
P-wave	Parallel	Series
S-wave	Series	Parallel

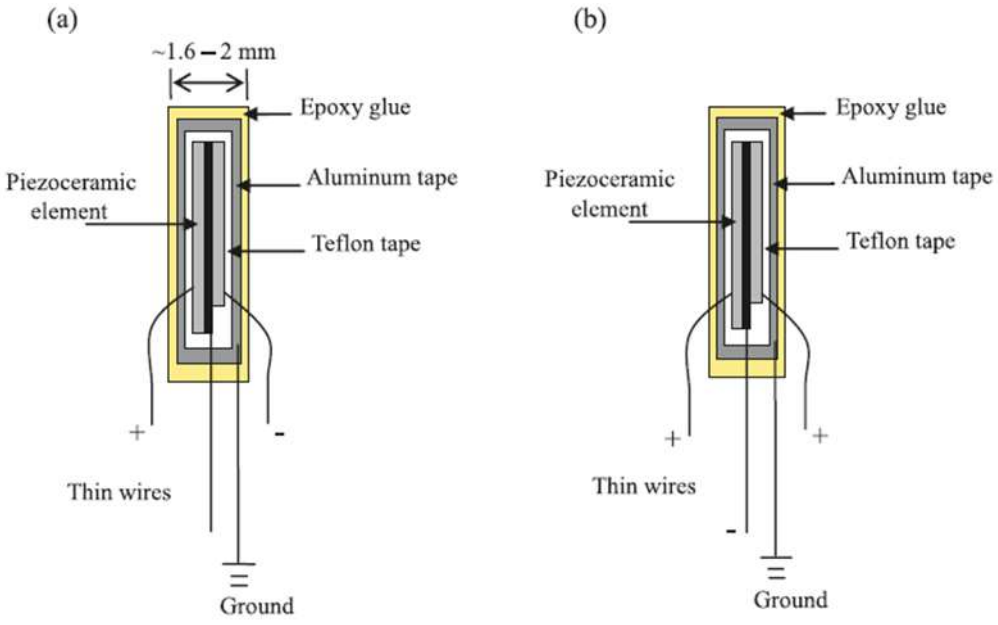

Figure 3.3 Insulation of bender elements and its (a) series and (b) parallel wiring configuration (from Leong et al., 2009)

3.4 Experimental Set-up and Sample Preparation

A standard digital pressure-volume controller from GDS was used to provide confining pressures of 50, 100, 200 and 400 kPa. A single sinusoidal voltage pulse was generated by the function generator (Hewlett-Packard model 33120A) to excite the bender elements amplified by a Piezo systems EPA-104 signal amplifier. Yokogawa DL750P digital oscilloscope was used to record the trigger and transmitted signals. The experimental set-up is shown in Figure 3.4.

The void ratio e of the SRM specimens were all maintained at 0.6. To prepare uniform specimens, the sand and rubber chips were divided into five equal parts. One part of sand and one part of the rubber chips were mixed and tossed in a plastic beaker for about 20 times (to ensure a homogenous mix) before pouring carefully into a split mould of 100 mm in height and 50 mm in diameter lined with rubber membrane that was attached to the bottom platen of the triaxial cell using a funnel. The SRM was pour into the spilt mould by moving the funnel in a circular motion and ensuring that the tip of the funnel is just above the SRM surface. Each layer is then compacted using a tamping rod of diameter 20mm for 20 times to achieve a void ratio of 0.6 before the next layer is poured. The SRM specimens were tested dry in the triaxial apparatus. Table 3.4 shows the weight compositions of sand and rubber chips to form the SRM of different rubber content used for this study. Cheng (2015) performed tests on perfectly segregated SRM specimen and concluded that the V_s shows a maximum

reduction of 19% from homogenous SRM specimen and suggested that intermediate segregation will incur less discrepancy.

Table 3.4 Weight compositions of sand and rubber chips in specimens of different rubber contents

Sand-rubber mix ratio (rubber percentage)	Mass of sand (g)	Mass of rubber (g)	Bulk density (kg/m^3)
0	227.6	0	1656
30	159.3	17.4	1286
50	113.8	29.1	1040
70	68.3	40.7	793
100	0	58.1	423

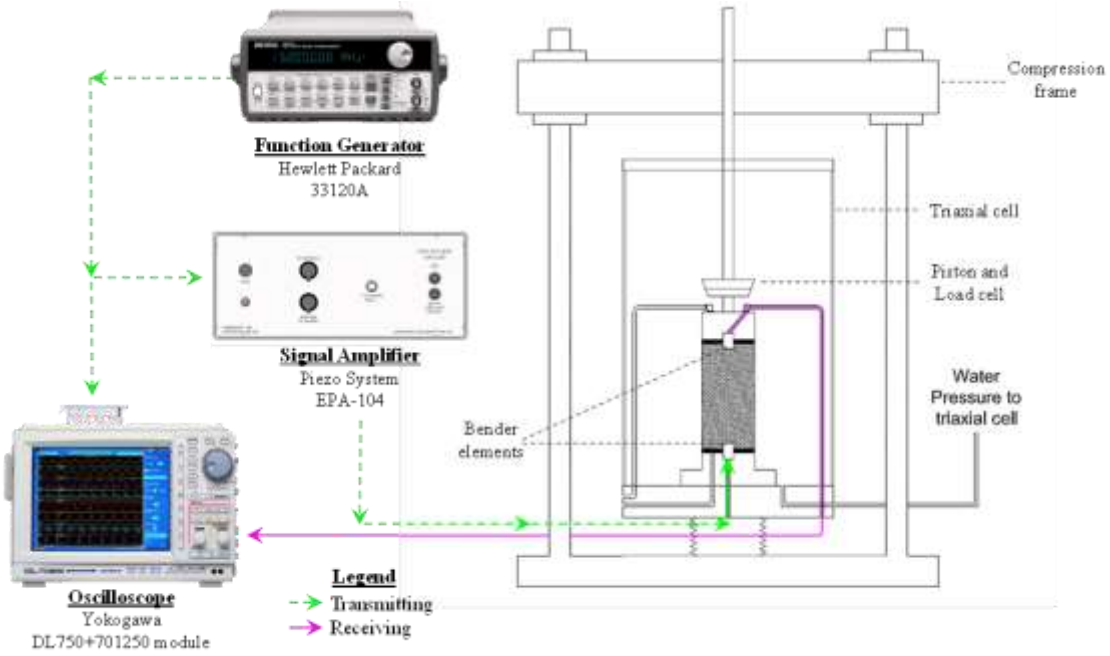

Figure 3.4 Schematic diagram of test set-up (from Cheng, 2015)

3.5 Bender Element Test

The excitation frequencies use for P and S waves were 10, 20 and 50 kHz and 3, 5, 10 and 20 kHz, respectively, as recommended by Cheng and Leong (2014b) to obtain signals of high signal to noise ratio. Signals obtained were processed using Matlab software. The signal was first Fast Fourier Transformed (FFT) to identify the frequency range of the signal. Cheng and Leong (2015) found that the dominating frequency range of the receiver signal is independent of the excitation frequency and there is a slight increase in intensity with the increase in confining pressure due to stiffening of the specimen. Typical FFT plots showing the effects of excitation frequency and effective confining pressure on the P-wave and S-wave signal are shown in Figure 3.5. From Figure 3.5, it is observed that the intensity for P-wave signal is significantly lower than the S-wave signal. This observation is due to smaller displacement of the bender element in the extension mode (Lings and Greenings, 2001) which resulted in the P-wave signal being weak and noisy. This problem becomes more pronounced with tests involving loose granular soil or specimen with high damping ratio at low confining pressure (Cheng, 2015).

The signal received or transmitted by the bender element can be distorted by noise, electrical drift and crosstalk (Lee and Santamarina, 2005). While noise and electrical drift, which is due to background electromagnetic signals, can be reduced by ensuring that the signal cables are in parallel and not crossing one another. However, crosstalk is difficult to eliminate. Crosstalk is attributed to the leaking of signals from transmitter to receiver through electromagnetic coupling (Lee and Santamarina, 2005). Crosstalk can only be reduced and not eliminated by providing adequate shielding.

A bandpass Butterworth digital filter was used to retain the dominating frequencies between 0.5 and 5 kHz. It was chosen such that it does not affect the signal to be analysed. Hence, low frequency electrical drift and high frequency noise which affect the determination of the arrival time and damping ratio are removed using the filter. Figures 3.6a and 3.6b show typical time-history plot for raw and filtered P-wave and S-wave signals.

a FFT for S-wave signals at excitation frequencies of 3, 5 and 10 kHz subjected to effective confining pressure of 100 kPa

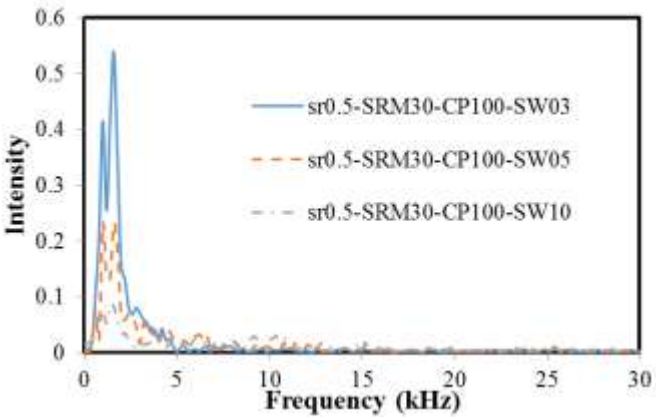

b FFT for P-wave excitation frequencies of 10, 20 and 50 kHz subjected effective confining pressure of 100 kPa

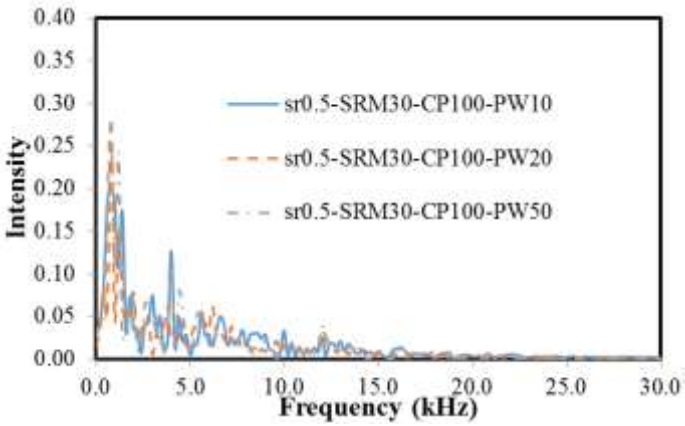

c FFT for S-wave signals at excitation frequency of 3 kHz subjected to effective confining pressures of 100, 200 and 400 kPa

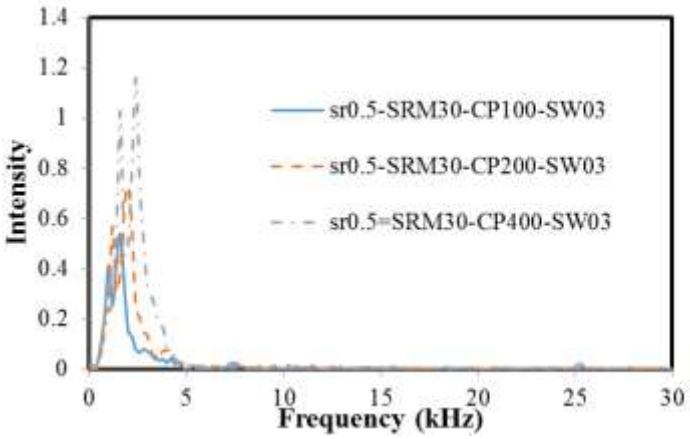

d FFT for P-wave signals at excitation frequency of 10 kHz subjected to effective confining pressures of 100, 200 and 400 kPa

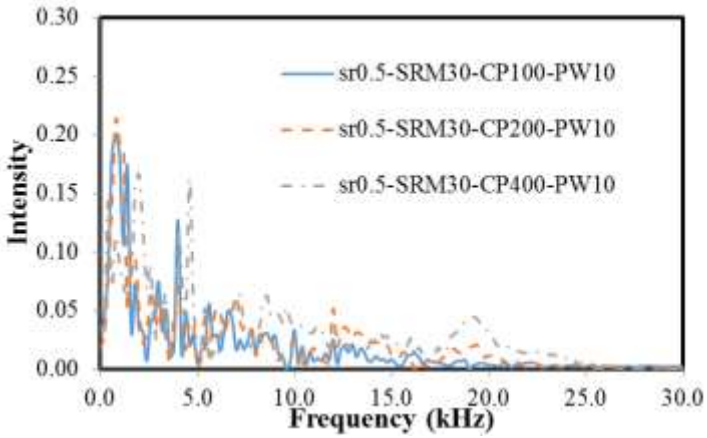

Figure 3.5 FFT plots of S and P wave signals

3.5.1 Determination of V_p and V_s

Determination of wave arrival time in bender element tests can be subjective and is still debated amongst researchers. Identification methods are generally categorized into time and frequency-domain methods. Frequency-domain methods can be further divided into cross-correlation and cross spectrum techniques. Cross-correlation technique works by picking up similar features between the transmitting and the receiving signals (Santamarina and Fratta, 2005) with the arrival time chosen based on the time where the feature peak amplitude (e.g) occurs. Cross spectrum technique on the other hand is an improvement of cross-correlation technique where phase

analysis is performed on the cross-power spectrum derived from the frequency spectra (Viggiani and Atkinson, 1995). The slope of the relationship between amplitude and phase angle with frequency gives the arrival time.

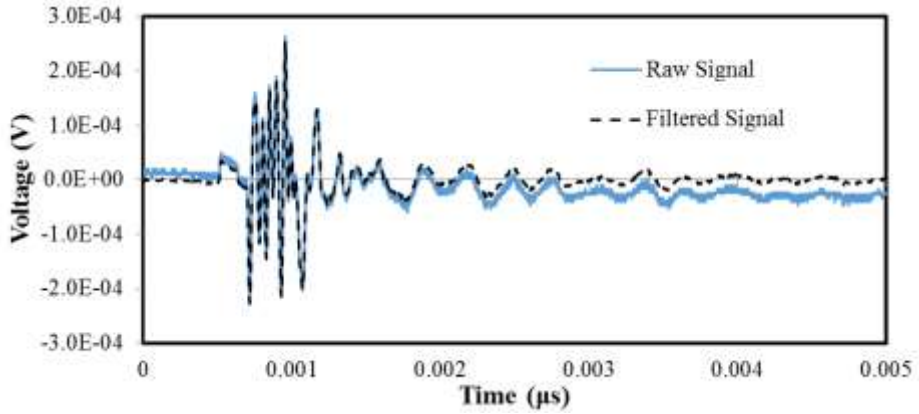

a) P wave

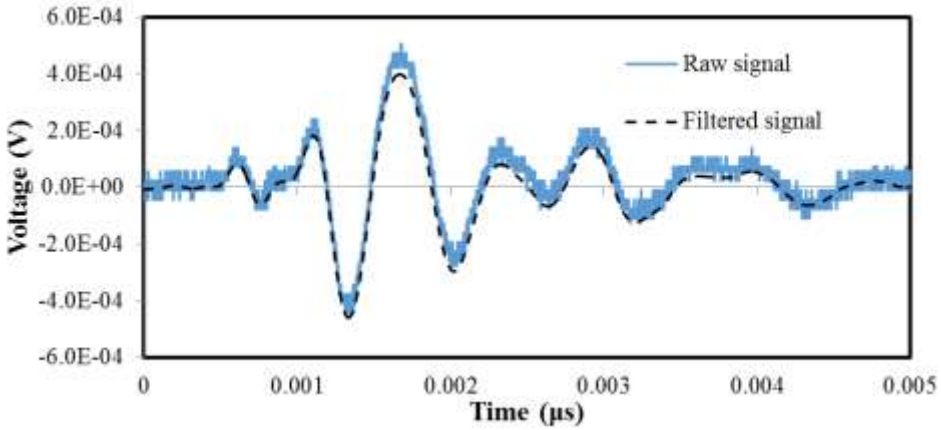

b) S wave

Figure 3.6 Raw and filtered signals

However, the transmitted wave is assumed to have the same frequency and shape as the receiver wave when using both cross-correlation and cross-spectrum technique (Jovicic et al., 1996, Santamarina and Fam, 1997). The reliability of frequency domain methods is questionable as this assumption only holds true when excitation frequency exceeds the natural frequency of the bender element (Rio 2006, Marjanovic and Germaine 2003) and there is no interference from the reflected waves.

Time-domain methods involve picking features on the receiver signal that indicate the wave arrival time. The feature can be the first defection, first maximum, zero after first bump and first major peak as shown in Figure 3.7 (Lee and Santamarina, 2005). In a S-wave signal, the receiver signal contains interference caused by the faster P wave known as the near-field effects, which further complicates the identification of the S-wave arrival time (Sanchez-Salinero et al. 1986, Arulnathan et al. 1998). Leong et al. (2009) recommended the following criterion for, a more reliable identification of the S-wave arrival time:

$$\frac{L_{tt}}{\lambda} = \left(\frac{L_{tt}}{V}\right) f_{in} = f_{in}\Delta t \geq 3.33 \tag{3.1}$$

where L_{tt} is the tip-to-tip distance of the bender element, λ is the wavelength, V is the wave velocity, f_{in} is the input excitation and Δt is the wave travel time. The input wavelength λ depends on the excitation frequency and may not coincide with the actual frequency due to coupling between the bender element and specimen. Brignoli et al. (1996) suggested the use of the predominant output frequency of the receiver, Arulnathan et al. (1998) and Leong et al. (2009) on the other hand, suggested the use of input excitation frequency as λ to calculate the $L_{tt}\lambda$ ratio. All researchers cited above agreed on the importance of using a wide range of excitation frequencies so as to effectively differentiate the near-field effect region and the arrival time. This is further illustrated in Figure 3.7. Since near-field effect is the result of interference caused by P wave, knowledge on the arrival time of P wave will assist in the identification of the near-field effect. From Figure 3.7, the near-field effect is represented by the region indicated as A, B and C. The zero crossing after first bump, point C in Figure 3.7 is recommended to be used by Leong et al. (1999) to be the S-wave arrival as convergence of arrival time was observed when $L_{tt}/\lambda > 3.33$. As the

time-domain method involves less assumption. The time-domain method is preferred for this study.

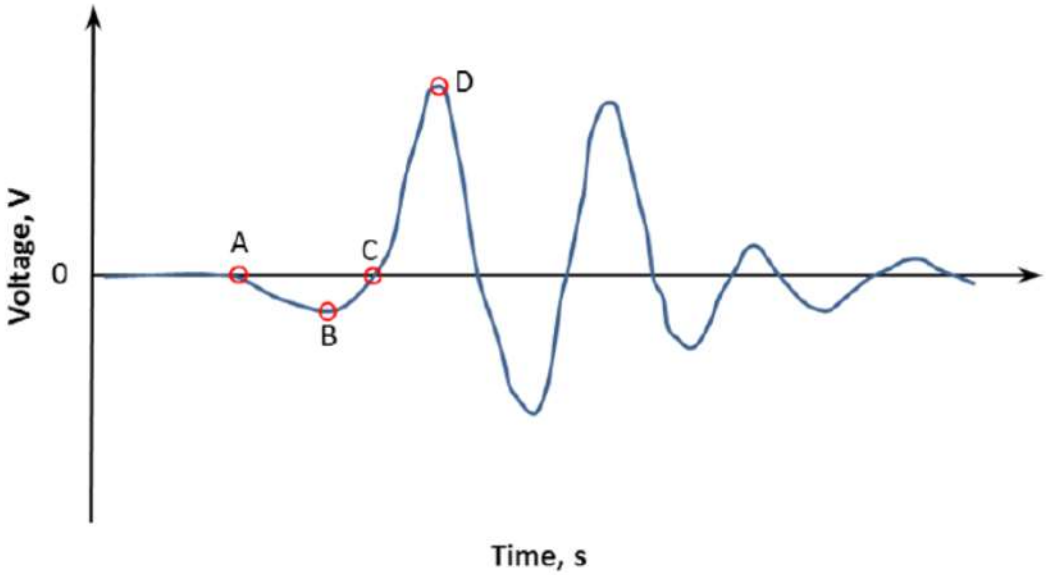

Figure 3.7 Characteristic signal displaying prospective features for arrival time: (A) First deflection, (B) First bump, (C) Zero after first bump and (D) First major peak (modified from Lee and Santamarina, 2005)

The P and S-wave velocities (V_p and V_s) were determined by dividing the tip-to-tip distance of the bender elements by travel time (t). Reliable travel time can be determined by evaluating the arrival times at various excitation frequencies of 3, 5, 10 and 20 kHz for S wave and 10, 20 and 50 kHz for P wave as recommended by Leong et al. (2009). Small-strain shear modulus G_{max} can be obtained using V_s and density of the specimen as shown in Equation 3.2:

$$G_{max} = \rho.V_s^2 \tag{3.2}$$

where ρ is the density and V_s is the shear wave velocity.

Figures 3.8a and b show typical time-histories of P and S waves excited at different frequencies. The time histories are amplified digitally to show the start and arrival times clearly. The early part of the receiver signal was affected by crosstalk. Some low frequency drift is due to electromagnetic interference. The crosstalk and drift can be minimized through proper shielding and grounding of the wires.

a)

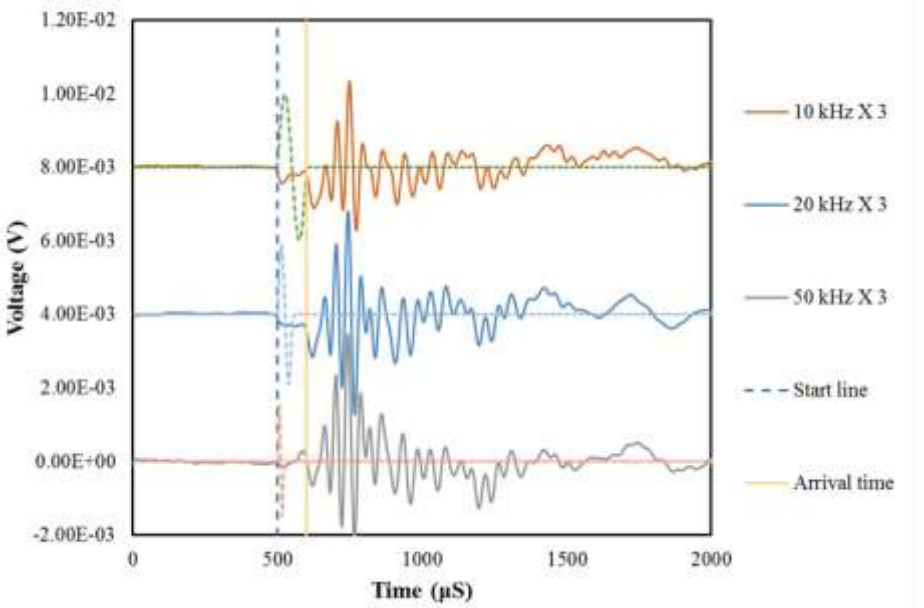

b)

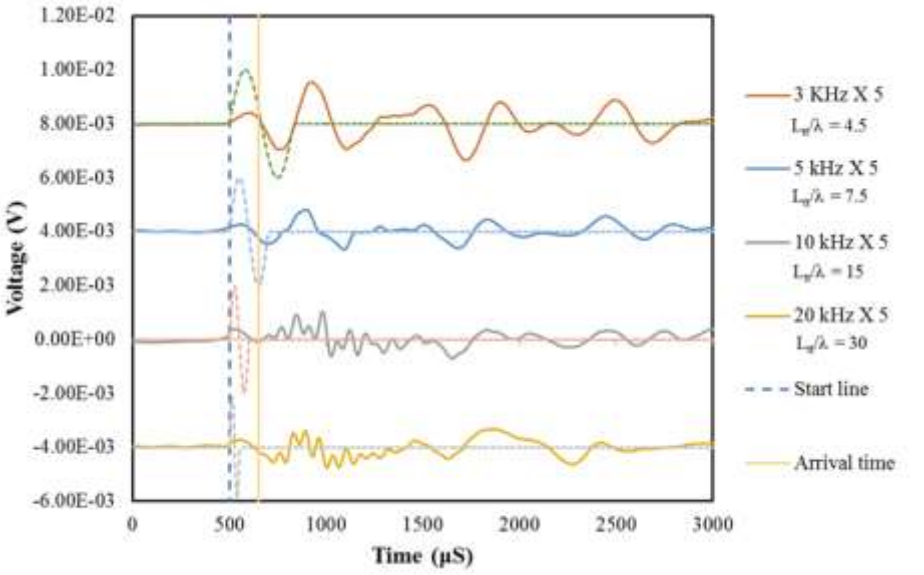

Figure 3.8 Time histories of P and S wave signals

3.5.2 Determination of damping ratio

Hilbert transformation method is selected for obtaining the damping ratio, over other methods such as the logarithmic decrement method, half-power bandwidth method and spectral ratio method. The S-wave receiver signal from the bender element tests was used to obtain the damping ratio. The receiver signal contains a transient signal which is caused by the initial excitation pulse and a steady-state free vibration decay corresponding to the natural frequency of the specimen when the transient effect from the excitation pulse dies off (Cheng and Leong, 2018). The steady-state free vibration decay signal is used to determine the damping ratio. The details of the determination of damping ratio can be found in Cheng and Leong (2018). A Matlab script file developed by Cheng and Leong (2018) was used for the determination of the damping ratio. Cheng and Leong (2018) has shown that the Hilbert transformation method is more robust over the other methods for bender element tests.

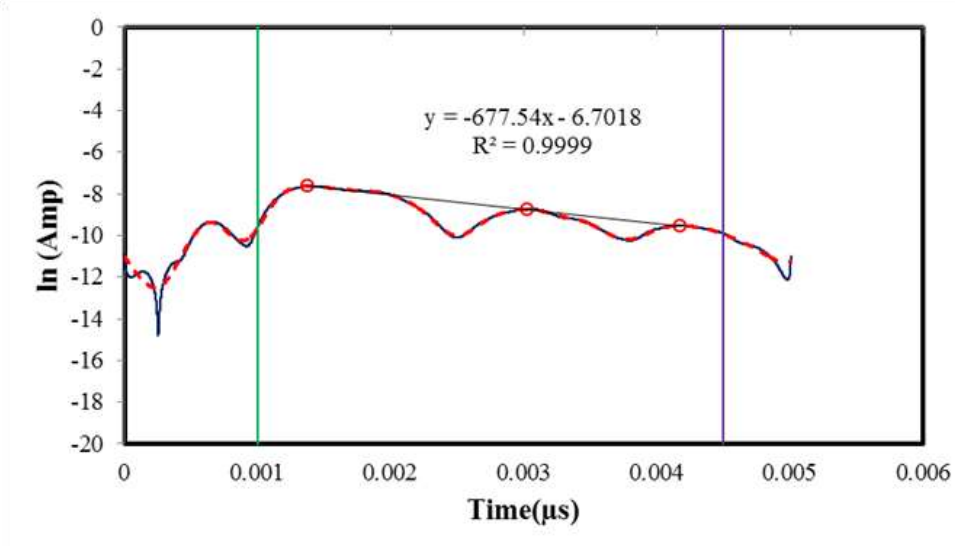

Figure 3.9 Magnitude of the analytical signal of S-wave

In Figure 3.9, a best fit line was drawn and the damping ratio was determined from the gradient of the best fit line using the following equation:

$$In(x_a(t)) = In(A) - (\xi\omega_n)t \quad (3.3)$$

Where ω_n is the natural frequency, A is the amplitude of the signal, ξ is the damping ratio and x(t) is the signal in the time domain. More details can be found in Cheng and Leong (2018) and is not repeated here.

3.6 Multi-stage Triaxial Compression Test

Multi-stage triaxial compression test was used to determine the shear strength of the SRM specimens. The main difference between the multistage triaxial compression test and the single stage triaxial compression test is that only a single specimen is required and reduces the discrepancies due to differences between "identical" SRM specimens in single-stage triaxial compression tests. The multi-stage triaxial compression test was performed using three different effective confining pressures of 100, 200 and 400 kPa. ASTM D4767 (2011) suggested that failure of the specimen generally occurs at about 4% axial strain and recommended the strain rate not more than 1mm/min. Failure of the specimen was not observed to occur below 4% strain. Chin's method was used to determine the failure stress for multi stage triaxial compression test. The shear strength of the specimen was obtained by plotting the Mohr circles on the shear stress versus normal stress plot.

3.7. Results and Discussions

3.7.1 P and S wave velocities

The V_p and V_s were determined for the two types of SRM with different rubber contents under effective confining pressures of 50, 100, 200 and 400 kPa. At low effective confining pressure, poor contact between the bender element and specimen results in low signal to noise ratio. Signals which are prone to this effect occur when softer specimens (high rubber content in SRM) are tested or low intensity signal (P-wave) is transmitted through the specimen. A signal with low signal to noise ratio will post difficulty in identification of the arrival time and therefore is not presented in the plots. Figures 3.10a to e show plots of wave velocities versus rubber content for series sr0.25, sr0.5, sr2, sr4 and sr8, respectively. From Figure 3.10, it is observed that both V_p and V_s decrease with increasing rubber content. As rubber content in SRM increases, the SRM shows rubber-like behaviour due to increase in rubber-to-rubber contact which resulted in lower wave velocity for all effective confining pressures. As

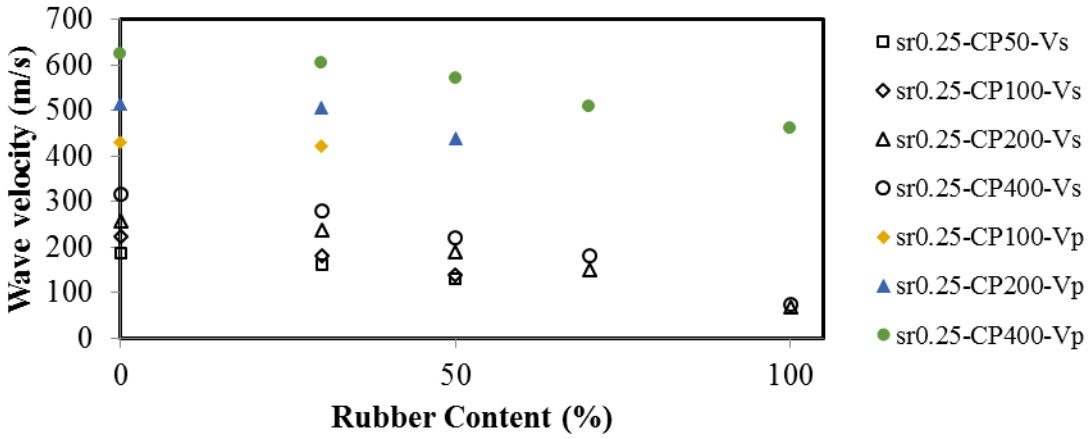

a) sr0.25

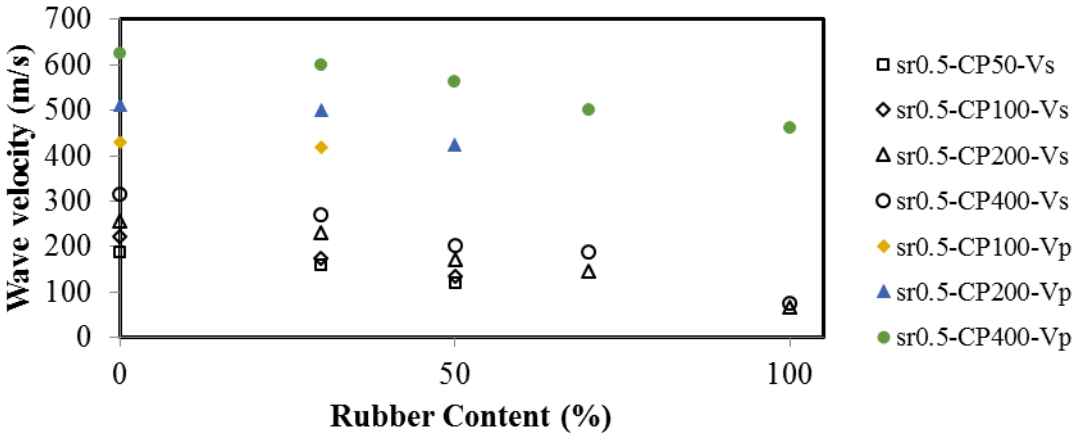

b) sr0.5

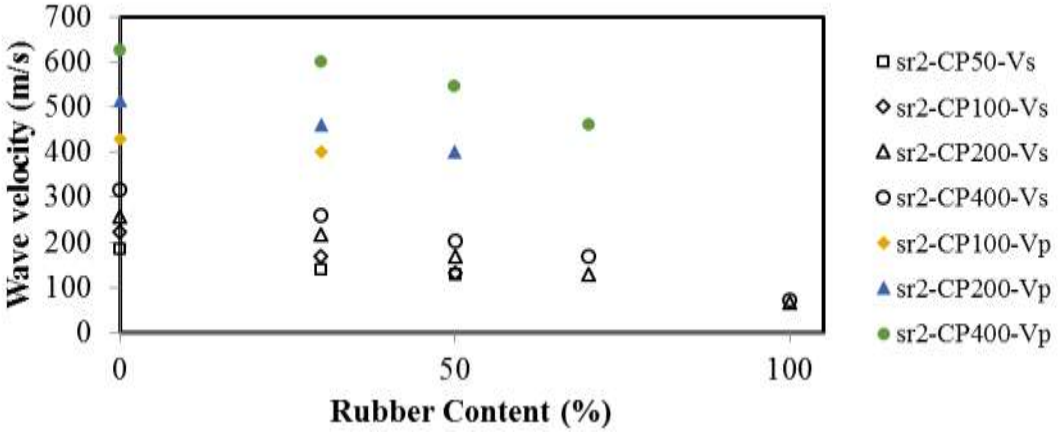

c) sr2

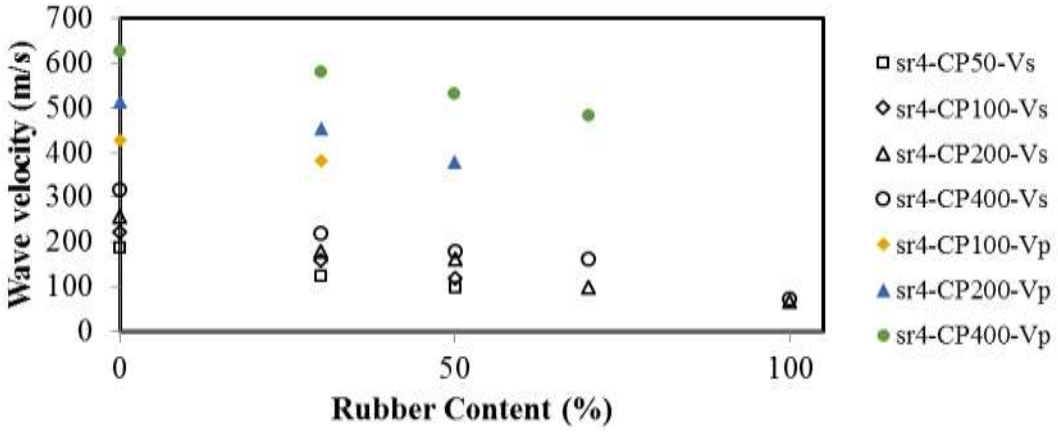

d) sr4

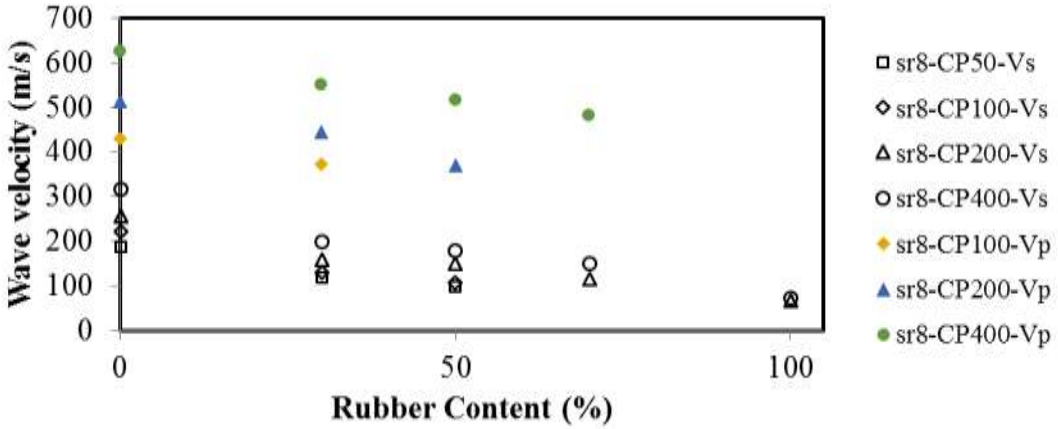

e) sr8

Figure 3.10 Plot of velocity versus rubber content

effective confining pressure increases, increase in both V_p and V_s for all series of SRM are observed due to better sand and rubber particles contact.

From Figures 3.11a to d, it is observed that as the SRM's size ratio with low rubber content increases from 0.25 to 8, there is a general decrease in both V_p and V_s. Thus SRM with sand particles smaller than rubber particles ($D_{s50} < D_{r50}$) will behave more sand-like (Higher V_p and V_s) and vice versa when $D_{s50}>D_{r50}$. However, as the rubber content in the SRM increases, the effect of size ratio on V_p and V_s becomes less

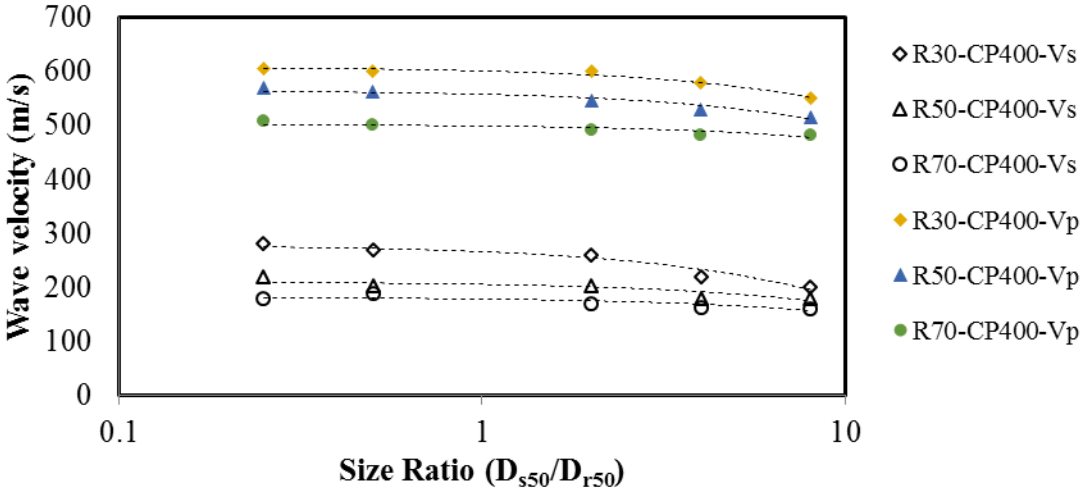

a) 400 kPa

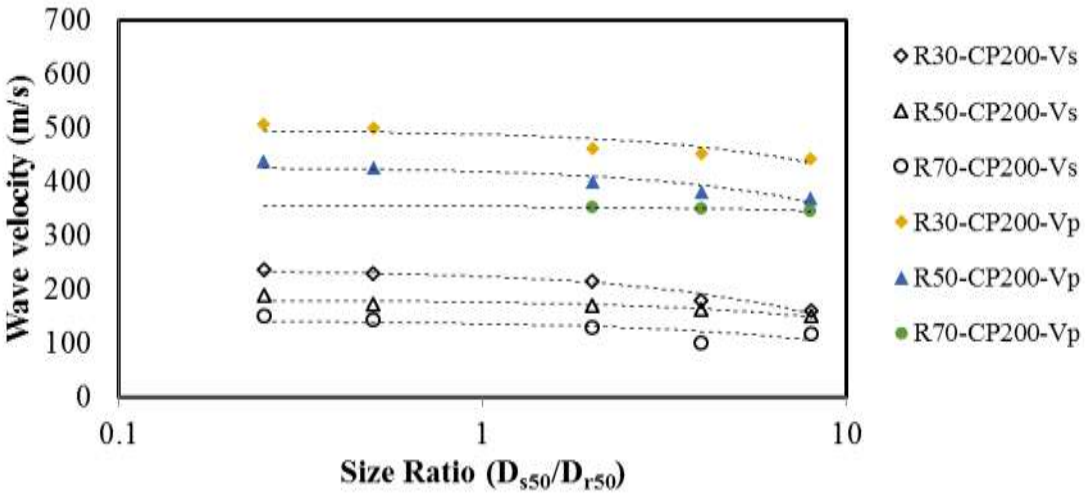

b) 200 kPa

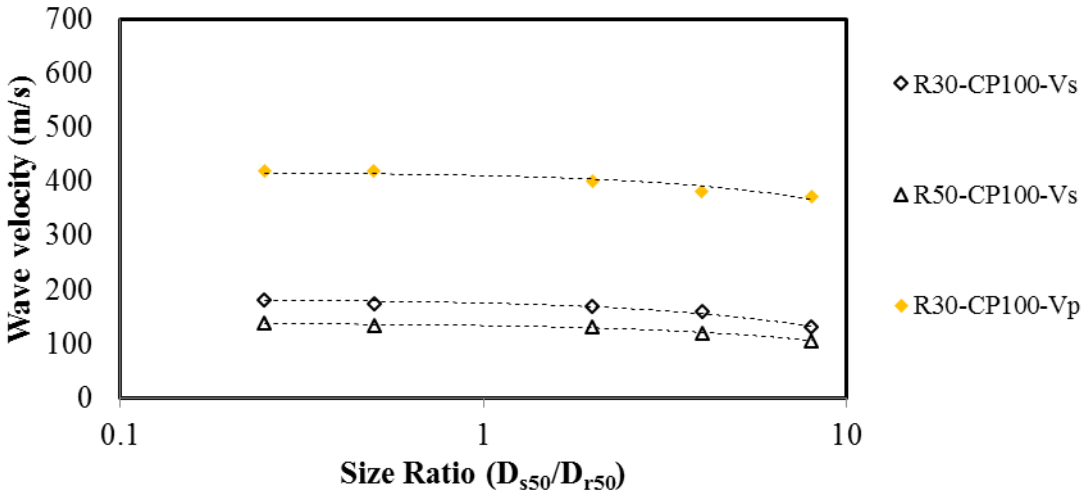

c) 100 kPa

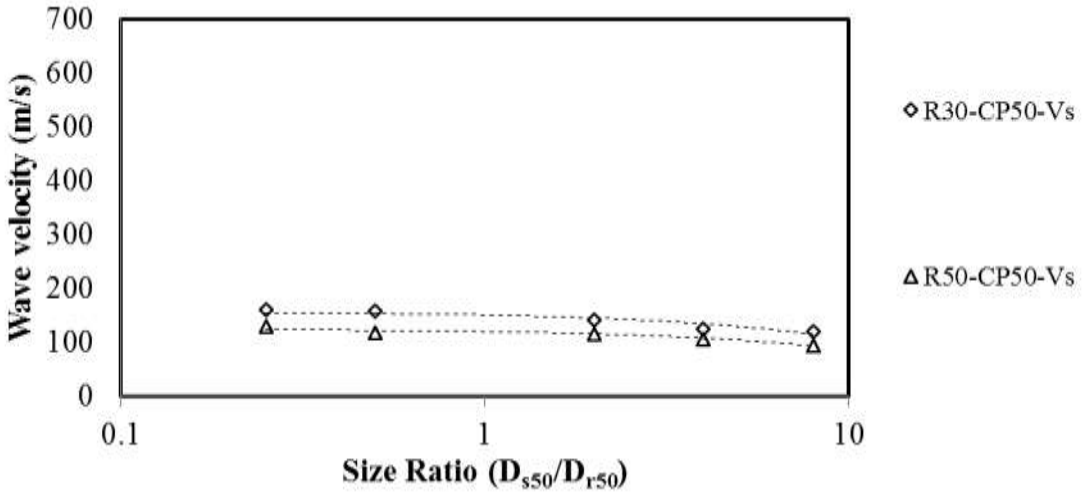

d) 50 kPa

Figure 3.11 Plot of wave velocity against size ratio for SRM of different rubber contents at various effective confining pressures

obvious as compared to SRM with low rubber content. This is due to SRM at high rubber content behaving more rubber-like which reduces the effect of size ratio.

3.7.2 Small-strain shear stiffness G_{max}

Lee et al. (2009) proposed that the effective stress governing the shear stiffness G_{max} of uncemented particulate materials when capillary effects are negligible can be estimated by the semi-empirical power relation shown in Equation 2.11. Equation 2.11 will allow the transition mixture (rubber-like behaviour at low confining pressure and sand-like behaviour at high confining pressure) to be identified. Figure 3.12 shows G_{max} plotted against different effective confining pressures while Figure 3.13 shows the experimentally determined factor A and exponent b for all rubber contents. When the rubber content present in the SRM is lower than the transitional volume, the properties and behavior of the SRM will gear towards sand like. As the rubber content present in the SRM goes beyond the transitional volume fraction, the properties and

behavior of the SRM becomes more rubber like. Figure 3.12 shows that an increase in rubber content leads to a general decrease in G_{max} for various effective confining pressure. Factor A is dependent on factors such as contact behaviour, particle properties and fabric change (Lee et al. 2009). According to Lee et al. (2009), the highest value of b-exponent can be observed at the transitional volume fraction. It is observed from Figure 3.13 that SRM

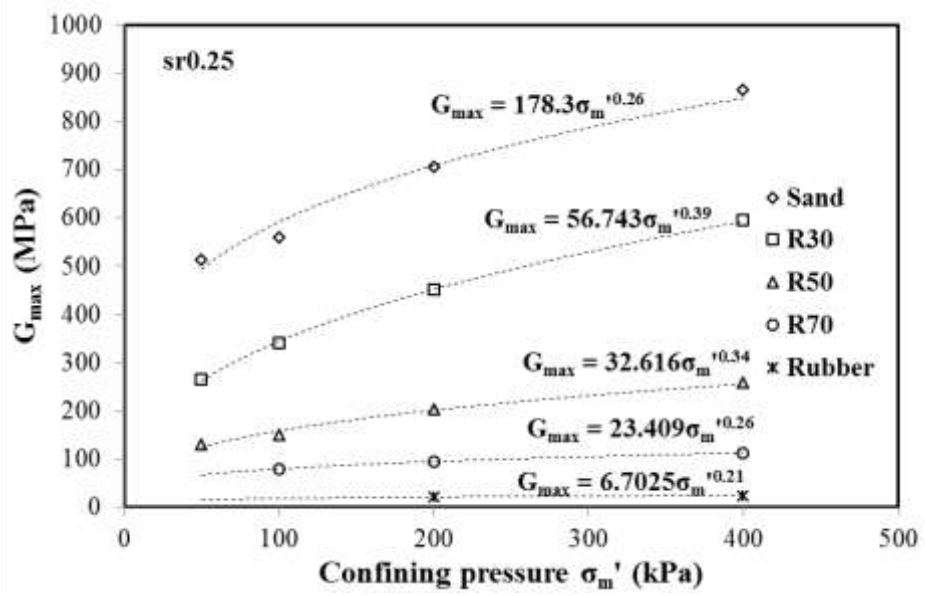

a) sr0.25

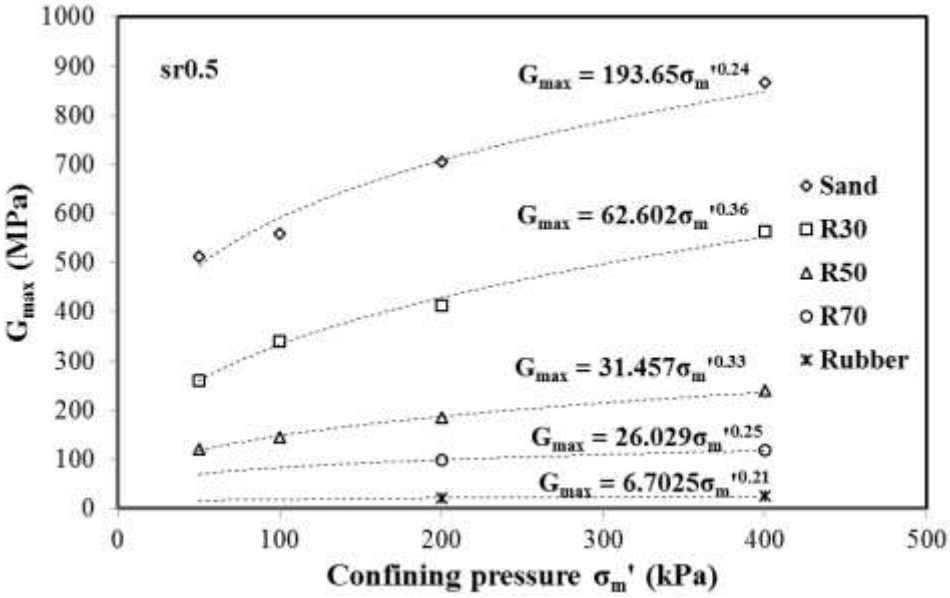

b) sr0.5

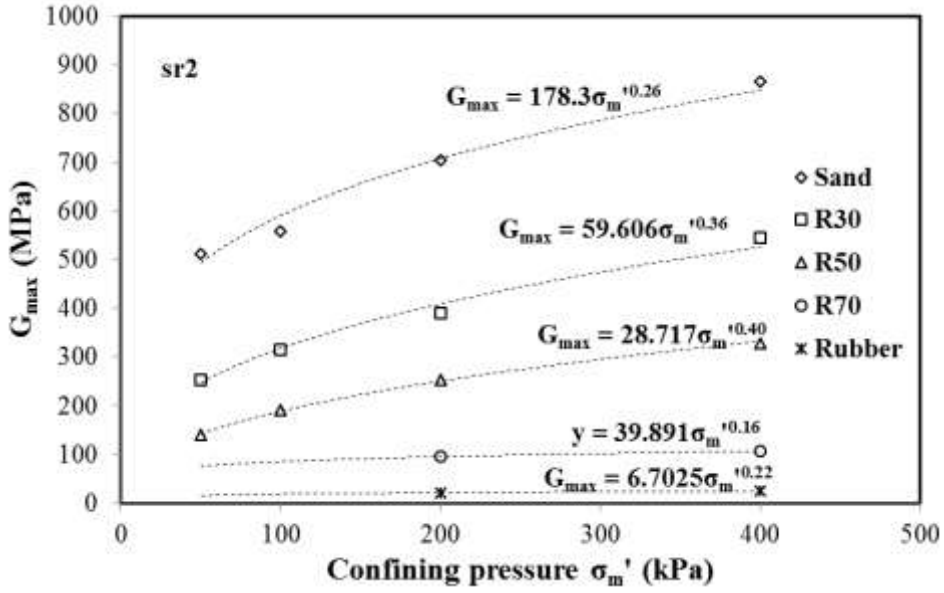

c) sr2

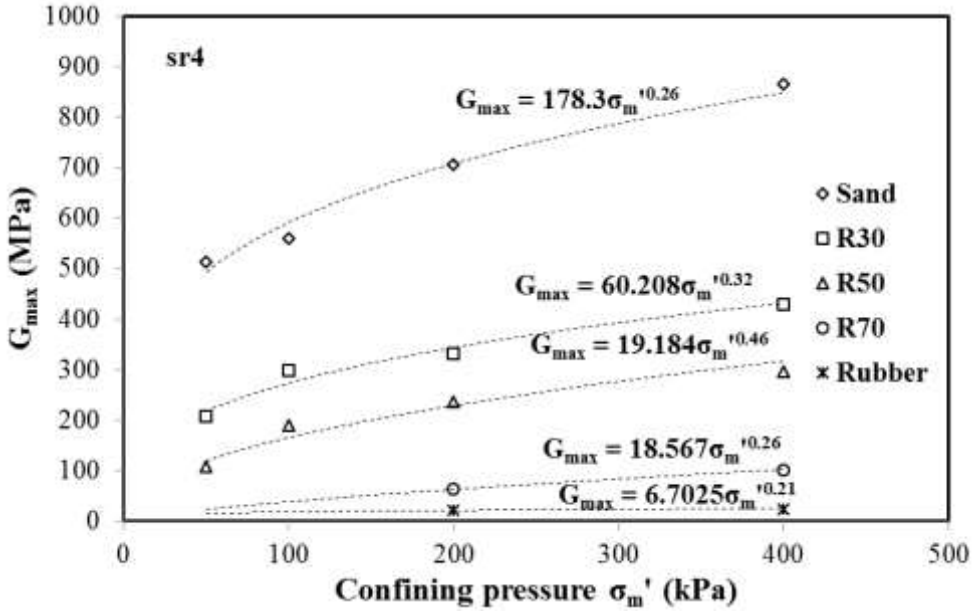

d) sr4

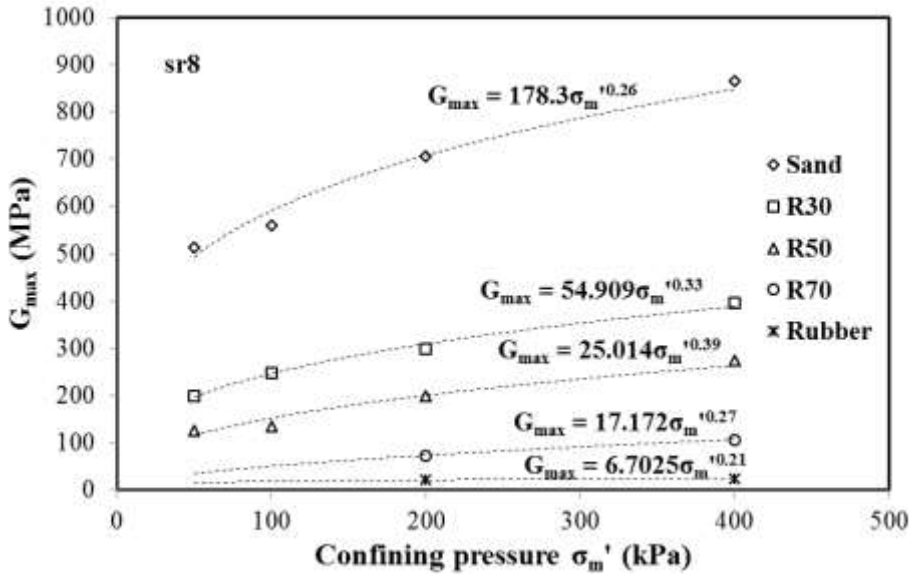

e) sr8

Figure 3.12 Plots of G_{max} against confining pressure

with bigger rubber particles (sr0.25 and sr0.5) tend to have lower transitional volume fractions compared to SRM with smaller rubber particles (sr2, sr4 and sr8). For SRM with larger rubber particles, primary load carrying chain can be easily formed by the rubber particles before they are deformed and therefore have a lower transitional volume fraction (Lee et al. 2009). These observations are in good agreement with observations made by Lee et al. (2009).

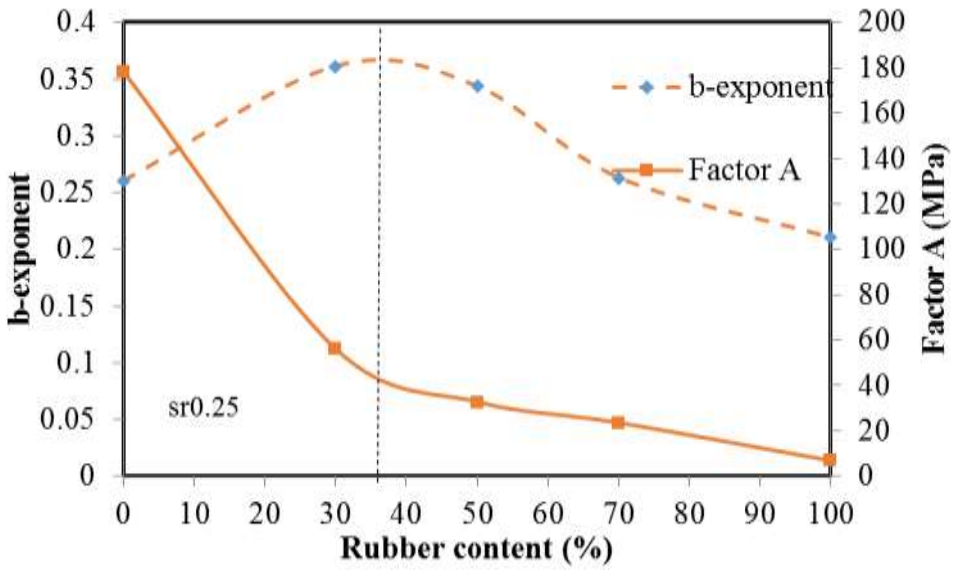

a) sr0.25

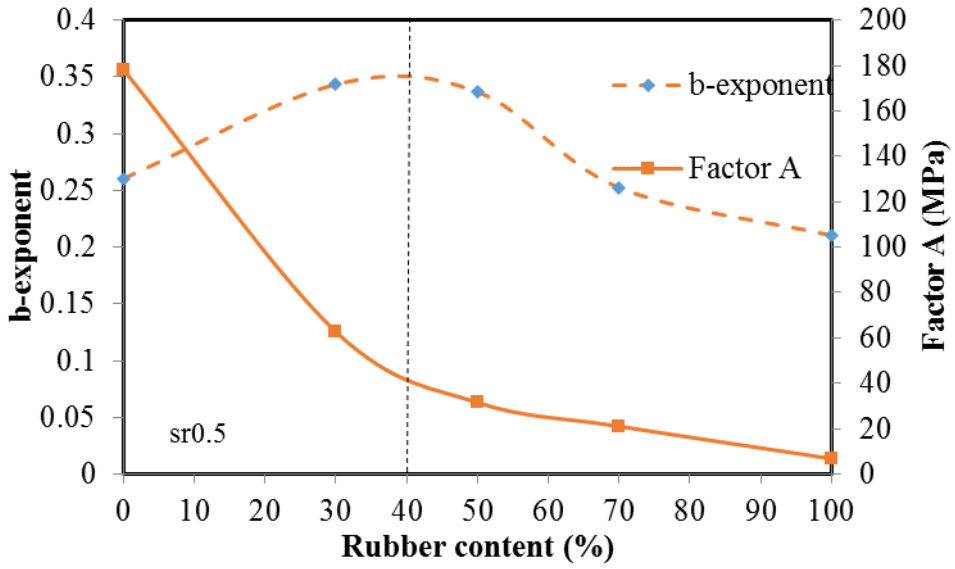

b) sr0.5

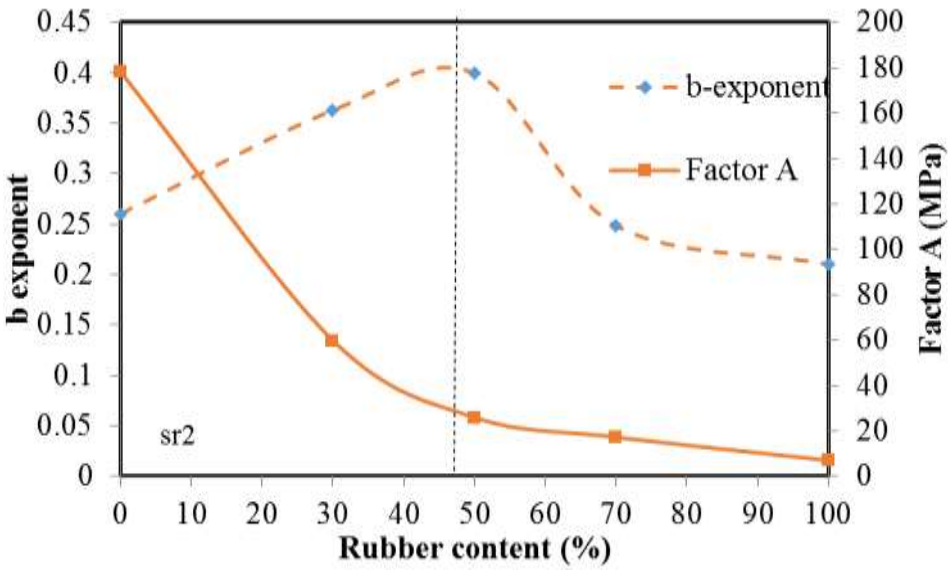
b exponent
Factor A (MPa)
b-exponent
Factor A
sr2
Rubber content (%)

c) sr2

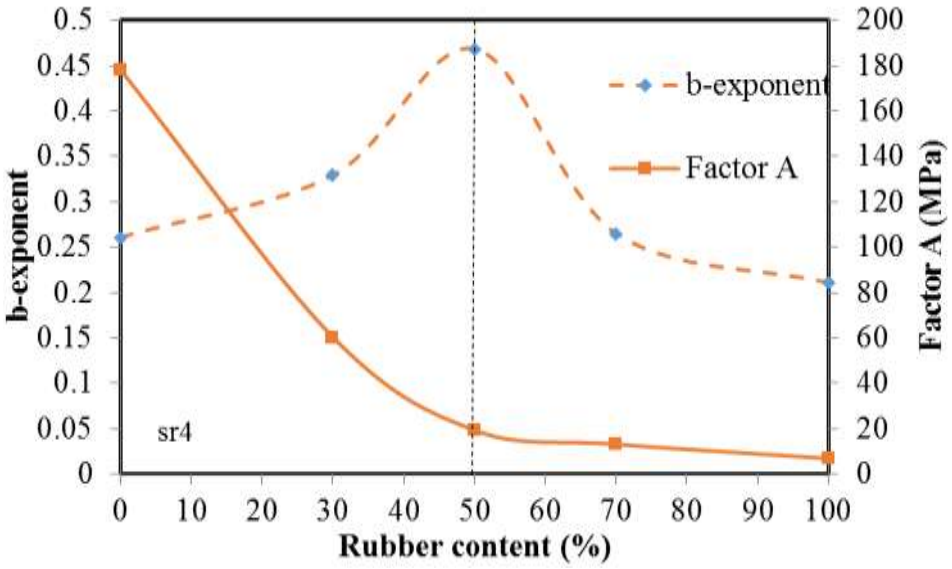
b-exponent
Factor A (MPa)
b-exponent
Factor A
sr4
Rubber content (%)

d) sr4

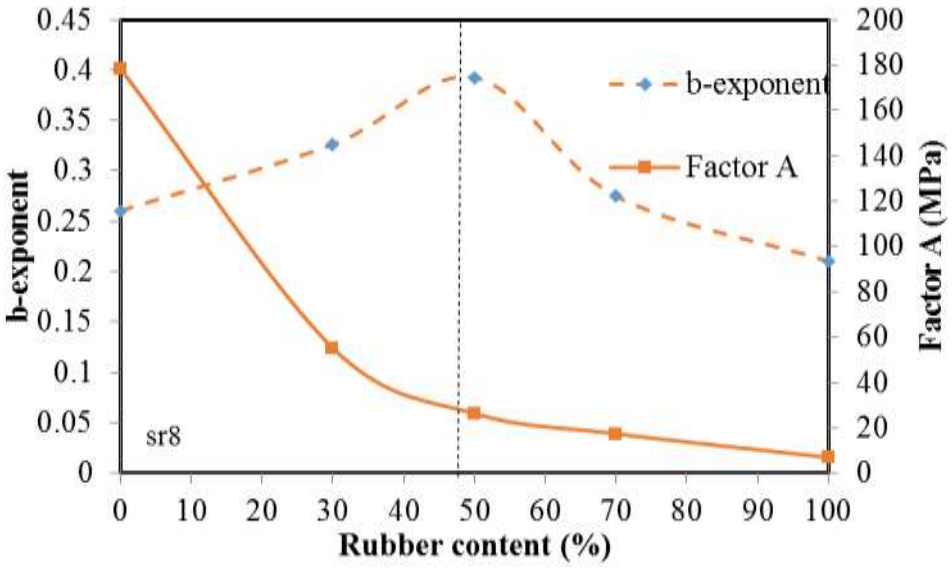

e) sr8

Figure 3.13 Factor A and b-exponent for all rubber content

3.7.3 Damping ratio

As P-wave signals damps out faster than S wave in the bender element test the material damping for P wave is expected to be higher than S wave. As the bender element has much smaller excitation in the extension mode, it was only possible to determine E_{max} from G_{max} as the P-wave velocity signal in the bender element test was weak as rubber content increases. Therefore, Hilbert transformation method was performed only on S-wave signals obtained from bender element tests for all rubber contents and size ratios under effective confining pressures of 50, 100, 200 and 400 kPa. Figure 3.14 shows plots of damping ratio against effective confining pressure for all size ratios and rubber contents. From Figure 3.14, damping ratio is observed to decrease with increasing effective confining pressure. Damping in SRM is affected by friction of the particle contacts as well as the deformation of particles. Therefore, at high confining pressure, sand particles tend to restore contact by deforming rubber

particles and rearrange to reduce inter-particle friction leading to diminished frictional losses which explains the reduction of damping ratio with increasing confining pressure (Brara et al., 2016). Figure 3.14 also shows that damping ratio increases with the increase in rubber content. This observation is due to the increase in rubber-to-rubber contact caused by the increasing rubber content in SRM.

Anastasiasdis et al. (2012) measured S-wave velocity and damping ratio of SRM using resonant column and proposed empirical Equation 2.12, for small-strain damping. Damping was measured at small strains up to 10^{-5}% (Kim and Stokoe II, 1994). The values proposed for the parameters by Anastasiasdis et al. (2012) are shown in Table 3.5. The damping ratio for all rubber contents and size ratios at different effective confining pressures obtained from this study are plotted together with the equation proposed by Anastasiasdis et al. (2012) as shown in Figure 3.15. From Figure 3.15, the empirical equation proposed by Anastasiasdis et al. (2012) fitted the damping ratios from this study poorly. This could be due to the different type of sand used for the SRM which resulted in different $\xi_{soil,100}$ of sand (0.58%) from Anastasiasdis et al. (2012) as compared to the $\xi_{soil,100}$ of sand (2.66%) from this study. It is however noted that material damping via the bender element tests depends on the contact condition of the receiver bender element. It is possible that 2.66% is high for D_{min} of sand due to experimental error. Equation 2.12 was developed for SRM with rubber content up to 35%. Figure 3.15 also shows that Equation 2.12 may have overestimated damping ratio of SRM with rubber content > 35%. In view of this, changing ψ for size ratio in Equation 2.12 gives a better match for the damping ratios obtained in this study as shown in Figure 3.16. The parameters used are shown in Table 3.5.

Table 3.5 Parameters used for Equation 2.12

Parameters	Anastasiasdis et al. (2012)	This study
ψ (D_{s50} << D_{r50})	0.1004	0.009
ψ (D_{s50} >> D_{r50})	0.3683	0.031
$\xi_{soil,100}$	0.58%	2.66%
φ	1.750	1.750
κ	-0.12	-0.12

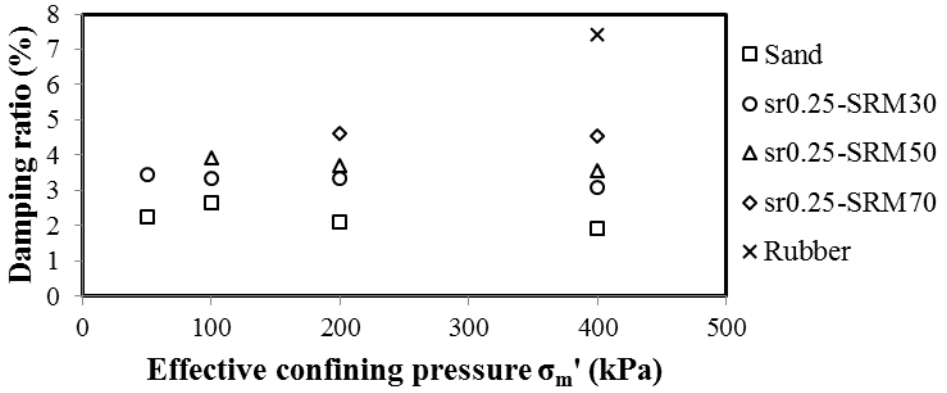

a) sr0.25

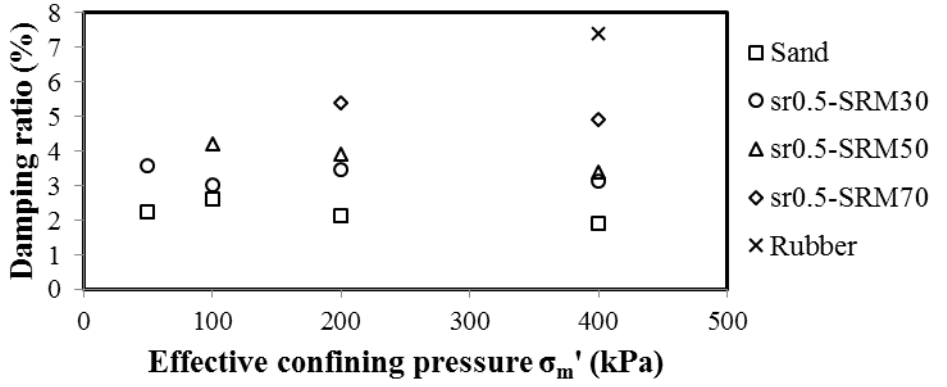

b) sr0.5

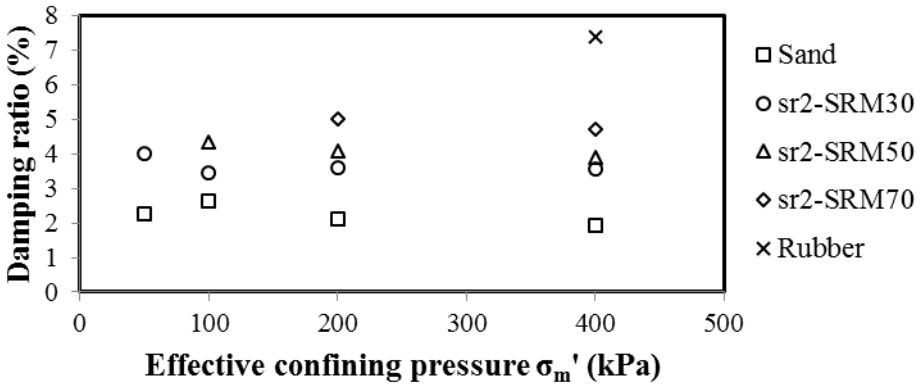

c) sr2

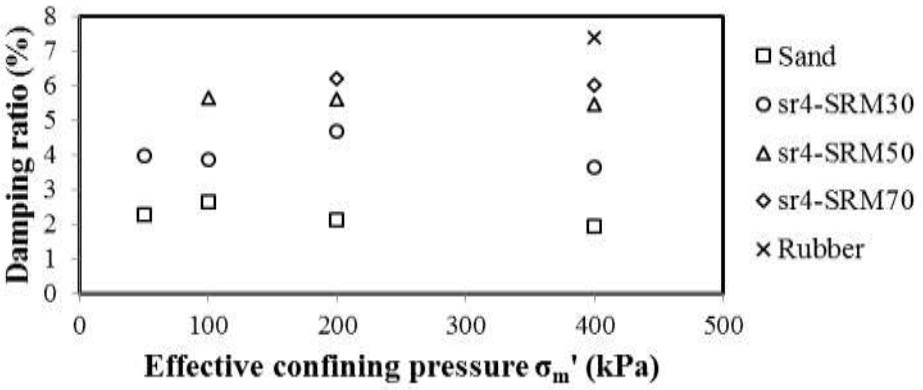

d) sr4

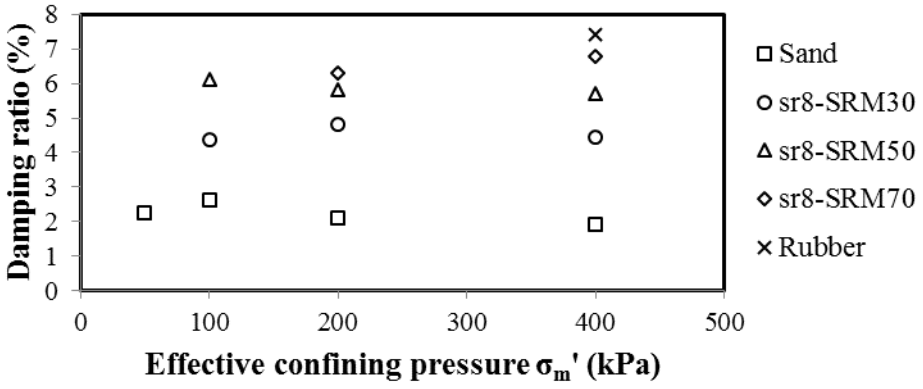

e) sr8

Figure 3.14 Damping ratio versus effective confining pressure for all rubber contents

3.7.4 Comparison with literature's V_s and damping ratio

The V_s and damping ratios obtained from the literature are plotted with V_s and damping ratio from this study. The V_s is normalised as suggested by Harbin and Richart (1963) and Rahman et al. (2012) where G_{max} is shown to be a function of specify volume, (1+e). As V_s is proportional to the square root of G_{max}, the normalised V_s is $V_s/\sqrt{(1+e)}$. Damping ratios from the literature were obtained mainly using resonant column tests and involve a range of shear strains. Hence, only damping ratio.

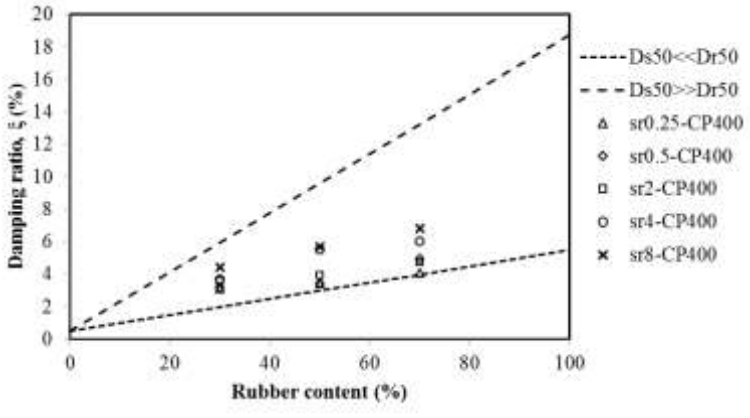

a) CP400

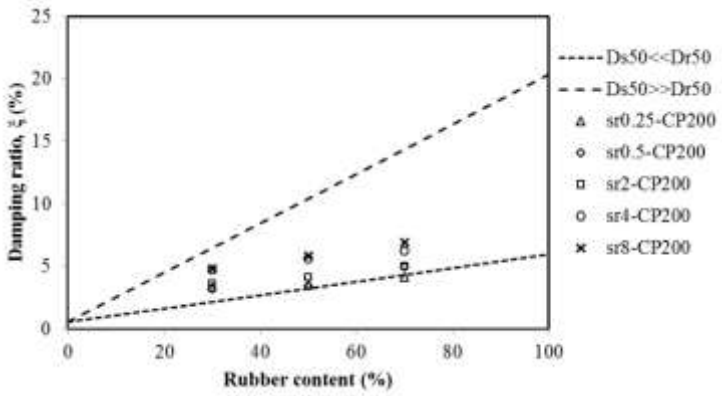

b) CP200

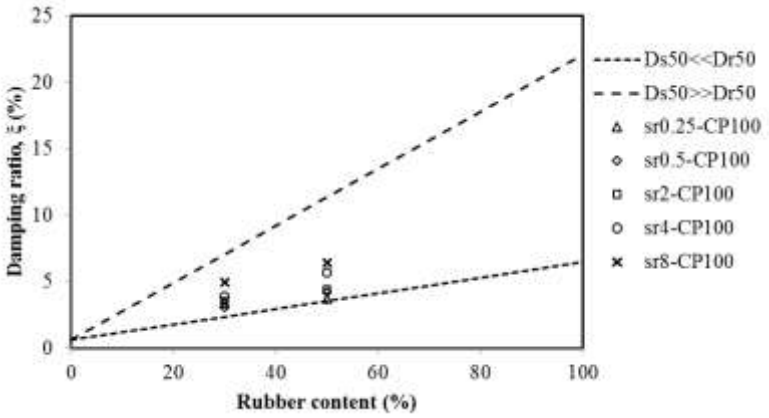

c) CP100

Figure 3.15 Damping ratios versus rubber content for all size ratios at different effective confining pressures with Equation 2.12 using parameters proposed by Anastasiasdis et al. (2012)

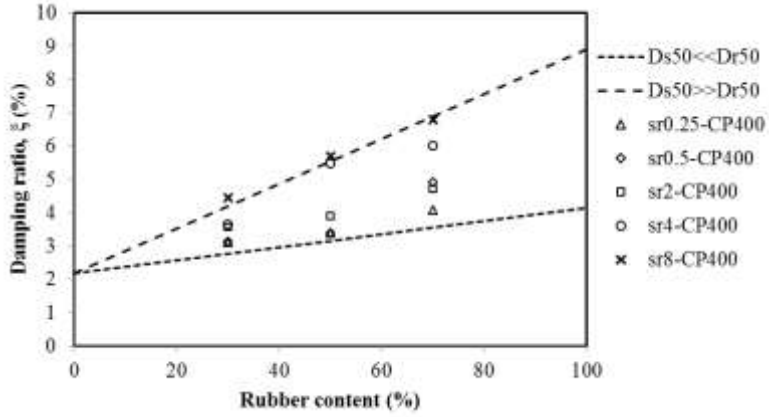

a) CP400

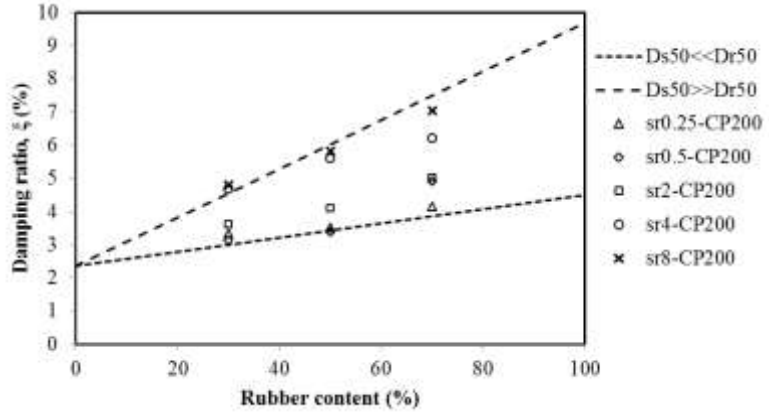

b) CP200

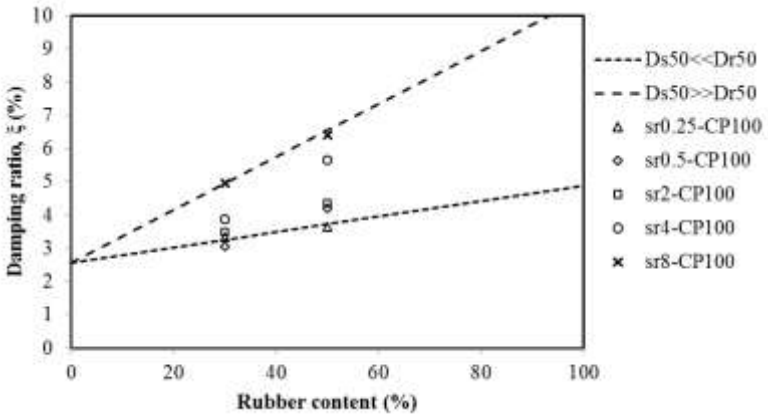

c) CP100

Figure 3.16 Damping ratio versus rubber content for all size ratios at different effective confining pressures with Equation 2.12 using parameters proposed for this study

at the lowest shear strain was extracted and plotted as strain level from bender element test does not exceed 0.0001% (Leong et al. 2005). Table 3.6 presents the references with their respective notations used in the plots. Figures 3.17 and 3.18 show the normalised V_s and damping ratio versus rubber content for normalised V_s and damping ratio, respectively, at different effective confining pressures. In Figures 3.17 and 3.18, hollow symbols are data from the literature and filled symbols are data from this study. All the plots in Figures 3.17 and 3.18 show a general decrease in normalised V_s and increase in damping ratio with increasing rubber content, respectively. To study the effects of size ratio on SRM, linear upper and lower bounds for this study are plotted in Figures 3.17 and 3.18. Normalised V_s and to the damping ratio obtained by Cheng (2015) and Anastasiadis et al. (2012) fall closer to the upper bound of the normalised V_s and to the lower bound of the damping ratio obtained for this study (low size ratio), respectively. This observation shows that the normalised V_s and damping ratio obtained for this study are reasonable.

Table 3.6 Literature data for Vs and ξ

References	Notations	Soil type	Size ratio (D_{50s}/D_{50rr})	Initial void ratio
Cheng (2015)	CH	Sand of different origin	0.11	0.6
Senetakis et al. (2012)	SE	Quarry Sandy Gravel	5.2	-
Anastasadis et al. (2012a, b)	AN1	Sand of different origin	0.0964	0.43-0.64
	AN2		0.18	0.57-0.67
	AN3		1.4	0.56-0.62
	AN4		0.2	0.42-0.59
Feng and Stutter (2000)	FS	Ottawa sand	0.215	0.36-0.46
Pamukcu and Akbulut (2006)	PA	Ottawa sand with 11% Kaolin	0.954	0.37-0.40
Rocco (2012)	RO	Kaolin	1.33e-6	0.948-1.915

3.7.5 Friction angle

Dry SRM specimens were sheared in the modified triaxial apparatus at effective confining pressures of 100, 200 and 400 kPa with drainage valves open, i.e. pore-air pressure is at atmospheric pressure. Multi-stage shearing was applied in accordance to ASTM D4767 (2011). Figure 3.19 shows typical Mohr circles for tests on sr0.25-R50. Figure 3.20 shows a plot of friction angle versus rubber content for all size ratios. From Figure 3.20, it is observed that with the increase in rubber content, friction angle decreases. This is due to the increase in rubber-to-rubber contact with increase in rubber content, in SRM which resulted in a decrease in friction angle. Table 3.7 shows the data collated from the literature. The data are plotted with the data obtained

from this study in Figure 3.21. From Figure 3.21 shows a general reduction in friction angle with increasing rubber content. Figure 3.21 also shows that friction angle decreases with increasing size ratio. These observations were due to SRM behaving more rubber-like with smaller rubber particle size. Singh and Vinot (2011), Balachowski and Gotteland (2007), Youwai and Begardo (2003) showed that the shape of rubber fine and small size ratio affects the trend of the friction angle in SRM.

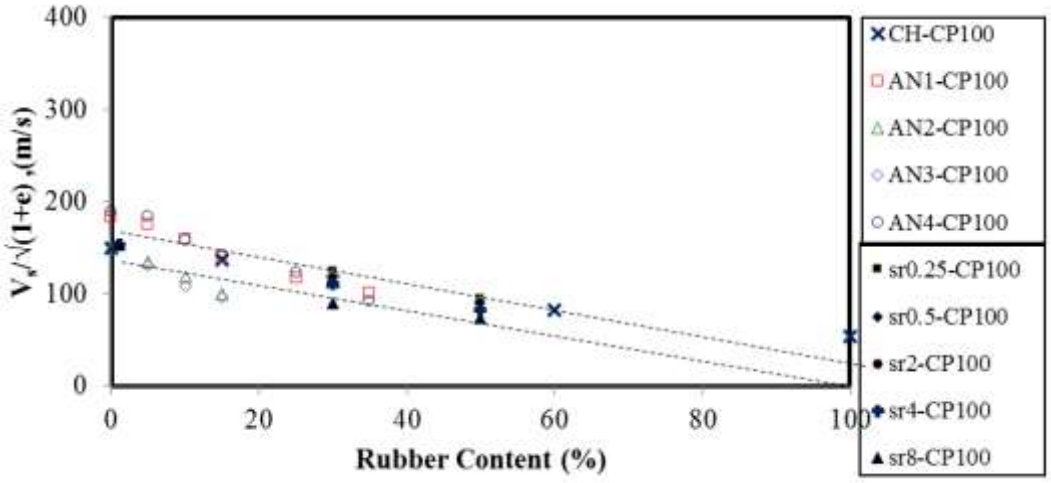

a) CP400

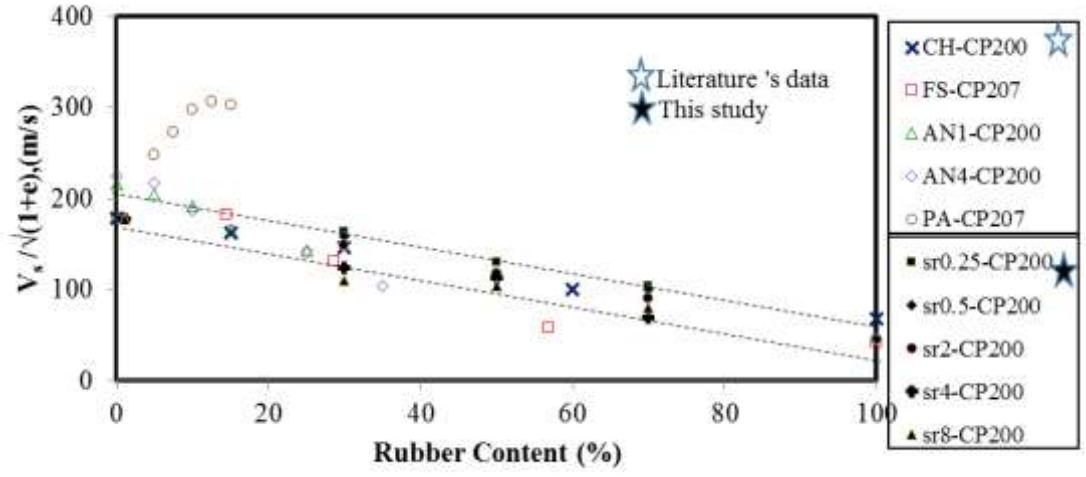

b) CP200

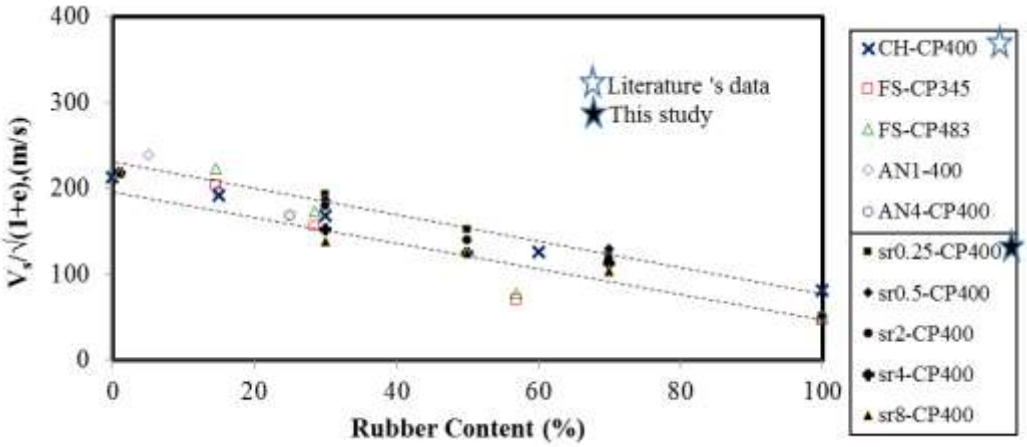

c) CP100

Figure 3.17 Comparison of normalised V_s with data from literature

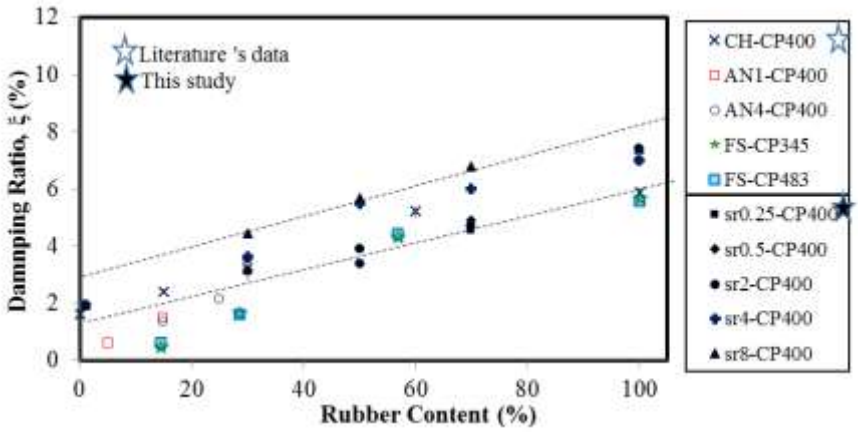

a) CP400

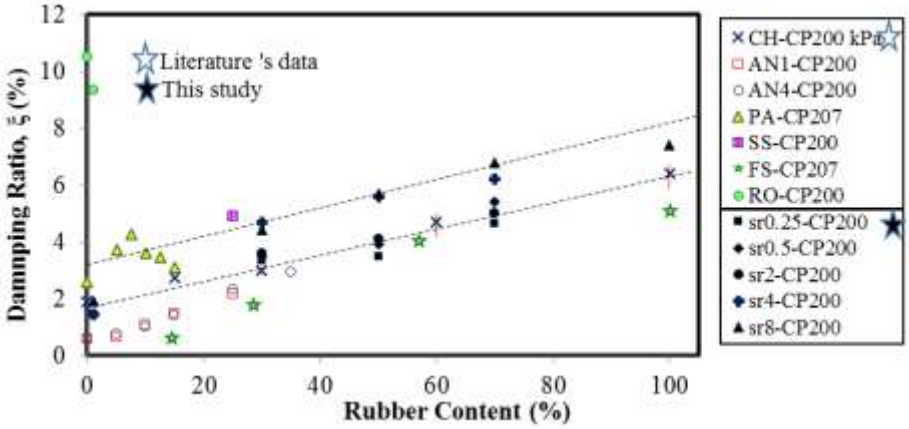

b) CP200

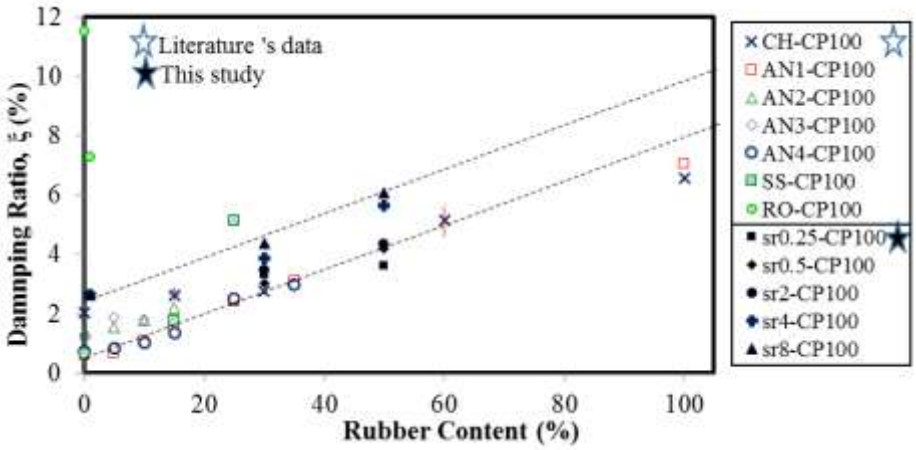

c) CP100

Figure 3.18 Comparison of damping ratio with data from literature

However, when differences in particle size between sand and rubber is large, segregation between sand and rubber particles are inevitable. This is reflected in data (SV-T1, SV-T2, and SV-T3) from Singh and Vinot (2011) (D_{s50}/D_{r50} = 0.02) and in data (BG) from Balachowski and Gotteland (2007) where the friction angle for SRM with rubber content of 10 to 30% is higher (sand-like) when compared to friction angle of SRM with similar rubber content obtained by from Mavroulidou et al. (2009) (D_{s50}/D_{r50} = 1 and 0.35) (MA-CS and MA-MS). Youwai and Begardo (2003) also mentioned that reduction in void ratio of SRM will result in higher friction angle.

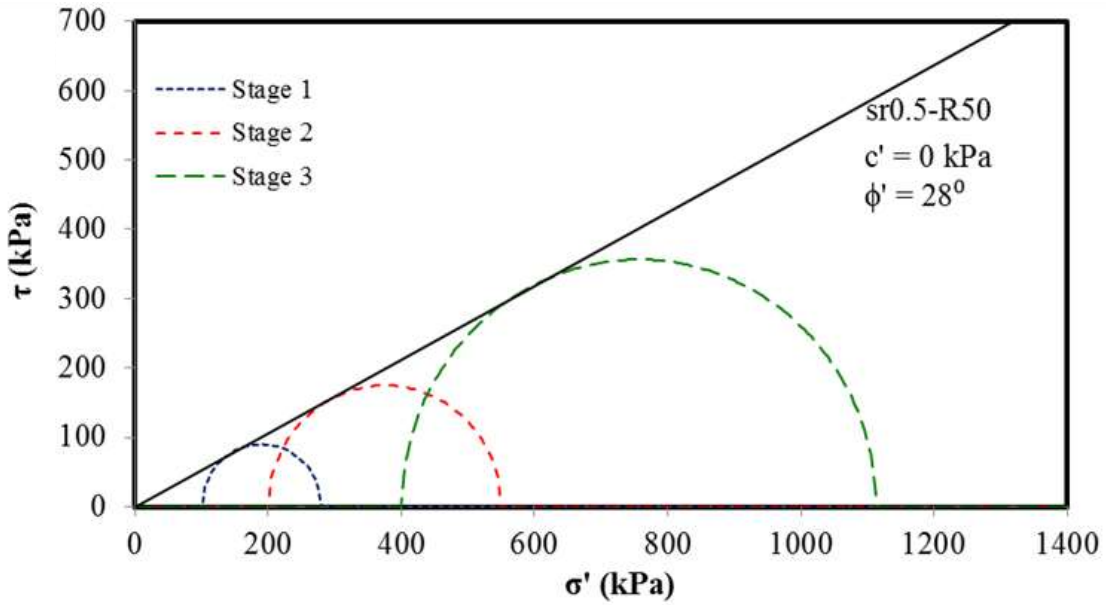

Figure 3.19 Typical failure envelope of specimen

Table 3.7 SRM from literature

References	Notations	Material type	Size ratio
Balachowski and Gotteland (2007)	BG	Lubiatowo sand	D_{s50}/D_{r50} = 0.0075
Cabalar (2011)	CA	CS: Ceyhan sand	CS: D_{s50} = 0.45mm
		LB: Leighton buzzard	LB: D_{s50} = 0.9mm
			Size of rubber not mentioned
Singh and Vinot (2011)	SV	T1: Rectangle rubber shred of 10 X 10 mm	D_{s50}/D_{r50} = 0.02
		T2: Rectangle rubber shred of 10 X 20 mm	
		T3: Rectangle rubber shred of 10 X 30 mm	
Youwai and Begardo (2003)	YB	Ayutthaya sand Shredded rubber tires	D_{s50}/D_{r50} = 0.054
Mavroulidou et al. (2009)	MA	CS: Coarse sand	CS: D_{s50}/D_{r50} = 1
		MS: Medium sand	MS: D_{s50}/D_{r50} = 0.35

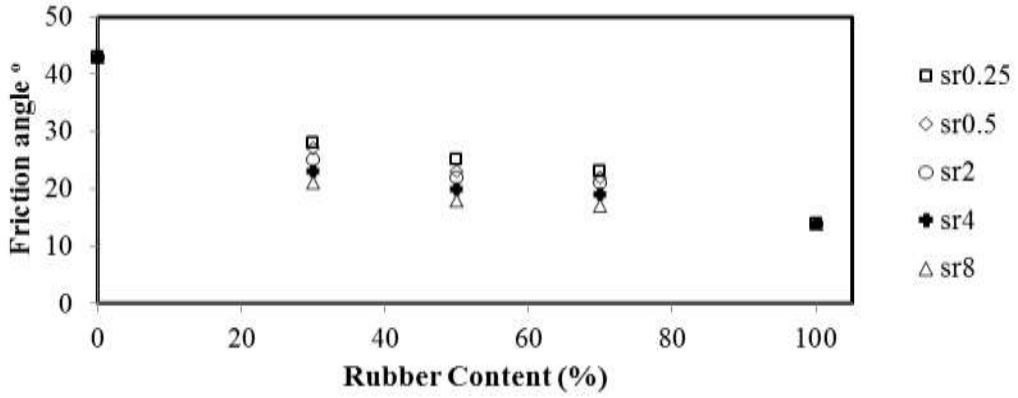

Figure 3.20 Friction angle against rubber content for all size ratio

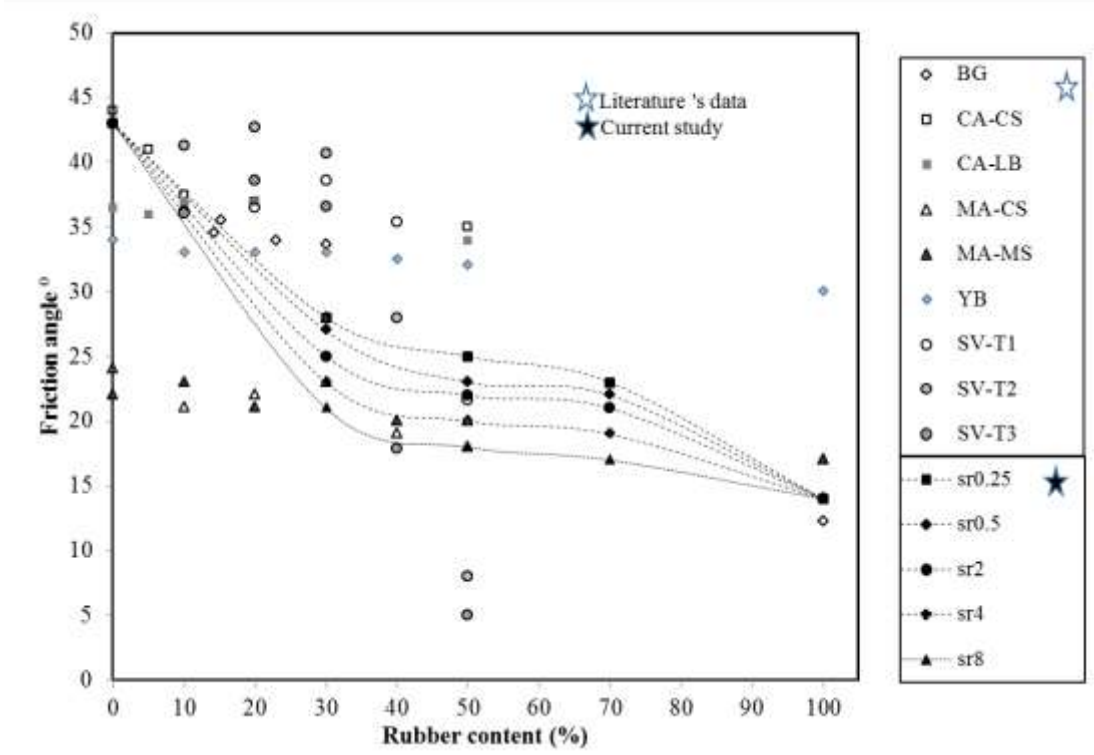

Figure 3.21 Collated literature friction angle of different rubber content

3.8 Selection of SRM for field test

The results obtained from the laboratory test contribute to the decision on the selection of rubber content in SRM to be used for the field test. To maintain stiffness without too much change in damping ratio, it is preferred to keep size ratio of the SRM to be small. Size ratio of 0.5 will be used. From the literature, density of the material used as the seismic wave barrier is an important consideration. Figure 3.22 reviews that the differences in dry densities between SRM with 30% (R30) and 70% (R70) rubber is almost two times which will be reflected in the impedance ratio. These two SRM, R30 and R70, will be used in subsequent field tests While it is known that materials with smaller density will perform better in reducing amplitudes of ground shock or surface wave at the expense of lower material strength, it is important to study SRM with different rubber contents to better understand application of SRM in the field.

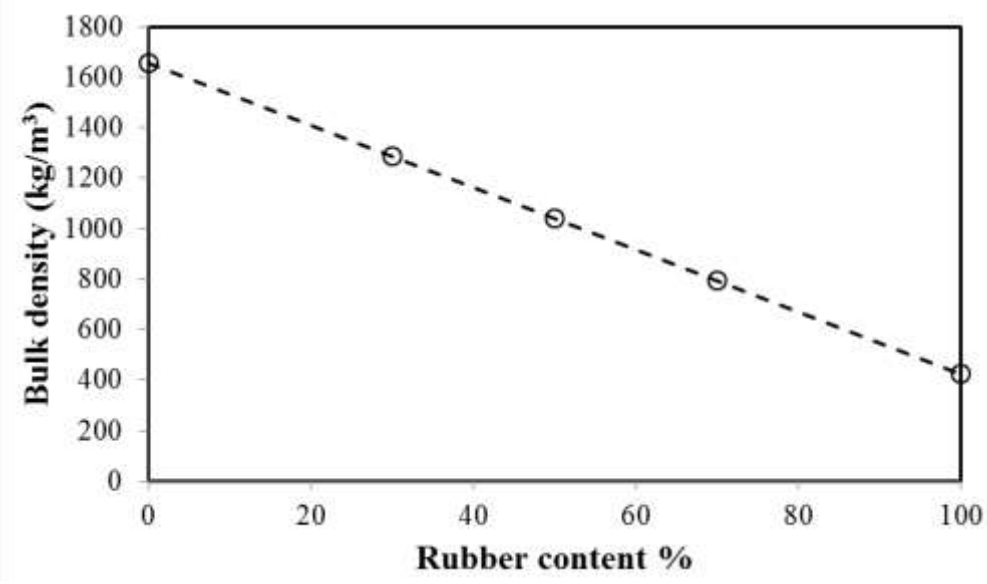

Figure 3.22 Dry densities of SRM with rubber content

The effective confining pressure in the field conditions is low (< 10m depth) compared to what is applied in the laboratory tests. Bender element tests in the laboratory at low confining pressure has weak signals and low signal to noise ratio. To overcome this problem, the empirical relationship between effective confining pressure with V_s and damping ratio proposed by Cheng (2015) will be used to extrapolate the test results to the relevant stress condition in the field tests. The equation proposed by Cheng (2015) is as follows:

$$V = V_0 e^{-B_R M_{ru}} \tag{3.4}$$

where V_0 represents the velocity of the sand, exponent B_R is a curve fitting constant and M_{ru} is the rubber chips content in percent. Values of V_0 and B_R are dependent on effective confining pressure σ_m' and can be represented by the following equations, respectively:

$$V_0 = \bar{a}_1 \ln\left(\frac{\sigma_m{}'}{P_{atm}} + \bar{a}_2\right) - \bar{a}_3 \tag{3.5}$$

$$B_R = -b_1\left(\frac{\sigma_m{}'}{P_{atm}}\right) + b_2 \tag{3.6}$$

where coefficients of $\bar{a}_1$, $\bar{a}_2$ and $\bar{a}_3$ have values of 62.03 m/s, 0.1846 and 184.8 m/s, respectively, coefficients of b_1 and b_2 have values of 2.429×10^{-4} and 1.049×10^{-2}, respectively. σ_m' is the effective confining pressure and P_{atm} is taken as 100 kPa for the purpose of normalising σ_m'. The results are shown in Figures 3.23a and b for R30 and R70, respectively.

3.9 Summary

Characterisation of dry SRM specimens with different rubber contents and size ratios were obtained using bender element tests and multistage triaxial tests. The tests were

performed in a triaxial cell equipped with bender elements. The findings are as follows:

1. The three main factors that affect the dynamic response of sand-rubber mixtures are (a) rubber content (b) effective confining pressure, and (c) size ratio between sand and rubber particles.
2. Wave velocities (V_p and V_s) and G_{max} decrease with increasing rubber content. With increasing rubber content, SRM shows rubber-like behaviour due to increase in rubber-to-rubber contact which resulted in lower wave velocity for all effective confining pressures. On the other hand, an increase in rubber content in SRM shows an increase in damping ratio. This is due to the high damping property of rubber when compared to sand.

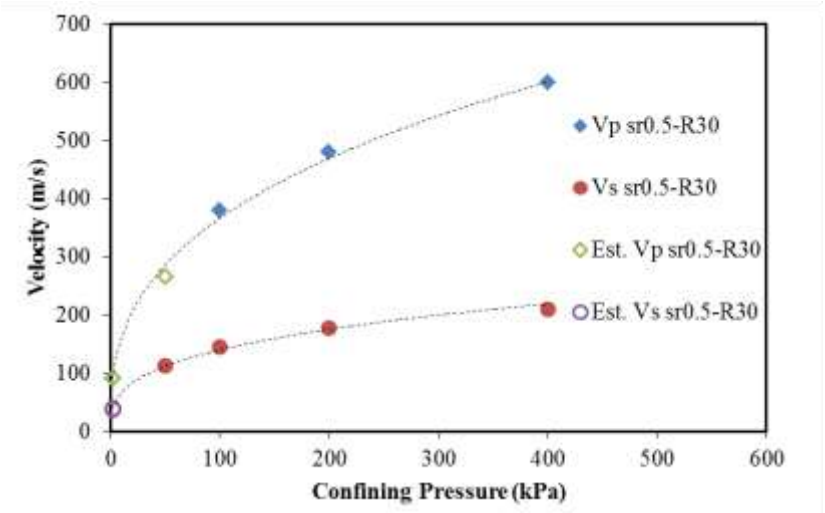

a) R30

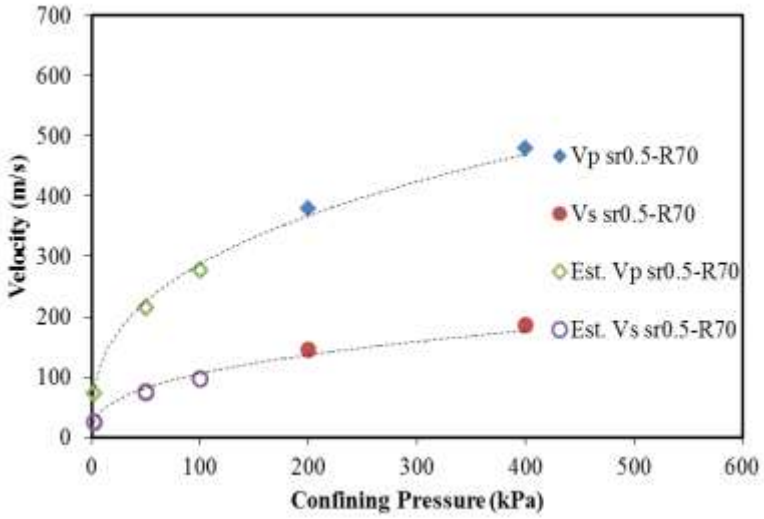

b) R70

Figure 3.23 Relationships P and S wave velocities with confining pressure

3. Wave velocities (V_p and V_s) and G_{max} increase with increasing effective confining pressure. This observation is due to better contact between sand and rubber particles under higher effective confining pressure.
4. Both V_s and G_{max} generally decrease as size ratio increase from sr0.25 to sr8 for all rubber contents. The values of V_s and G_{max} are determined by the stiffness of the interparticle contact and amount of small particles in the SRM which increases the coordination number or particle contact area. This strongly suggests that V_s and G_{max} are governed by the smaller particles (Lee et al. 2007). It is observed that SRM with larger rubber particles (sr0.25 and sr0.5) tends to have lower transitional volume fractions compared to SRM with smaller rubber particles (sr2, sr4 and sr8). For SRM with larger rubber particles, primary load carrying chain can be easily formed by the rubber

particles before they are deformed and therefore such SRM have a lower transitional volume fraction (Lee et al. 2009).

5. Damping ratio increases with increasing effective confining pressure. Damping in SRM is dependent on the friction of the particle contacts as well as the deformation of particles (Brara et al., 2016). At high confining pressure, sand particles tend to restore contact by deforming rubber particles and rearranging, thereby reducing the interparticle friction leading to diminished frictional losses which explains the reduction of damping ratio with increasing confining pressure.
6. Damping ratio generally decreases as rubber content decreases for all size ratios. An increase in damping ratio with increasing size ratio can also be observed. Damping ratios for all size ratios and rubber contents do not follow the empirical equation proposed by Anastasiadis et al. (2012). This is attributed to Anastasiadis et al. (2012) empirical equation being based only on SRM with rubber content up to 35% only and the different sand for SRM. However, the empirical equation when modified gave a good agreement with the damping ratios obtained in this study.
7. An increase in rubber content leads to a decrease in friction angle which is due to increase in rubber-to-rubber contact in SRM. An increase in size ratios leads to a decrease in friction angle. This observation is in good agreement with the data collated from the literature.

Chapter 4 Sand-rubber Mixture as a Seismic Wave Barrier

4.1 Introduction

Vibrations generated by traffic, railway, machine foundation and blasting activities can potentially cause significant disturbance to people, equipment and buildings. Seismic wave barrier can effectively reduce the amplitude of vibrations (mainly from surface wave comprising of Rayleigh waves). Studies on the effectiveness of seismic wave barrier have being done with unequal success. To date, most of these studies were investigated using numerical modelling and actual field tests were rarely performed (Alzawi and Nagger 2011). The materials that have been used as seismic wave barrier includes open trench, bentonite slurry, geofoam, concrete and rows of piles. The efficacy of sand-rubber mixtures (SRM) as a seismic wave barrier has yet to be studied both experimentally and numerically. Thus, field tests and numerical modelling on SRM as a seismic wave barrier were performed in this study.

The SRM used in this study have been characterised in the laboratory as described in Chapter 3. This chapter describes small-scale field tests which investigates efficacy of SRM as seismic wave barrier against surface wave generated by a mass vibrator. The seismic wave barrier consists of two SRMs (R30 and R70 with sr = 0.5) and an open trench. The field tests were complemented with finite element (FE) modelling using LS-DYNA. Amplitude ratio (Ar) contour plots were obtained from the FE results which were then further developed into dimensionless Ar contour plots to serve as a preliminary guide for the implementation of seismic wave barrier on site. Example on how the dimensionless contour plot can be utilised is demonstrated with a few examples.

4.2 Site Investigation

The site chosen for the field test is at the Nanyang Technological University campus situated in the western part of Singapore. The location of the field test site is shown in Figure 4.1. The site was assessed using the continuous surface wave test to obtain the stiffness profile of the site. The continuous surface wave (CSW) system is from GDS Instruments Pte Ltd and is shown in Figure 4.2. The Continuous Surface Wave System consists of a mass vibrator as vibration source which generates continuous sinusoidal waves at one frequency. The frequency can be varied from about 5 to 600 Hz. Geophones were positioned in a co-linear array with the mass vibrator to detect the ground motion data and a data-acquisition system for data recording. The data acquisition system, which has a maximum sampling frequency of up to 300 kHz, has six channels in total. The geophone used have a resonant frequency of 2 Hz. The calibration constant for the geophone is provided by the manufacturer (GDS). The calibration constant is verified using a calibrated accelerometer. It is expected that the geophones will give reasonable response at frequencies above the resonant frequency. Prior to conducting CSW test, huddle tests were first performed by placing all the geophones at the same distance away from the mass vibrator to verify that all the geophones are functioning correctly. Figure 4.3 shows the velocity-time histories for vibration at 60 Hz. From Figure 4.3, it is observed that all the geophones exhibit identical responses. A total of three separate CSW tests (arrays 1, 2 and 3) were performed on the test site to obtain the average dispersion curve for the test site. Figure 4.4 shows the test layouts. The dispersion curve data from the three arrays are shown in Figure 4.5a and the average dispersion curve was inverted using the forward modelling method referred to as weighted average velocity (WAVe) method

developed by Leong and Aung (2013). Figure 4.5b shows the V_s profiles of the site obtained by inverting the dispersion curves. The stiffness profiles show that the site consists of three soil layers with V_s increasing with depth. The thickness and V_s of the soil layers are summarised in Table 4.1.

Figure 4.1 Location of field test site

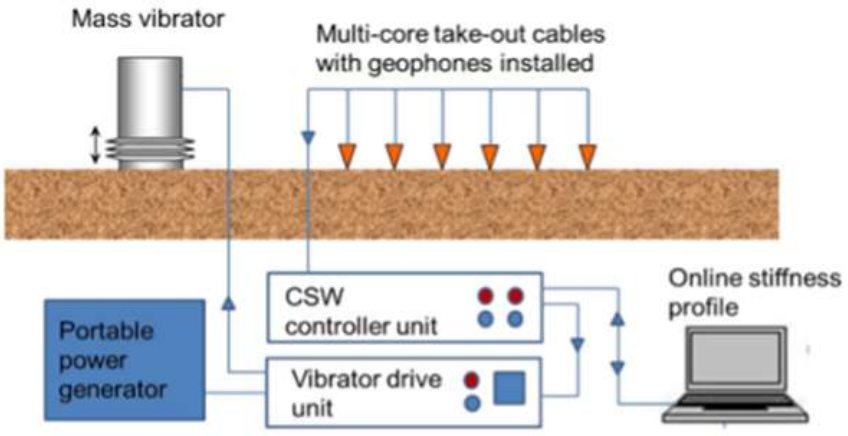

Figure 4.2 Schematic diagram of CSW test (from GDS, 2012)

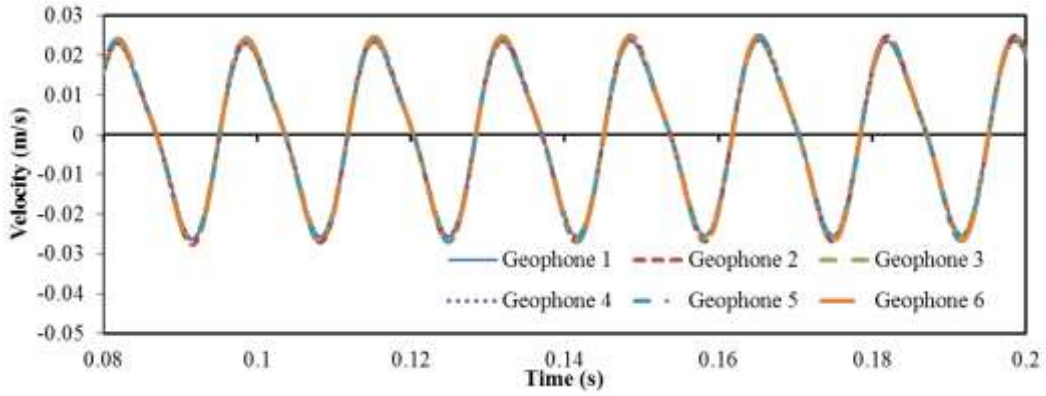

Figure 4.3 Huddle test

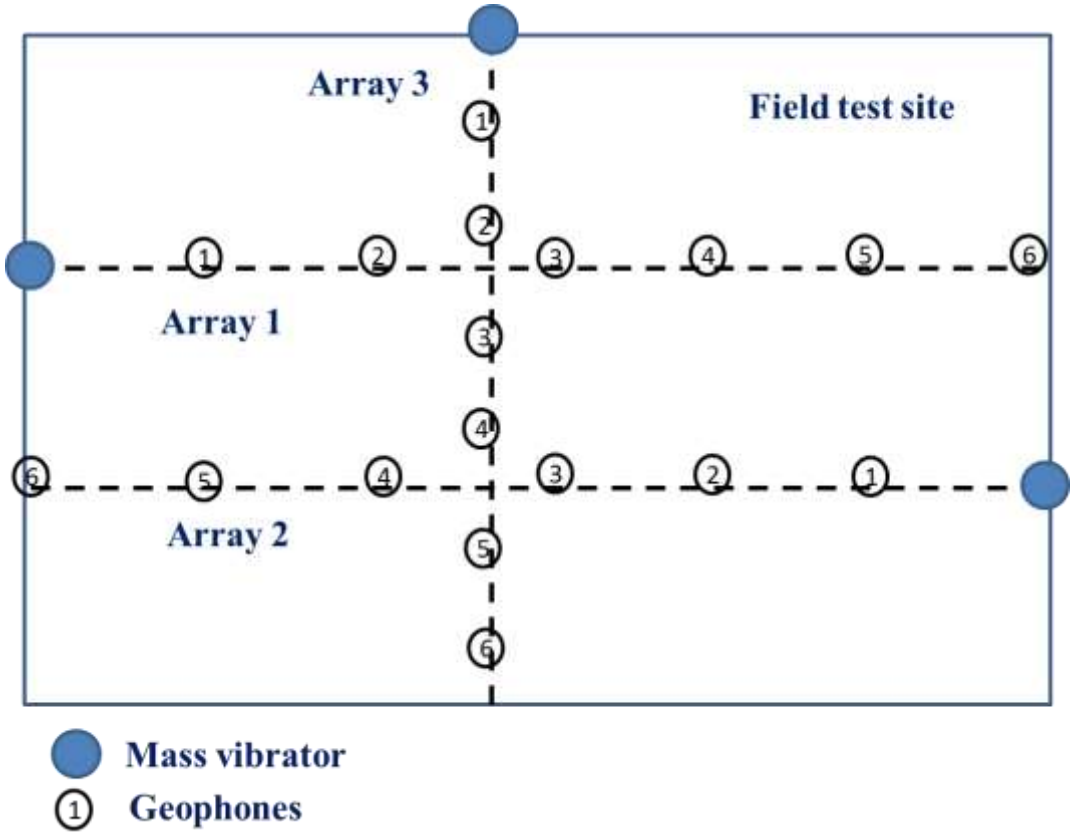

Figure 4.4 CSW test arrays on site

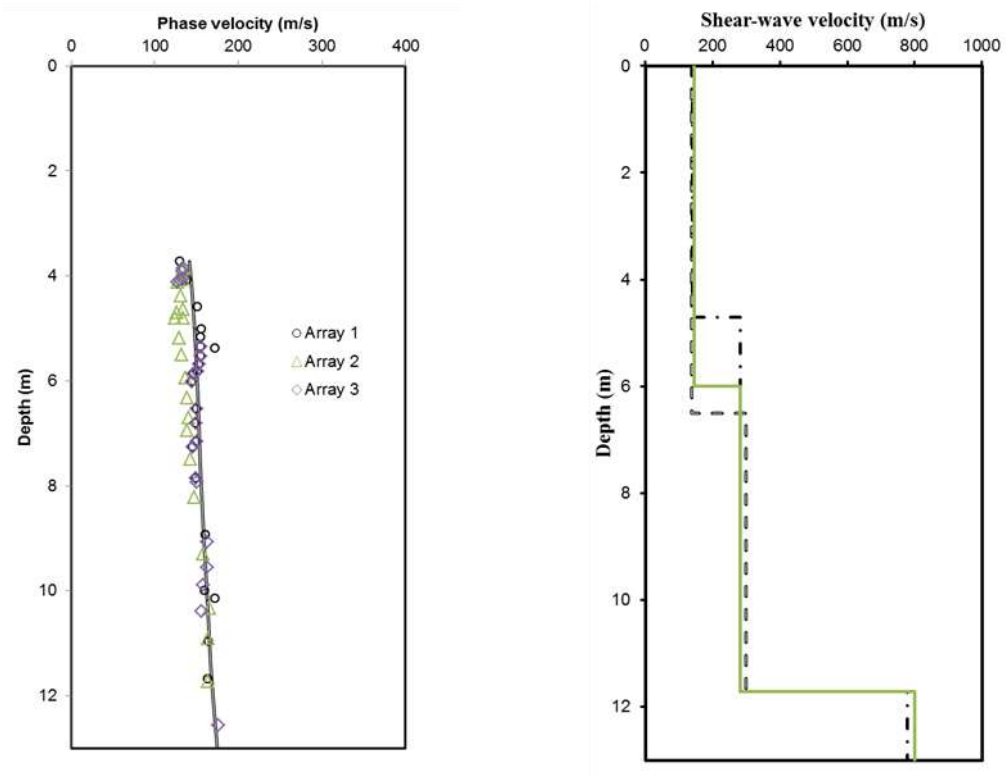

a) Dispersion curve b) V_s profile of site

Figure 4.5 Profile of the site from CSW test

Table 4.1 Summary for the CSW tests

Layers	Average Thickness (m)	V_s (m/s)
1	6.0	145
2	5.7	300
3	23.3	800

The P-wave velocity V_p of the top soil layer can be estimated by comparing the arrival times of vibrations caused by a vertical impact (Luna and Jadi, 2000). Measurement of V_p were performed over the period in which the small-scale field test was conducted. The P-wave arrivals were measured using three accelerometers placed collinearly from the vertical impact point over the area where the test was conducted. For each line, the three accelerometers were moved further and further away from the

vertical impact point such that the arrival times of P-waves arrival could be measured up to 9m from the vertical impact point. A digital oscilloscope (Yokogawa DL750P) was used to record the signals from the accelerometers. Figure 4.6 shows a plot of distance versus arrival time obtained from the vertical impact test. The gradient of the plot in Figure 4.6 gives the V_p of the top soil layer and is estimated to be 275 m/s. The V_p and V_s obtained from the tests were used to calculate the Poisson's ratio of the first soil layer for numerical simulation in the later part of this chapter. The Poisson's ratio was estimated to be 0.3.

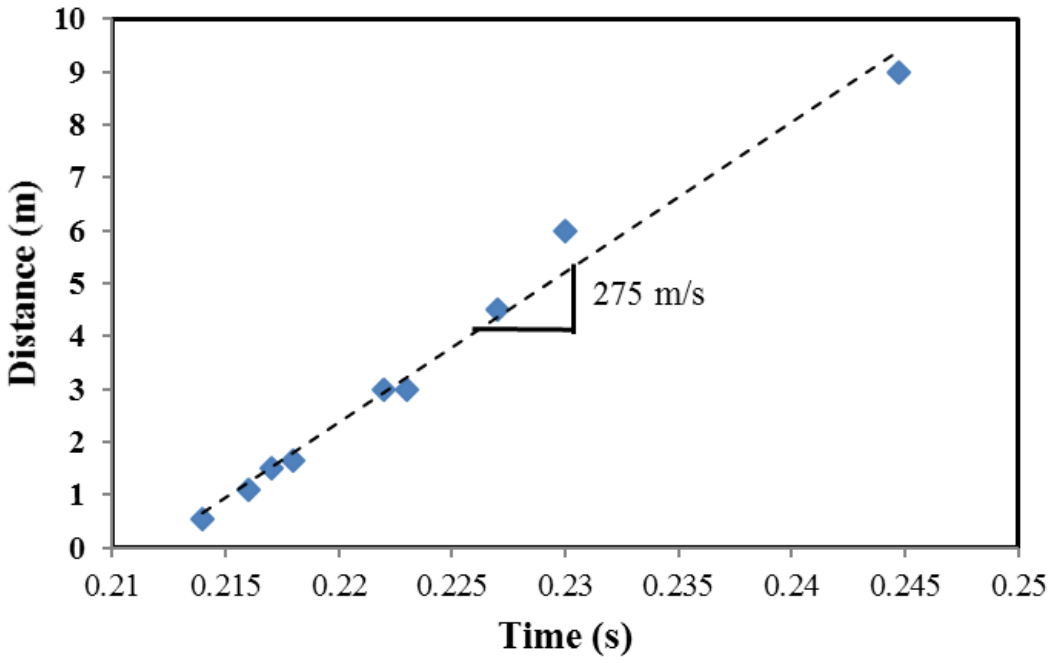

Figure 4.6 Measurement of V_p of first soil layer by impact test

4.3 Test Set-up and Procedure

The field tests involve open trench or SRM as seismic wave barrier. First, locations of mass vibrator and trench of 1.1 m and 0.25 m width were marked on the ground. The

layout of the field test is shown in Figure 4.7. Four lines radiating from the source were marked and geophone position were marked at about 0.5 m from each other along each line after the barrier as shown in Figure 4.7b. Due to symmetry, geophones were located only in one half of the test layout. The CSW system was reconfigured to perform the test and the software was modified to record the geophone readings for a duration. The frequency of the mass vibrator (source) is controlled via the CSW drive and controller unit. The mass vibrator was set to vibrate at a particular frequency for a duration and the geophones record the steady-state sinusoidal wave.

a) Picture of the layout test

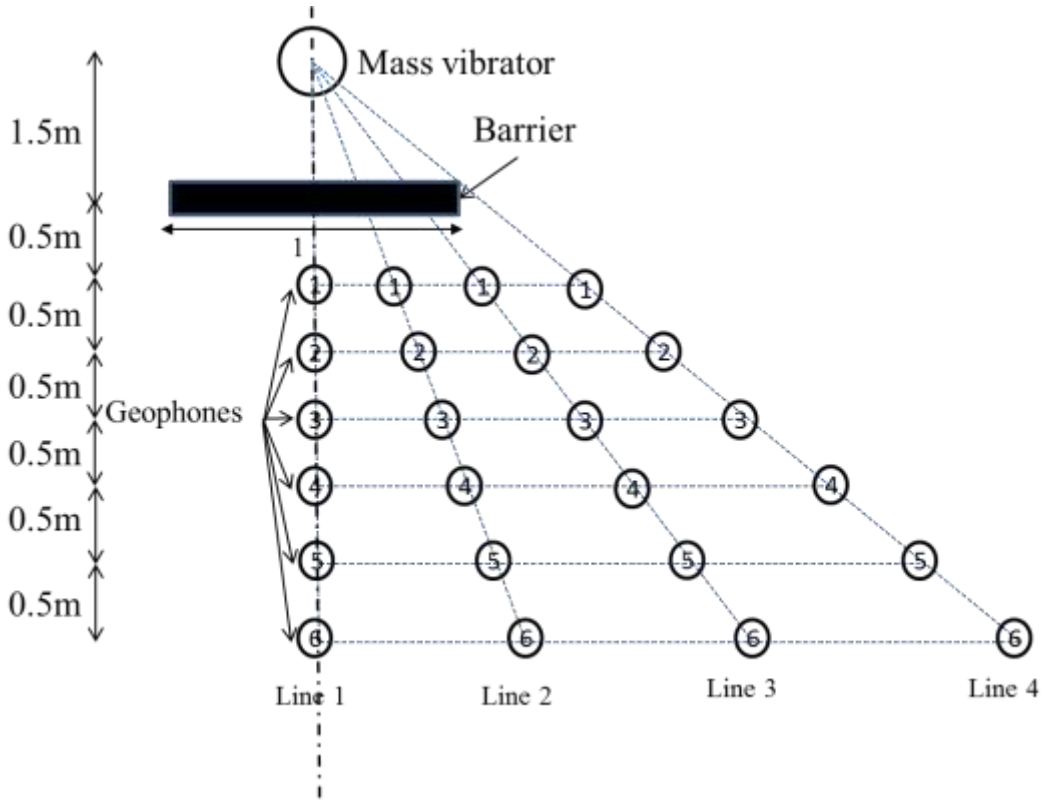

b) Schematic diagram of test layout

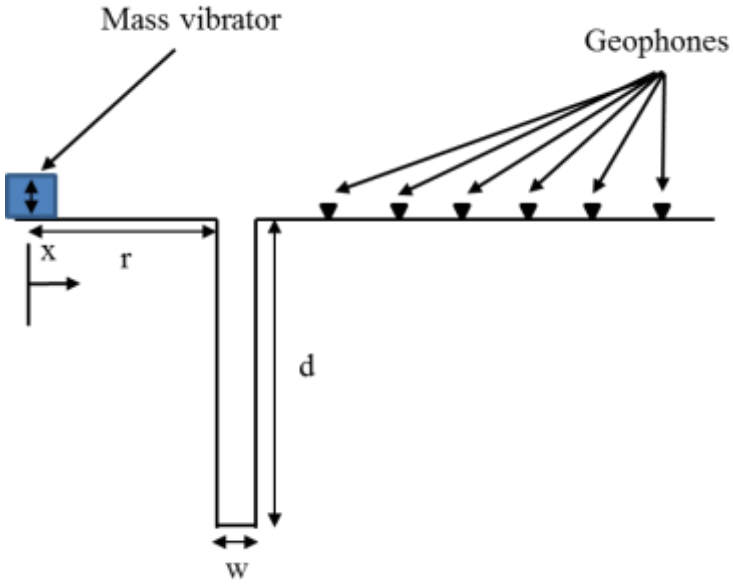

c) Section view of test layout

Figure 4.7 Small-scale field test layout

Tests were conducted prior to the excavation of the trench to provide the readings for the "no trench" condition. After the "no trench" tests were conducted, the trench was excavated manually. The trench depth was 1m. A total of four test series were conducted. The test series with their notations are summarised in Table 4.2. The frequency of the sinusoidal wave generated by the mass vibrator covers a range from 20 Hz to 100 Hz (20, 40, 60, 80, 95 and 100 Hz) for each test series. Based on the V_s of the first soil layer (145 m/s), Rayleigh wave velocity V_R is equivalent to approximately 0.924 of V_s for Poisson's ratio of 0.3 (Stokoe et al., 1994); the wavelength of the Rayleigh waves can then be calculated ($V_R = d/\lambda_R$) which ranges from 1.34 m to 6.7 m. Rayleigh waves are heavily attenuated at one wavelength depth (Massarsch 2005). Hence, only some effects of the second soil layer may be present in the 20 Hz test results. However, Ahmad and Al-Hussaini (1991) reported that the effect due to material impedance will only be significant when the trench cuts through the top layer into the second layer. In addition, Besko et al. (1986) suggested that the second layer has minimal effect on amplitude reduction. The normalised depth D = d/λ_R corresponding to the wave frequency is presented in Table 4.3. According to the literature review, trench or barrier with D of at least 0.6 was found to be effective. Thus, the frequencies selected for the tests are suitable for investigating the efficacy of the seismic wave barrier. For test series 3 and 4, the SRMs were compacted in lifts of 0.1m to ensure that each layer was properly compacted to the targeted dry density and the SRM was in good contact with the trench walls.

Table 4.2 Test series

Test series	In-filled materials	Denotation
1	No trench	Normal
2	Open trench	Open
3	70% sand and 30% rubber	R30
4	30% sand and 70% rubber	R70

Table 4.3 Frequencies for each test series and their corresponding normalised depth D

Frequency (Hz)	Rayleigh wavelength λ_R (m)	Normalised depth D
20	6.70	0.14
40	3.35	0.29
60	2.23	0.44
80	1.68	0.55
95	1.41	0.70
100	1.34	0.74

4.4 Results and Discussion

The effectiveness of the barrier is determined by Ar (Wood 1968) defined as

$$\text{Ar} = \frac{\text{Amplitude with the barrier}}{\text{Amplitude without the barrier}} \tag{4.1}$$

The barrier is considered to be effective if Ar falls below 0.25 (Wood 1968). The raw data for each geophone was first low-pass filter at + 5 Hz of the input frequency. Figures 4.8a and b show the raw and filtered FFT and geophone signals for 60 Hz, respectively. From Figure 4.8a, the FFT for the raw data shows the presence of frequency at 120 Hz resulted from the first harmonic caused by the vibrator at 60 Hz. The frequency can be eliminated with application of the low-pass filter. The amplitude in Equation 4.1 is determined as the mean amplitude of the steady-state vibration shown in Figure 4.8b.

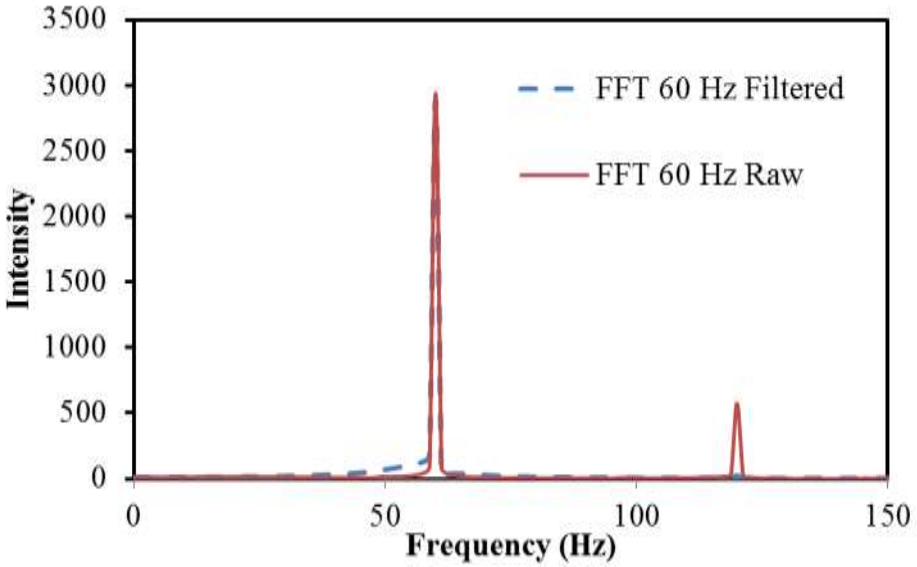

a) FFT for 60 Hz 2m away from source

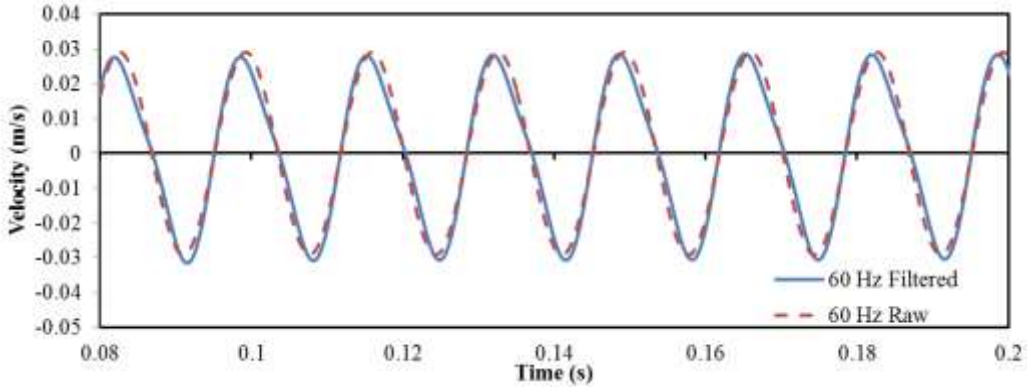

b) Typical velocity-time history at 60 Hz 2m away from source

Figure 4.8 Typical raw and processed signal, from geophone at 60 Hz

4.4.1 Effect of barrier type and frequency

Figures 4.9 and 4.10 show signals of geophones 1 to 6 of line 1 at 60 Hz and 95 Hz, respectively. From Figures 4.9 and 4.10, it is evident that the open trench provides the best barrier effect, followed by the SRM barriers R70 and R30. Between the two SRM barriers, R70 is more effective which shows that the barrier effect is improved by increasing the rubber chip content in SRM. Figures 4.11 to 4.14 show Ar plotted

against D for geophones 1 to 6 of lines 1 to 4, respectively. From Figures 4.11 to 4.14, a few observations can be made:

1. An increase in D causes a general decrease in Ar. At vibrating frequency of 95 Hz (corresponding D = 0.7), Ar for open trench and R70 barrier falls below 0.25 which is deemed efficient by Woods (1968). Barrier being effective at $D \geq 0.7$ is more stringent than $D \geq 0.6$ suggested by Woods (1986), Besko et al. (1985), May and Bolt (1982) and Alzawi and Nagger (2011). Haupt (1981) and Dolling (1970) suggested $D \geq 1.0$ and 0.8, respectively, to be effective.
2. There is a general increase in Ar from geophones 1 to 6. For instance, when comparing the Ar between geophones 1 and 6 for line 1 at D = 0.7, there is an increase of 0.2, 0.24 and 0.09 in Ar for open trench, R70 and R30, respectively. There is a general increase in Ar from lines 1 to 4 (Figure 4.11 to 4.14), where line 4 shows that the barrier has almost no effect on the Ar. These observations are in agreement with the observations made by Barkan (1962) and Dolling (1970) who reported an increase in Ar with increasing distance away from the barrier.

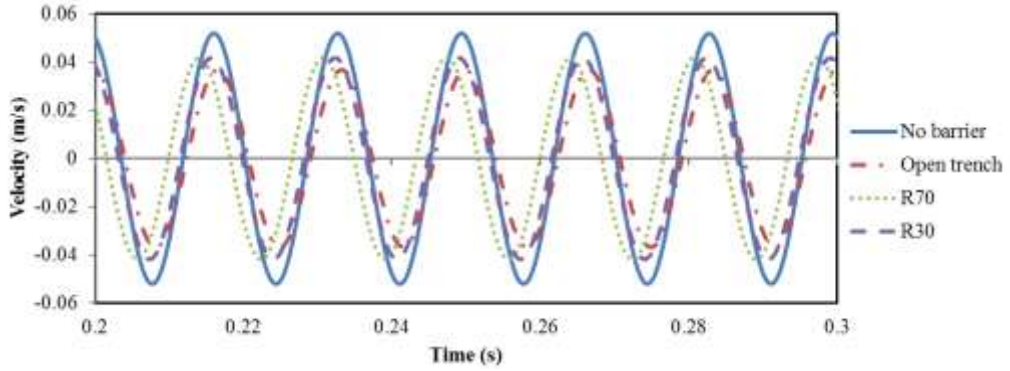

a) Geophone 1

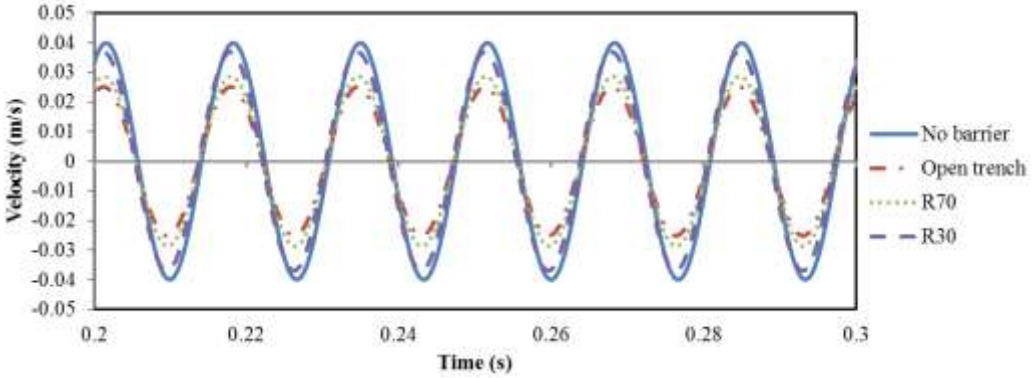

b) Geophone 2

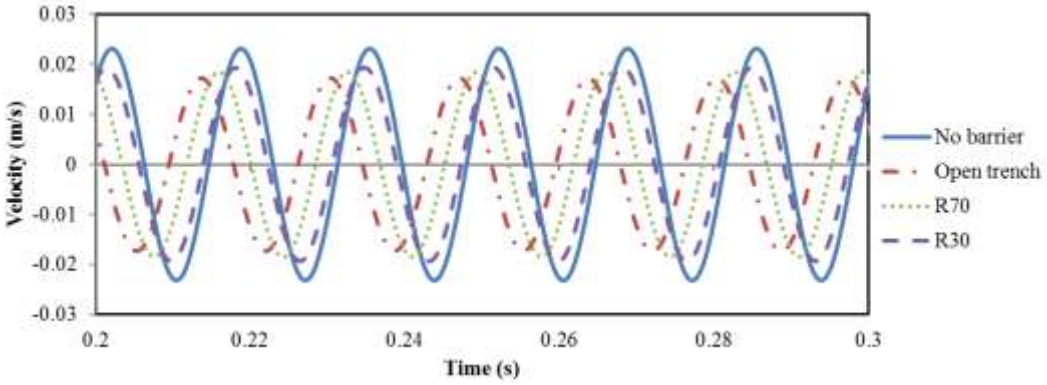

c) Geophone 3

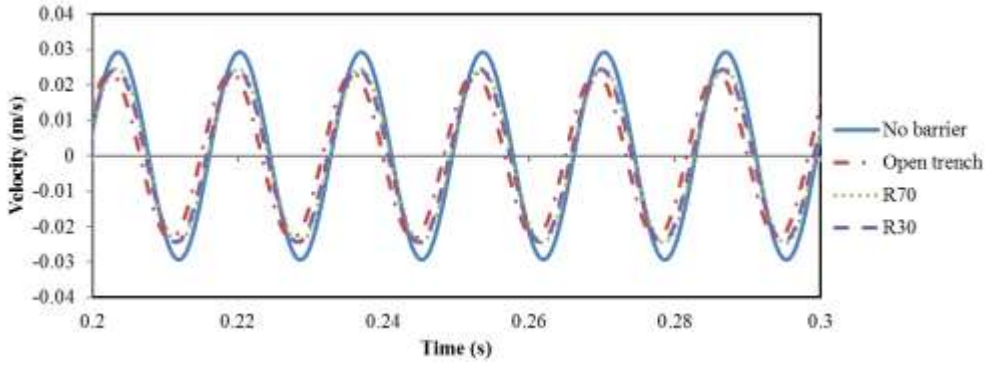

d) Geophone 4

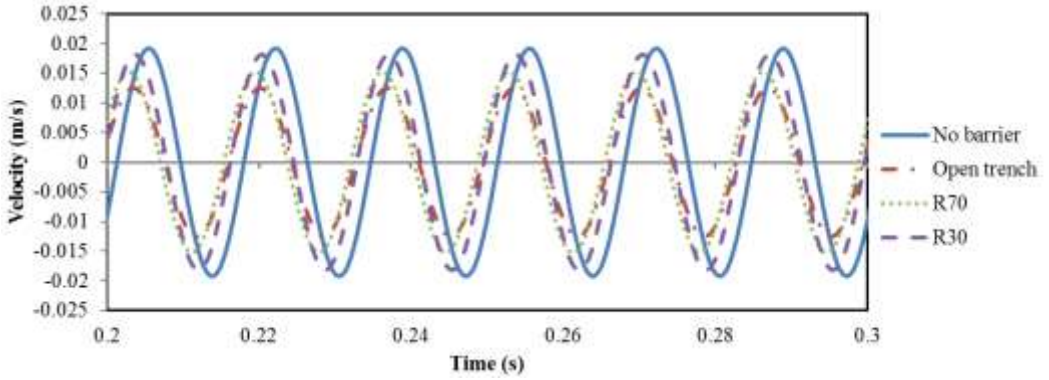

e) Geophone 5

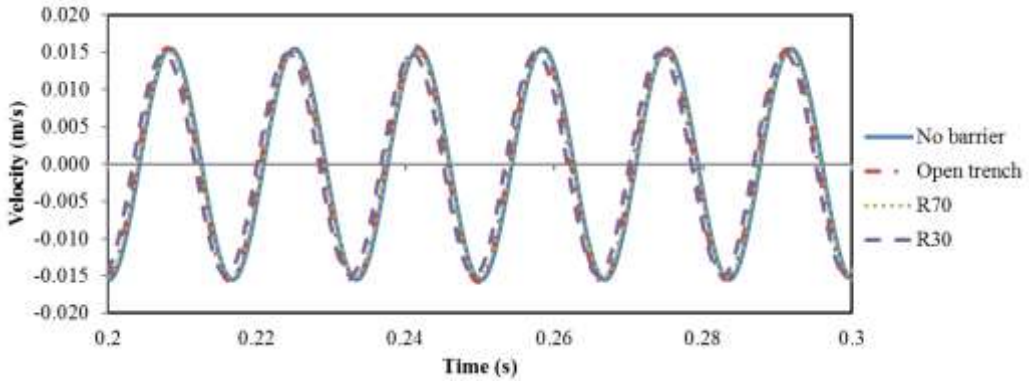

f) Geophone 6

Figure 4.9 Geophones' signals for 60 Hz, line 1

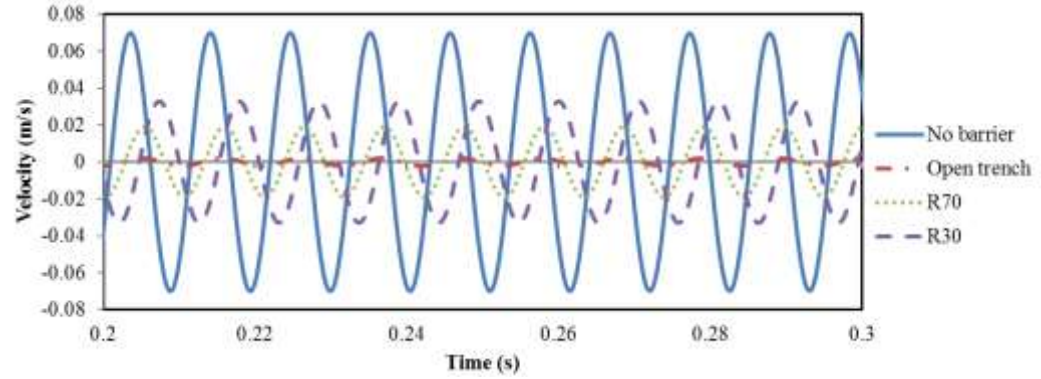

a) Geophone 1

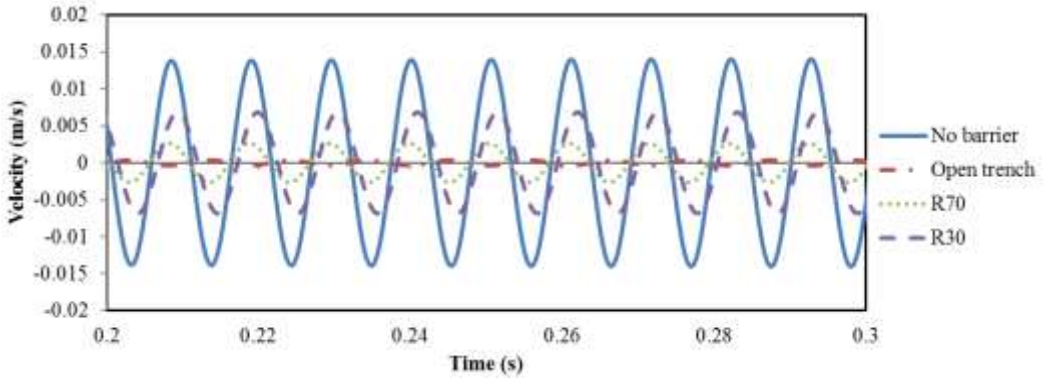

b) Geophone 2

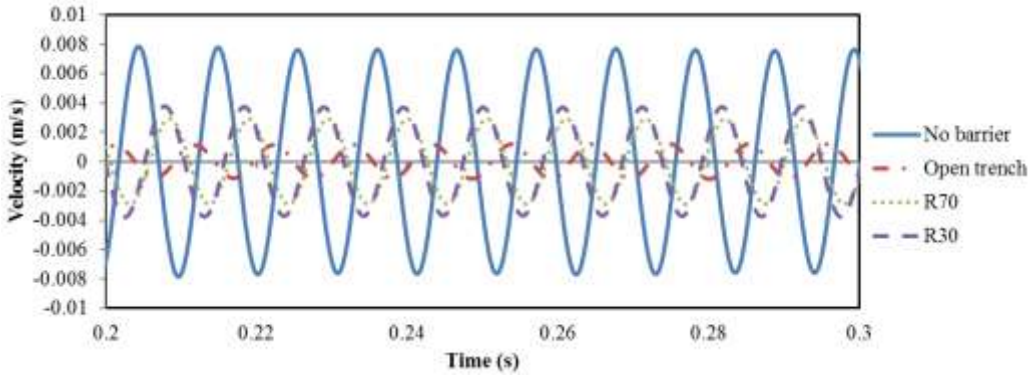

c) Geophone 3

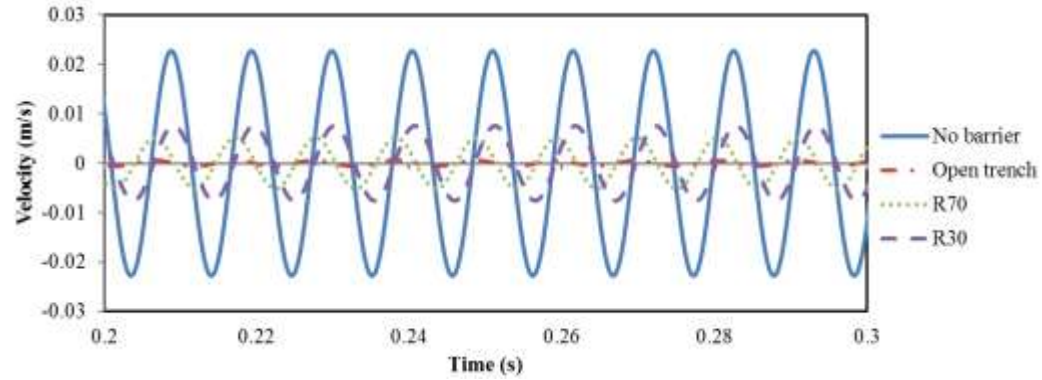

d) Geophone 4

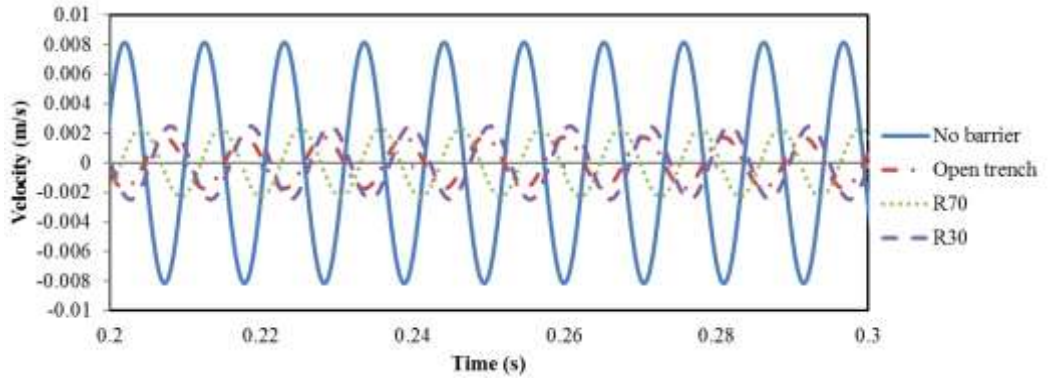

e) Geophone 5

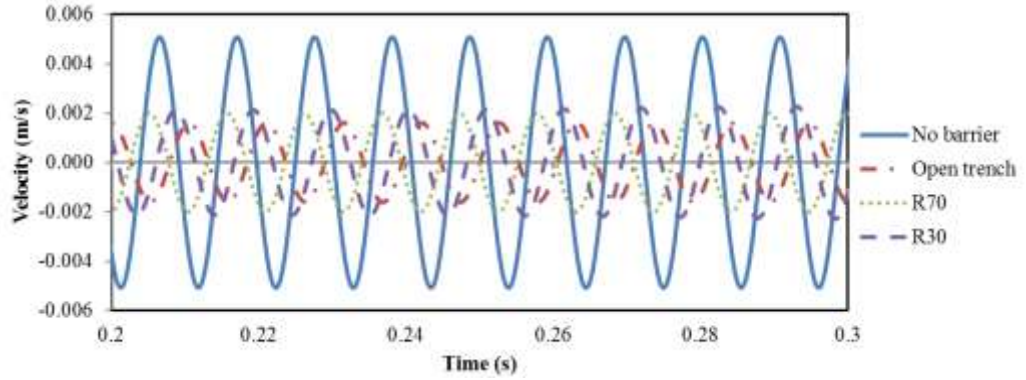

f) Geophone 6

Figure 4.10 Geophones' signals for 95 Hz, line 1

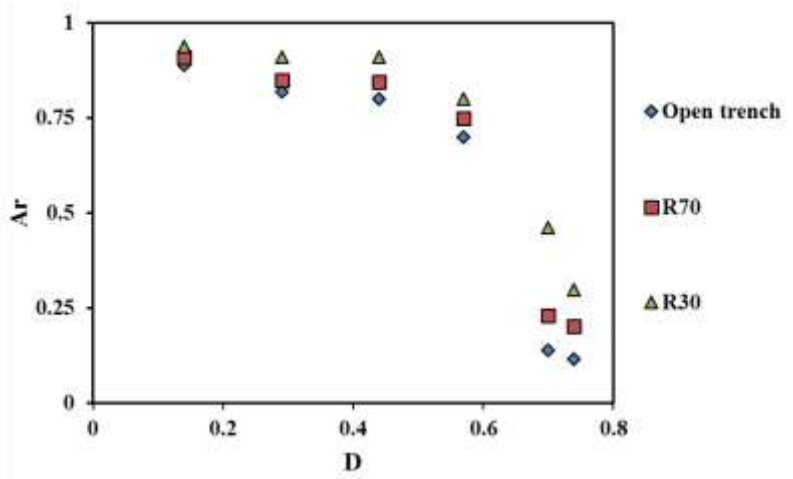

a) Geophone 1

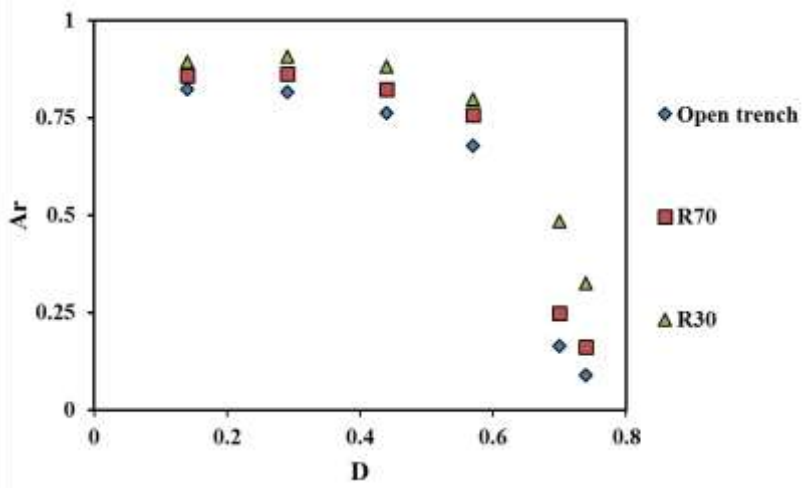

b) Geophone 2

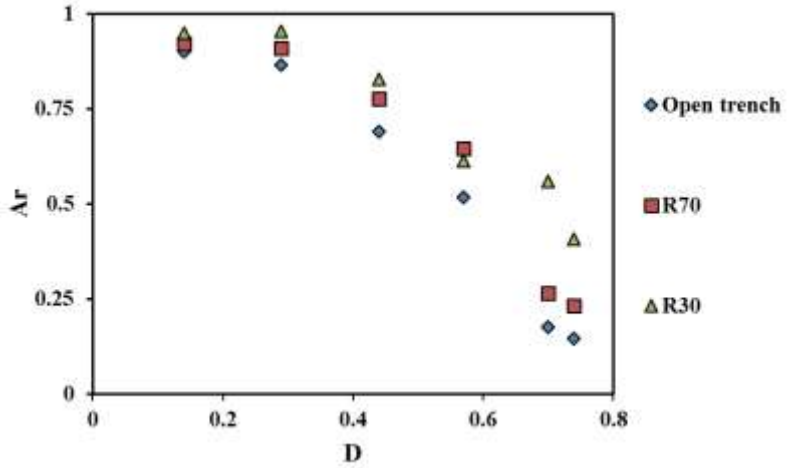

c) Geophone 3

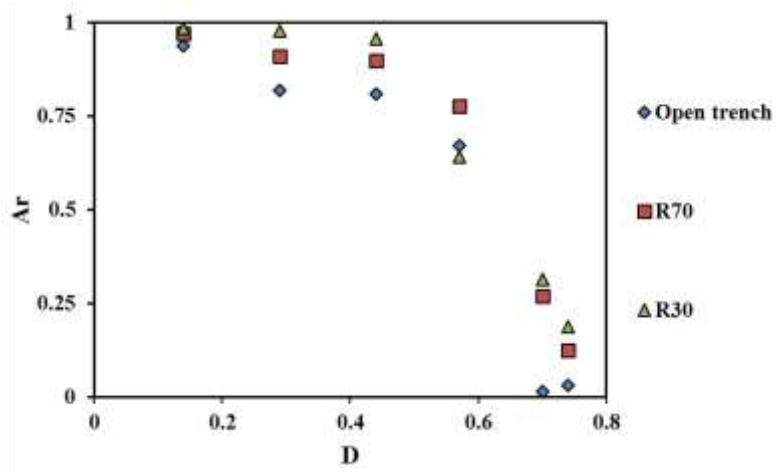

d) Geophone 4

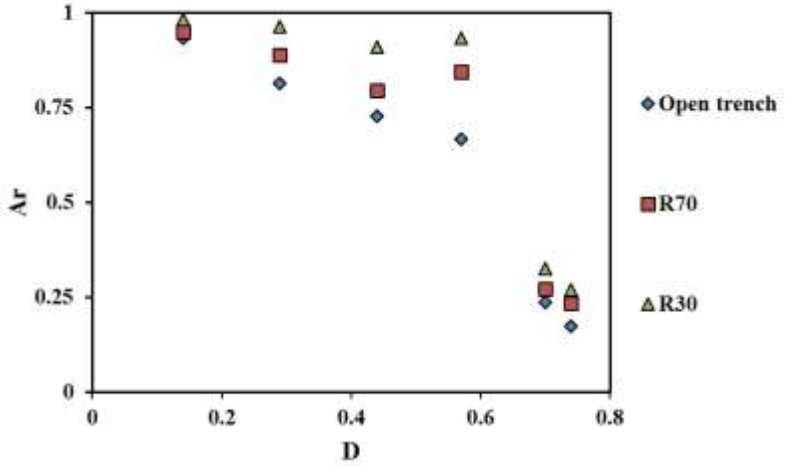

e) Geophone 5

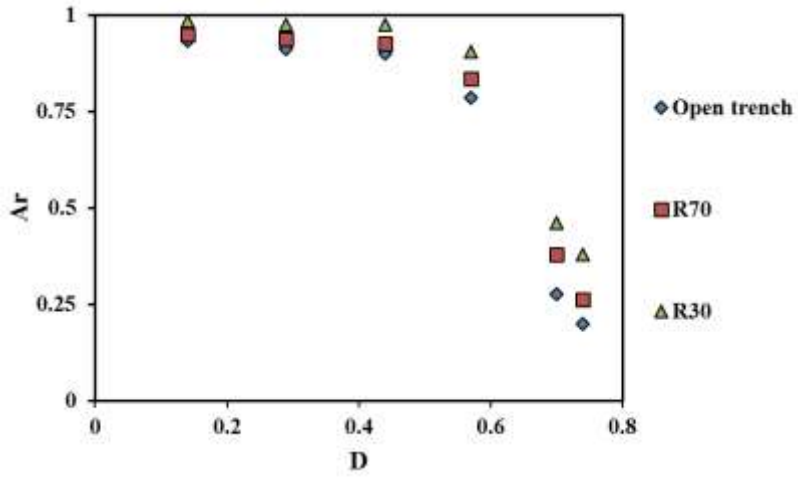

f) Geophone 6

Figure 4.11 Line 1 Ar versus D

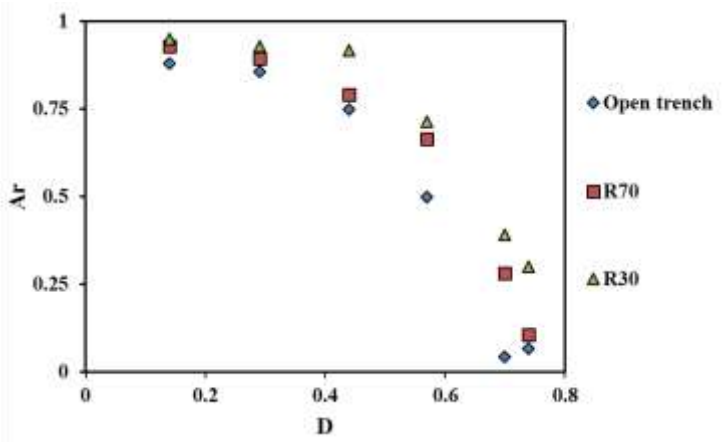

a) Geophone 1

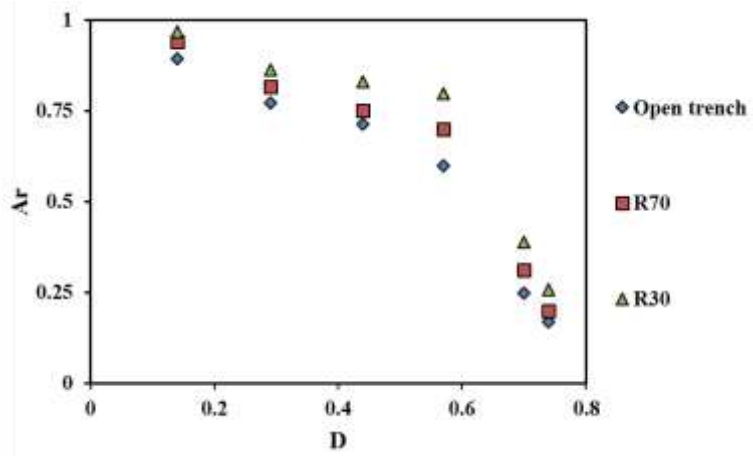

b) Geophone 2

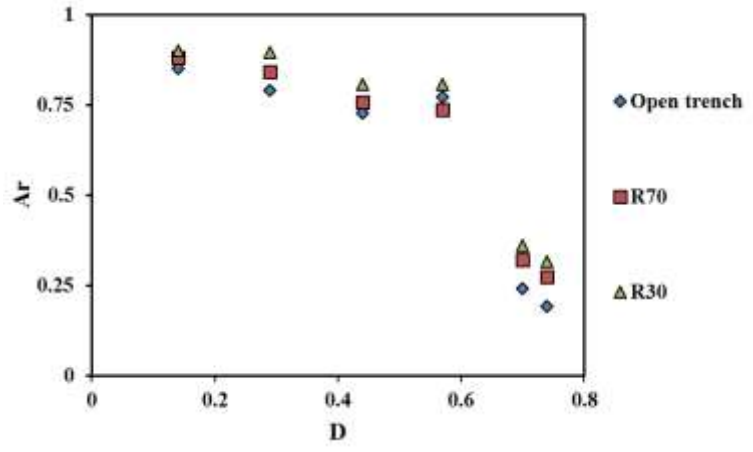

c) Geophone 3

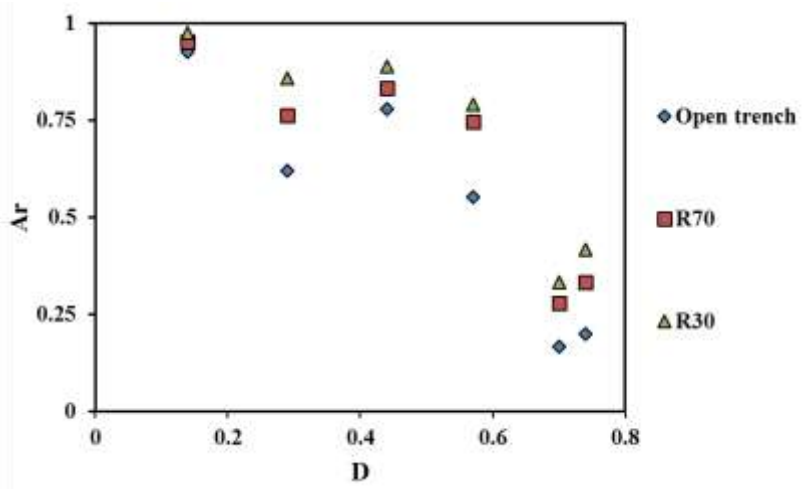

d) Geophone 4

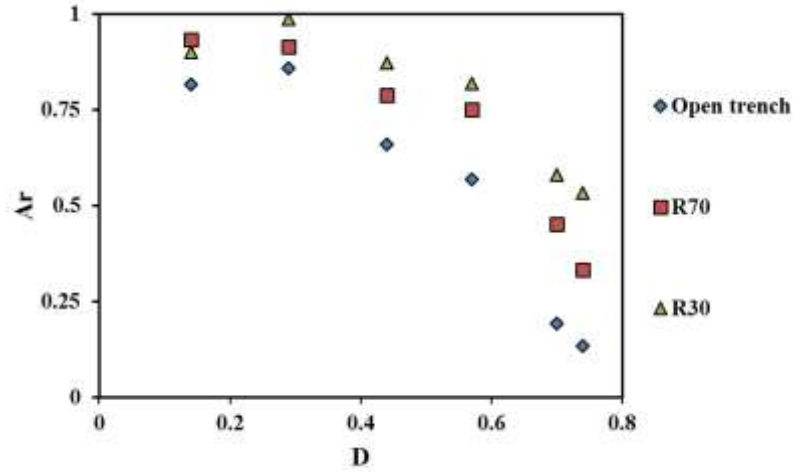

e) Geophone 5

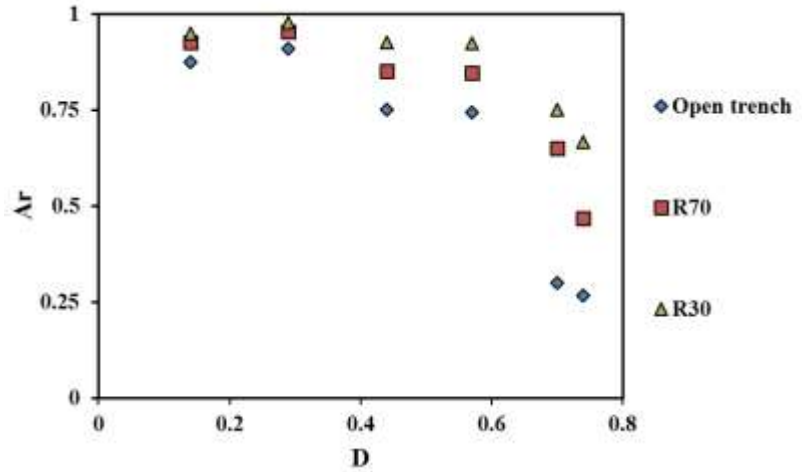

f) Geophone 6

Figure 4.12 Line 2 Ar versus D

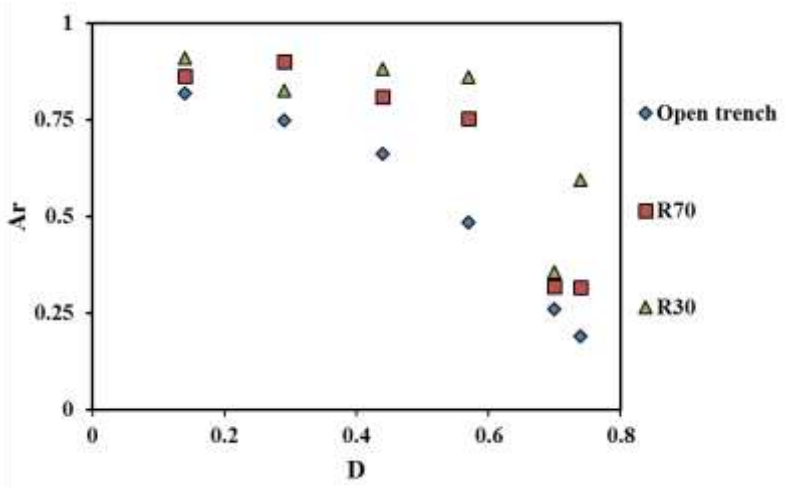

a) Geophone 1

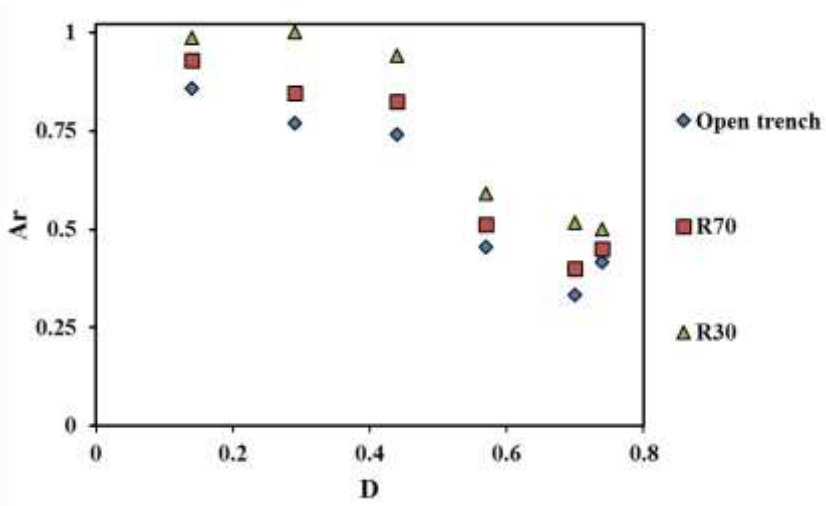

b) Geophone 2

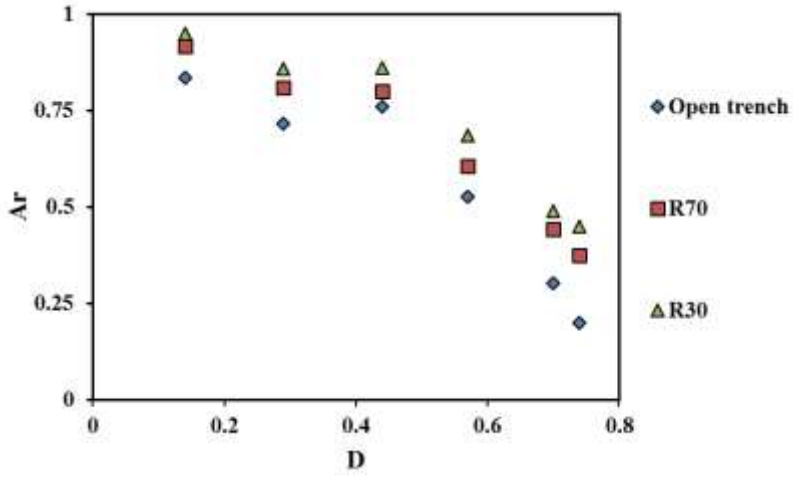

c) Geophone 3

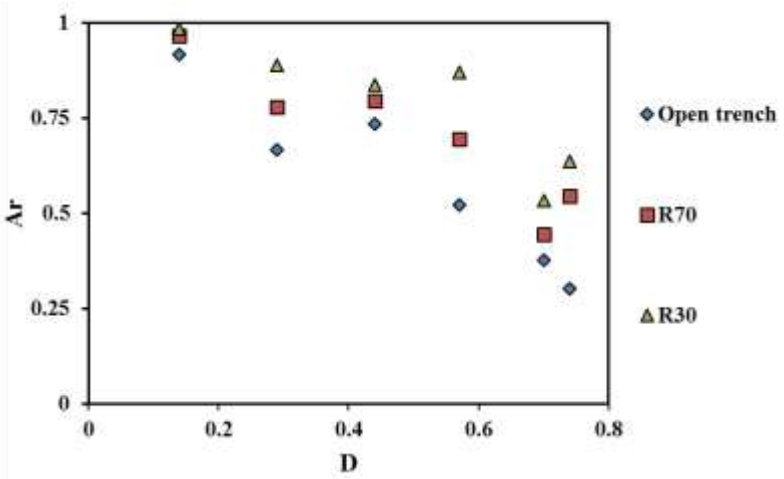

d) Geophone 4

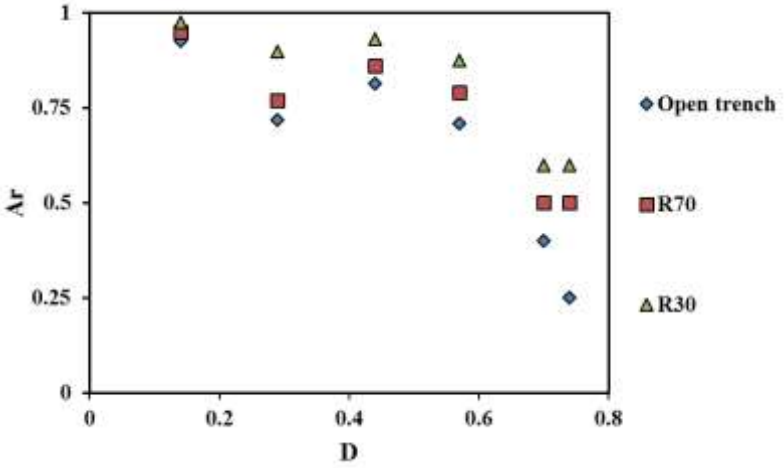

e) Geophone 5

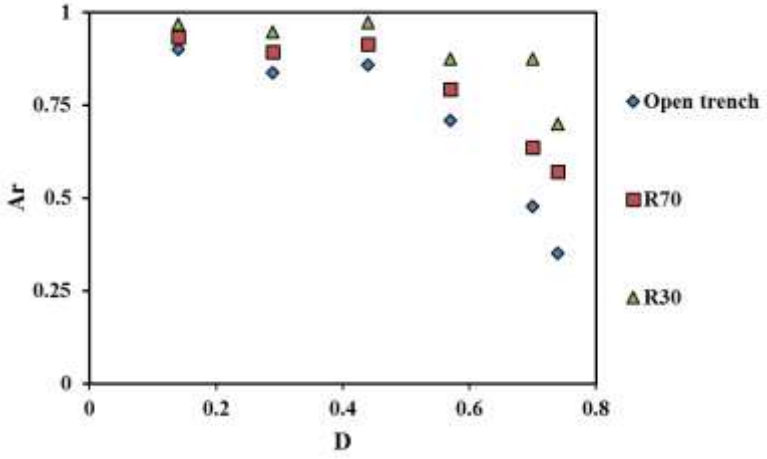

f) Geophone 6

Figure 4.13 Line 3 Ar versus D

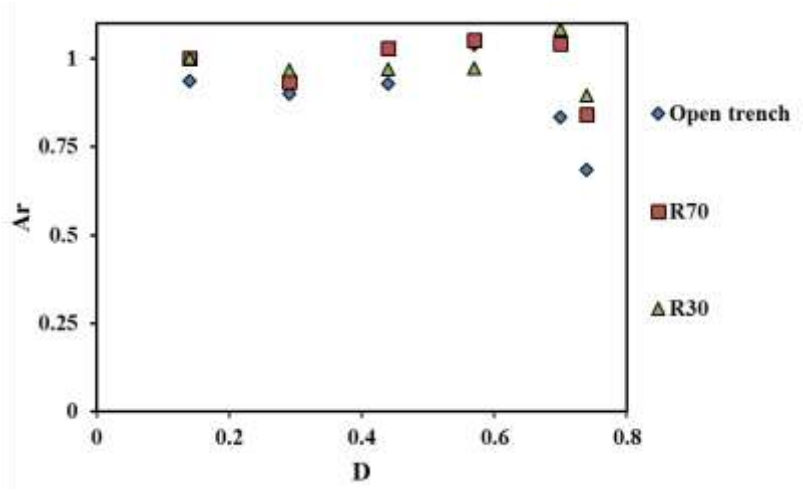

a) Geophone 1

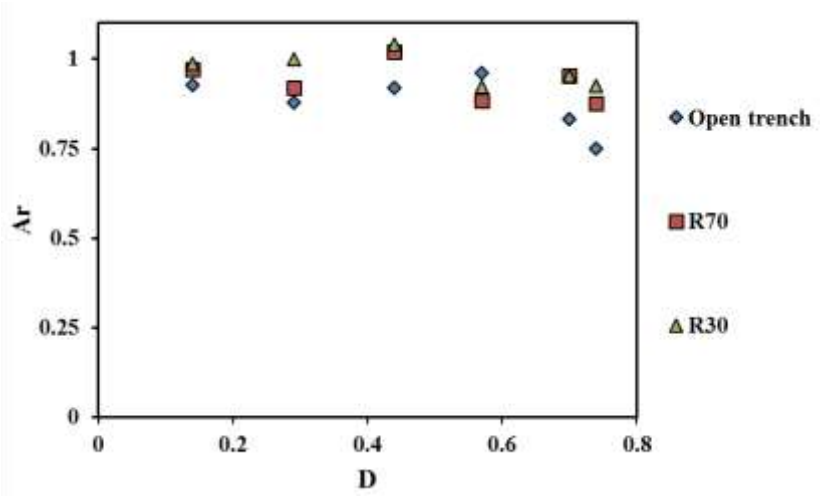

b) Geophone 2

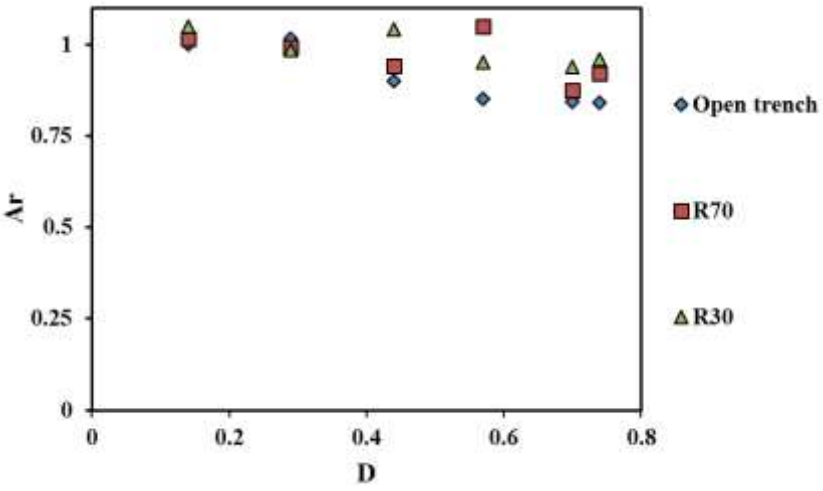

c) Geophone 3

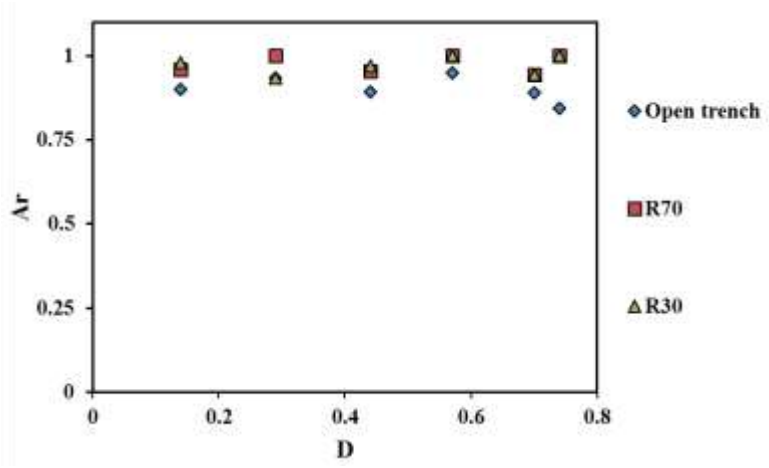

d) Geophone 4

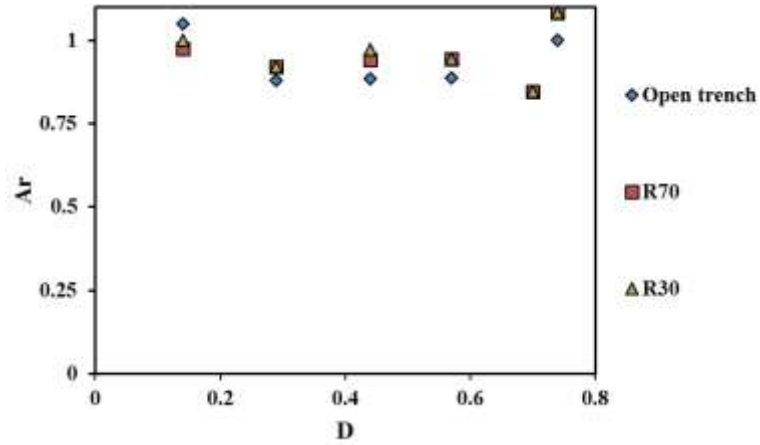

e) Geophone 5

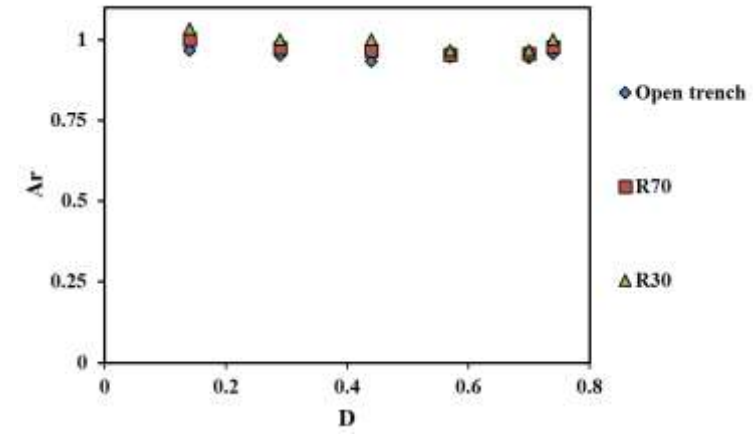

f) Geophone 6

Figure 4.14 Line 4 Ar versus D

4.5 Finite Element (FE) Modelling of Field Test

The field tests performed have limitations due to equipment and site constraints. To better understand the test results, numerical modelling by finite element method can be used to complement the field tests. LS-DYNA has a user-friendly pre-processor to build and construct finite element models. The finite element model should be simple and yet able to replicate the mechanics of the simulated problem. LS-DYNA has proven to be reliable in simulating and solving dynamic problems by others. LS-DYNA also has a post processor that could output results and perform functions such as integration, differentiation and filtering of the results. Aung and Leong (2011) have used LS-DYNA to simulate CSW test successfully. For these reasons, LS-DYNA is chosen as the software to model the field test. The choice of the materials models is important to obtain reasonable and reliable results. The shape of the element and the element type affects the accuracy of the results. It is suggested in the LS-DYNA Users' Manual that uniformly shaped quadrilateral elements will produce more reasonable results. However, the finite element mesh should be as fine as possible to ensure that accurate results are obtained. The run time and the memory required depend greatly on the number of elements in the finite element mesh and the integration order. Hence, balance between accuracy of the results and the run time is required.

4.5.1 FE model

The field test is modelled using a quarter finite element (FE) model. The modelling approach used follows the recommendations in Aung and Leong (2011). The quadrant has dimensions of 5.2m by 3m by 4m (area of test site) and the mesh consisted of

24,960 eight-noded solid elements with elements size of 0.1m cube and 0.1m by 0.1m by 1.0 m cuboid. Marburg (2002) concluded that six elements per wavelength produced about 10% error, increase in number of elements per wavelength will yield diminishing returns. Hence 13.4 elements per wavelength (smallest mesh size/ shortest wavelength) will give an error much less than 10%. The FE model can be small because the boundaries can be modelled using non-reflecting boundaries (Aung and Leong 2011). Figure 4.15a and 4.15b show the section and plan views of the 3-D FE model, respectively. Dimensions of the trench and model (r, l, w, d, x and y) are indicated in Figure 4.15. A cyclic vertical vibration was applied at the top node of the axis of symmetry of the model to simulate the continuous vibration of the mass vibrator. The equation of the cyclic vertical vibration is as follows:

$$V(t) = V_o \mathrm{Sin}(2\pi ft) \tag{4.5}$$

where V_o is the velocity amplitude, f is the cyclic frequency and V(t) is the velocity at time t. No material damping was applied to the FE simulation for a conservative analysis.

The material model used for the soil and SRM is MAT_001 Elastic (soil and SRM). The open trench is modelled using null material MAT_009 in the LS-DYNA material library coupled with a linear polynomial equation of state (EOS) to avoid calculating the deviatoric stress in the model. The general form for the linear polynomial equation of state is given by:

$$p = C_0 + C_1\mu + C_2\mu^2 + C_3\mu^3 + (C_4 + C_5\mu + C_6\mu^2)E_0 \tag{4.2}$$

$$\mu = \frac{1}{V_c} - 1 \tag{4.3}$$

where C_0, C_1, C_2, C_3, C_4, C_5 and C_6 are constants that can be defined by the user, μ is the volumetric parameter, V_c is the current volume and $E_0 = \rho_0 C_v T$ is the internal energy where C_v is the specify heat capacity at constant volume and T is the temperature.

For ideal gas, only C_4 and C_5 are non-zeros. The relationship between the linear polynomial EOS and the idea gas equation is:

$$C_4 = C_5 = \gamma - 1 \tag{4.4}$$

where $\gamma = C_p/C_v$ is the ratio of the specify heat capacities of constant pressure and constant volume (=1.403 for air), C_p is the specify heat capacity at constant pressure. Therefore, $C_4 = C_5 = 0.403$. Table 4.4 shows the input for soil, R30, R70 and air. The properties of soil, R30 and R70 were obtained through lab and field test as presented in Sections 4.2 and 3.8, respectively. The velocity amplitudes V were obtained from huddle test where the geophones were planted right beside the mass vibrator to measure the velocity output at each vibrating frequency. The results were then compared with field data in terms of velocity amplitudes. Figure 4.16 shows a typical velocity-time history obtained from the FE model. Figures 4.17 and 4.18 show the comparison of the velocity amplitude of the FE results with the field data for 20 and 100 Hz, respectively, for all the measuring points from lines 1 to 4. The comparison shows that the velocities from the field tests match reasonably well with the velocities obtain from the FE model. Any discrepancy is due to the inhomogeneous ground condition and coupling between geophone and the ground in the field tests. As recommended by Kim and lee (2000), Figure 4.17e shows that when both geometric and material damping is considered, the resulting velocity becomes lower in

comparision.

Table 4.4 Properties input in LS-DYNA

	Material model	Density (kg/m^3)	Young's modulus (kPa)	Poisson's ratio
Soil	MAT_001	1800	9.8e4	0.3
SRM30	MAT_001	1360	3.5e3	0.4
SRM70	MAT_001	977	2.7e3	0.42
Open trench	MAT_009	1.225	-	-

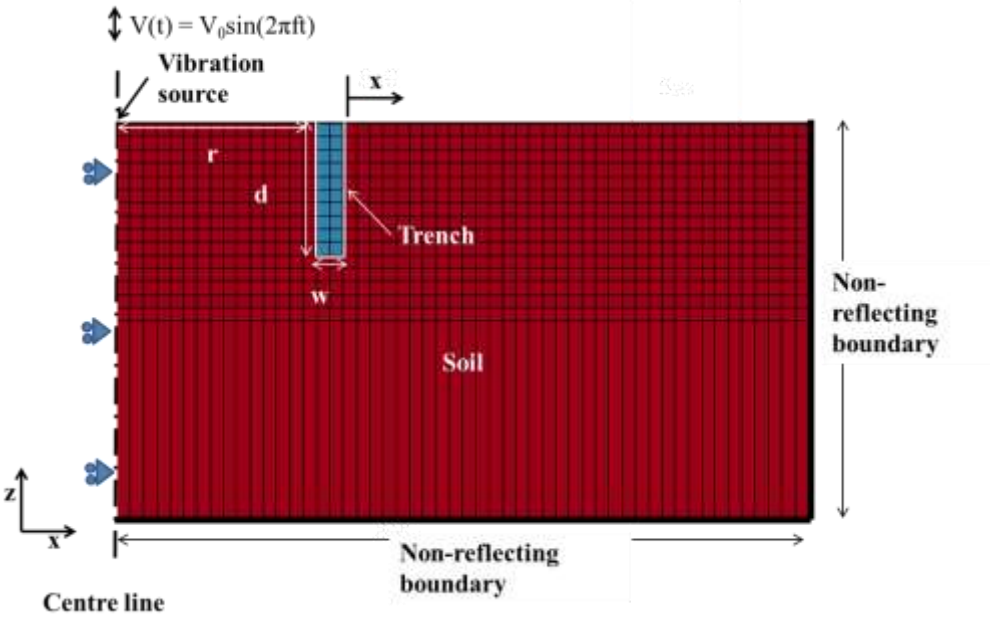

a) Section view

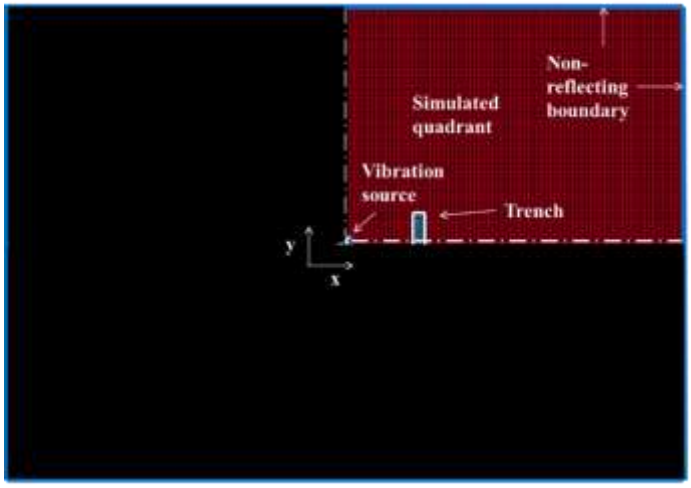

b) Plan view

Figure 4.15 FE model

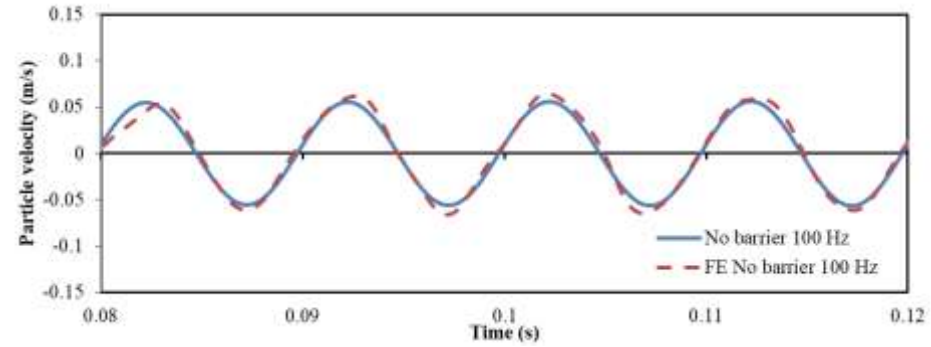

a) No barrier

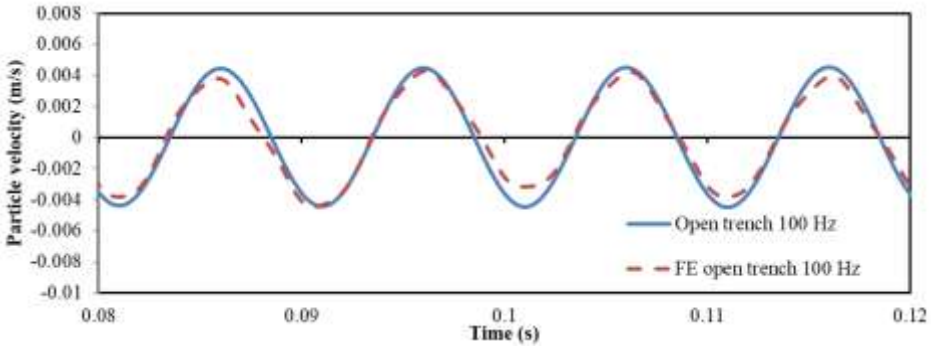

b) Open trench

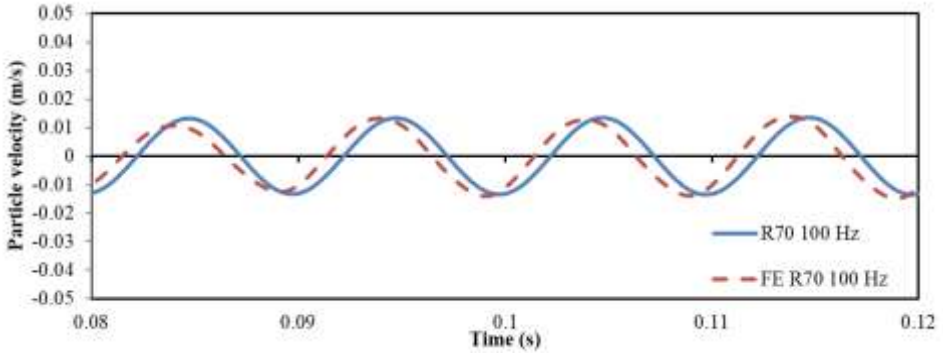

c) R70 barrier

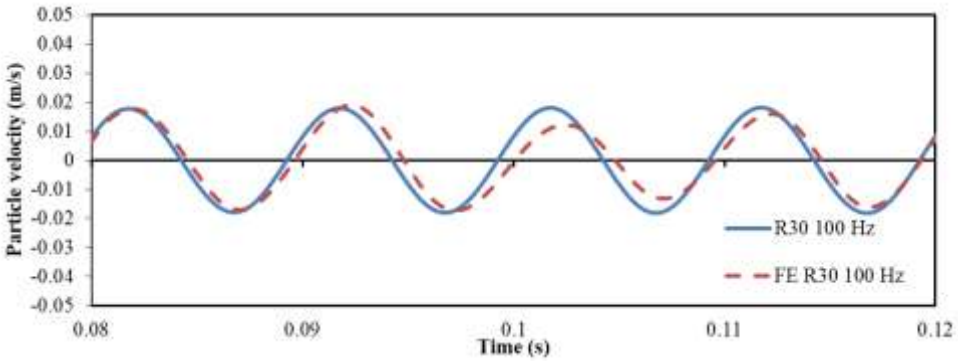

d) R30 barrier

Figure 4.16 Typical velocity-time histories for both field test and FE model for geophone 1 at 100Hz

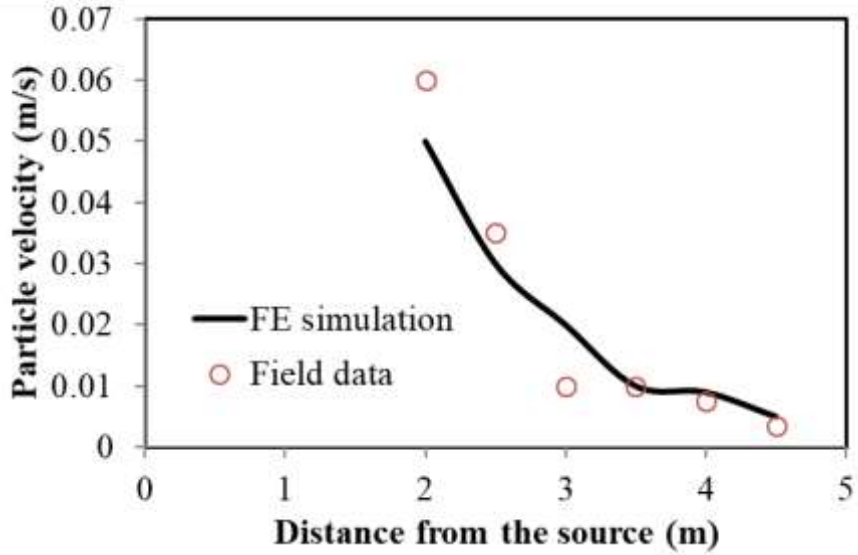

a) Line 1

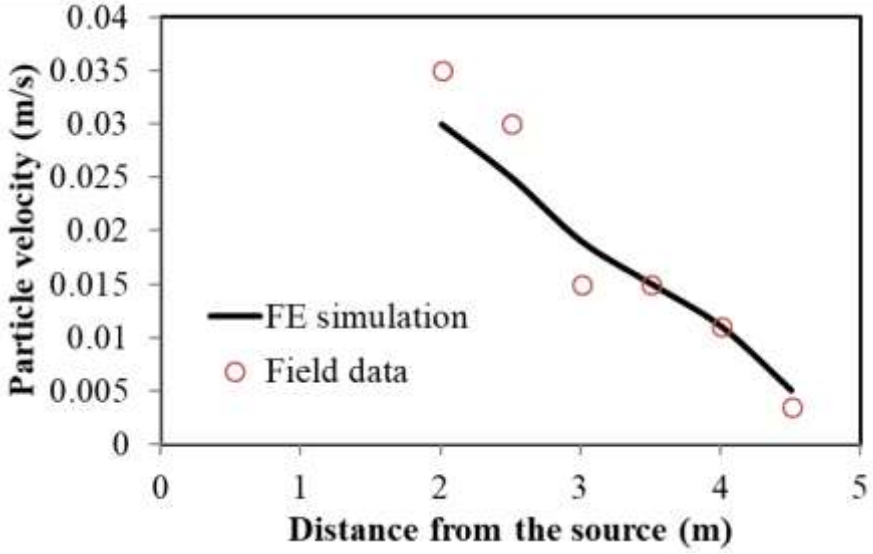

b) Line 2

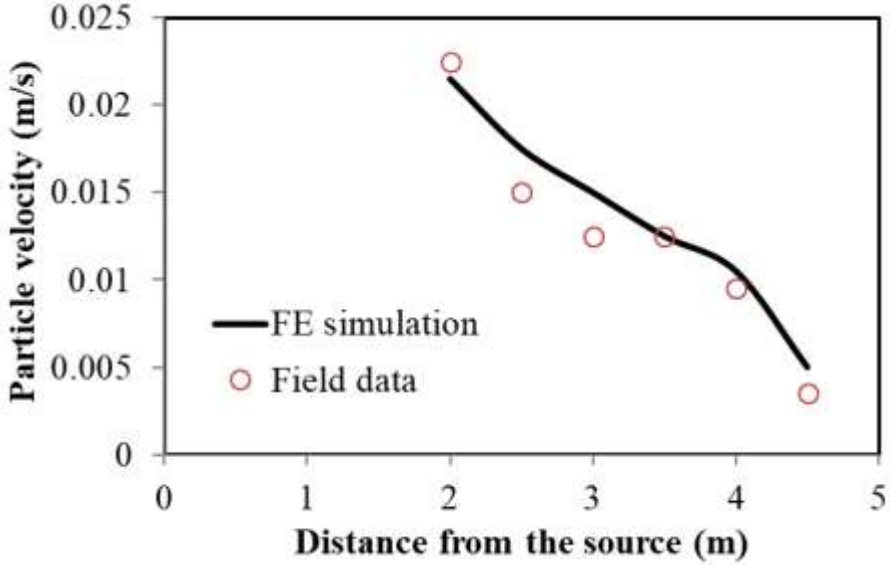

c) Line 3

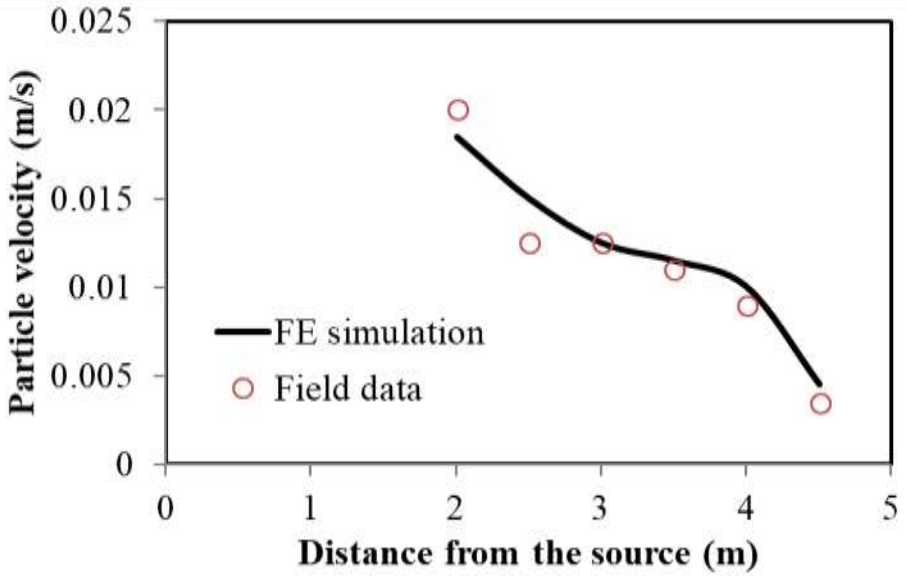

d) Line 4

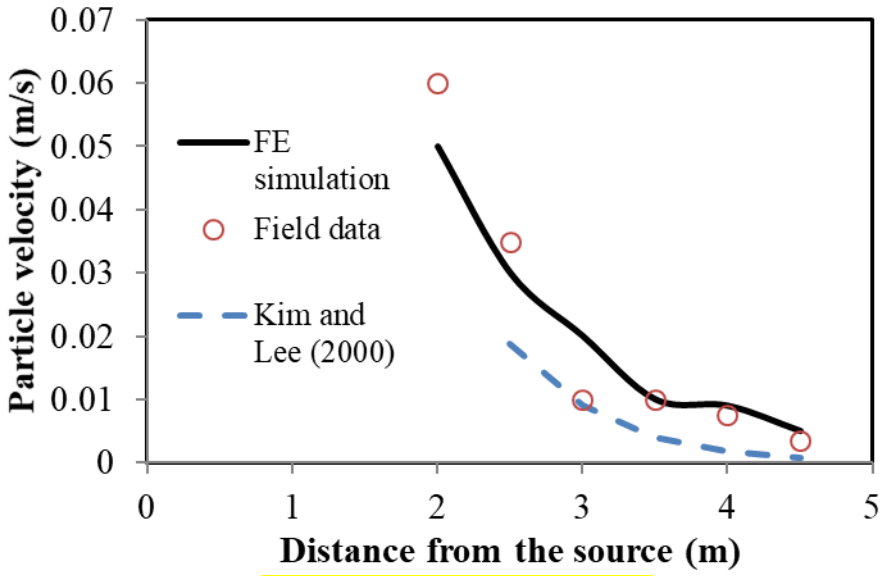

e) Line 1 (Kim and Lee, 2000)

Figure 4.17 Comparison of FE results and field data for 100 Hz

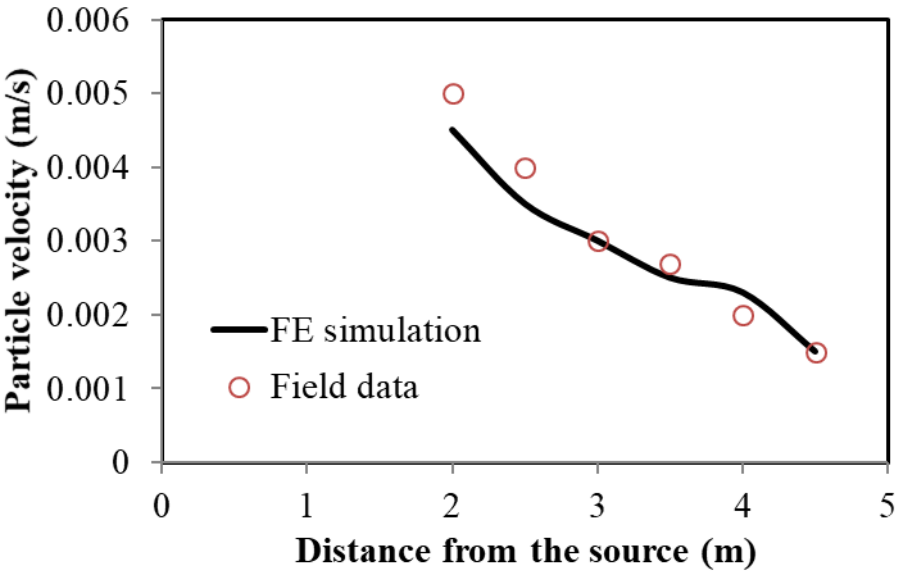

a) Line 1

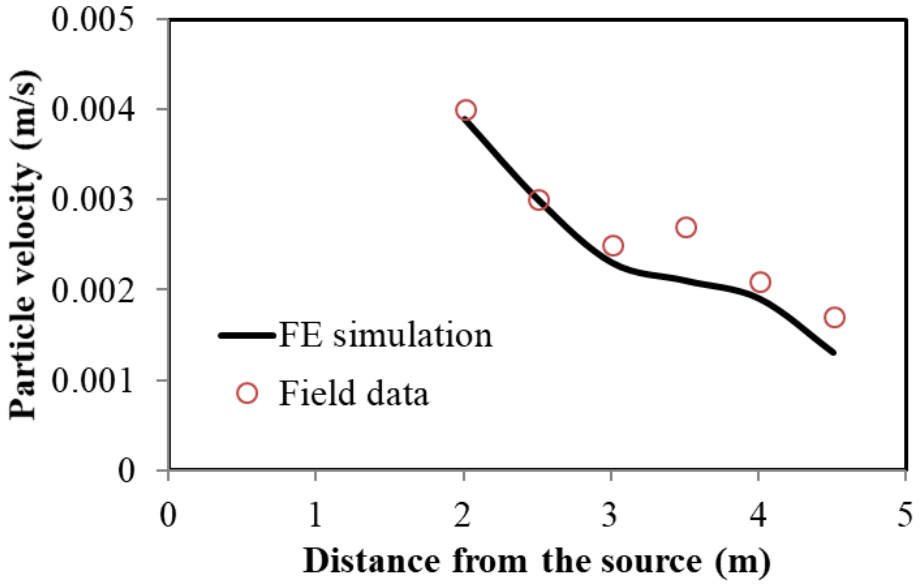

b) Line 2

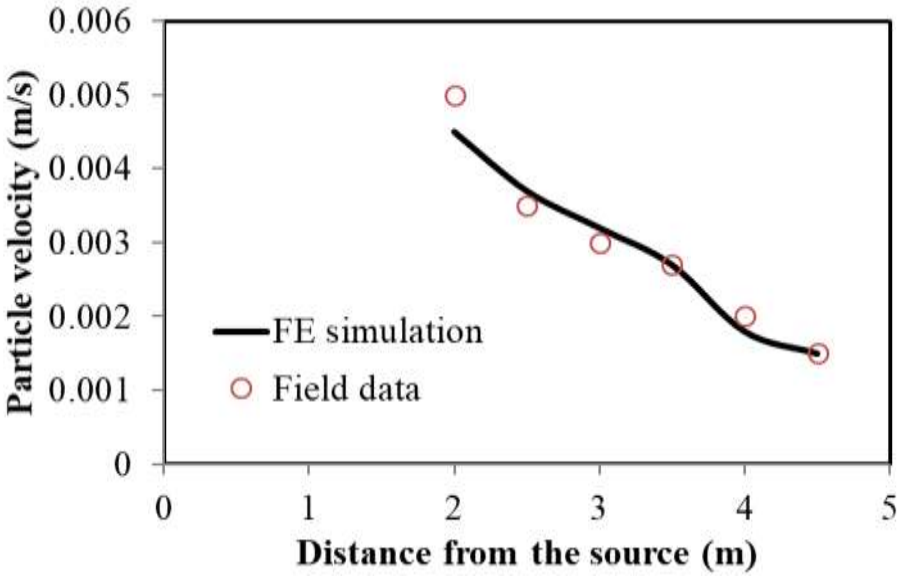

c) Line 3

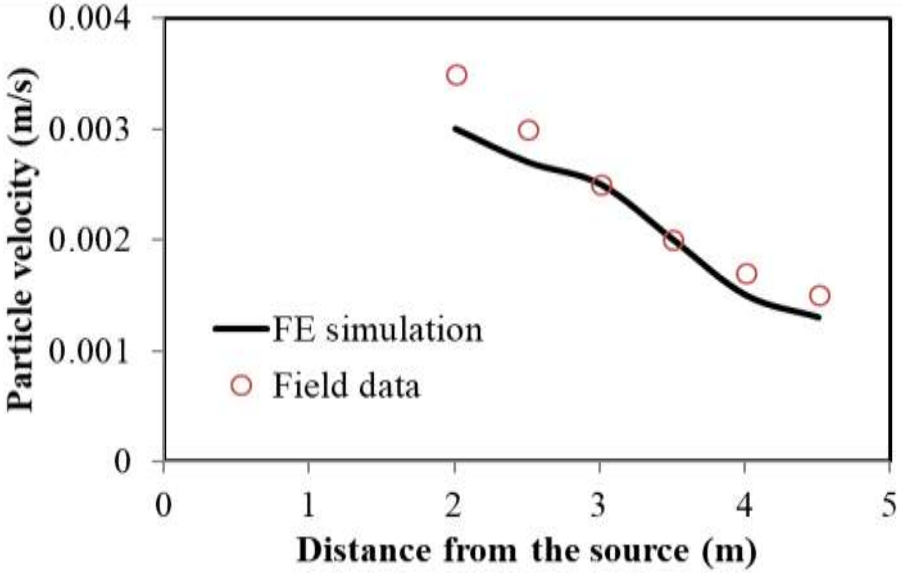

d) Line 4

Figure 4.18 Comparison of FE results and field data for 20 Hz

4.5.1.1 Amplitude ratio (Ar) contour plots

Amplitudes on the surface layer of the FE model were output and normalised with maximum results for the "no trench" results to obtain Ar for open trench and SRM barriers. The Ar obtained are then plotted and contoured to provide spatial distribution of the Ar. Figures 4.19a to 4.19c show the Ar contour plots from FE modelling at f = 100Hz for open trench, R70 and R30 barriers, respectively. Field test results are indicated by the Ar in a circle plotted on the contour plots. Observations of the AR contour plots revealed the following:

1. The field test results are generally in good agreement with the FE Ar contour plots for all three barriers.
2. Amplification due to reflected waves is observed at the front of the barrier where Ar > 1.0.
3. The Ar is lowest behind the trench and gradually increases with increasing distance away from the trench.
4. The Ar is still less than 1.0 at the lateral edge of the barrier.

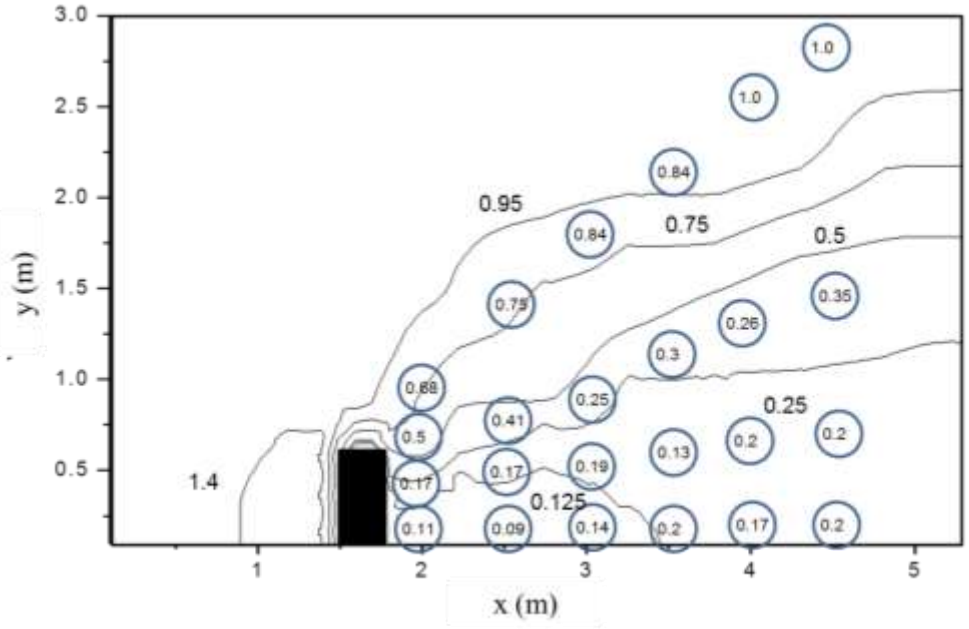

a) Open trench

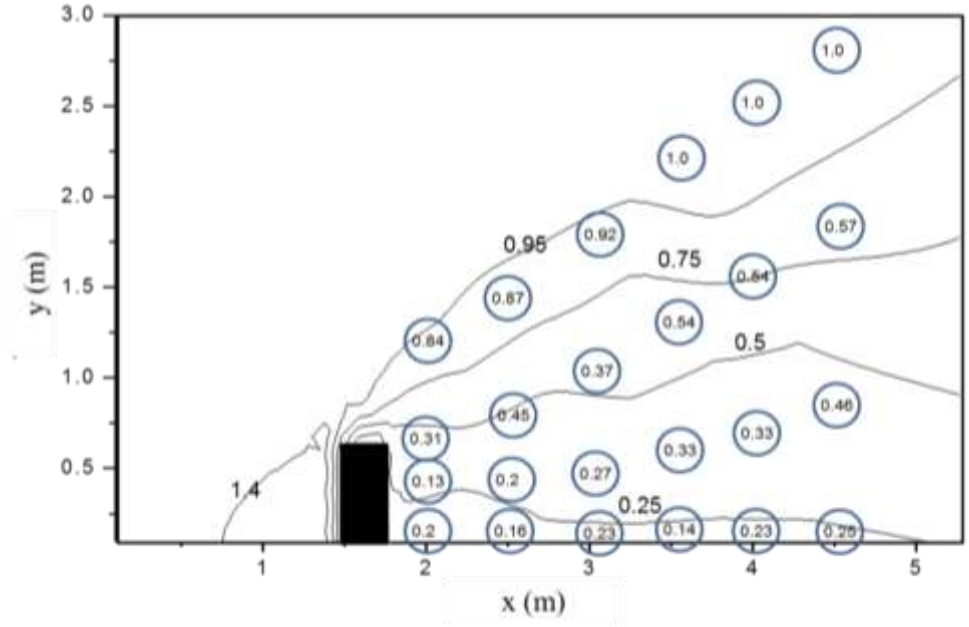

b) R70

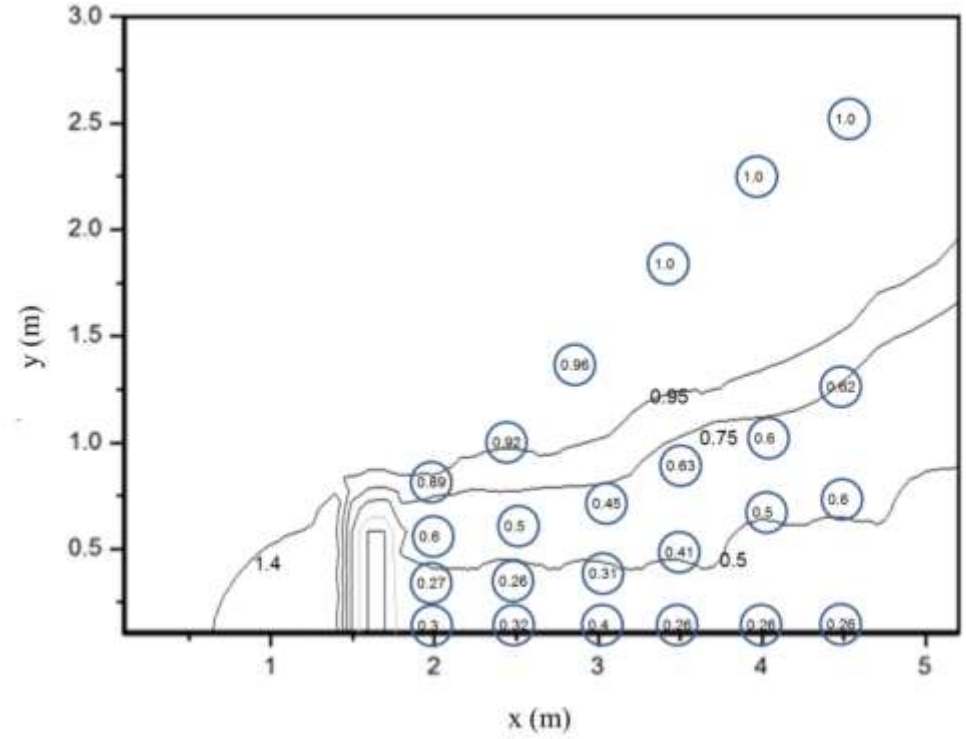

c) R30

Figure 4.19 Contour plots of Ar for 100 Hz

4.5.2 Verification of FE results with literature

The results obtained from the FE modelling were also compared with the literature. Table 4.5 shows the cases studies which were compared. The comparison of FE results and the case studies follows the presentation as given in the literature. The dimensions in each case study were modelled accordingly. Figure 4.20 shows the Ar contour plots for Case 1 together with contour plot obtained from the FE model. Figure 4.21 shows a plot of Ar versus normalised distance X for cases 2, 3 and 4. Normalised X is defined as x/λ_R. Figure 4.22 shows a plot of Ar versus X for case 5 and Figure 4.23 shows a plot of Ar versus X for case 6. For case 6, Geofoam was modelled by adjusting the impedance ratio provided by Alzawi and El Naggar (2009).

Figures 4.21, 4.22 and 4.23 show that the FE results are generally in good agreement with the published results. Figure 4.23 further suggests that as impedance ratio increase, Ar decreases.

Table 4.5 Case studies for verification of finite element model

Case	References	Trench material	Notations	D	R	W	L
1	Woods (1968)	Open trench	*	1.19	5.96	0.17	1.79
2	Beskos et al. (1986)	Open trench	*	1	5	0.1	-
3	Ahmad and Al-Hussaini (1991)	Open trench	*	1	5	0.1	-
4	Alzawi and El Naggar (2011)	Open trench	*	1	5	0.1	-
5	Alzawi and El Naggar (2009)	Open trench	AN 45 Hz	0.64	1.04	0.053	4.25
			AN 50 Hz	0.71	1.15	0.059	4.72
			AN 55 Hz	0.78	1.27	0.065	5.2
6	Alzawi and El Naggar (2009)	Geofoam	AN 45 Hz	0.64	1.04	0.053	4.25
			AN 50 Hz	0.71	1.15	0.059	4.72
			AN 55 Hz	0.78	1.27	0.065	5.2

***** As reference

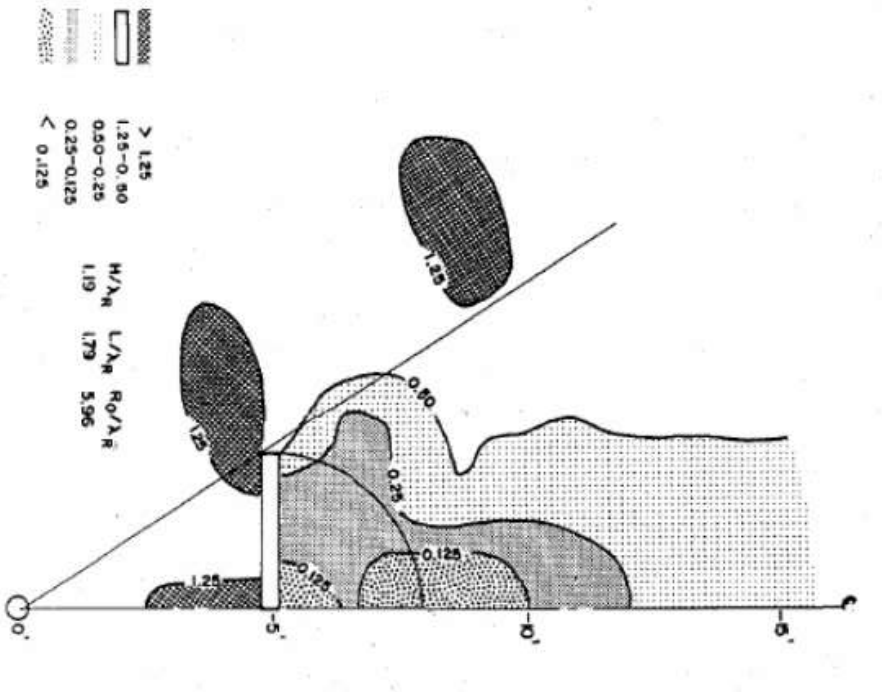

a) Contour plots of Ar from Woods (1968)

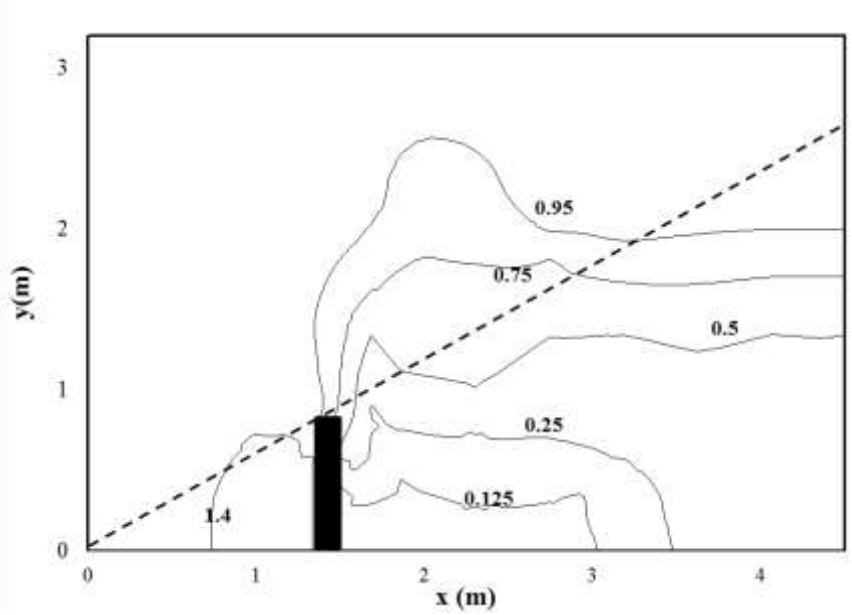

b) Contour plots of Ar from present study

Figure 4.20 Contour plots pf Ar for Case 1

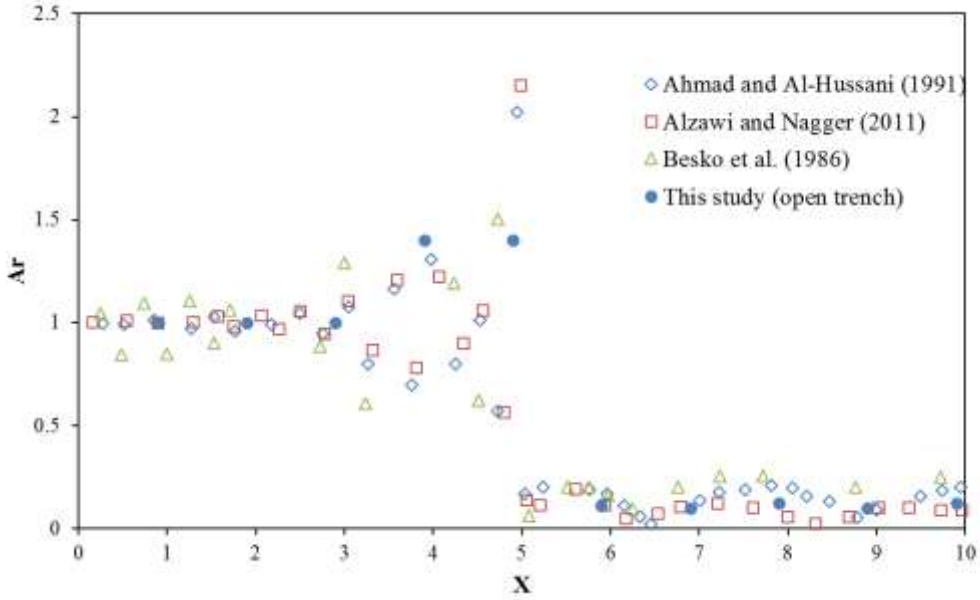

Figure 4.21 Plot of Ar versus X plot for case 2, 3 and 4

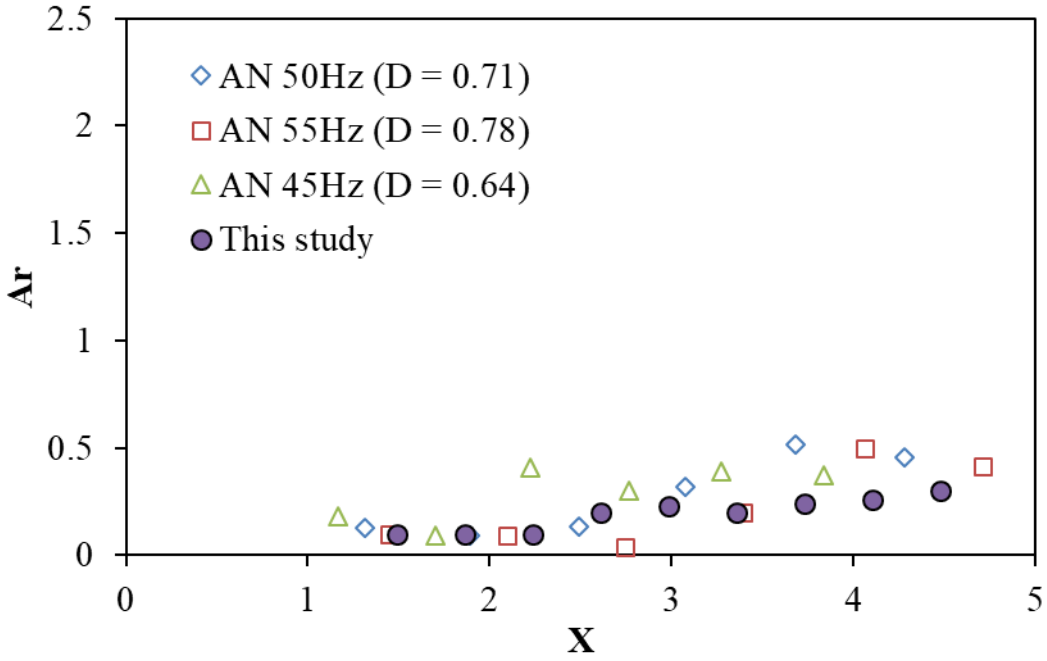

Figure 4.22 Plot of Ar versus X plot for case 5 (Open trench)

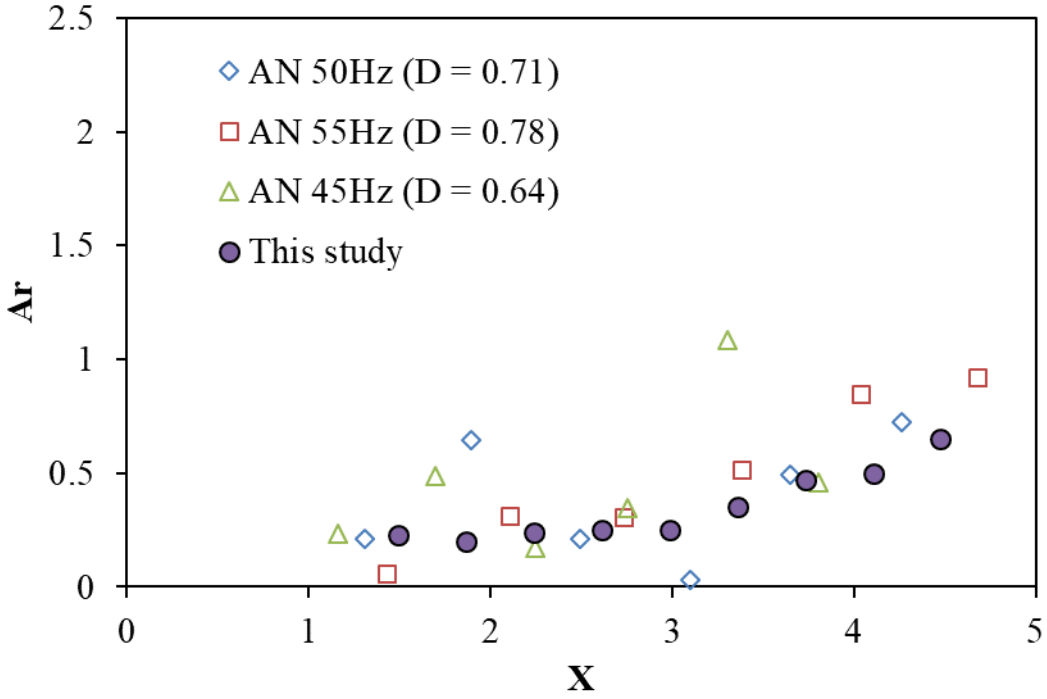

Figure 4.23 Plot of Ar versus X plot for case 6 (Geofoam)

4.5.3 Contour plots of Ar

As LS-DYNA is able to model the field test with good accuracy, effects of different soil properties and barrier dimensions can be examined. Parametric studies using LS-DYNA were then performed. The Ar contour plots for open trench, R30 and R70 barrier will be presented. This section aims to provide a guide for preliminary design of the barrier required to achieve the amount of amplitude reduction needed for a project.

4.5.3.1 FE model for Ar contour plots

The material model and material properties used for the FE model are the same as described in Section 4.5.1. However, the dimensions of the model have to be expanded so that a larger area of Ar can be contoured. The dimensions of the 3D FE model were varied. A typical case shown in Figure 4.24 is a quadrant with dimension of 20m by 15m by 15m and the mesh consisted of 2,450,000 eight-node solid elements with element size of 0.1m cube. Similar boundary conditions and loads as described in Section 4.6.1 were prescribed for the FE model.

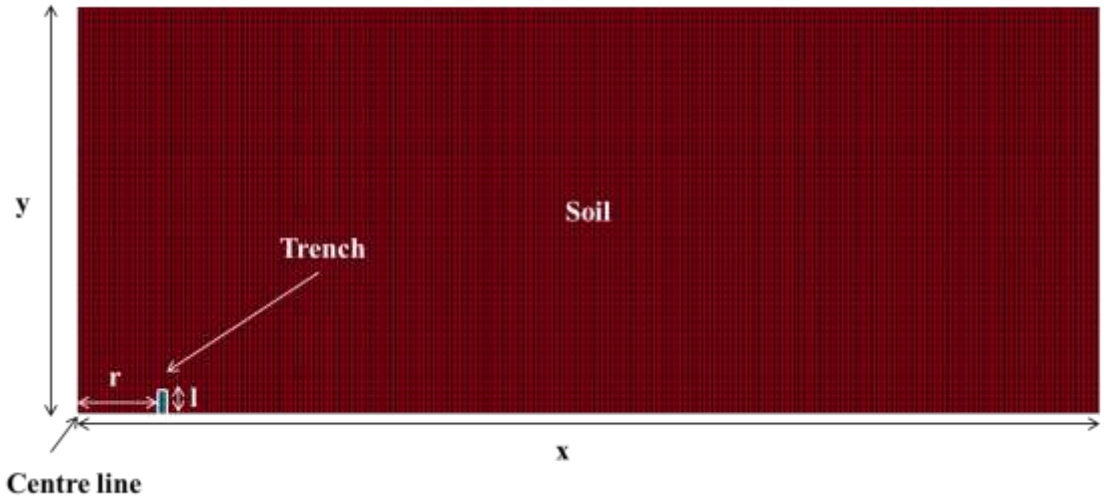

a) Plan view

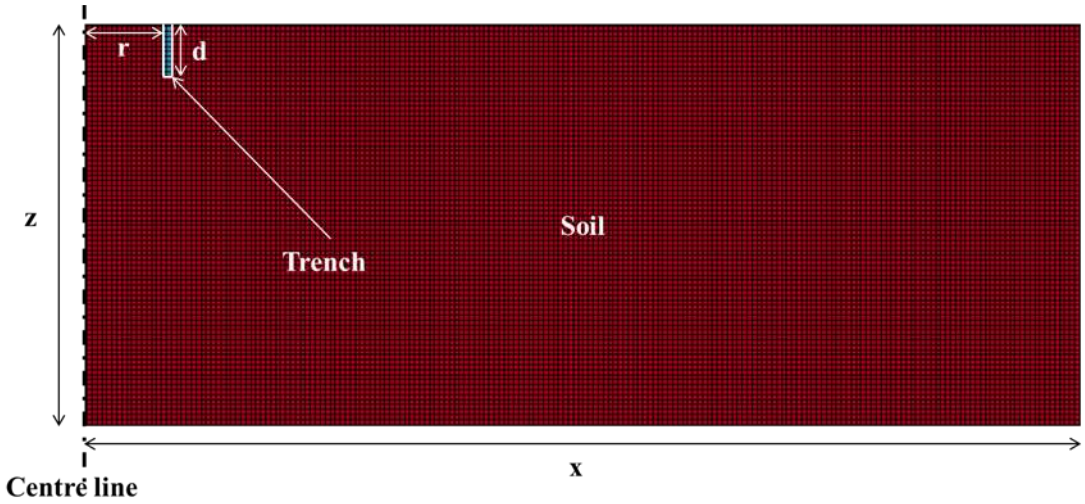

b) Section view

Figure 4.24 Typical case of finite element model

4.5.3.2 Parametric studies

To ensure the Ar contour plots are invariant for true dimensionless plots, different barrier dimensions were modelled. It is noted from the literature that effects of barrier width on Ar is insignificant. Hence, the barrier width is fixed at 0.1m for this parametric study. Table 4.6 shows the case studies with various barrier dimensions

considered in the parametric study. To illustrate the interrelationships between source locations, barrier dimensions, and Rayleigh wavelength λ_R, normalised r, l, d represented by R*(= r/d), L(= l/λ_R) and D(= d//λ_R), respectively, are needed.Cases 1, 2 and 3 involve changing the vibration frequencies (33, 50 and 100 Hz) of the source while maintaining all the other normalised parameters constant. The Ar contour plots for Cases 1, 2 and 3 are shown in Figure 4.25. The dimensionless Ar contour plots obtained for Cases 1, 2 and 3 as shown in Figure 4.26 show that as long as R*, L and D are kept constant, the dimensionless Ar contour plots are identical. In Figure 4.26, the x and y-axis are made dimensionless by setting X(= x/λ_R) and Y(= y/λ_R).

Cases 1-X1 and 1-X2 involve increasing D while keeping R* and L constant. Cases 1-Y1 and 1-Y2 on the other hand, involve increasing L while keeping R* and D constant. The purpose of Cases 1-X1, 1-X2, 1-Y1 and 1-Y2 is to understand the effect of D and L on the Ar contour plots. The Ar contour plots of Cases 1-X1 and 1-X2, and Cases 1-Y1 and 1-Y2 are shown in Figures 4.27 and 4.29, respectively. The corresponding dimensionless Ar contour plots are shown in Figures 4.28 and 4.30, respectively. The difference between the Ar contour plots and dimensionless Ar contour plots are the scale on the x and y axes. The dimensionless Ar contour plots are for dimensionless distance of source to barrier R* at 1.5.

Table 4.7 shows the parametric studies for Cases 1-M1 and 1-M2. The barrier dimensions (R*, L and D are constant) of Case 1 are used in Cases 1-M1 and 1-M2. Impedance is calculated as the density of the material multiplied by the Rayleigh wave velocity (V_R) of the material. The Ar contour plots of cases 1-M1 and 1-M2 as shown in Figures 4.31a, b and c are identical if the impedance ratio between the soil and the barrier material is kept constant.

The Ar contour plots for open trench, R70 and R30 barrier are plotted in Figures 4.32a, b and c, respectively. Table 4.8 shows the impedance ratio for open trench, R70 and R30.

Table 4.6 Case Studies for model dimension

Cases	r (m)	l (m)	d (m)	f (Hz)	λ_R (m)	R*	L	D
1	1.5	0.5	1	100	1.35	1.5	0.37	0.74
2	3	1	2	50	2.70	1.5	0.37	0.74
3	4.5	1.5	3	33.3	4.05	1.5	0.37	0.74
1-X1	2.25	0.5	1.5	100	1.35	1.5	0.37	1.11
1-X2	3	0.5	2	100	1.35	1.5	0.37	1.48
1-Y1	1.5	0.75	1	100	1.35	1.5	0.555	0.74
1-Y2	1.5	1	1	100	1.35	1.5	0.74	0.74

*R = r/d

Table 4.7 Case Studies Impedance

	Density (kg/m^3)		Velocity (m/s)		Impedance (Z)		Impedance Ratio (IR)
Case	Soil	Barrier	Soil	Barrier	Soil	Barrier	
1	1800	793	275	74	495,000	58,682	0.118
1-M1	1600	900	309	65.2	495,000	58,682	0.118
1-M2	2000	1100	247	53.3	495,000	58,682	0.118

Table 4.8 Impedance ratio for open trench, R70 and R30

	Density (kg/m^3)		Velocity (m/s)		Impedance (Z)		Impedance Ratio (IR)
Barrier	Soil	Barrier	Soil	Barrier	Soil	Barrier	
Open trench	1800	1.013	275	330	495,000	334	0.000674
R70	1800	793	275	74	495,000	58,682	0.118
R30	1800	1286	275	100	495,000	128,600	0.260

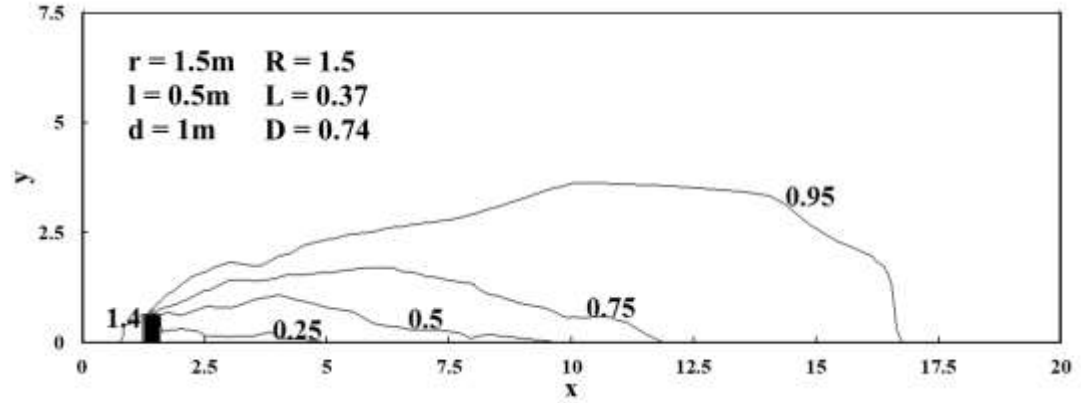

a) Case 1

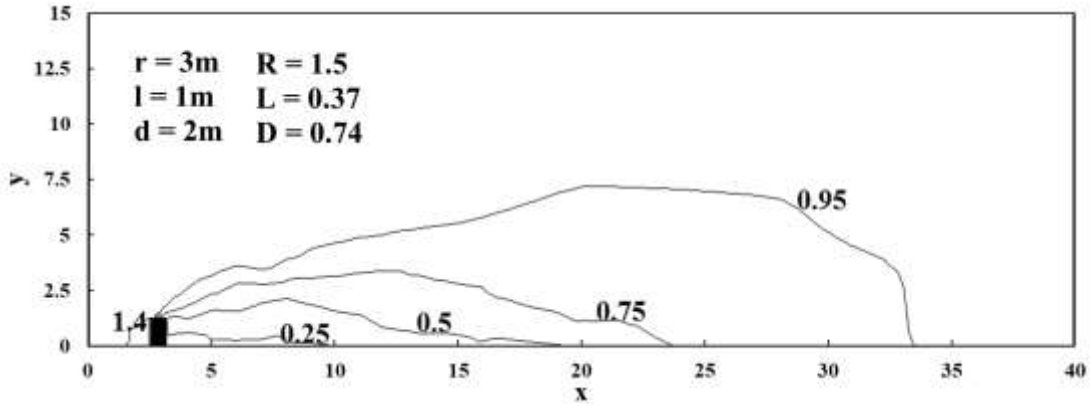

b) Case 2

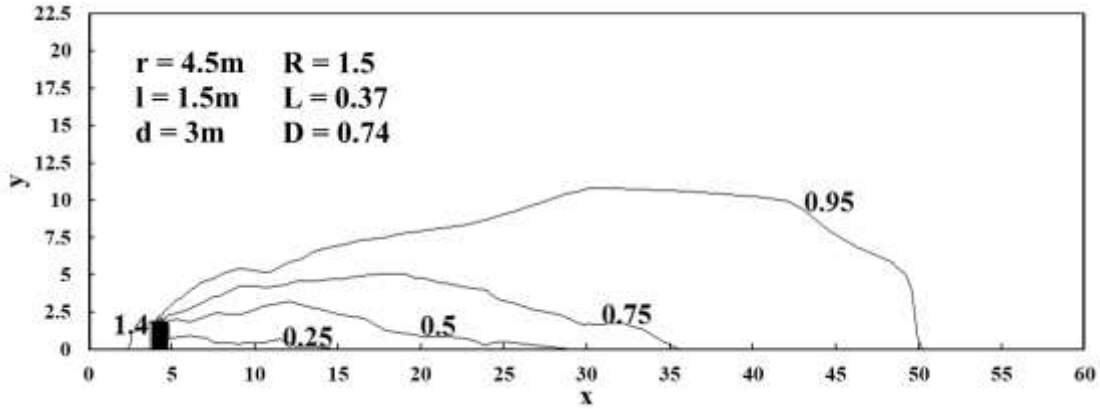

c) Case 3

Figure 4.25 Ar contour plots for Cases 1, 2 and 3

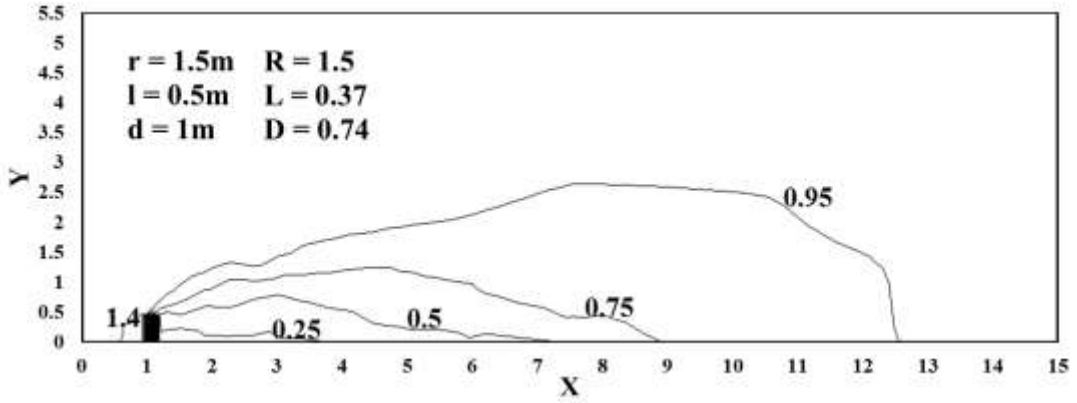

a) Case 1

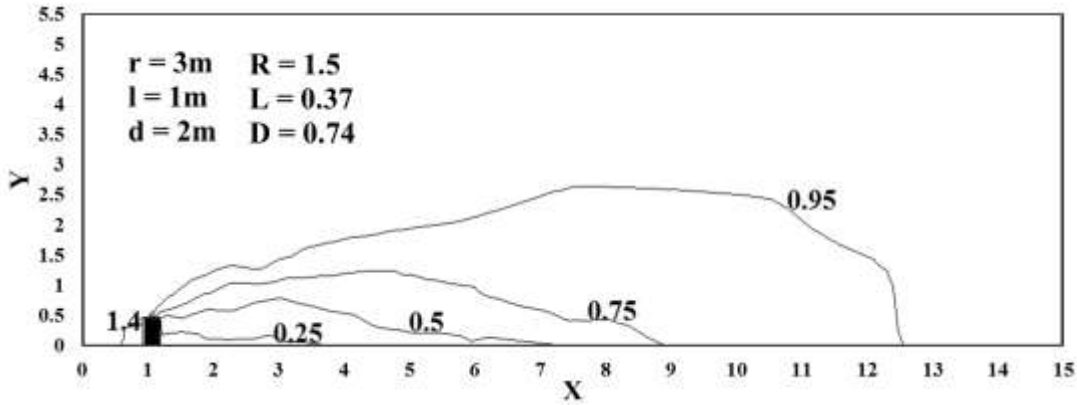

b) Case 2

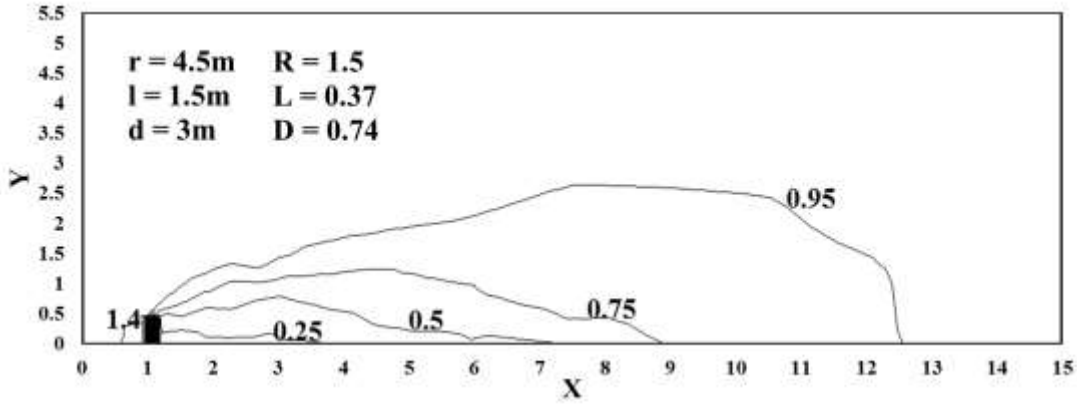

c) Case 3

Figure 4.26 Dimensionless Ar contour plots for Cases 1, 2 and 3

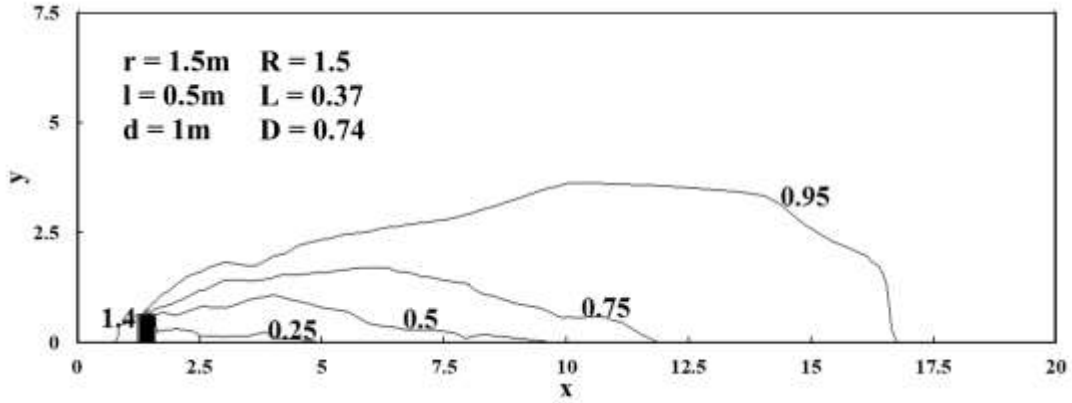

a) Case 1

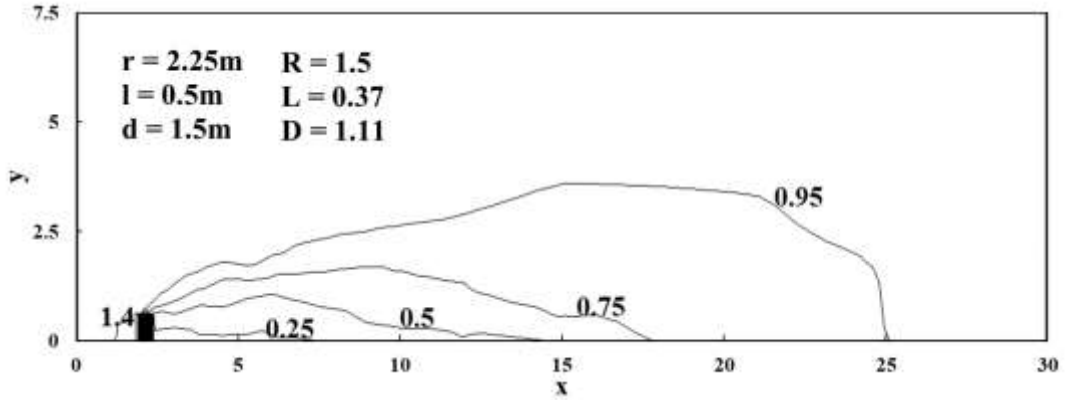

b) Case 1-X1

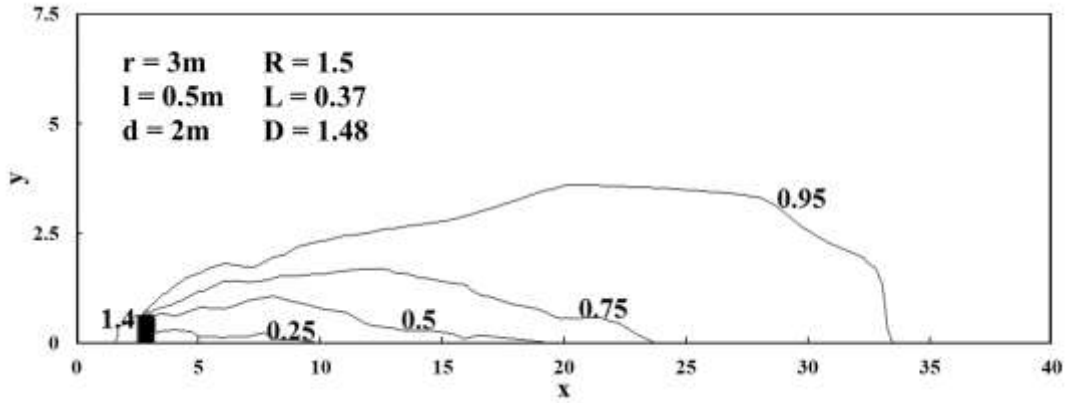

c) Case 1-X2

Figure 4.27 Ar contour plots for Cases 1,1-X1 and 1-X2

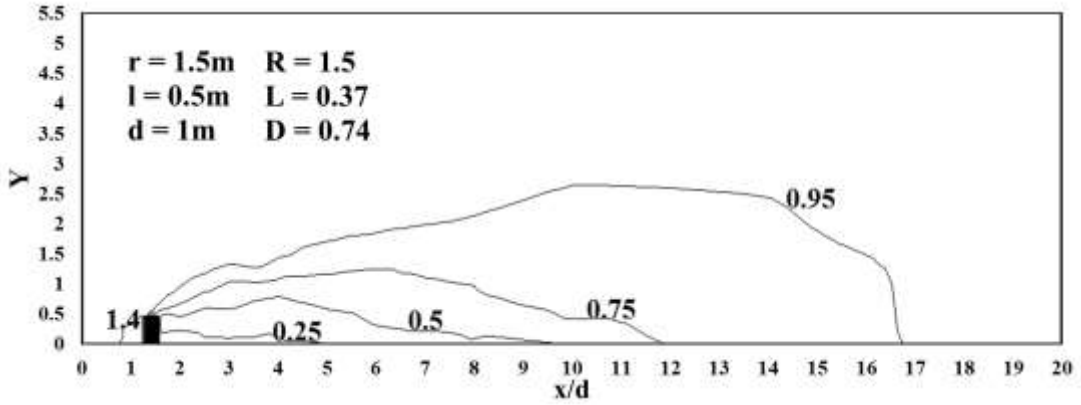

a) Case 1

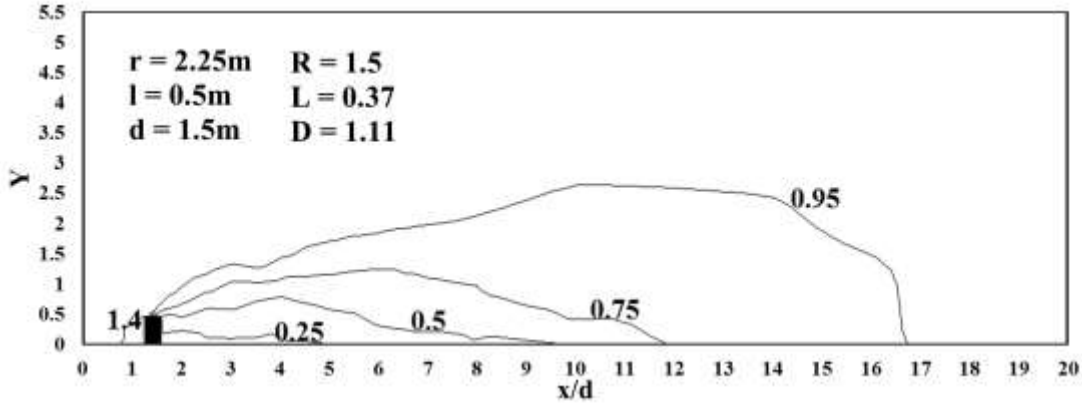

b) Case 1-X1

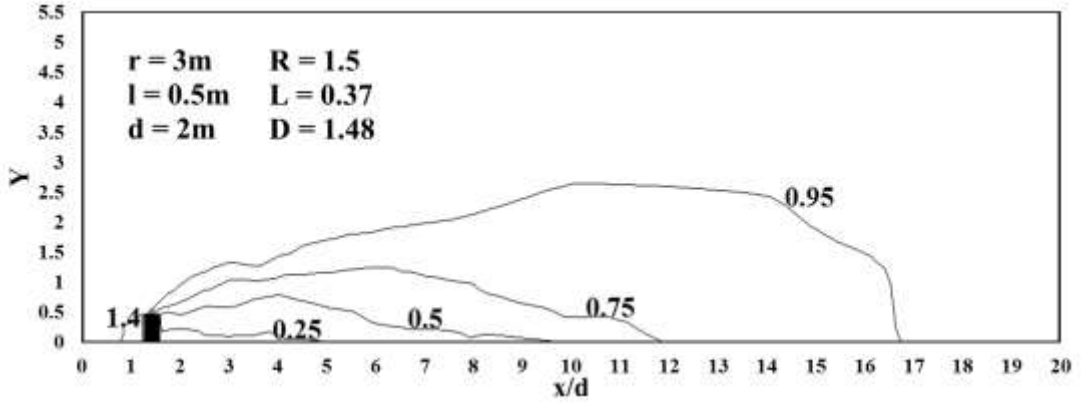

c) Case 1-X2

Figure 4.28 Dimensionless Ar contour plots for Cases 1,1-X1 and 1-X2

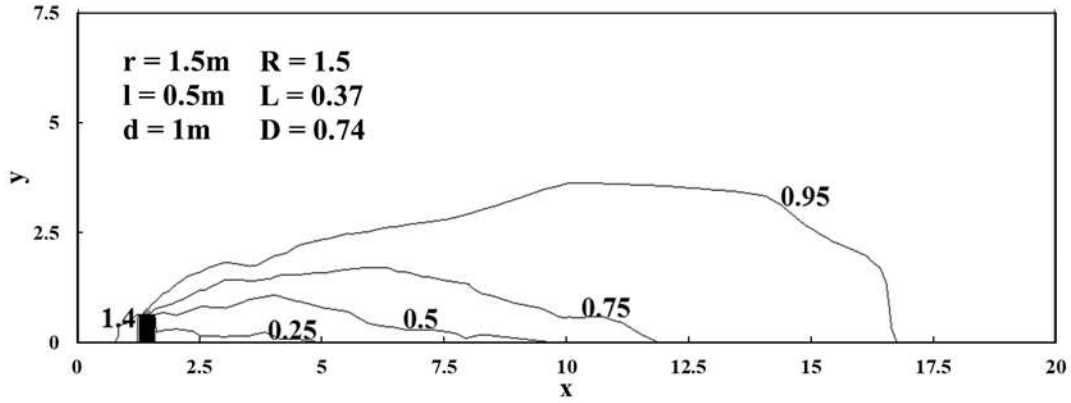

a) Case 1

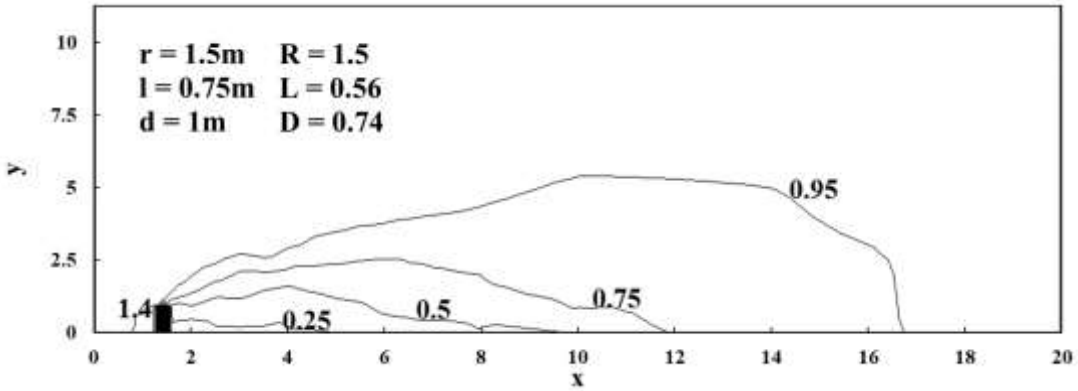

b) Case 1-Y1

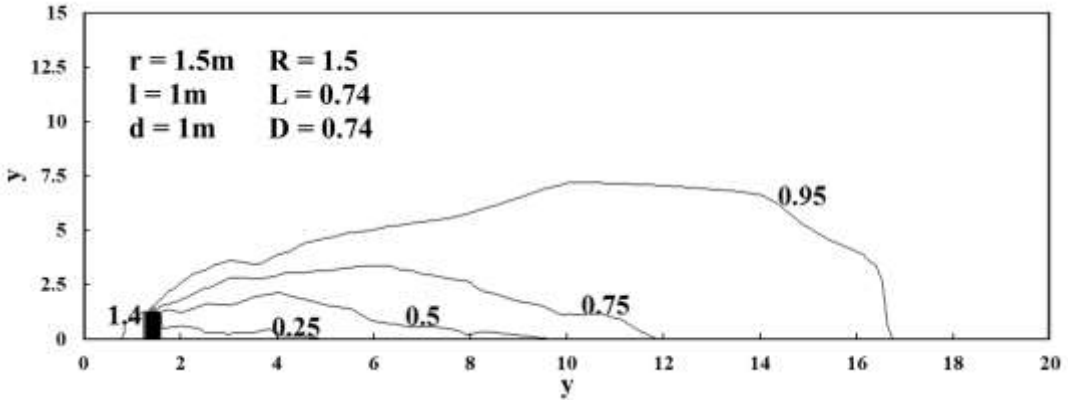

c) Case 1-Y2

Figure 4.29 Ar contour plots for Cases 1, 1-Y1 and 1-Y2

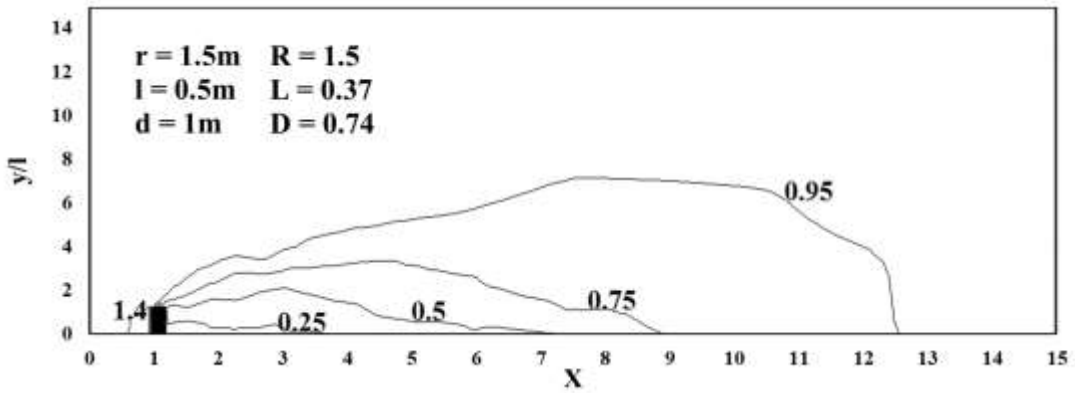

a) Case 1

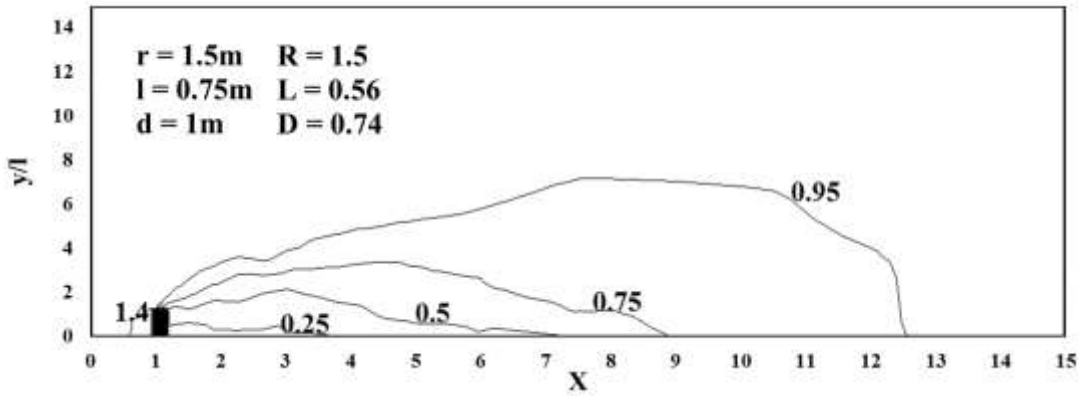

b) Case 1-Y1

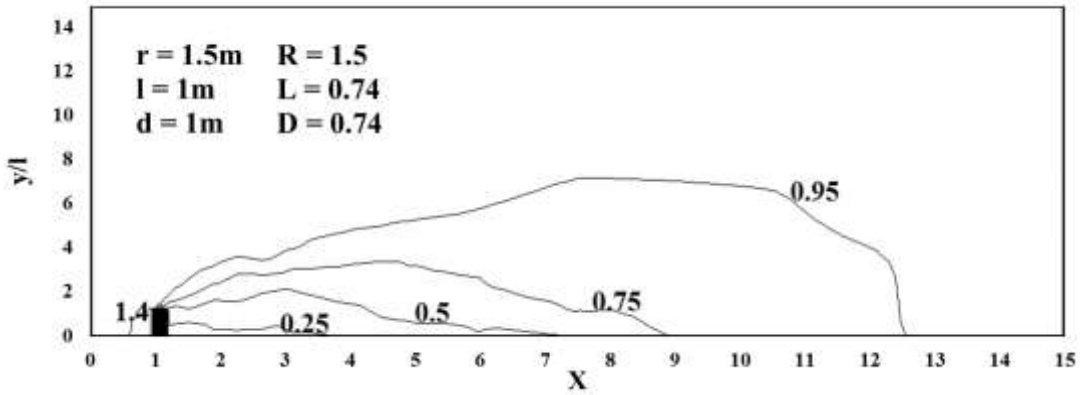

c) Case 1-Y2

Figure 4.30 Dimensionless Ar contour plots for Cases 1, 1-Y1 and 1-Y2

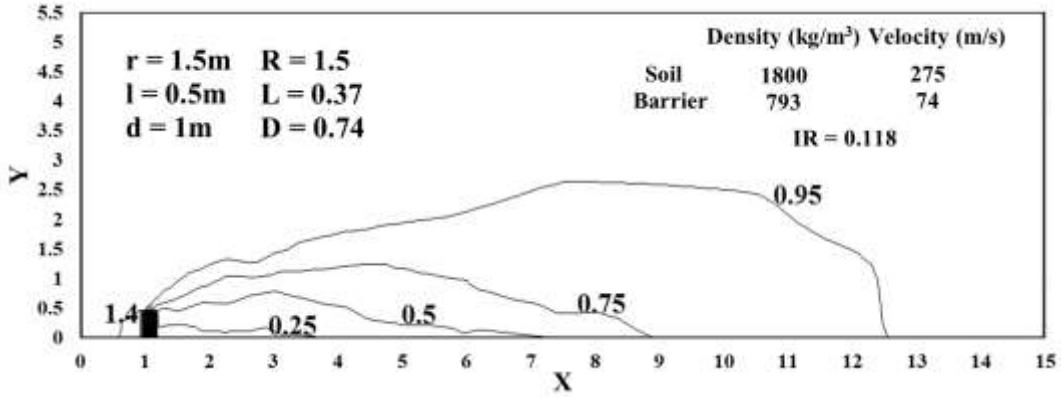

a) Case 1

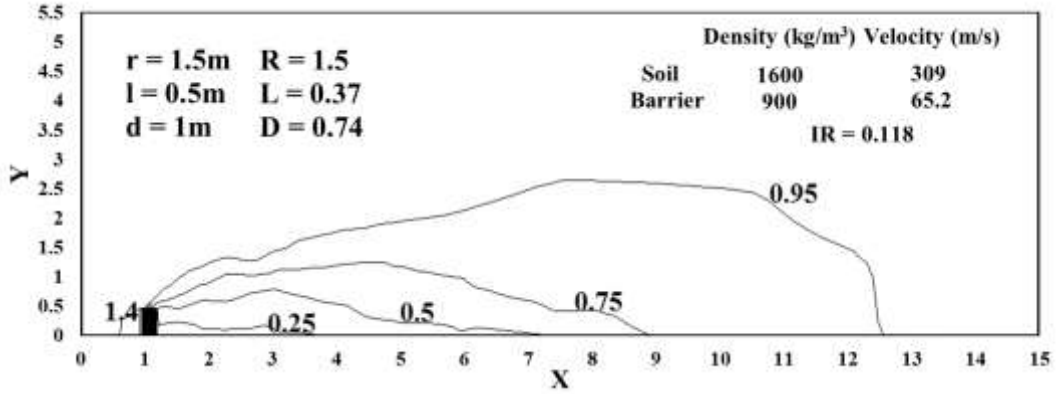

b) Case 1-M1

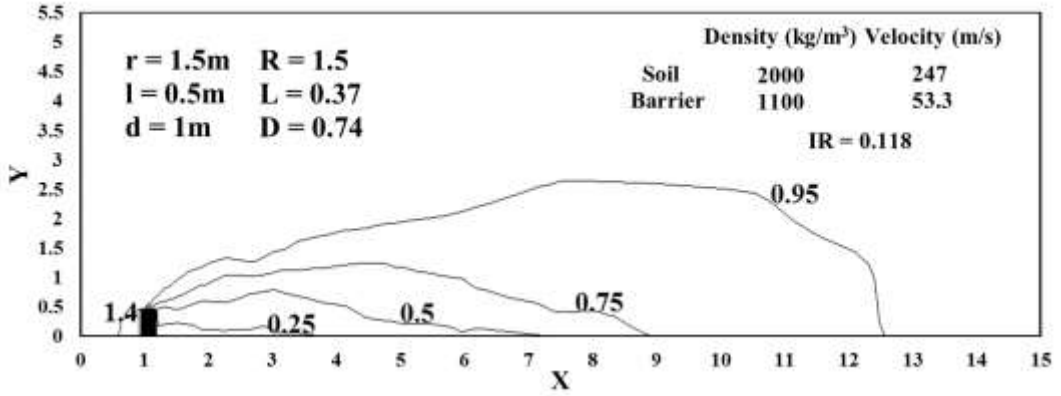

c) Case 1-M2

Figure 4.31 Dimensionless Ar contour plots for Cases 1, 1-M1 and 1-M2

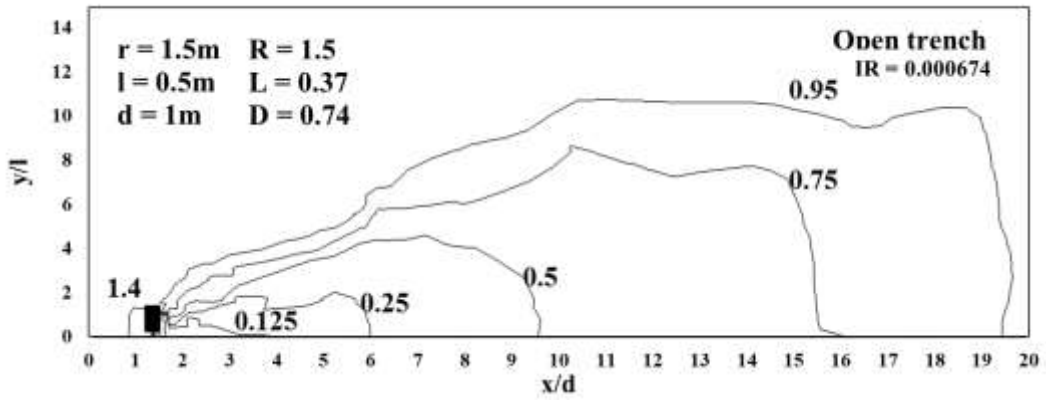

a) Open trench

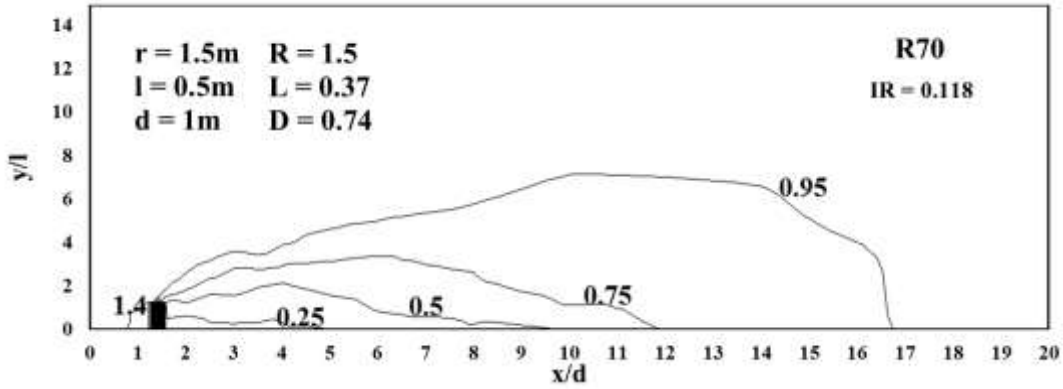

b) R70

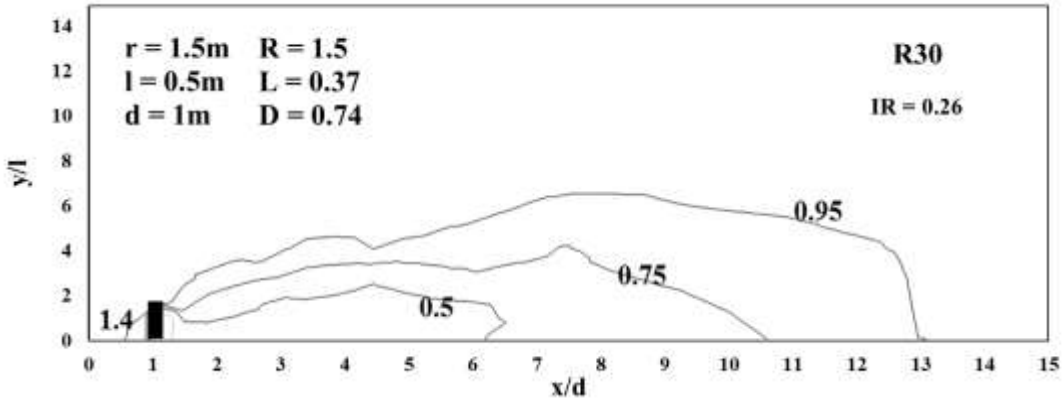

c) R30

Figure 4.32 Dimensionless Ar contour plots for open trench, R70 and R30

4.5.3.3 Application of dimensionless Ar contour plots

The dimensionless Ar contour plots can be used as a preliminary guide to implement in projects. It is noted that the dimensionless Ar contour plots were plotted based on R* = 1.5 and IR of 0.000674, 0.118 and 0.26. In the case of vibration generated from a moving train (line source), Ar along the centre line is only applicable as shown in Figure 4.33.

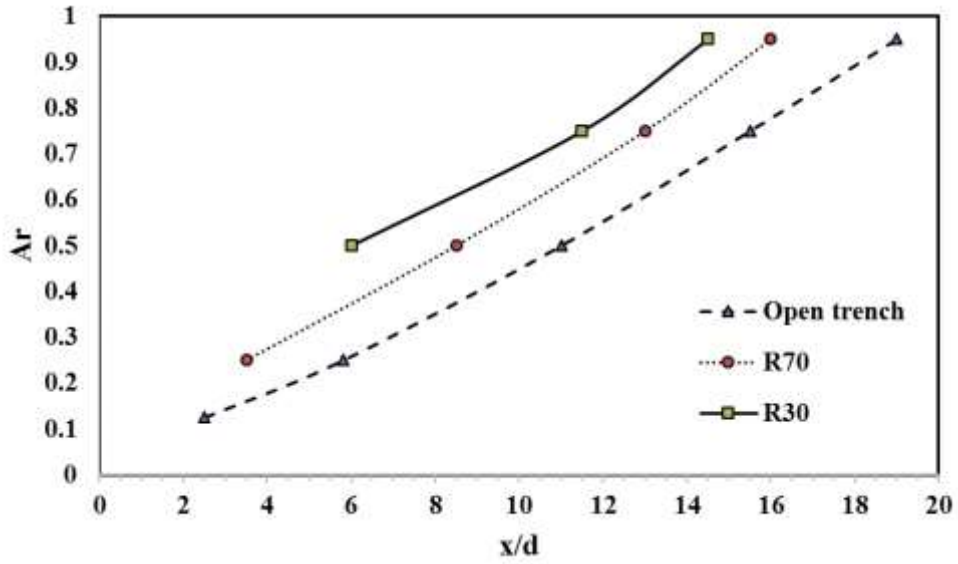

Figure 4.33 Ar Contour plot for line load (open trench, R70 and R30)

Massarsch (2005) described air cushion in place of an open trench as seismic wave barrier to mitigate vibrations resulted from a moving train. Massarch (2005) concluded that the Ar obtained when using air cushion barrier is comparable to an open trench. To put the dimensionless Ar contour plot to test, cases studies reported by Massarsch (2005) were examined. A total of four case studies were reported by Massarsch (2005). The descriptions of the cases studies and the corresponding dimensions of the barrier and soil's Rayleigh wave velocities are presented in Table 4.9 and Table 4.10, respectively. Other details such as dimensions of the structure and

structure's distance behind the barrier are not provided (area of interests). With the information provided, in Table 4.10, the zone behind the barrier where Ar = 0.25 can be identified as shown in Figure 4.34. Project Saffle is not presented in Figure 4.34 as it was unsuccessful.

Table 4.9 Case studies reported by Massarch (2005)

S/no	Case study location	Objective	Findings
1	Project Gnarp Sweden (1984)	Protect residential building from railway induced vibrations	Vibration reduced more than 70% ($Ar \leq 0.3$)
2	Mormon Temple project, Sweden (1985)	Protection of vibration-sensitive building	Vibration reduced more than 65% ($Ar \leq 0.35$)
3	Project Saffle (1985)	Protection of more than 20 residential timber house	Collapse of trench at depth more than 8m which resulted in damage of air cushion. Consequently, the air cushion provides no reduction.
4	Project Dusseldof (1991)	Protection of two-story residential buildings	Vibration reduced more than 40 to 60% ($0.4 \leq Ar \leq 0.6$)

Table 4.10 Case studies' barrier dimensions reported by Massarch (2005)

Case study location	f (Hz)	V_R (m/s)	λ_R (m)	d (m)	D	r (m)	▲x/d	▲x (m)
Project Gnarp Sweden (1984)	15	120	8	6.5	0.81	-	4.5	29.5
Mormon temple project, Sweden (1985)	25	200	8	6.5	0.81	6	7	35.75
Project Saffle (1985)	4	60	15	12	0.80	10	-	-
Project Dusseldof (1991)	15	135	9	12	1.33	-	7	84

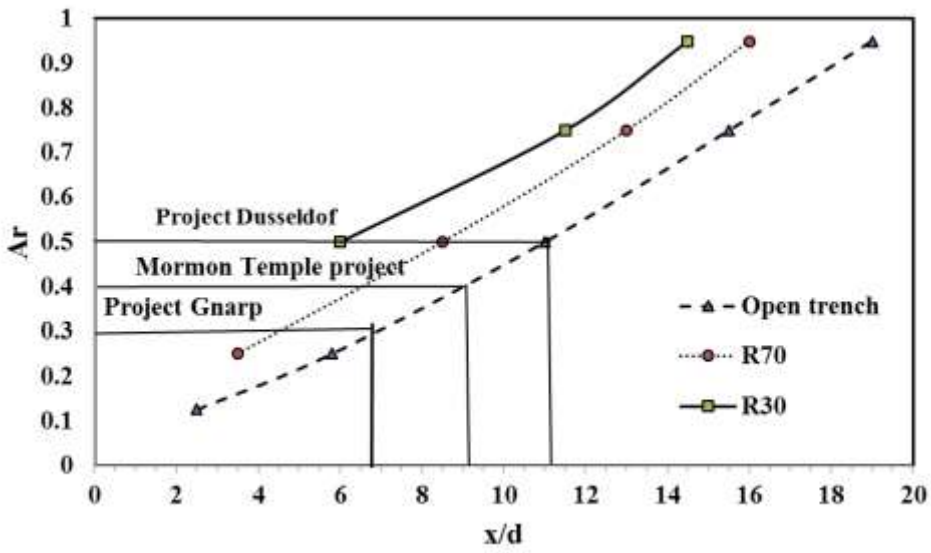

Figure 4.34 Ar contour plot for case studies reported by Massarsch (2005)

The dimensionless Ar contour plots can be also used for cases surface vibration is caused by a point source. The main difference between application of the Ar contour plots on line source and point source is that point source involves x and the y axes. Often, projects are bounded by constraints such as limited land area, limited size of seismic wave barrier allowed or unfavourable soil conditions. The dimensionless Ar contour plots can be used to determine actual dimensions of barrier required and the applicable area of interest. Table 4.11 shows the procedures on the application of dimensionless Ar contour plots for point source vibrations.

Table 4.11 Procedures for the application of dimensionless Ar contour plots for point source vibrations

S/No	Action
1	Information required 1) Area of interest and permissible Ar 2) Rayleigh wave velocity of soil ($\lambda_R = V_R/f$) 3) Critical frequency of vibrating source (f) 4) Distance of source to area of interest (r)
2	Selection of impedance ratio
3	Position area of interest with in the permissible Ar zone. 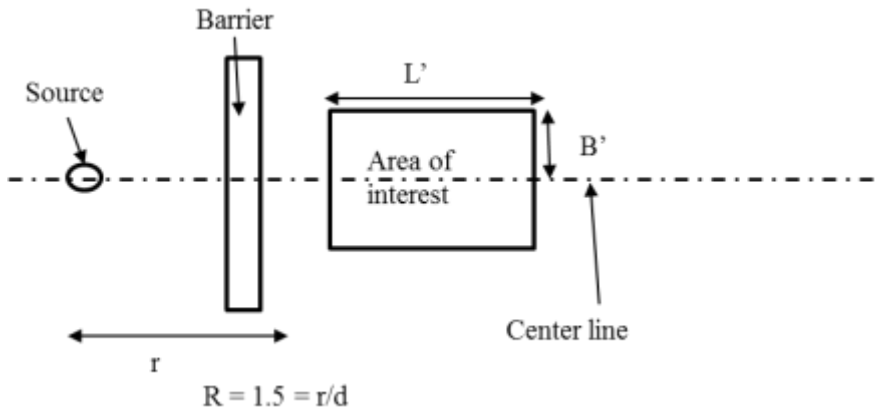
4	Mark the area of interest on the dimensionless Ar contour plots and read off the x and y axis to obtain x/d and y/l
5	Determine d using the value read off from x axis of dimensionless Ar contour plots
6	Determine l using the value read off from y axis of dimensionless Ar contour plots
7	Determine r based on R* = r/d = 1.5
8	The structure can be anywhere within the zone (L', B') determined.

A hypothetical case will demonstrate the procedures listed in Table 4.11. The case is to reduce the peak velocity induced by construction activities from plate compaction performs near the residential area. In absence of barrier to reduce the peak velocity, a minimum distance between the construction activities and residential area must be

observed. Table 4.12 shows the requirements imposed by different design codes on the peak particle velocities (PPV) and frequency tolerances for residential area.

Table 4.12 Various design codes

S/No	Design codes	Limits in PPV
1	BS5228-2:2009	1) 15mm/s at 4 Hz 2) 20mm/s at 15 Hz 3) 50mm/s at 40 Hz and above
2	Eurocode 3	1) 5 mm/s for continues type of structure 2) 5 mm/s for transient type of structure
3	DIN 4150 1999	1) 5 mm/s for less than 10 Hz 2) 15 mm/s for all frequencies for tall structures

* PPV Limits are based on residential requirements

The vibration source is based on vibration measurement performed by Hao (2014) generated by a plate compactor (LH 700) vibrating at 53 Hz on Perth Metropolitan area reported to comprise fine to medium grained sands. Figure 4.35 shows the peak velocity versus distance away from the source. Based on Table 4.12, it is reasonable to set the limit of peak velocity as 5 mm/s.

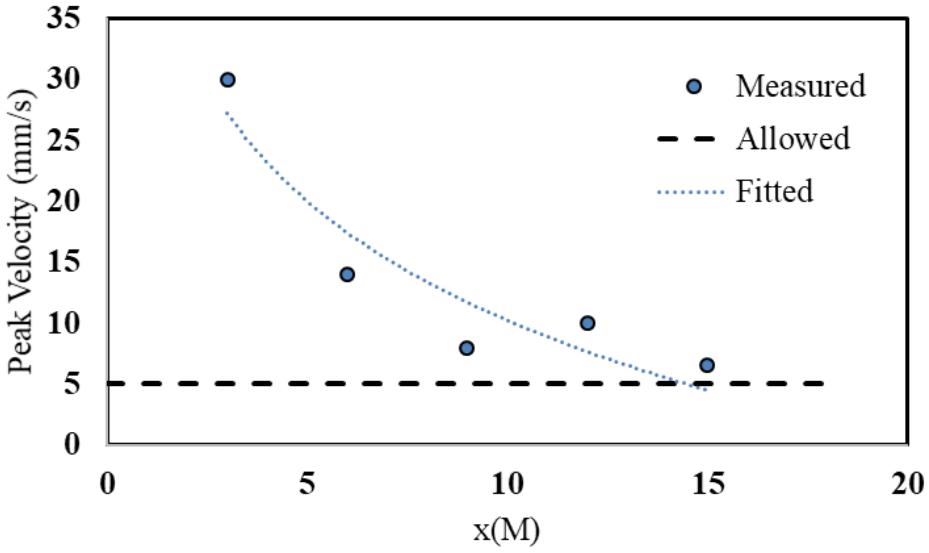

Figure 4.35 Measured and fitted resultant peak velocity (from Hao, 2014)

The area of interest would be a typical house in Perth which measures about 231m^2 (8m by 29m). A plate compactor is place 5m away from the house. From the findings by Hao (2014), at 5m away from the source, the peak velocity is 20 mm/s. To remain within the limit, the peak velocity will have to be reduced by 75%. This can be achieved by introducing an open trench in between the plate compactor and the house. Figure 4.36 shows how the area of interest is placed on the Ar contour plots to meet the requirements. Table 4.13 shows the parameters and the dimensions of the trench required. As calculated in Table 4.13, the open trench dimensions required are d = 1.67m by l = 14.5m with r = 2.5m away from source.

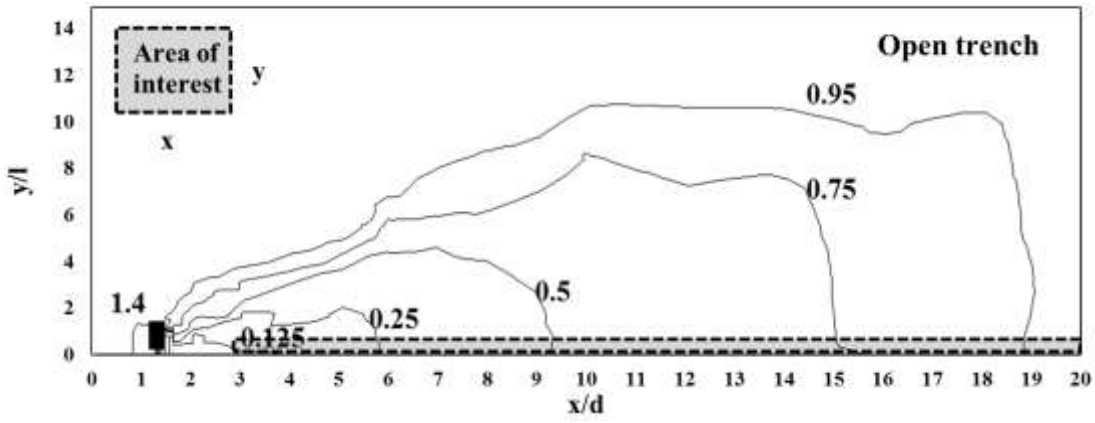

Figure 4.36 Area of interest

Table 4.13 Example one

Given parameters		Calculated parameters	
R	1.5	r	2.5m
D	0.74	d	1.67m
L	0.37	l	14.5m
x/d	4.5		
y/l	1		
L’	8m		
B’	14.5m		

4.6 Summary

Field tests were carried out to investigate the effectiveness of open trench and SRM barriers in mitigating surface vibrations due to Rayleigh waves. The effectiveness of the barrier was evaluated through the use of Ar, where Ar ≤ 0.25 is considered to be effective. To corroborate the field test results, the field tests were modelled using LS-DYNA using independently measured properties of soil and SRM. The FE model was also verified against data obtained from the literature. Parametric studies involving variations of barrier dimensions and impedance were carried out using LS-DYNA. Dimensionless Ar contour plots were developed from the parametric studies.

The findings in the chapter are as follows:

1. Open trench provides the best barrier effect, followed by R70 and R30. For the SRM barriers, the barrier effect is improved by increasing the rubber chip content of the SRM.
2. The barrier becomes effective (Ar < 0.25) beyond D of 0.7 for both open trench and R70 barrier. The R30 barrier gives a minimum Ar value greater than 0.25 which shows that rubber chip content must be greater than 30% for SRM barrier to be effective.
3. A general increase in Ar is observed from Geophones 1 to 6. There is also an increase in Ar of corresponding geophone from lines 1 to 4. This shows that the efficiency of the barrier decreases with distance away from the barrier and when the line radiates away from the centre line.
4. The FE model was able to replicate the field test results for all the three types of barrier.

5. FE modelling enabled a contour plot of Ar to be made. The Ar contour plot shows that amplification due to reflected waves is seen in front of the barrier and the barrier effect is only effective up to some distance behind the barrier.
6. Parametric studies using FE modelling shows that the Ar contour plots remain identical if R*, L, D and IR are kept constant.
7. Useful dimensionless Ar contour plots with y/l as y-axis and x/d for x-axis can be used for preliminary implementation of seismic wave barrier for fixed R* and IR, dimensionless Ar contour plots can be scaled independently.

The usage of these dimensionless Ar contour plots were demonstrated through case studies to illustrate how the dimensionless Ar contour plots can be use as a preliminary guide for the implementation of seismic wave barrier to achieve desired Ar for a project.

Chapter 5: Small-scale Field Explosion Test

5.1 Introduction

Use of SRM as material for seismic wave barrier has proven to be effective as a seismic wave barrier against surface vibrations as shown in Chapter 4. In this chapter, the use of SRM as a seismic wave barrier against ground shock caused by explosion will be investigated and discussed. Ground shock caused by buried explosives could potentially be devastating to both above and below ground structures and their occupants. With the rising threat of act of terrorism, methods to reduce the effect of explosion have become even more important. As such, the ability to reduce ground shock due to buried explosion should be implemented to safeguard properties and lives. Various materials such as geofoam, water, glycerine, aerogel, CAB-O-SIL, glass beads, expanded foam and tuff have being tested as seismic wave barrier against ground shock caused by explosion (e.g. Schimizze et al. 2012, Davis 1994, Kobielak et al. 2006). To date, the effectiveness of SRM as seismic wave barrier against ground shock caused by explosion has yet to be determined and should be investigated.

In this chapter, small-scale field explosion tests on the effectiveness of SRM as seismic wave barrier will be described. The field tests were modelled using LS-DYNA. Before modelling the field explosion tests, explosions in the free-field condition were modelled. The free-field peak pressure curves presented in TM5-855-1 (1986) were compared with the numerical modelling results using LS-DYNA. The effect of buried charge depth was also investigated as crater may be formed when the buried charge depth is shallow and the explosion energy may not be fully transmitted through the ground. The crater's dimensions of shallow-depth buried explosions and

depth at which camouflet is formed were investigated and compared with those given in TM5-855-1 (1986). Once the free-field condition is modelled correctly, modelling of the small-scale field explosion tests was carried out.

5.2 Small-scale field test

The aim of the small-scale field test is to investigate the efficiency of SRM as seismic wave barrier against ground shock caused by buried explosion. This was achieved by comparing results obtained from a concrete structure without SRM barrier and another concrete structure with SRM barrier. The small-scale field explosion tests were performed as part of a bigger field test programme of Defence Science Technology Agency (DSTA), Singapore. The field test programme area, amount of budget and resources allocation to the field test programme were fixed. As a result, constraints such as limited site investigations, limited channels for data acquisition (10 in total), limited configuration of small-scale field test, limited equipment (limited number of sensors and length of wires connecting to the data acquisition system) and number and size of explosion were inherent in the test programme.

5.2.1 Site characterisation

The test was conducted on an offshore island situated south of Singapore. From the site investigation report based on two boreholes, soil consists of a sandy silt. The stiffness of the sandy silt increases with depth. The groundwater table was measured at a depth of 4.7m. Figure 5.1 shows the soil condition of the site drawn based on borehole 1 and 2. As the test was performed up to a depth of 2m below the ground level, disturbed soil samples were taken from depths of 0.5, 1 and 1.5m and brought back to the laboratory for characterisation tests. According to the Soil Investigation

report, the in-situ density of the site soil is 1700 kg/m^3. The tests performed were specific gravity test, grain size distribution test, relative density test, triaxial compression test and wave propagation test. The tests were performed in accordance to the test standards shown in Table 5.1. Prior to testing, the soil samples were dried in the oven at 105^0 for two days. Figure 5.2 shows the grain size distribution of the sandy silt. Table 5.2 shows the basic properties of the soil. Figure 5.3 shows a plot of V_p and V_s at different confining pressures obtained from the bender element test conducted on samples reconstituted to the in-situ density. Properties of the SRM were presented in Chapter 3.

Table 5.1 Test standards

Tests	Standard
Specify gravity	ASTM D854 - 14
Grain size distribution	ASTM D6913 / D6913M - 17
Relative density	ASTM D4254 - 16
Triaxial compression	ASTM D2850 - 03
Wave propagation	ASTM D2845 - 08

Table 5.2 Properties of sandy silt

Specify gravity	2.45
Minimum density (kg/m^3)	1116
Maximum density (kg/m^3)	1629
e_{max}	1.16
e_{min}	0.50
Friction angle (^{0})	38

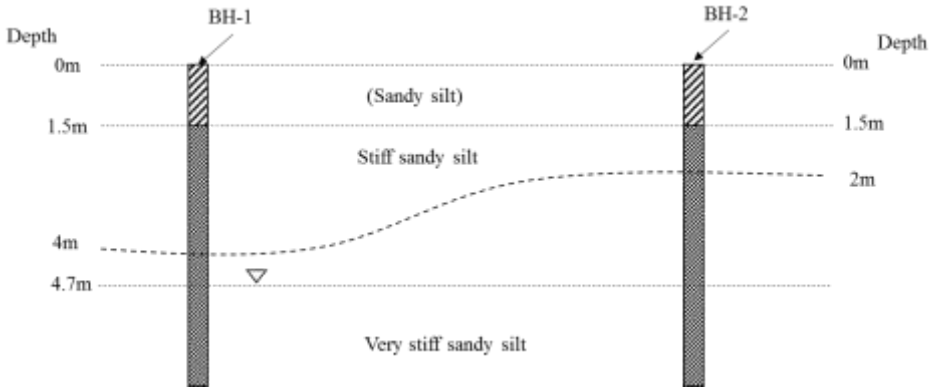

Figure 5.1 Geological cross section of the site drawn from boreholes 1 and 2

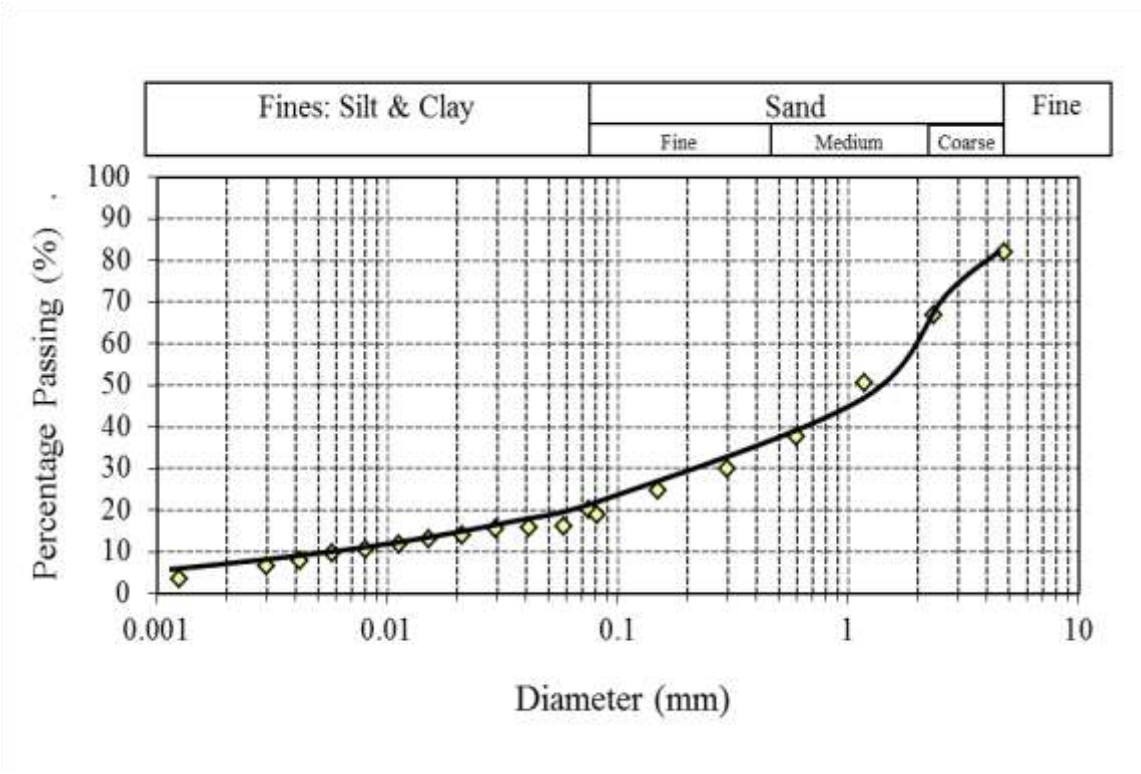

Figure 5.2 Grain size distribution of soil from site.

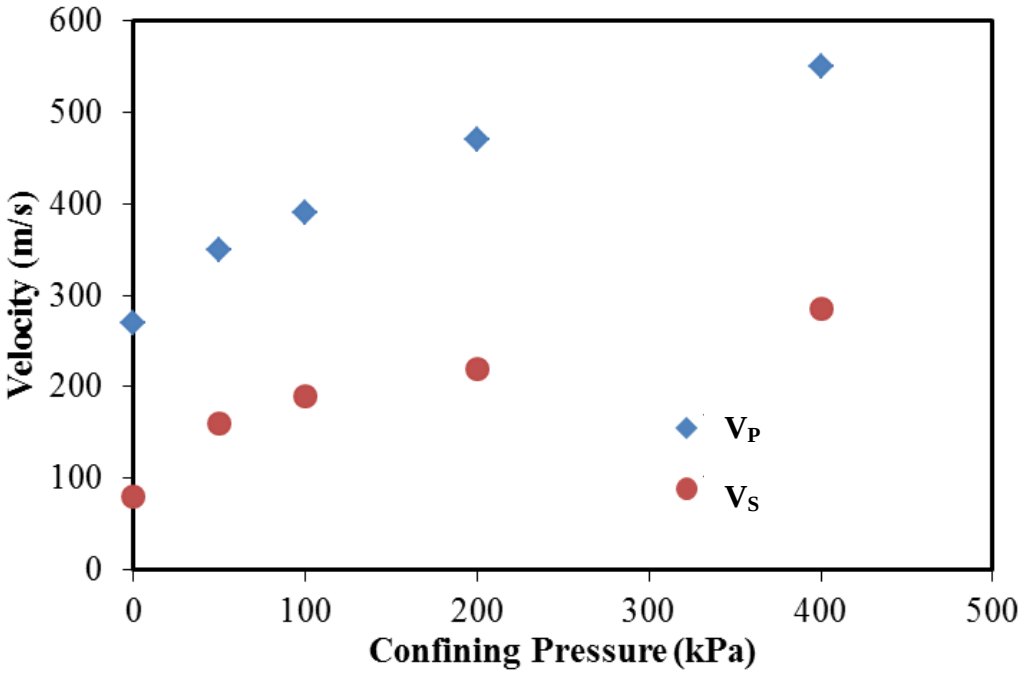

Figure 5.3 Wave velocities, V_p and V_s of site soil

5.2.2 Sensors

Pressure transducers and accelerometers were used in the small-scale field test. The accelerometers used were Piezoelectric PCB series 353 quartz-shear accelerometers with a range of ± 500g with flat amplitude response of up to 2 kHz. The pressure transducer used were Kulite LQ-080U series of soil-stress gauges which has a range of 0 to 1000 Psi (6.89 MPa). Prior to the small-scale field test, check on the sensors were performed.

A hand-held calibrator from PCB (Model: 394C06) was used to verify the calibration of the accelerometer. This was accomplished by attaching the accelerometer onto a hand-held calibrator which will excite at 9.81 m/s^2. The reading (voltage) of the accelerometer was output using a digital oscilloscope. Only when the output of the accelerometer matches the excitation provided by the hand-held calibrator, was the accelerometer selected for the field test.

Pressure transducers were verified with the dead weight tester. The output of the pressure transducers is in voltage. As such, a multi-meter was used to output the readings of the pressure transducers. The pressure transducer is selected for the field test when the calibration factor given by the manufacturer.

5.2.3 Concrete structure

A total of four concrete structures were casted for this small-scale field explosion test. The concrete structures were 450 mm concrete cubes with a hollowed-out sections to house two pressure transducers and three accelerometers. Figures 5.4a and d show the schematic diagrams of the concrete structure. Figures 5.4b and c show that the concrete structure hollowed-out section with two steel screws casted and secured at

the base of the hollowed-out section. The hollowed-out section of the concrete structures was used to secure a 150 mm housing to mount the accelerometers in three orthogonal directions. The steel housing has two 6 mm diameter holes drilled 112 mm apart at the base, matching the orientation and distance as the steel screws in the concrete structure. The steel housing was fastened and secured using nuts as shown in Figure 5.5a. Accelerometers' wires were passed through a 1.4m long PVC pipe while wires for the pressure transducer were secured along the PVC pipe using cable tie. The PVC pipe is used to protect the wires whilst buried in the ground and to provide the exact location of the buried concrete structure for retrieval after the test. The entrance of the hollowed-out section of the concrete structure was then secured with an aluminium plate with a hole for the PVC pipe to pass through the hollowed out section as shown in Figure 5.5b.

The pressure transducers were mounted on two faces of the concrete structure using 30mm diameter button magnets (same diameter as pressure transducer) epoxied onto a recess specially made to ensure that the mounted pressure transducer was flushed with the face of the concrete structure. Figure 5.5c shows a mounted pressure transducer on one face of the concrete structure. Figure 5.5d shows a completed setup of the concrete structure without SRM. A pair of handles formed using Y-16 rebars were casted for lifting and moving of the concrete structure.

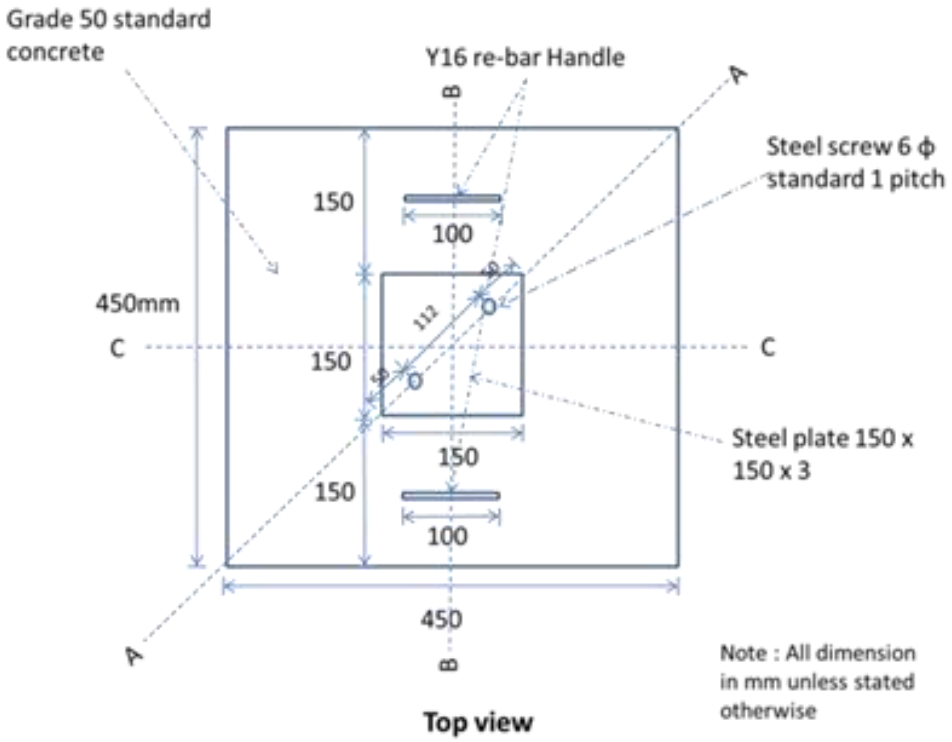

a) Top view

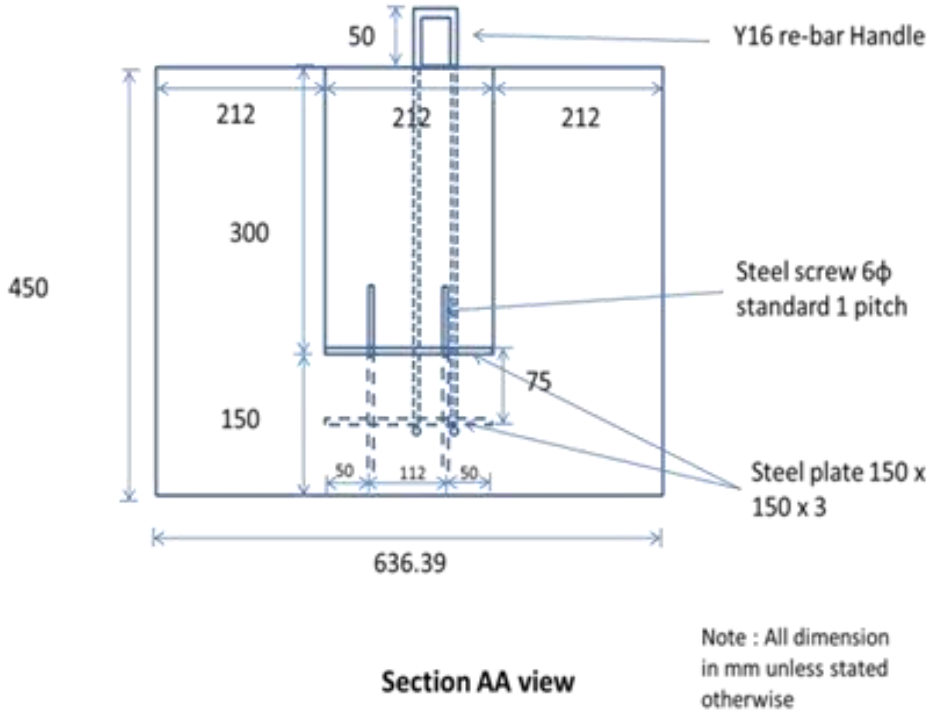

b) Section A-A view

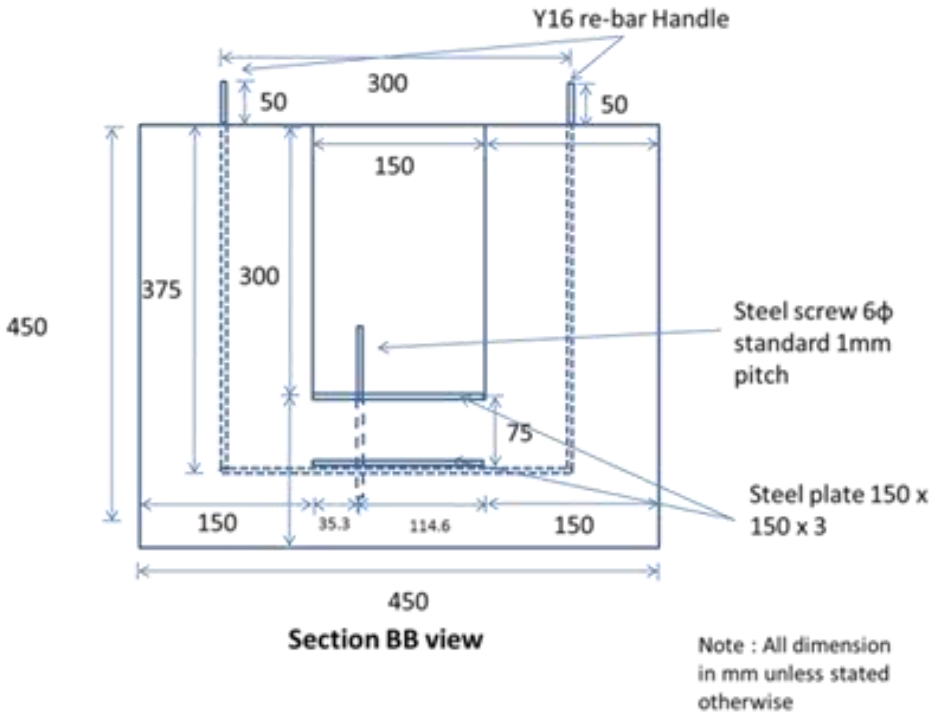

c) Section B-B view

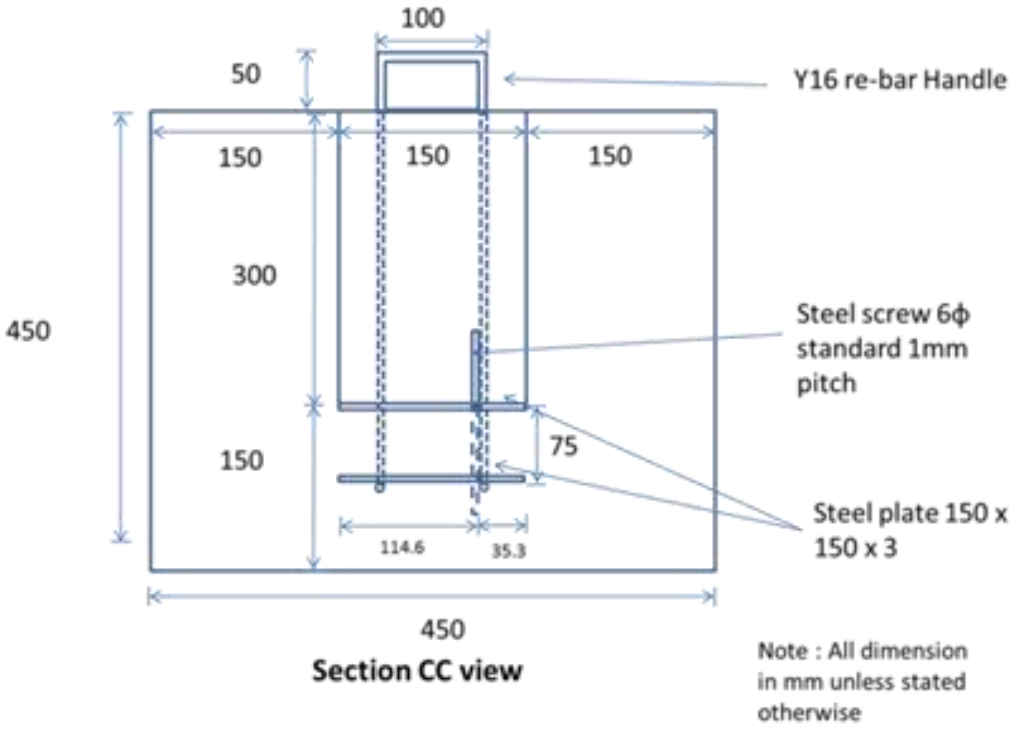

d) Section C-C view

Figure 5.4 Schematic drawing showing the concrete structure

a) Triaxial accelerometer steel housing

b) Prior to sealing of the hollowed-out section

c) Mounted pressure transducer

d) Completed bare concrete structure

Figure 5.5 Concrete structure set-up

5.2.4 SRM barrier

The SRM used for the seismic wave barrier comprising of 70% rubber chips and 30% sand (R70 at sr0.5) were packed into a large plastic bag and sealed in several lines in the vertical and horizontal directions to prevent segregation between rubber and sand particles, movement of SRM and to prevent saturation during the test if it was raining.

Each SRM pocket consist of equal amount of SRM to maintain a consistent dry density. The SRM packages were then secured onto a chicken wire mesh measuring 550 mm by 550 mm using fabric tape as shown in Figures 5.6a and b. Each of these panels were placed the sides of concrete structure and connected using cable tie as shown in Figures 5.6c and d. In effect, the concrete structure was warped with SRM panels. A pit of 2m by 2m by 1.5m was first dug by the excavator before lowering of the concrete structure into the pit using chain and hooks attached to the bucket of the excavator. Prior to positioning the concrete structure in the pit, a SRM panel was positioned at the bottom of the pit. Extra care was taken in guiding the concrete structure into the correct position and orientation as per layout before allowing it to rest on the SRN panel at the bottom of the pit. The bottom SRM panel was then secured to the other SRM panel on the sides of the structure. The top part of the concrete structure was covered using a SRM panel without the chicken wire to accommodate the lifting handles and protruding PVC pipe. Once the concrete structure was in place, the excavator carefully backfills the pit till the soil levels with the pressure transducer. To ensure good contact between the pressure transducer and the surrounding soil, the surrounding soil was compacted by tamping with a spade. Once compaction was completed, backfilling of the pit continue till it levels with ground surface. The surrounding soil was then compacted with the bucket of the excavator. A pit of 1.5m by 1.5m by 1.5m was dug for the placement of the 50 kg TNT cylindrical shaped bare charge. The centre of the charge is at a depth of 1.4m. The pit was then backfilled. The placement of the concrete structure without SRM follow the same procedures as above.

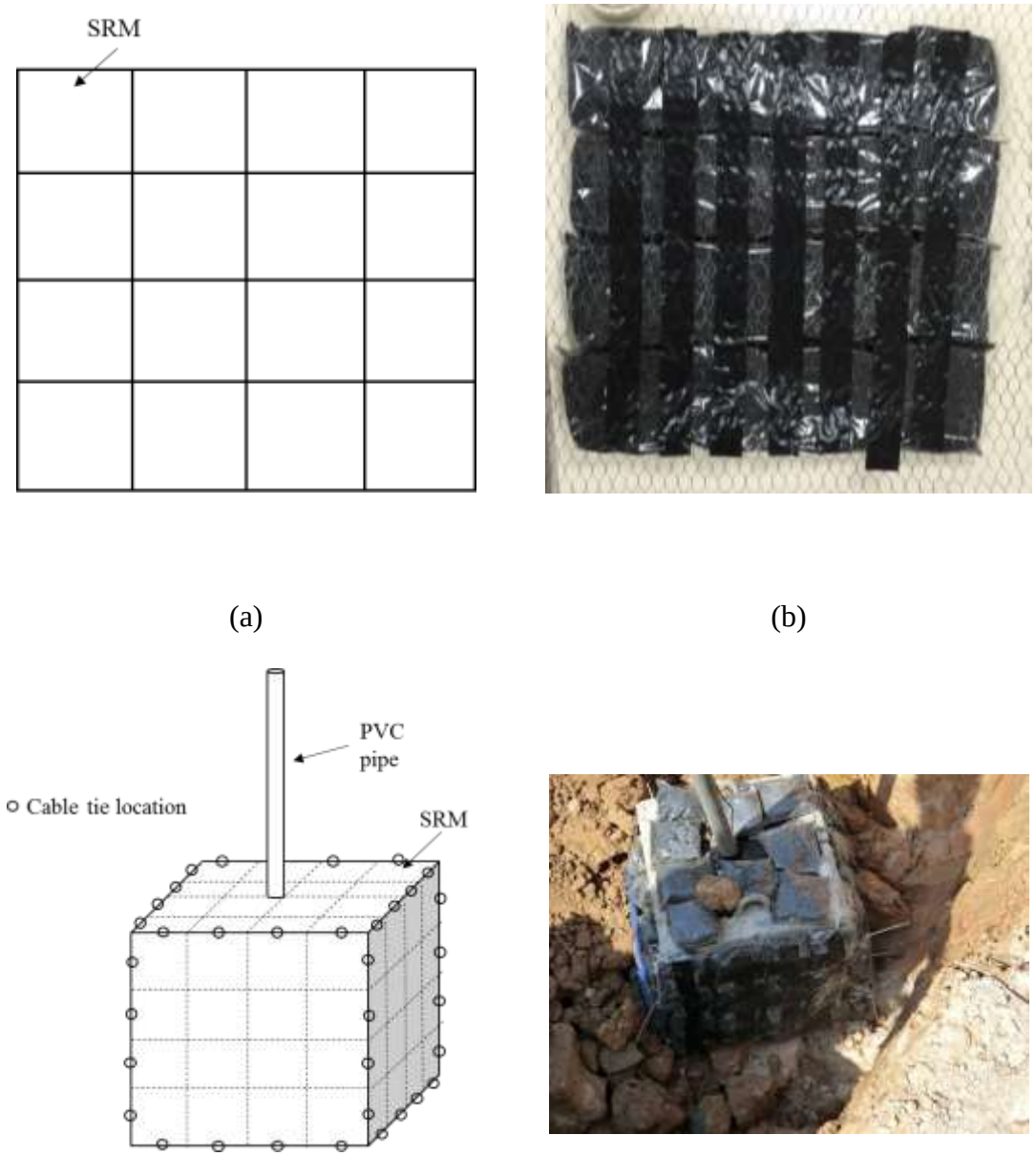

(a) (b)

(c) (d)

Figure 5.6 a) and b) A panel of SRM c) and d) Panels of SRM attached to bare concrete structure before burial

5.2.5 Field test layout, test site preparation and target placement

A total of four concrete structures were buried below the ground level with the centre of the structure at a depth of 1.4m. Of the four, two are with a SRM barrier while the

other two are without a SRM barrier, the field test layout was designed with the constraints mentioned in Section 5.2. The plan view of the field test layout is as shown in Figure 5.7. From Figure 5.7, the concrete structures without SRM barrier is are indicated as concrete structure 1a and 1b while the concrete structures with SRM barrier are indicated as concrete structure 2a and 2b. Due to limitations on the number of detonation of explosives allocated for the tests, the positions of the concrete structures were orientated to ensure that a right-angle triangle was formed as shown in Figure 5.7. The positions and orientations of the concrete structures were set in such a way that the separate detonation of explosives provided data that can be compared. Unfortunately, the 1st detonation for concrete structures 1a and 2a damage the main data acquisition cable for concrete structures 1b and 2b as well as the accelerometers cables for concrete structures 1a and 1b (which resulted in no accelerometer data for the second detonation). Hence, concrete structure 1b and 2b had to be abandon in the tests.

Two detonations of 50 kg bare TNT charge were made. The detonations were set off two days apart as per scheduled. For each detonation in the x-direction, six sensors were hooked up to the data acquisition system. Pressure transducers, x and z directions for accelerometers for each concrete structure to capture the pressure and acceleration facing the explosion (x-direction) an acceleration in the vertical direction (z-direction). The naming and locations of the sensors are as shown in Figure 5.7. Figure 5.8 shows the section view of the field test.

It is well known that the peak pressure and accelerations can be affected by factors such as degree of saturation as well as distance from detonations in which measurements were made (TM5-855-1 1986). The soil conditions considered, which

are dependent on the amount of rainfall prior to the field test, were dry, partially saturated and fully saturated. To ensure that the peak pressures and accelerations were within the measurement range, estimation of free-field peak pressures and accelerations were made using TM5-855-1 (1986) as well as numerical simulations using LS-DYNA for dry, partially saturated and fully saturated conditions (presented in the later section). Table 5.3 shows the amount of amplification required to suit the respective conditions. The measurements were recorded with DTS slice pro data acquisition system at sampling rate of 5 MHz. The DTS slice pro data acquisition system, which comes with an inbuilt amplifier, was designed specially to record data for explosion tests.

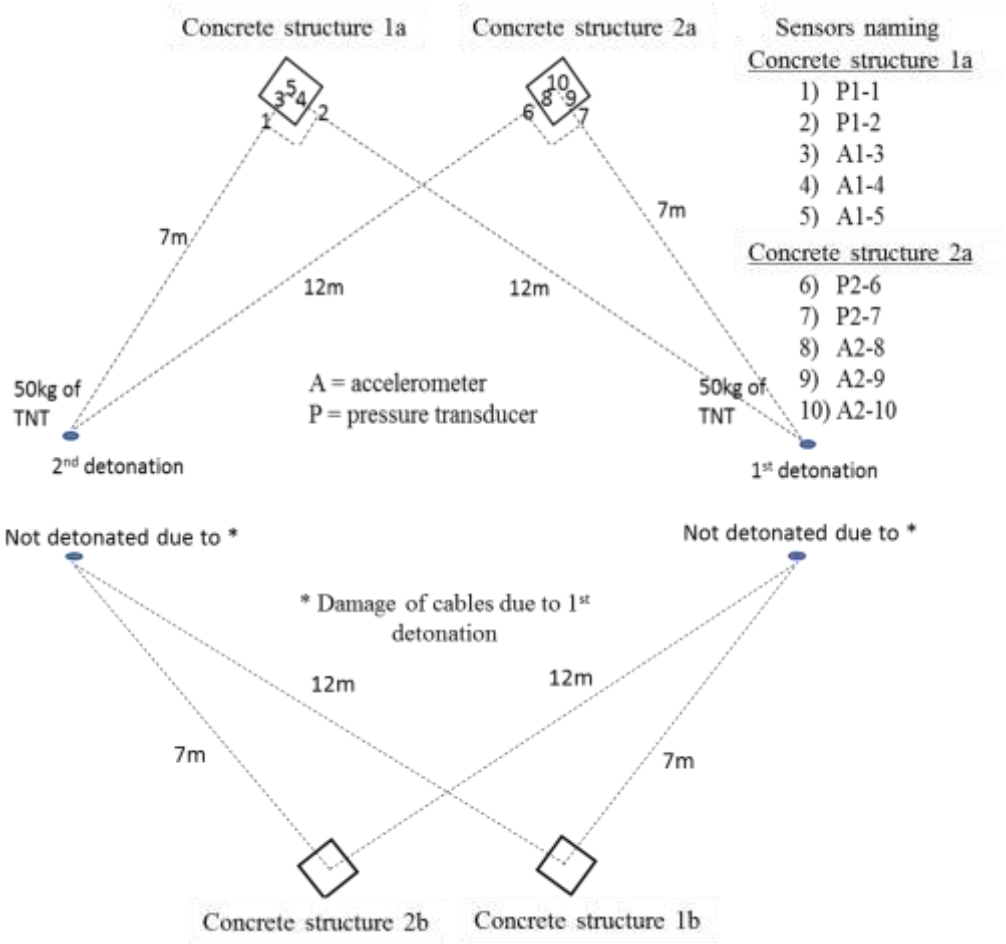

Figure 5.7 Plan view of small-scale field test layout

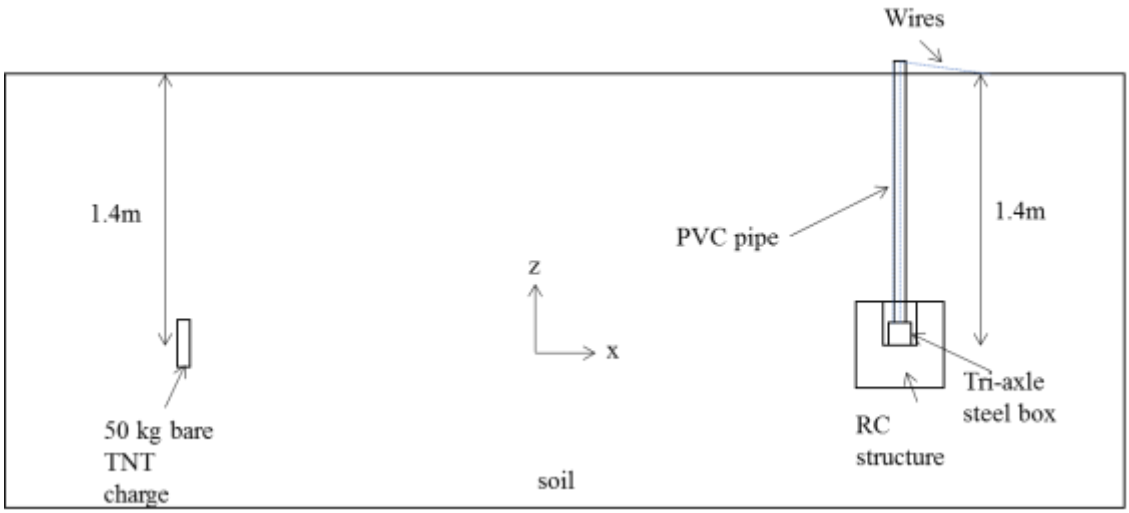

Figure 5.8 Section view of small-scale field test

Table 5.3 Free-field peak pressure and acceleration predictions

Sensors	Distance (m)	Mounted Directions	Dry	Partially saturated	Fully saturated
P1-1, P2-7	7		80 kPa	250 kPa	400 kPa
P1-2, P2-6	12		7.5 kPa	30 kPa	50 kPa
A1-3, A2-9	7	x	15 g	31 g	45 g
A1-4, A2-8	12	x	4.5 g	10 g	15 g
A1-5, A2-10	7	z	7 g	15 g	21 g
A1-5, A2-10	12	z	2.5 g	5 g	7.5 g

* Charge weight of 50kg TNT

5.2.6 Tests results and discussion

Precautions were taken to ensure that all sensors are in working condition in all phases of the field test. The phases of the field test can be generally divided into before and after the first detonation and before the second detonation. The actions taken were tabulated as follows.

Table 5.4 Table of action taken

S/N	Timeline	Actions
1	Before first detonation	• Connectivity of wires to the sensors was checked using a multi-meter after the concrete structures were buried. • The cables connecting the sensors to the data logger were check for breakages. • Ensuring the right amount of amplification was set for the sensors at the data logger.
2	After first detonation	• Connectivity of wires to the sensors was checked using a multi-meter after the concrete structures were buried. • The cables connecting the sensors to the data logger were check for breakages.
3	Before second detonation	• Repeat actions taken for 1

All sensors were able to pick up readings during the first detonation. However, after the first detonation, besides the main cable damage to the concrete structures 1b and 2b, the cable connecting the accelerometers of concrete structure 1a and 2a were found to be damaged by the fallen debris from the first detonation. Due to time constraint, replacement of the cable was not possible before. As a result, none of the accelerometers gave readings for the second detonation. Figures 5.9 to 5.14 show the pressure and acceleration time-histories obtained from the sensors. Figure 5.9 and 5.10 show a reduction of 28% and 30% of the peak pressure, respectively. The reduction in peak pressure due to the SRM barrier was found to be comparable to reduction found by Davis (1994) for geofoam barrier against ground shock in a centrifuge test.

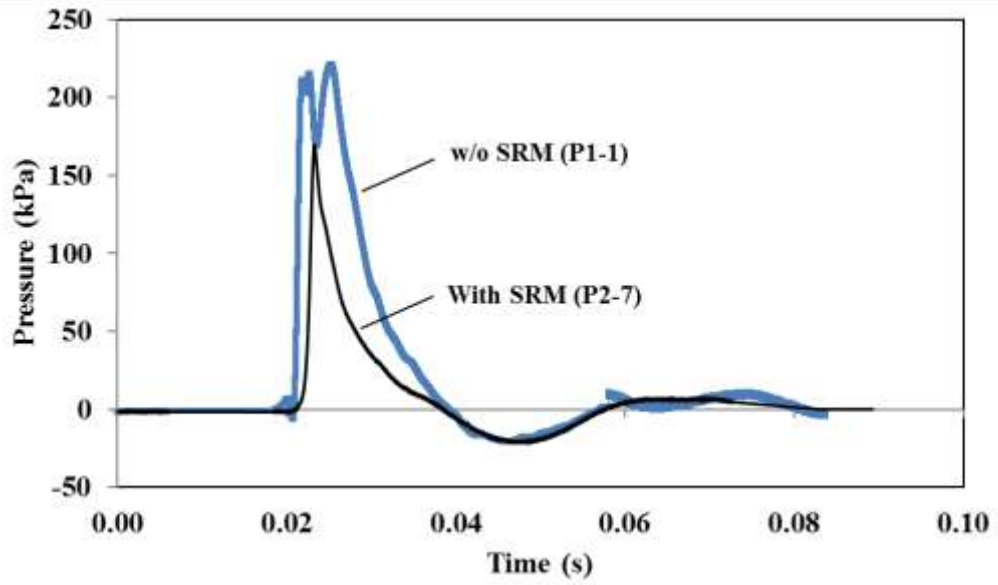

Figure 5.9 Pressure-time histories at 7m away from source

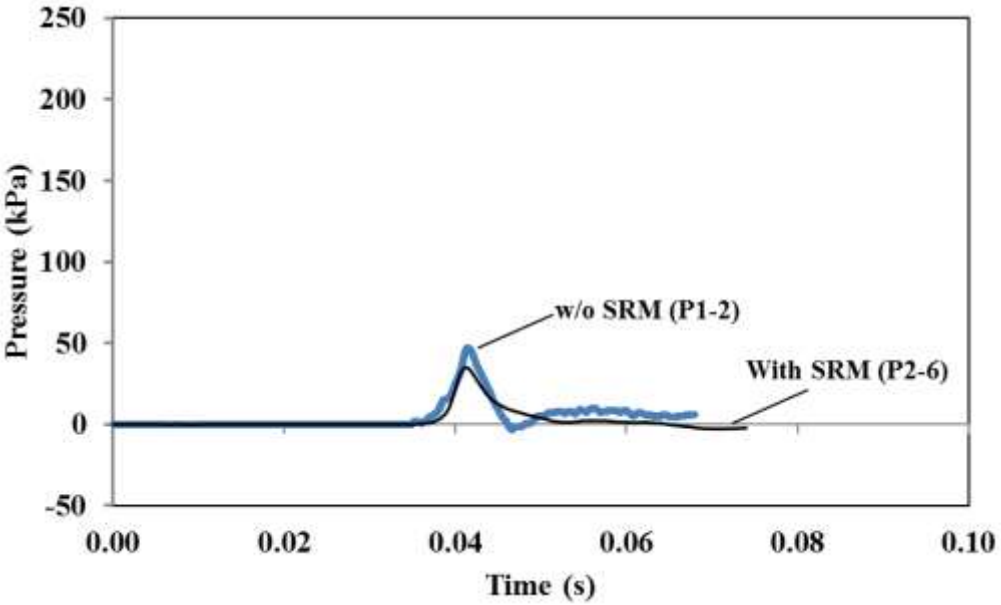

Figure 5.10 Pressure-time histories at 12m away from source

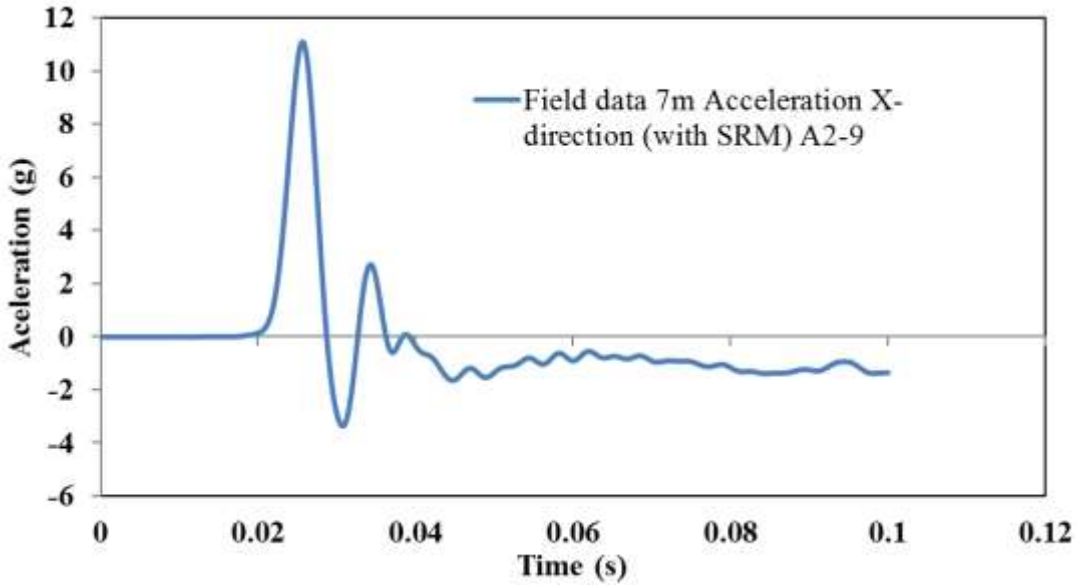

Figure 5.11 Acceleration-time histories for x-direction at 7m away from the source

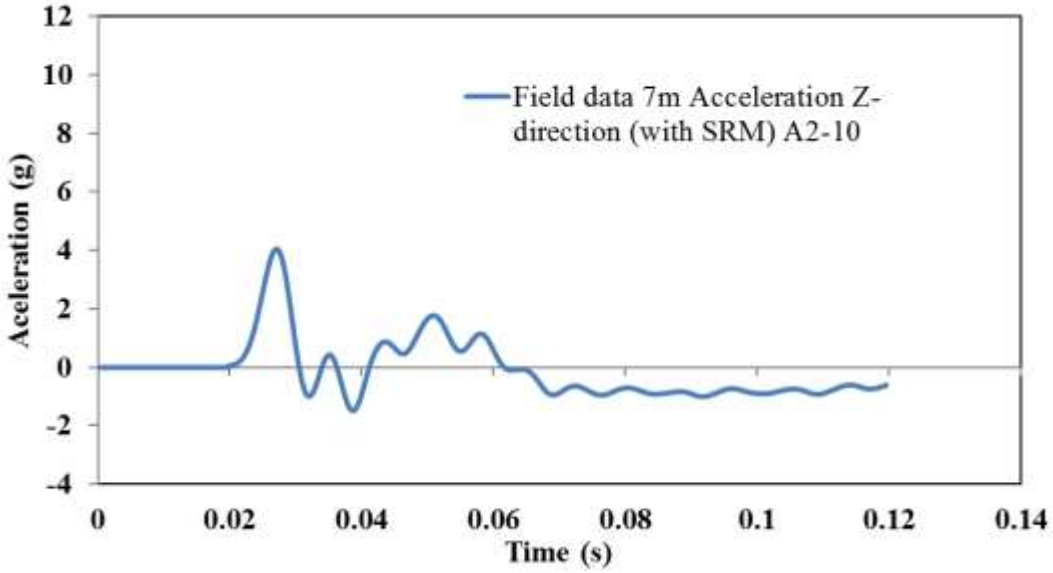

Figure 5.12 Acceleration-time histories for z-direction at 7m away from the source

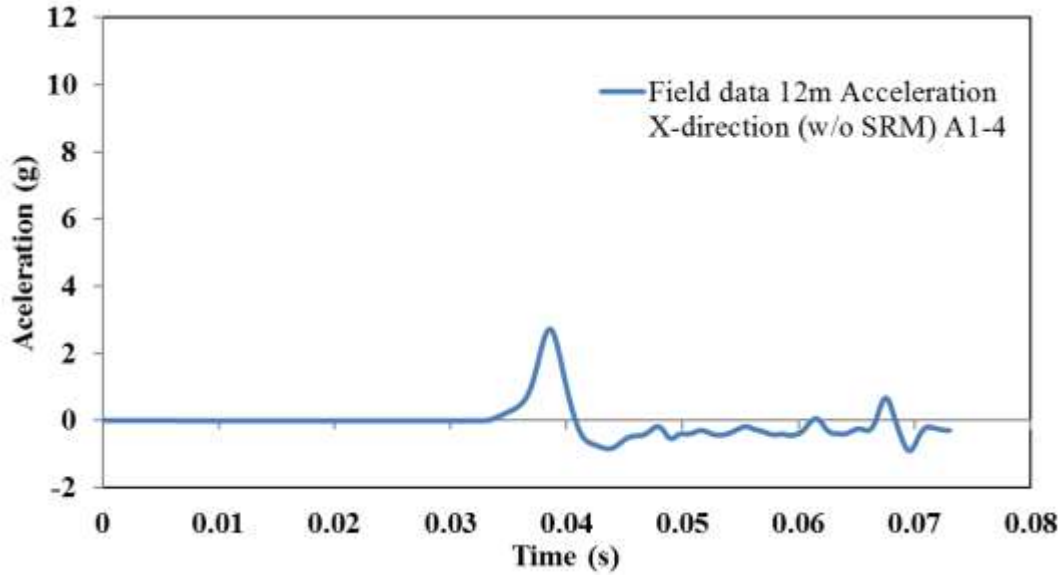

Figure 5.13 Acceleration-time histories for x-direction at 12m away from the source

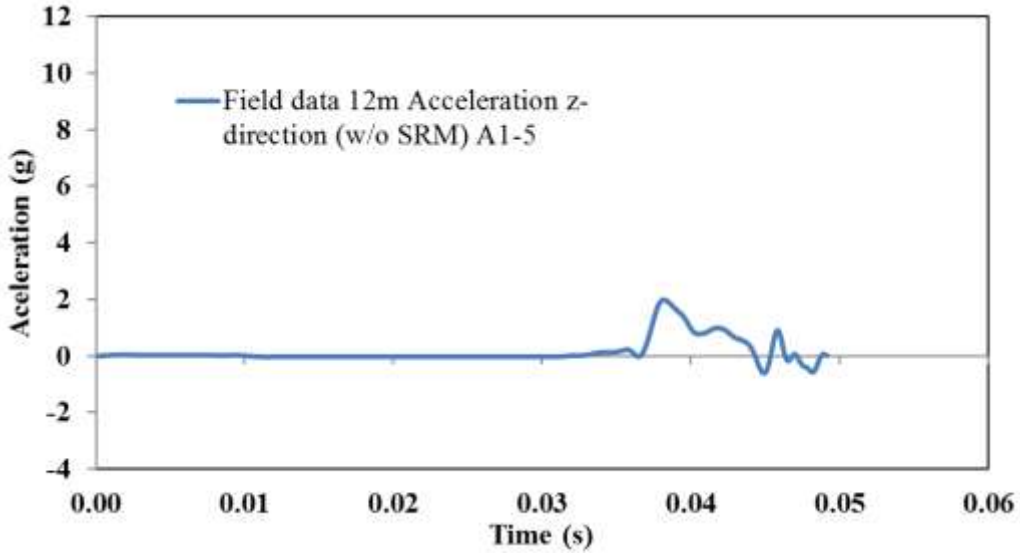

Figure 5.14 Acceleration-time histories for z-direction at 12m away from the source

5.3 Verification of FE model for free-field condition

Numerical software, LS-DYNA was used to model the field test. As non-reflecting boundary in LS-DYNA could not be applied for transient dynamic problem (Aung and Leong 2011), the extent of the FE mesh was chosen such that the FE results

within the modelled elapsed time were not affected by wave reflections. Before the small-scale field tests were simulated, the FE model was first checked against the peak pressure and crater curves from TM5-855-1 (1986). This is to ensure that the model used is able to correctly reproduce the field conditions.

5.3.1 Material properties

In this study, four material models were used: MAT_008 (HIGH EXPLOSIOVE BURN material), MAT_005 (SOIL AND FOAM material), MAT_078 (SOIL CONCRETE material) and MAT_009 (NULL material).

5.3.1.1 Soil and foam

The material model Soil and Foam (MAT_005), created by Kreig (1972), was used to model the soil. The elasto-plastic model has a paraboloid yield surface capped by an ellipsoid. With the application of small strain under compression or tension, the model is linearly elastic with shear strength increasing with strain until yield. On yielding, the yield function of the model Y is described by Equation 5.1

$$Y_e = (p-f_s)[J_2 - (a_0 + a_1 p + a_2 p^2)] = 0 \quad (5.1)$$

where p is the pressure, a_0, a_1 and a_2 are constants, f_s is the function of mean total strain and J_2 is the second invariant of the stress deviator. The yield function Y_e can be split into two parts, the deviatoric part represented by the paraboloid (Y_s) given in Equation 5.2 and the volumetric part represented by a plane normal to the hydrostatic axis (Y_p) given in Equation 5.3.

$$Y_s = J_2 - (a_0 + a_1 p + a_2 p^2) \quad (5.2)$$

$$Y_p = (p-f) \quad (5.3)$$

The volumetric part can be solved with either incremental or deformation plasticity theory and the deviator part is solved using conventional plasticity theory (Krieg, 1972).

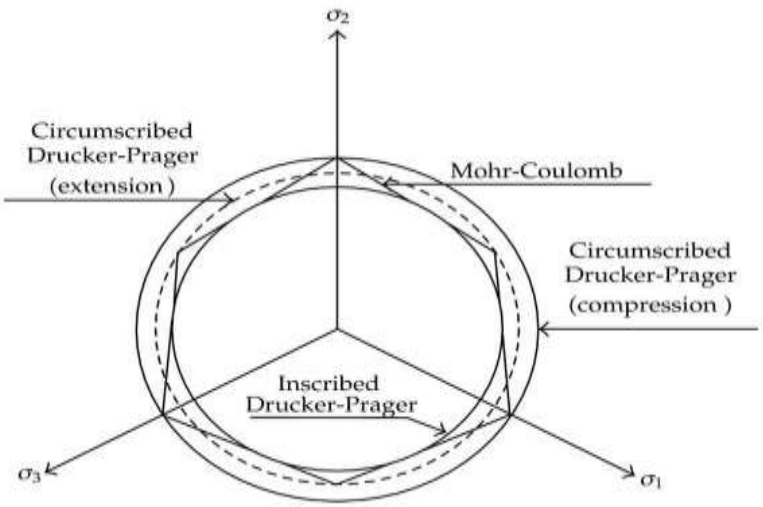

Figure 5.15 Mohr-Coulomb and Drucker-Prager yield criteria in stress space (from Nayak and Zienkiewicz, 1972)

Constants a_0, a_1 and a_2 can be derived in conventional plasticity theory using the Drucker-Prager yield function Y_{DP} shown in Figure 5.16:

$$Y_{DP} = \alpha' I_1 + \sqrt{J_2} - k = 0 \qquad (5.4)$$

where α' and k are constants and I_1 is the first invariant of the Cauchy stress. The first invariant of Cauchy stress I_1 is given as:

$$I_1 = (\sigma_{11} + \sigma_{22} + \sigma_{33}) \qquad (5.5)$$

where p is the mean stress:

$$p = 1/3(\sigma_{11} + \sigma_{22} + \sigma_{33}) \qquad (5.6)$$

The constants α and k are (Nayak and Zienkiewicz 1972):

$$\alpha = \frac{2\sin\phi'}{\sqrt{3}(3 - \sin\phi')} \quad (5.7)$$

$$k = \frac{6c'\cos\phi'}{\sqrt{3}(3 - \sin\phi')} \quad (5.8)$$

where ϕ' is the effective friction angle and c' is the effective cohesion of the soil

Rearranging Equation 5.24 and making $\sqrt{J_2}$ the subject:

$$\sqrt{J_2} = k - \alpha I_1 = k - 3\alpha' p \quad (5.9)$$

From Equation 5.2:

$$J_2 = a_0 + a_1 p + a_2 p^2 \quad (5.10)$$

Squaring Equation 5.9 gives:

$$J_2 = k^2 - 6\alpha k p + 9\alpha^2 p^2 \quad (5.11)$$

By comparing Equations 5.10 and 5.11, the coefficients a_0, a_1 and a_2 are given, respectively, by

$$a_0 = k^2 \quad (5.12)$$

$$a_1 = 6\alpha' k \quad (5.13)$$

$$a_2 = 9\alpha'^2 \quad (5.14)$$

From Equations 5.12 to 5.14, a_0, a_1 and a_2 can be calculated using c' and ϕ' A low c' and ϕ' would mean that the soil is soft and have bigger plastic zone around the explosion compared to one with high c' and ϕ'.

Material model MAT_005 also requires a pressure versus volumetric strain curve as an input. The pressure versus volumetric strain curve can be obtained by conducting a hydrostatic compression test (Verdugo and Ishihara, 1996; Wang and Yan, 2006). This test can be carried out in a triaxial laboratory apparatus by increasing the

confining pressure and measuring the change in volume. In a triaxial test, the mean stress p is given by:

$$p = (\sigma_1 + 2\sigma_3)/3 \quad (5.15)$$

The volumetric strain ε_v can be calculated from the axial and lateral strains as shown in Equation 5.16.

$$\varepsilon_v = \varepsilon_{kk} = (\varepsilon_1 + 2\varepsilon_3) \quad (5.16)$$

where ε_1 and ε_3 are the axial and radial strains, respectively.

A typical pressure versus volumetric strain curve is shown in Figure 5.16. From Figure 5.16, it is observed that volumetric strain increases with increasing pressure during the loading phase. When the applied pressure is reducing (unloading), the original volume is not recovered due to the plastic deformation caused by the applied load. The recovered deformation is a result of the elastic deformation of individual particles and the permanent deformation is caused by sliding of the particles (EL-Sohby and Andrawes, 1972). The recovered deformation can be quantified by taking the ratio of stiffness of the loading phase K_L (slope of the loading phase) and unloading phase K_{uL} (slope of the loading phase) which gives us the strain recovery ratio (K_L/K_{uL}).

Hedron and Auld (1967) suggested that the stress-strain behavior of the soil can be represented by a bilinear curve, where both the loading and the unloading phases are approximated using straight lines as shown in Figure 5.17. The area under the stress-strain curve determines the energy absorption capability of the soil medium as shown in Figure 5.17 (Hendron and Auld, 1967). This energy absorption dictates how fast the peak pressure attenuates with distance; the bigger the area under stress-strain curve, the faster the peak pressure attenuates. It is well known that the behavior of soil is strain-rate dependent; a higher strain rate will result in higher stress. Under high

strain rate, the stress at each contact point of the particles is large and the movements of the particles are restricted. As a result of the limited movement of particles, the specimen is able to recover 'more' compared to specimen under slower strain rate during unloading phase (Kikawa et al., 2008). This explanation is further supported by experiments performed by Wilson and Sibley (1962) on Playa silt. Wilson and Sibley (1962) observed that at faster loading rate, the strain recovery ratio is 0.7 while slow loading rate give a strain recovery ratio of 0.3. This observation is also shown in hydrostatic compression tests on sand conducted by Verdugo and Ishihara (1996) and Wang and Yan (2006). Verdugo and Ishihara (1996) obtained a higher strain recovery ratio of (0.52) for a loading strain rate of 1 mm/min compared to Wang and Yan (2006) who obtained a strain recovery ratio of 0.3 for loading rate of 0.07 mm/min.

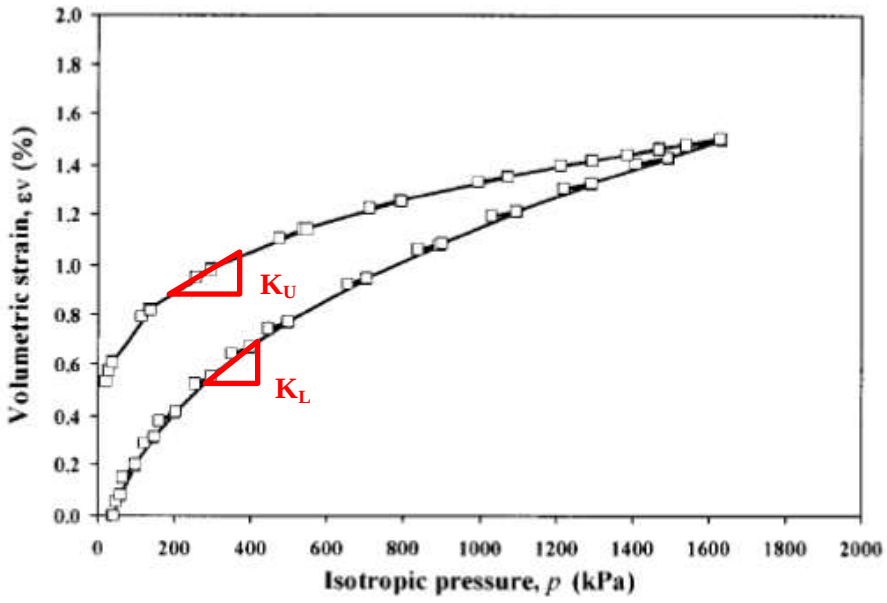

Figure 5.16 Hydrostatic compression of sand (modified from Lade and Abelev, 2005)

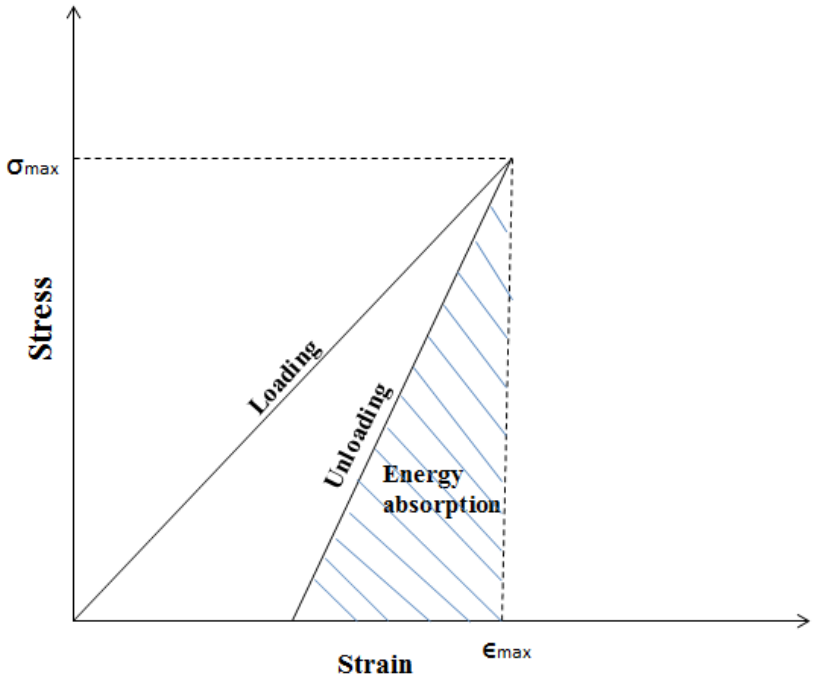

Figure 5.17 stress strain curve modified from (Hendron and Auld, 1967)

5.3.1.2 Concrete

Concrete can be simulated using Mat_078 from the LS-DYNA material library. This model can correctly simulate the hardening effects when the concrete undergoes compression. The input parameters for the load curves can be obtained by carrying out triaxial compression test. The concrete first deforms elastically till it reaches the yield stress σ_y which is described by the Von Mises yield function V_m:

$$V_m = \sqrt{3J_2} - \sigma_y \qquad (5.17)$$

where J_2 is the second invariant of the Cauchy stress. The yield stress of the concrete σ_y degrades when strain exceeds ε_1 and reach as a residual constant value at strain ε_2. The degradation is represented by a strength reduction factor f_r shown in Figure 5.18. When the model undergoes tension, the yield function is changed to:

$$\phi = J_2 - F(p) \qquad (5.18)$$

The deformation modulus of the concrete at plastic strains ε_1 and ε_2 are defined using load curves shown in Figure 5.19.

Laboratory tests to characterise mechanical properties of concrete have been widely performed by numerous researchers (e.g. Farnam et al. 2008, 2010, Tai and Tang 2006, Hao et al. 2012) and were not performed in this study. The mechanical properties of concrete obtained from the literature review are collated in Table 5.5. Besides properties such as density, shear and bulk moduli, various pressure and strain curves are required for the material model input. The curves that are required for the input are load curve (LCFP) for plastic strain at which fracture begins versus pressure, load curve (LCRP) for plastic strain at which residual strength is reached versus pressure and load curve (LCYP) for yield stress versus pressure. These curves are required to determine the condition of the concrete at various stages of degradation when subjected to pressure. These curves can be determined using triaxial test (Farnam et al. 2008).

The properties of concrete used for this study were those suggested by Farnam et al. (2008). Farnam et al. (2008) performed experimental and numerical investigation on impact behavior of concrete. Farnam et al. (2008) simulated the experiment using LS-DYNA with material model MAT_078. The material properties input for the numerical simulations performed by Farnam et al. (2008) were obtained from laboratory tests. Farnam et al. (2008) concluded that the material model MAT_078 is able to effectively model plain concrete. Material properties obtained from Farnam et al. (2008) were found to be within reasonable range of properties of reinforced concrete obtained by other researchers as shown in Table 5.5. The properties of

concrete used in this study are summarized in Table 5.6 and the input curves are shown in Figures 5.20 to 5.22.

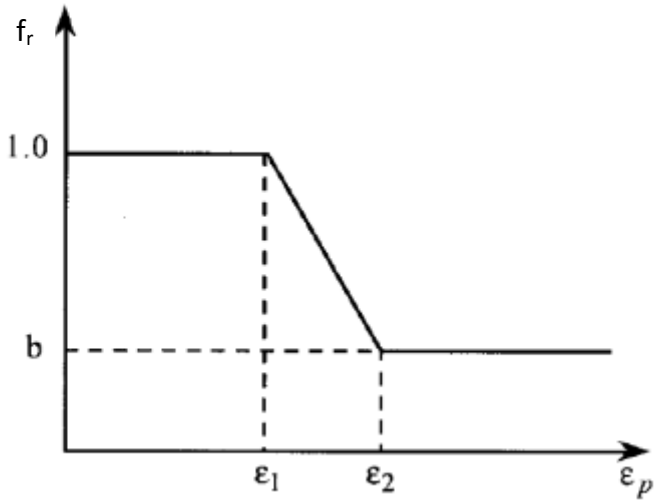

Figure 5.18 Strength reduction factor f (from LSTC 2006)

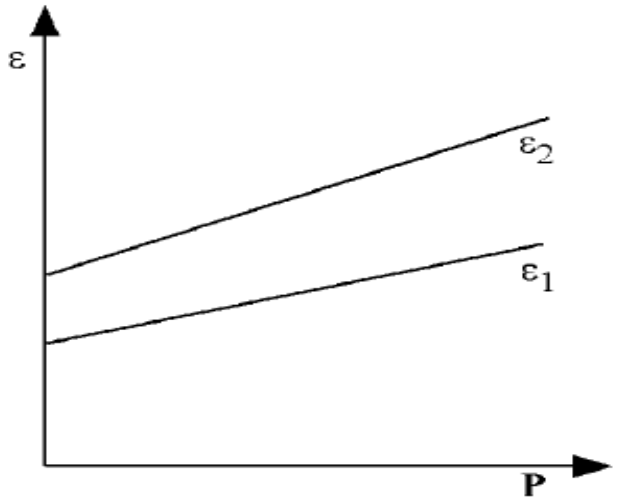

Figure 5.19 Cracking strain versus pressure (from LSTC 2006)

Table 5.5 Concrete Material's properties

Reference	Description	Density (kg/m^3)	K(kPa)	G(kPa)	E(MPa)	Poisson's ratio	P_{cut} (Mpa)	B_f
Wang et al. (2009)	Concrete constitutive model	2400	-	-	3e4	0.3	-2	3
Farnam et al. (2010)	Plain concrete	2291	1.47e7	1.103e7	-	0.2	-3	0
	High-performance fiber-reinforced cement	2376	1.641e7	1.130e7	-	0.22	-30	0.9
Farnam et al. (2008)	Plain concrete	2100	1.471e7	1.103e7	-	0.20000	-	-
	Fibre reinforce lightweight aggregate concrete	2200	1.641e7	1.098e7	-	0.22	-2.1	0.50000
Lin et al. (2010)	Polyethylene (PE)-fibrous ferrocement	2100	-	-	1.980e4	0.24	-2.58	-
	Calcined Bauxite Concrete	2594	-	-	4.040e4	0.22	-3.19	-
	Mortar	2273	-	-	3.270e4	0.21	-2.46	-
Xu et al. (2012)	Concrete MAT_Pseudo_tensor	2750	-	1.580e7	-	0.2	-	-
Tai and Tang (2006)	Concrete	2240	-	1.357e7	-	-	-	-
Hao et al. (2012)	Mortar	2750	3.52e7	-	-	-	-2.5	-
Huang et al. (2005)	Concrete	2520	1.08e7	8.76e6	2.07e4	0.18	-	-
Agardh and Laine (1999)	Soil concrete	2400	2.80e7	3.40e7	5.00e4	0.2	-	-
Pankaj and Kaushia (2002)	Ferrocement layer	-	-	2.14e7	7.22e3	0.2	-	-

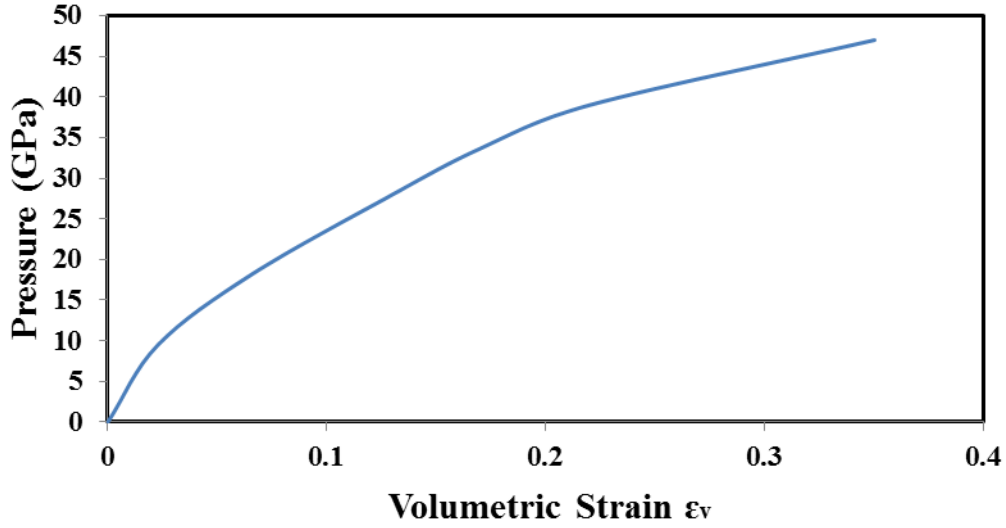

Figure 5.20 Pressure versus volumetric strain LCFP

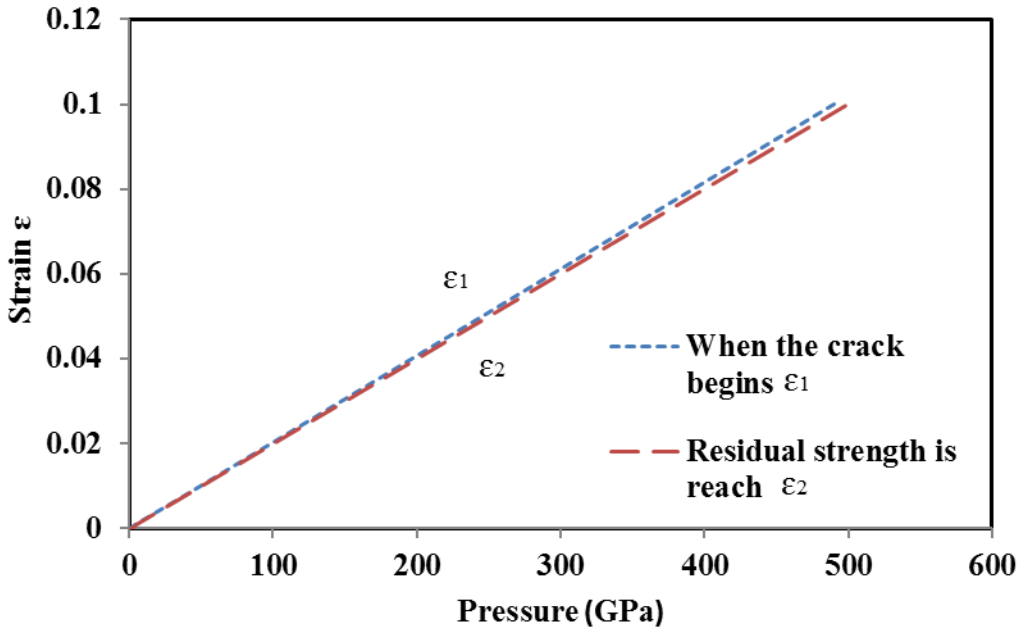

Figure 5.21 Strain versus pressure LCRP

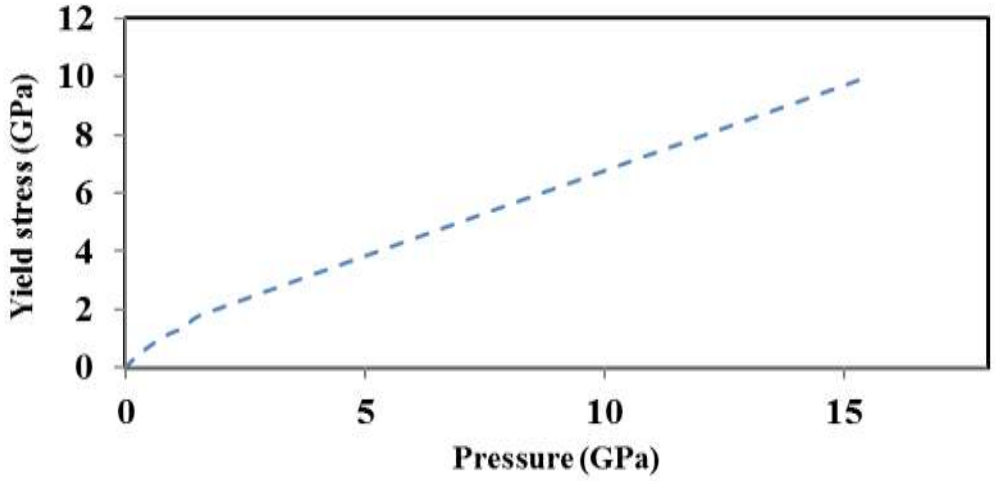

Figure 5.22 Yield stress versus pressure LCYP

Table 5.6 Properties of concrete

Mass density, ρ (kg/m^3)	2100
Shear modulus, G (kPa)	1.103e7
Bulk modulus, K (kPa)	1.471e7
Tension cutoff, PC (kPa)	-2e3
Residual strength factor, B_f	0.5

5.3.1.3 Explosive

The MAT_008 model in LS-DYNA material library was used to model the TNT explosive. Initially, MAT_008 behaves like a perfectly-plastic material before detonation. Following which, the material undergoes detonation and interaction between the gas produced by the detonation and the surrounding soil occurs, following the equation of state (EOS). In LS-DYNA, the burning fraction controls the release of chemical energy from the material. As the simulation marches forward in time, the burn fraction increases and eventually reaches unity. Upon achieving unity, burn fraction F remains constant as the time step marches forward. Burning fraction F

can also determine if the explosive charge is fully consumed during detonation. In this project, the default value of F = 1 was selected and the charge material was considered to be fully detonated.

Properties of TNT are well established. The TNT properties given in Dobratz (1981) were used in MAT_008 for this study. The properties are summarised in Table 5.7

Table 5.7 MAT_008 input for TNT from Dobratz (1981)

Mass density (kg/m^3)	1630
Detonation velocity (m/s)	6930
Chapman-Jouget pressure (kPa)	2.1e7

In MAT_008, the Jones-Wilkins-Lee (JWL) is used as the EOS for the explosive. The Jones-Wilkins-Lee (JWL) EOS models the development of the detonation products gas pressure P as:

$$P = A\left(1 - \frac{\omega}{R_1 V}\right)e^{-R_1 V} + B\left(1 - \frac{\omega}{R_2 V}\right)e^{-R_2 V} + \frac{\omega E_0}{V} \qquad (5.19)$$

where A, B, and C are linear coefficients in GPa, R_1, R_2, and ω' are nonlinear coefficients, V is the relative volume (= v/v_0 where v_0 is the original volume of the detonation products), and E_0 is the detonation energy per unit volume. The JWL EOS parameters for TNT are summarized in Table 5.8

Table 5.8 Equation of state JWL parameters of TNT from Dobratz (1981)

Parameter	Value
A (GPa)	3.71e11
B (GPa)	3.23e9
R_1	4.15
R_2	0.95
ω'	0.35
E_0 (kJ/m^3)	4.35e6
V (m^3)	1

5.3.2 Validation of numerical model against TM5-855-1 curves

TM 5-855-1(1986) free-field peak pressure curves due to contained explosions were developed from field tests conducted in the early 1950s (Drake et al. 1983). These free-field peak pressure curves were replotted by Leong et al. (2006) into a dimensionless peak pressure versus scaled distance plot. The objective of this section is to validate the numerical model to simulate explosion in soils.

5.3.2.1 Convergence studies

The free-field ground shock condition can be simulated using a two-dimensional (2D) axisymmetric finite element (FE) model with the axis of symmetry at the centre of the charge. Using a 2D model as shown in Figure 5.23 reduces the run time to analyse the problem. However, before proceeding with the parametric runs, convergence studies have to be performed to determine the most economical element size while striking a balance between run time and accuracy.

The FE mesh was 40 m by 40 m with the charge buried at a depth of 20 m. The effect of element size on the accuracy of the FE results was investigated using three different element sizes of 0.2m by 0.2m, 0.1m by 0.1m and 0.05m by 0.05m while maintaining the FE mesh at 40 m by 40 m. Figure 5.23 shows the pressure-time histories for a point at a radial distance of 8m from the charge at the same depth as the charge (20 m). Figure 5.23 shows that the peak pressure decreases as the element size decreases. The difference between the FE peak pressures with element sizes of 0.2 by 0.2m and 0.1m by 0.1m is 20%. However, the difference between the FE models with element sizes of 0.1 by 0.1m and 0.05 by 0.05m is only 3.5%. Therefore, the results from FE models with element sizes of 0.1m by 0.1m and 0.05m by 0.05m were considered to have converged. As the run time required for the FE model with

element sizes of 0.05m by 0.05m was almost twice that of the FE model with element size of 0.1m by 0.1m, the FE model with element size of 0.1m by 0.1m is preferred for this study.

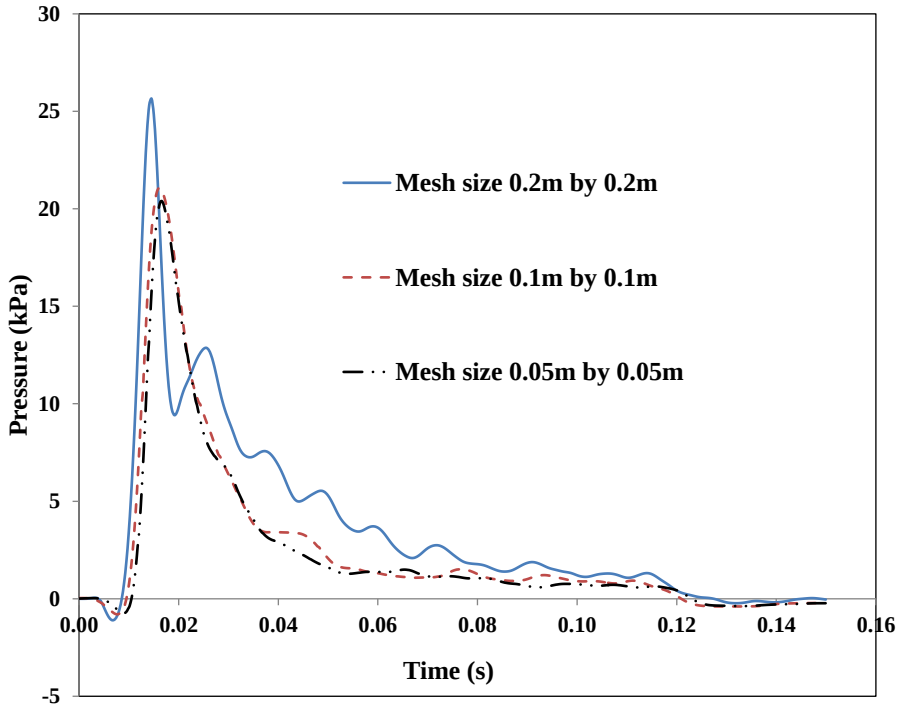

Figure 5.23 Pressure-time histories for FE models with different element sizes

5.3.2.2 Finite Element Model (free-field)

The dimensions of the FE mesh are as per section 5.3.2.1. The size of this FE model was chosen to ensure that there were sufficient results at various distances that span one logarithm cycle of scaled distance when plotted onto the dimensionless peak pressure plot proposed by Leong et al. (2007). As non-reflecting boundary in LS-DYNA could not be applied for transient dynamic problem, the extent of the FE mesh was chosen such that the FE results within the modelled elapsed time were not affected by wave reflections. The nodes on the axis of symmetry and on the right

boundary were constrained from horizontal movements while the nodes on the bottom boundary were constrained from vertical movements. Based on the convergence studies performed, the FE model (Figure 5.24) comprises 640,000 4-noded shell elements with each element size of 0.1m by 0.1m. The weight of the charge was limited such that the explosion will be fully contained within the soil.

Since the problem involved large distortion of the mesh caused by the explosion, ALE (Arbituary-Lagrangian-Eulerian) formulation was used to perform automatic smoothing and rezoning of the mesh throughout the simulation. Figure 5.25 illustrates how ALE works with a 2D solid mesh. The Lagrangian formulation works well for problem involving small distortion (movement) of the mesh. At any point of time, the Lagrangian formulation only allows one material type to be present in the mesh and the material moves with the mesh. When severe distortion of the mesh takes place, the Lagrangian formulation breaks down. In such cases, the Eulerian formulation is used. In the Eulerian formulation, the mesh is fixed in space and allows the material to flow through, for good example, gases and fluids flowing through a medium. ALE involves material moving through the reference mesh which is also moving unlike the Eulerian formulation. Considering two overlapping materials, a background mesh is fixed in space while another material is flowing through this mesh. The two processes require a two-step computational cycle. First, the Lagrangian formulation is used in which the material is deformed, following which the deformed materials are mapped back through the process of advection. Without the ALE capability, manual rezoning of the FE mesh is needed to avoid run-time error which involves pausing the calculations when the mesh becomes severely distorted, smoothing the mesh, and remapping before continuing with the calculations. The accuracy of the calculation with the

application of the ALE is generally better as compared to manual rezoning of the mesh.

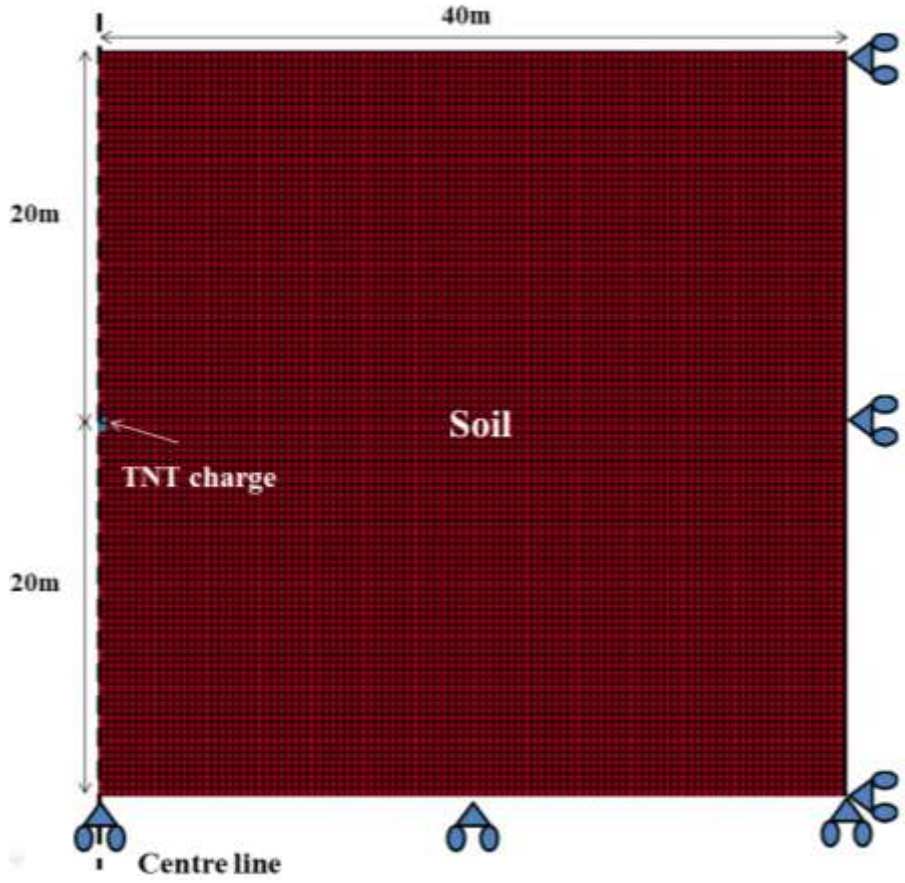

Figure 5.24 2D axisymmetric FE model

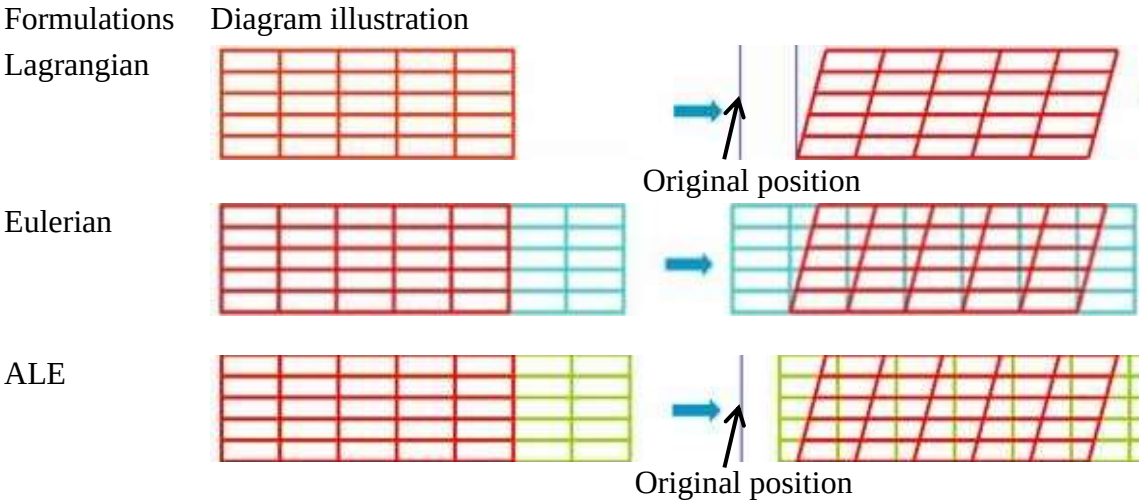

Figure 5.25 Illustration of ALE

5.3.2.3 Spurious oscillations in dynamic problem

It is well-known that numerical simulations involving dynamic problems contain high frequency noises known as spurious oscillations and simulations performed in LS-DYNA are no exception. This occurrence is due to spatial and time discretization resulting in artificial elongation and amplitude decays seen as numerical dispersion and dissipation (Diehl et al. 2000, Noh and Bath 2013, Holmes and Belytschko 1975, Noh et al. 2013, Babuska et al.1997, Chin 1975, Tedesco and Macdougal 1999). Noh and Bath (2013), Noh et al. (2013), Kuhl and Crisfield (1999) and Fung (2003) recommended the use of modified time integration scheme to dissipate high frequency spurious oscillation numerically. On the other hand, Diehl et al. (2000), Holmes and Belytschko (1975) and Idesman et al. (2009,2011) suggested the use of a low pass filter to filter off the high frequency oscillation present in the numerical solution. The post processor in LS-DYNA has capability to filter out high frequency noise. Eerden and Berg (2010), Gottlied et al. (1981), Kleinschmit (2011) and Maestas et al. (2014) reported that blast wave contains mainly low frequency content below 125 Hz.

Figure 5.26 shows the Fast Fourier Transform (FFT) of a typical pressure-time history. From the FFT shown in Figure 5.26, high frequency noises are present in the simulation signal ranging from 125 Hz to 600 Hz. Hence, it is appropriate and reasonable to retain signal with frequency ranging from 0 Hz to 125 Hz by applying a low-pass filter of 125 Hz to the signal. Figure 5.27 shows signals before and after application of filter.

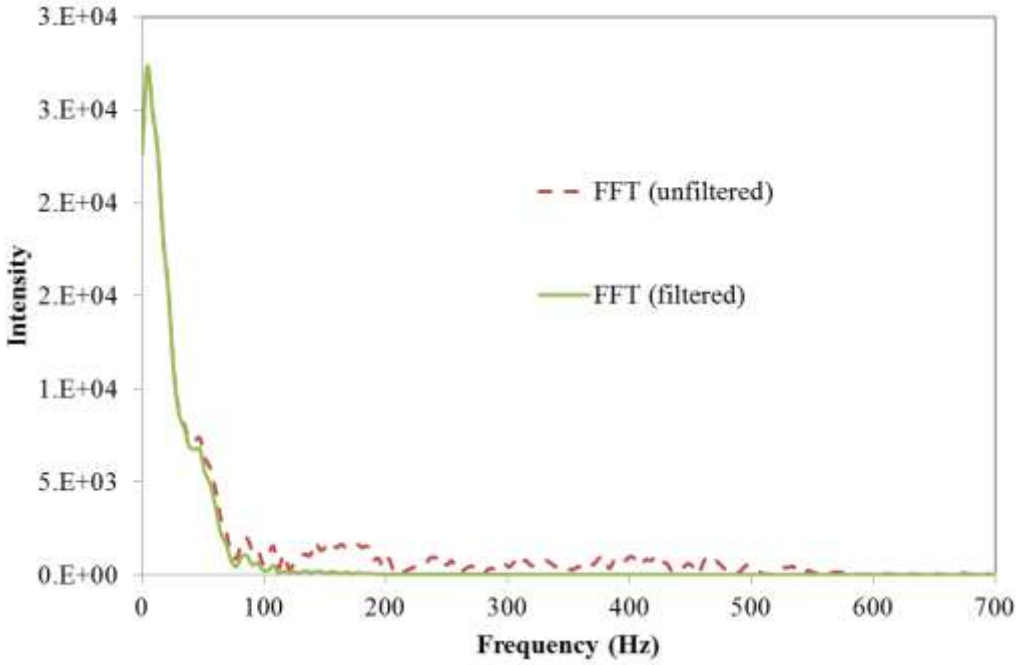

Figure 5.26 FFT of unfiltered and filtered pressure signal at 7m away from the source

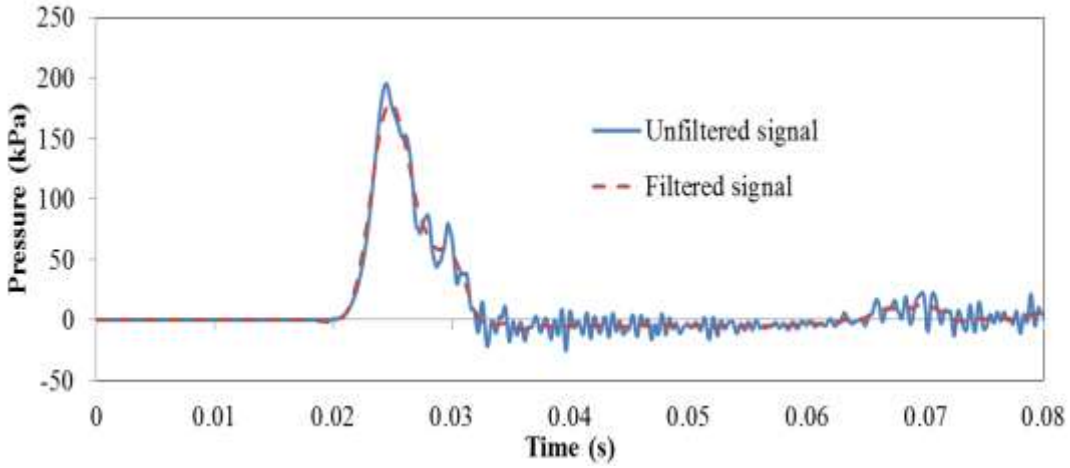

Figure 5.27 Pressure-time histories 7m away from the source

5.3.2.4 Dimensionless peak pressure versus scaled distance plot

The peak pressure plot presented in the TM5-855-1 (1986) is for different soil types and properties. Since these curves were developed from field explosion tests (Drake and Little, 1986), they were used to validate the FE model for simulating free-field response of ground shock from a contained explosion. It was hypothesized that the different soil types in the peak pressure plot is due to different degrees of saturation rather than soil type which can be simulated by varying the Poisson's ratio of the soil. Therefore, a series of FE runs were conducted with the same soil properties but with different Poisson's ratios by changing the unloading bulk modulus. The Poisson's ratio υ is related to the shear modulus and unloading bulk modulus as follows;

$$\frac{3K_{uL} - 2G}{2(3K_{uL} + G)} \tag{5.20}$$

where K_{uL} is the unloading bulk modulus and G is the shear modulus.

Table 5.9 summarises the soil properties that were input into MAT_005 in LS-DYNA. To show that the peak pressure obtained is not unique to the input soil properties in Table 5.9, another series of FE runs (series 2) were performed for soils with different shear moduli and bulk moduli while maintaining the Poisson's ratio. For the purpose of illustration, simulations on series 2 will only include input soil properties of Poison's ratios of 0.3 and 0.499 as shown inn Table 5.10.

It was also found from computing the P-wave velocity from the results that the input bulk modulus in the MAT_005 should be the unloading bulk modulus K_{uL}. While the unloading bulk moduli were represented with one input value, the loading bulk moduli which are essentially the slope of the pressure versus volumetric strain.

Table 5.9 Soil properties for MAT_005

Poisson's ratio	0.3	0.45	0.465	0.49	0.499
Mass density (kg/m^3)	1800	1800	1800	1800	1800
Shear modulus (kPa)	1.6e4	1.6e4	1.6e4	1.6e4	1.6e4
*loading Bulk Modulus (kPa)	3.47e4	1.55e5	2.23e5	7.95e5	7.99e6
Unloading Bulk Modulus (kPa)	4.95e4	2.21e5	3.19e5	1.14e6	1.14e7
a_0 (kPa^2)	2.43e6	2.43e6	2.43e6	2.43e6	2.43e6
a_1 (kPa)	2.16e3	2.16e3	2.16e3	2.16e3	2.16e3
a_2	0.48	0.48	0.48	0.48	0.48
Pcut (kPa)	-3.9	-3.9	-3.9	-3.9	-3.9

* Represented in the form of pressure versus volumetric strain curve, As recommended by Wilson and Sibley (1962), the ratio between the loading and unloading bulk moduli is taken as 0.7

Table 5.10 Soil properties for MAT_005 (series 2)

Poisson's ratio	0.3	0.499
Mass density (kg/m^3)	1800	1800
Shear modulus (kPa)	2.0e4	2.0e4
*loading Bulk Modulus (kPa)	4.33e4	9.99e6
Unloading Bulk Modulus (kPa)	6.18e4	1.42e7
a_0 (kPa^2)	2.43e6	2.43e6
a_1 (kPa)	2.16e3	2.16e3
a_2	0.48	0.48
Pcut (kPa)	-3.9	-3.9

The LS-DYNA software will automatically reset the loading bulk modulus K_L to the unloading bulk modulus K_{uL} if K_L exceeds K_{uL}. The input strength parameters is found to govern the size of the plastic zone and has insignificant effect on the elastic zone. Hence, reasonable values of c' = 1.3 kPa and $\phi' = 28^0$ were used to calculate the a_0, a_1 and a_2 coefficients. Based on the charge weight used and the radial distances of interest, the FE results showed no significant effect of c' and ϕ' on the

dimensionless peak pressure versus scaled distance plot as the radial distances of interest falls outside the plastic zone. A typical pressure-time history at a radial distance of 25 m and Poisson's ratio υ of 0.45 is shown in Figure 5.28. More results are shown in Appendix A. The Poisson's ratios to match the soil types in TM5-855-1 (1986) are shown in Figure 5.29. The Poisson's ratios to match the soil types in TM5-855-1 (1986) for series 2 are shown in Figure 5.30.

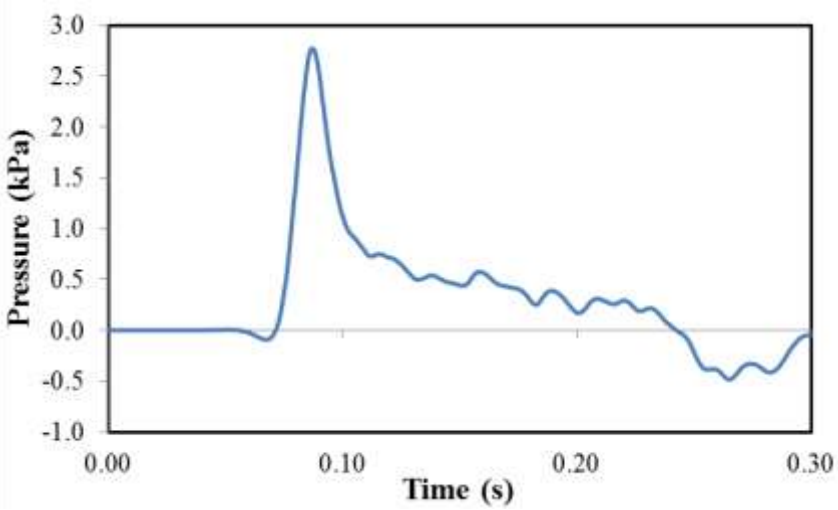

Figure 5.28 Pressure-time histories at a radial distance of 25 m and Poisson's ratio υ of 0.45

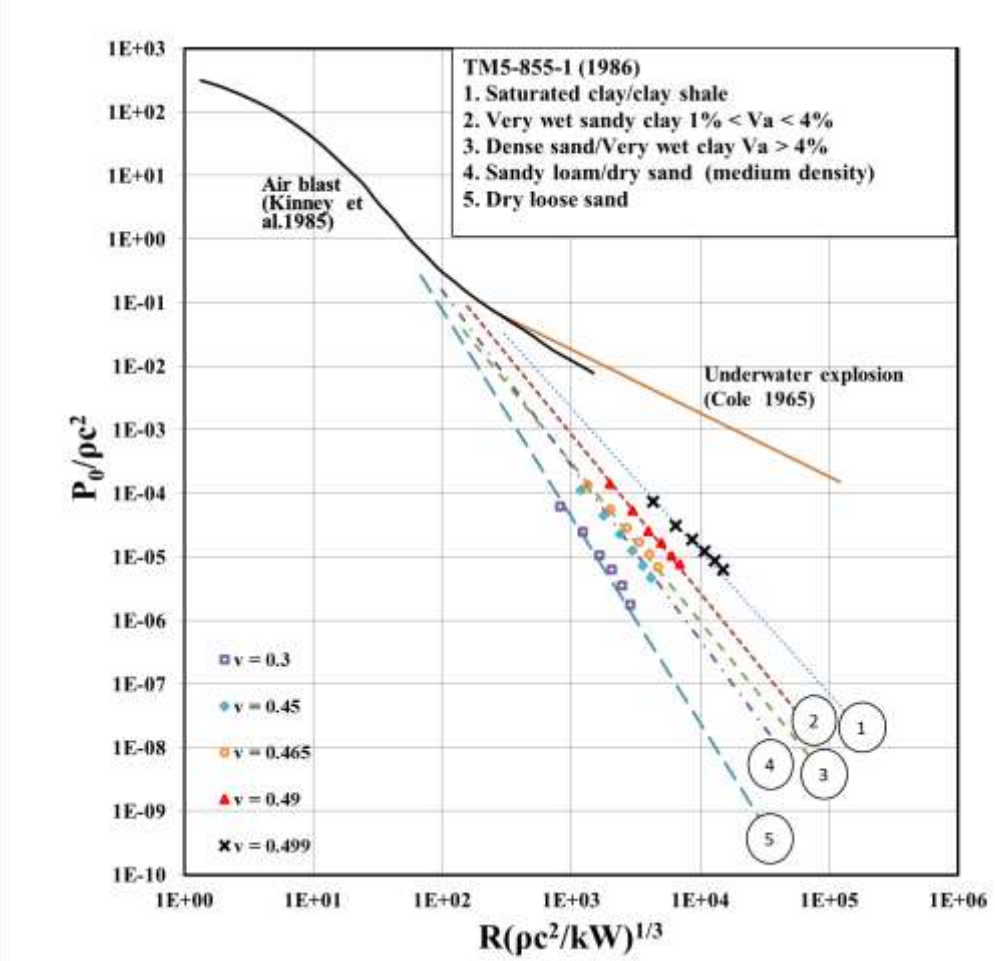

Figure 5.29 Calibration of FE model by varying Poisson's ratio on the dimensionless peak pressure versus scaled distance plot

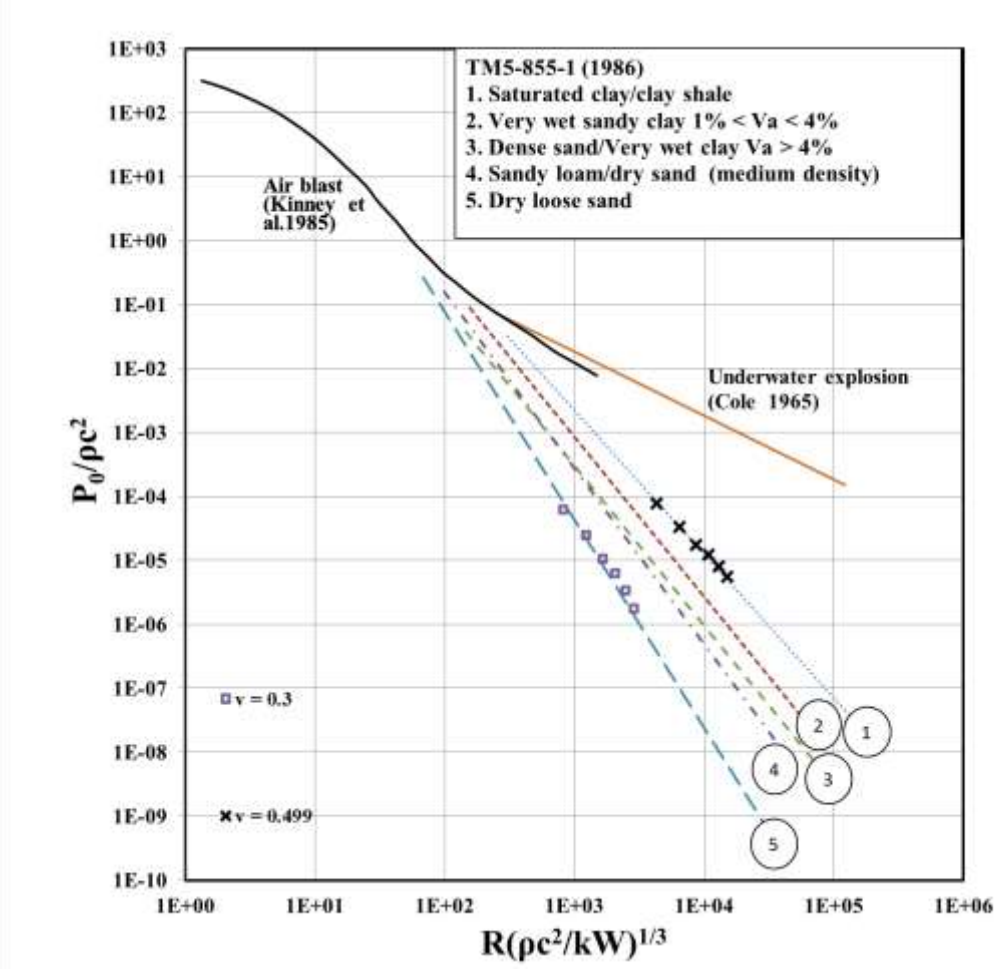

Figure 5.30 Calibration of FE model by varying Poisson's ratio on the dimensionless peak pressure versus scaled distance plot for series 2

5.4 Crater dimension study

As the coupling factor between the explosion and soil depends on the depth of buried charge, it is important to check that should crater be formed, the correct energy is transmitted to the ground. The previous section focuses mainly on effects of buried explosion in the elastic region of the soil. For completeness, the immediate zone in which the explosion occurs should be investigated. In TM5-855-1 (1986), plot of apparent crater diameter and depth curves for various soil types (clay, sand and mixed soils) are presented. The curves were proposed by Lampson (1946) using wartime experiments for the National Research and Development Committee in U.S.A and

were later incorporated into TM5-855-1 (1986). This section examines crater and camouflet formations due to buried explosions. In TM5-855-1 (1986), full coupling between explosion and ground is assumed when the scaled depth of buried charge is 1.4 ft/lb$^{1/3}$. However, the correct condition for full coupling is when a camouflet is formed.

5.4.1 Evaluation of TM5-855-1 (1986) crater curves

To evaluate the apparent crater diameter and depth curves provided in TM5-855-1 (1986), crater data (Table 5.11) were gathered from extant literature not used in TM5-855-1 (1986). The data are plotted onto TM5-855-1 (1986) crater curves. The plot contains both the ordinate (diameter and depth) and abscissa (depth of buried charge) using dimensionless scaled length as proposed by Leong et al. (2006) for scaled distance as shown in Figures 5.31 and 5.32. Only data for dimensionless scaled depth of charge from -0.5 to 4.5 are plotted. From the plot, the data which falls within the correct soil types band is counted as "within zone". Table 5.12 shows the percentage of data that fall within the zone for crater diameter and depth. The percentage of 'within zone' ranged from 73 to 100% for crater diameter and 64 to 100% for crater depth. Having a relatively high 'within zone' percentage shows that TM5-855-1 (1986) curves are still valid and applicable to estimate the crater dimensions with reasonable accuracy. According to the literature (Nuclear Geoplosics sourcebook, 1979; TM5-855-1, 1986; Bull and Woodford, 1988), there can be up to 40% differences in field test data with similar soil condition which are attributed error in measurement or inhomogeneous in-situ soil conditions.

Table 5.11 Field test data information

Author/Source	Test name/series	Medium
Busch et al. (2015)	Series A	Silty Clay
Busch et al. (2015)	Series C	Silty Clay
Wang et al. (2016)	Series E	Wet sand
Ambrosini et al. (2002)	Series A	Mixed soil
Ambrosini et al. (2002)	Series B	Mixed soil
Ambrosini et al. (2002)	Series C	Mixed soil
Schmidt and Housen (1987)	Series QX	Sand
Schoutens (1979)	Dugway	Dry sand
Schoutens (1979)	Dugway	Dry clay
Schoutens (1979)	Dugway	Wet clay
Schoutens (1979)	Sandia Lab	Alluvium

Table 5.12 'Within zone' diameter and depth for different soil type

Soil type	Within zone diameter (%)	Within zone depth (%)
Clay	78 - 80	66 - 80
Mixed soil	80 - 90	87 - 100
Sand	73 - 100	64 - 100

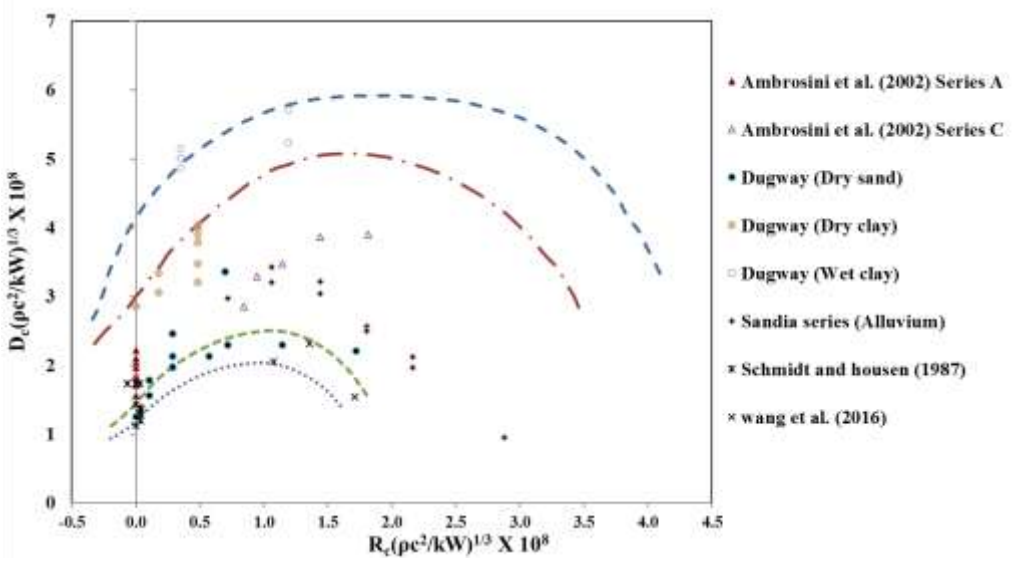

Figure 5.31 Literature field crater diameter plotted on TM5-855-1 (1986) crater diameter curves

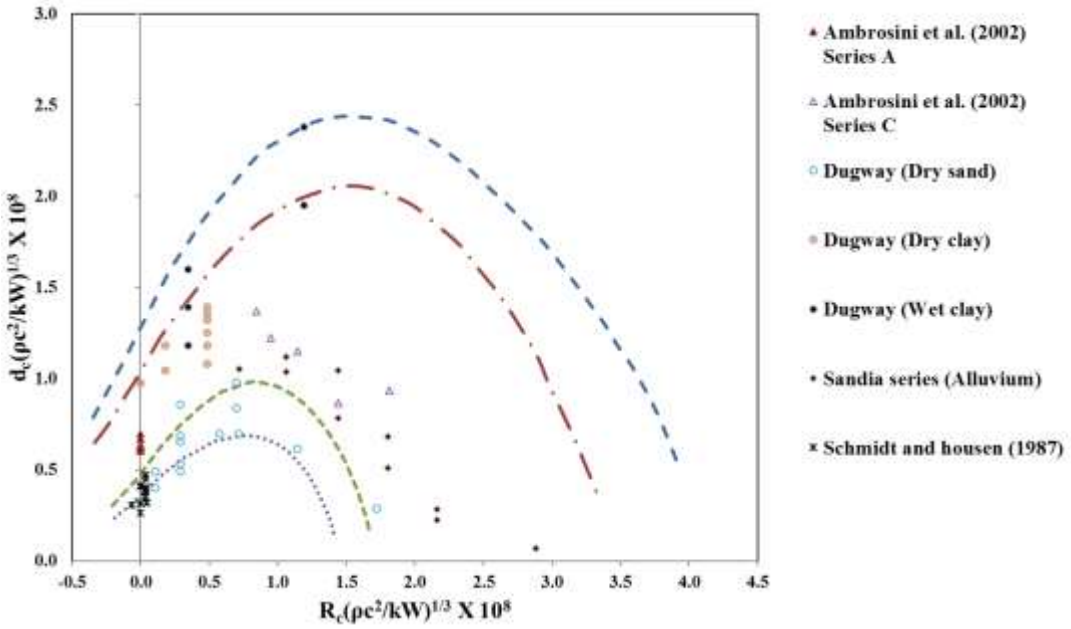

Figure 5.32 Literature field crater depth plotted on TM5-855-1 (1986) crater depth curves

5.4.2 Finite element (FE) simulation of crater and camouflet formations

In this study, crater and camouflet formations due to a buried charge was modelled as a two-dimension (2D) axisymmetric problem with the charge at the axis of symmetry. To study the effect of depth of buried charge on the crater dimensions, the charge was placed at, above and below the ground surface along the axis of symmetry such that the dimensionless depth of buried charge varies from -0.5 to 4.5. To keep the run time short, charge weight of 81.9g of TNT was used in all the runs. For this charge weight, the range of scaled depth of burial from -0.5 to 4.5 is achieved for depth of buried charge from 0.08m above the ground surface to 0.7m below the ground surface, thus reducing the size of the FE mesh and run time.

The material models used to simulate the soil, air and explosive are MAT_005, MAT_009 and MAT_008, respectively, as in Section 5.3.3. The upper and lower bounds for the sand and the clay curves from TM 5-855-1 (1986) can be simulated with reasonable soil shear strength properties in LS-DYNA. A typical range of friction angle for sand is 30^0 for loose sand and 45^0 for dense sand. A typical range of undrained shear strength for clay ranges from 10 to 100 kPa. It is well known that the shear strength of soil under high loading rate increases under dynamic loading. The friction angle of sand is expected to increase by 1 to 2^0 while the undrained shear strength of clay increases by 1.4 times (Das and Luo, 2016). The soil properties that are used to replicate the bounds of the crater curves in TM5-855-1 (1986) are shown in Table 5.13. From the numerical simulations of Charwick et al. (1964), Ambrosini et al. (2004) and Fiserova (2006), it is suggested that the crater dimension is dependent largely on the change in soil strength parameter and is insensitive to changes in elastic soil properties such as density, seismic velocity and Poisson's ratio.

Table 5.13 Input soil parameters

Parameters	Sand lower bound	Sand upper bound	Clay lower bound	Clay upper bound
Density (kg/m^3)	1800	1800	1800	1800
Seismic velocity (m/s)	176	176	230	230
Poisson's ratio	0.3	0.3	0.4	0.4
Cohesion (kPa)	0	0	200	15
Friction angle (degree)	45	30	0	0

5.4.3 FE results

Figure 5.33a shows a crater formed with a dimensionless buried charge depth of 0.58 and Poisson's ratio of 0.3 for the soil (sand bound) at t = 0.35 s. While Figure 5.33b shows a camouflet formed with a dimensionless buried charge depth of 4.06 and

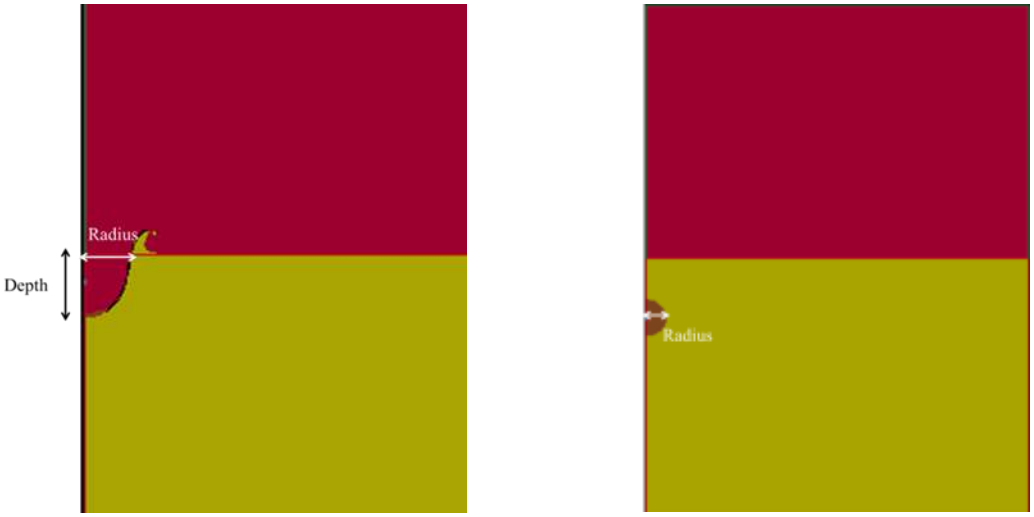

a) Crater b) Camouflet

Figure 5.33 Crater and camouflet formation

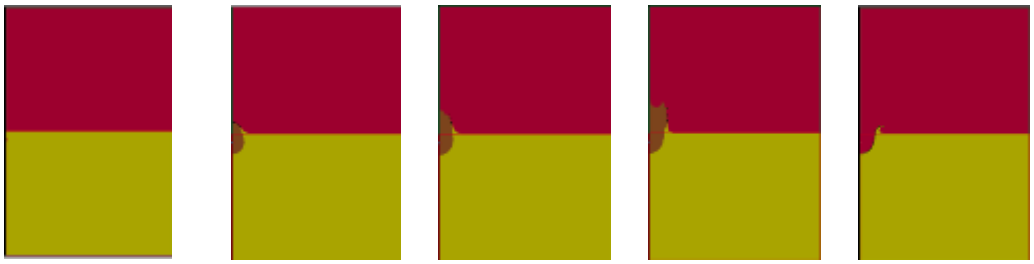

a) Crater formations

a) Camouflet formations

t = 0s t = 0.05s t = 0.1s t = 0.2s t = 0.35s

Figure 5.34 Crater and camouflet formations at different time instances

Poisson's ratio of 0.3 for the same soil at t = 0.35 s. Figure 5.34 shows the formations of crater and camouflet at different time instances for the cases illustrated in Figure 5.33. Figure 5.34a shows how the explosive was initially set off, pushing against the

top soil and eventually bursting out through the ground surface forming a crater while Figure 5.34b shows that the explosive did not breach through the ground surface and results in a camouflet formation.

5.4.4 TM5-855-1 curve fitting

The FE results for sand and clay soils for crater diameter and depth are shown in Figures 5.35 and 5.36, respectively. LS-DYNA is unable to simulate the fall back of the ejecta into the crater. Hence, the crater depth from FE simulations increases as the depth of buried charge increases as shown in Figure 5.36. This is well known as can be seen in Ambrosini et al. (2002). Thus, the crater obtained from FE simulation in LS-DYNA can be treated as the "true" crater. As the FE model is 2D axisymmetric, to obtain the volume of the "true" crater, area of the "true" crater must first be computed. The area of the "true" crater by counting the number of element "occupied" by the crater. Attempt to estimate the volume of the "true" crater using a half ellipsoid function was carried out. A comparison of the two methods as illustrated in Figure 5.37 and is presented in Table 5.15. Table 5.15 shows that the error is less than 5% for the three cases. Therefore, "true" crater from FE simulations can be idealised as a half ellipsoid described using the equation below.

$$\frac{x^2}{a'^2} + \frac{y^2}{b'^2} + \frac{z^2}{c'^2} = 1 \tag{5.21}$$

where x, y and z are the coordinates, a', b' and c' indicate the half major and half, minor axis length of the ellipsoid. Comparing the apparent crater depth d_c' given in TM5-855-1 (1986) and true crater depth d_c as shown in Figure 5.38, shows that the fall back of the ejecta occurs only when dimensionless depth of buried charge is greater than 0.5 x 10^8.

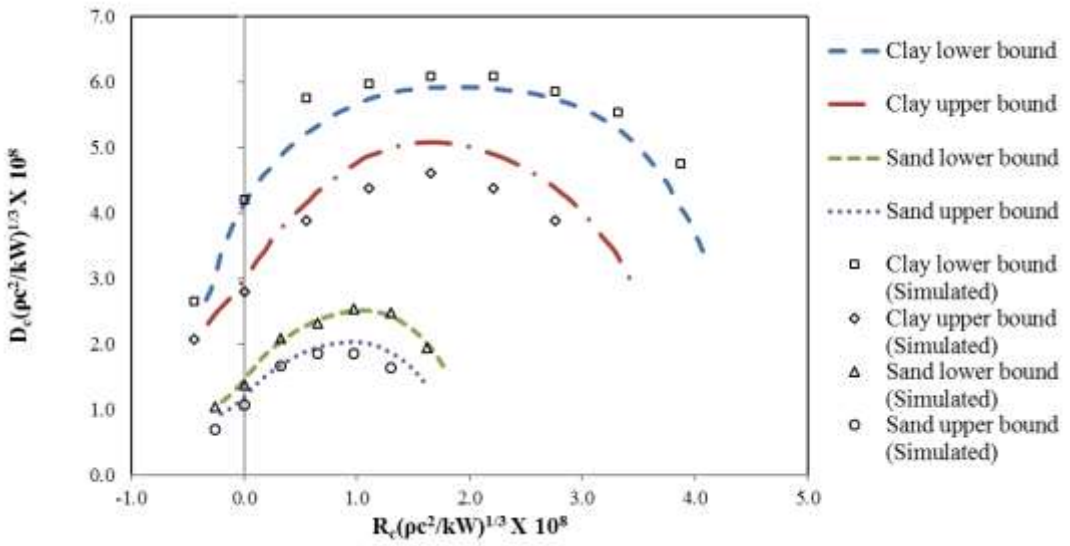

Figure 5.35 Simulated scaled crater diameters on TM5-855-1 (1986) crater diameter

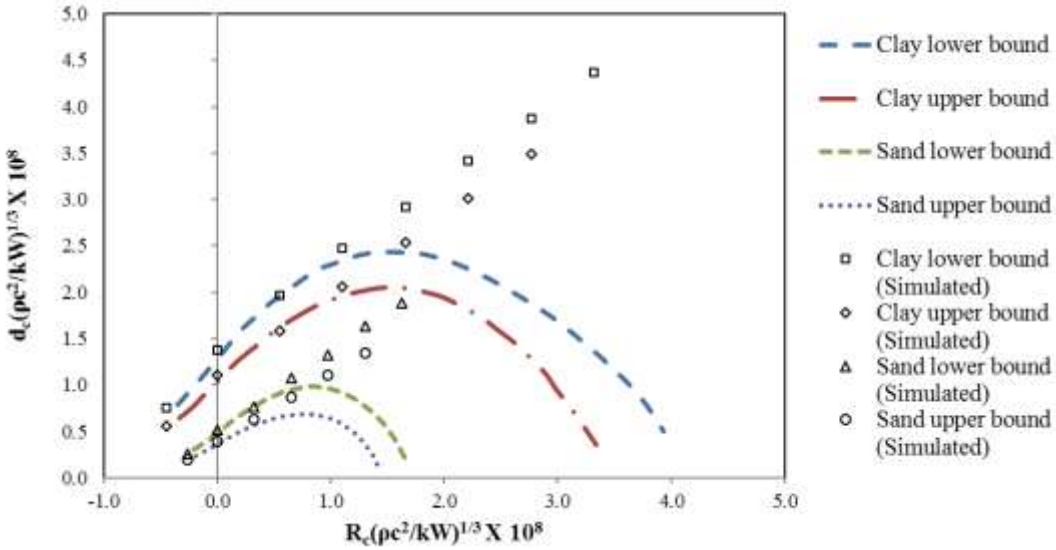

curves

Figure 5.36 Simulated scaled crater depth on TM5-855-1 (1986) crater depth curves

Table 5.14 Equations that can be used to estimate the true crater depth

Soil boundaries	**Equation**
Sand lower bound	$y = 0.931x + 1.345$
Sand upper bound	$y = 0.894x + 1.044$
Clay lower bound	$y = 0.860x + 0.500$
Clay upper bound	$y = 0.736x + 0.389$

*Where $y = d_c(\rho c^2/kw)^{1/3}$ and $x = R_c(\rho c^2/kw)^{1/3}$

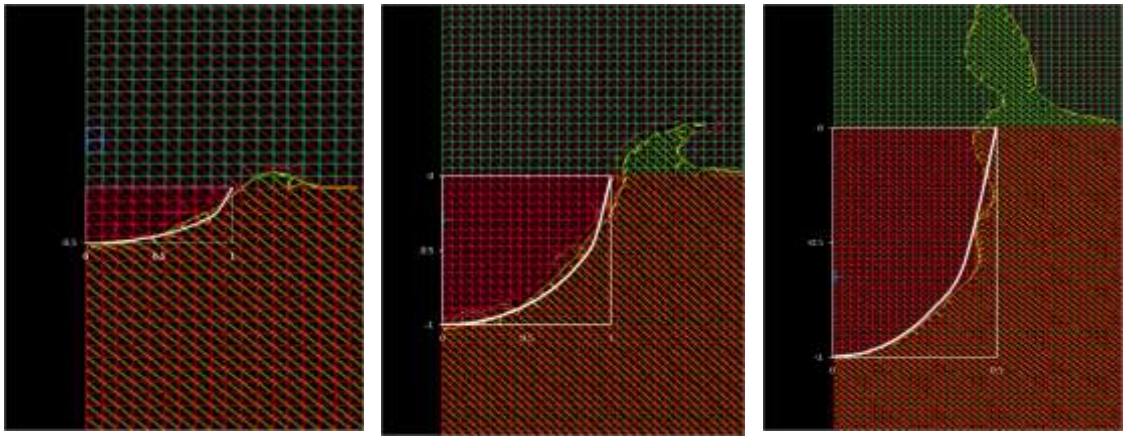

$R_c/W^{1/3} = -0.4645$ $R_c/W^{1/3} = 0.5876$ $R_c/W^{1/3} = 2.9031$

Figure 5.37 Crater formed at different scaled depth fitted with the ellipsoidal function

Table 5.15 Comparison study on the method of volume calculation

$R/W^{1/3}$	Counted area (m^2)	Estimated area (m^2)	Error (%)
-0.4645	0.0121	0.0127	4.72
0.5876	0.0980	0.1017	3.63
2.9031	0.2332	0.2386	2.26

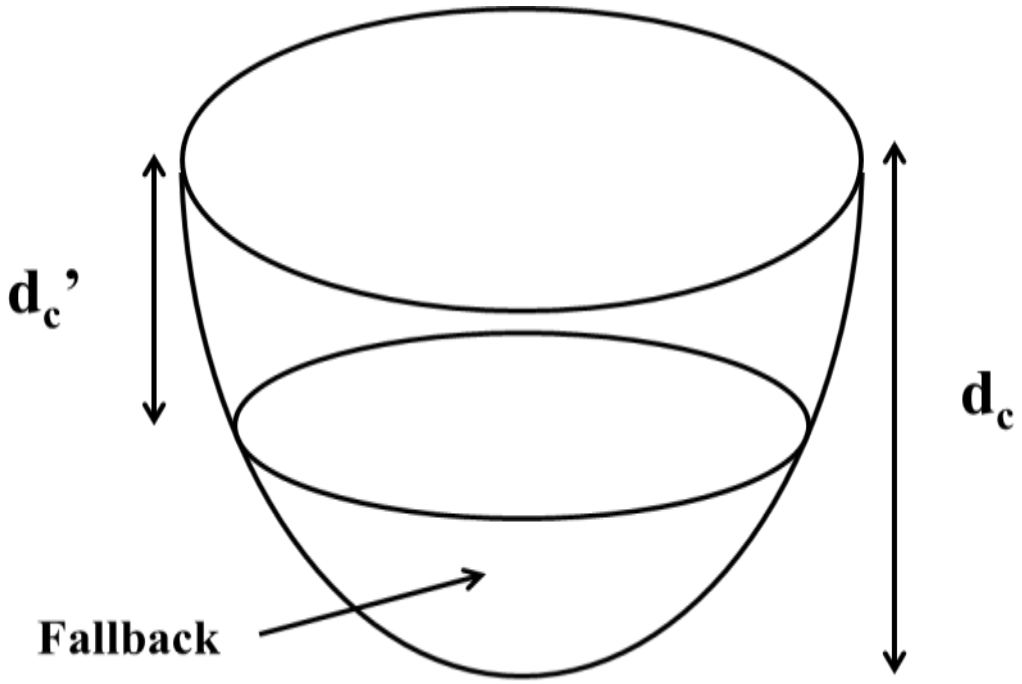

Figure 5.38 Assumption of fall back of soil into crater

5.4.5 Camouflet

As depth of buried charge increases, the energy from the explosion is insufficient to throw the material and camouflet is formed as shown in Figure 5.39. The transition from crater to camouflet formation is shown as a line of gradient $d_c/R_c = 1.0$. This transitional line indicates that any explosion occurring at $R_c > D_c$ will only result in the formation of a camouflet. Also shown in Figure 5.39, as dimensionless charge depth increases, the diameter of the camouflet only decreases slightly for the same soil type. Verification of the boundary line in Figure 5.39 using field test data and numerical simulations from the literature was performed. Anand (2007) detonated three different charge weights of plastic explosive (PETN) (4, 6 and 10 kg) (corresponding TNT equivalent of 6.84, 10.26 and 17.1 kg, respectively) at a depth of 2.5m. While charge weight of 10 kg of PETN produces a crater, charge weights of 4 and 6 kg of PETN resulted in the formation of camouflets. The soil on site was

described as coarse to medium sand with traces of silt. In this study, field tests involving 50 kg of TNT buried and detonated at 1.4m below ground level when resulted in formations of craters of 4m in diameter and 3m in depth as shown in Figure 5.40. The soil condition in the field test is sandy silt. The above data are plotted in Figure 5.41. As shown in Figure 5.41, the dimensionless scaled diameter of the crater and camouflets fall within the sand bound which fits the soil descriptions provided. A logarithmic scale is adopted for the dimensionless buried depth of charge for clarity.

Numerical simulations performed by Charwick et al. (1964) showed camouflet formation for 1 lb of TNT in clay with undrained shear strength of 137 kPa and sand with 30^0 friction angle are also plotted in Figure 5.39. From Figure 5.41, the numerical results fall accordingly within the bounds of the soil type. Similar to the discussion in the preceding paragraph, the diameter of the camouflet decreases slightly as the depth of buried charge increases.

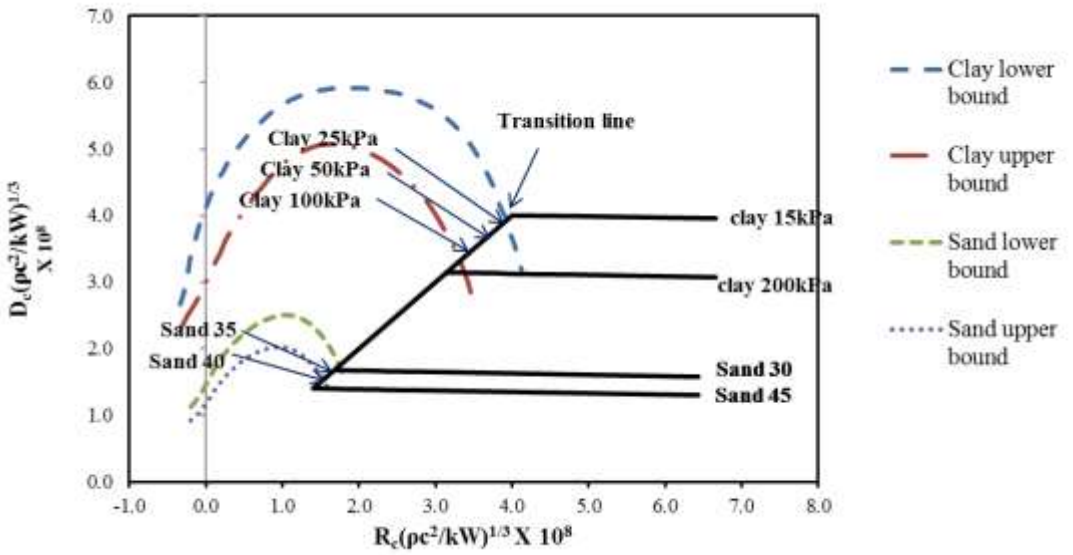

Figure 5.39 Modified TM5-855-1 (1986) crater curves

Figure 5.40 Crater formation resulted from 50kg TNT buried and detonated below 1.4m deep

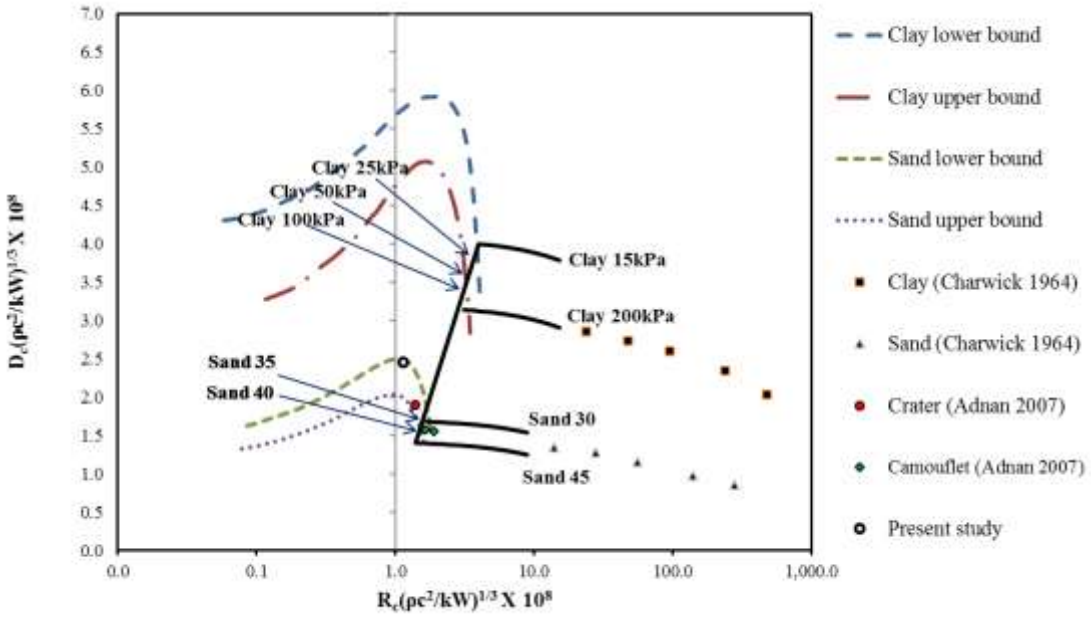

Figure 5.41 Camouflet diameter obtained from literature review and this study

5.4.6 Estimation of fall back material

The fall-back volume ΔV_c of ejecta as a ratio of the true crater volume V as well as ratio between d_c'/d_c can be estimated as shown in Figure 5.42 by assuming that the fallback occupies the bottom of the half ellipsoid as shown in Figure 5.38. In Figure 5.42, the ordinate represents the fall-back volume of soil and the abscissa represents the dimensionless depth of buried charge. Figure 5.43 shows the plot of apparent crater depth versus scaled depth of burial upon application of Figure 5.36.

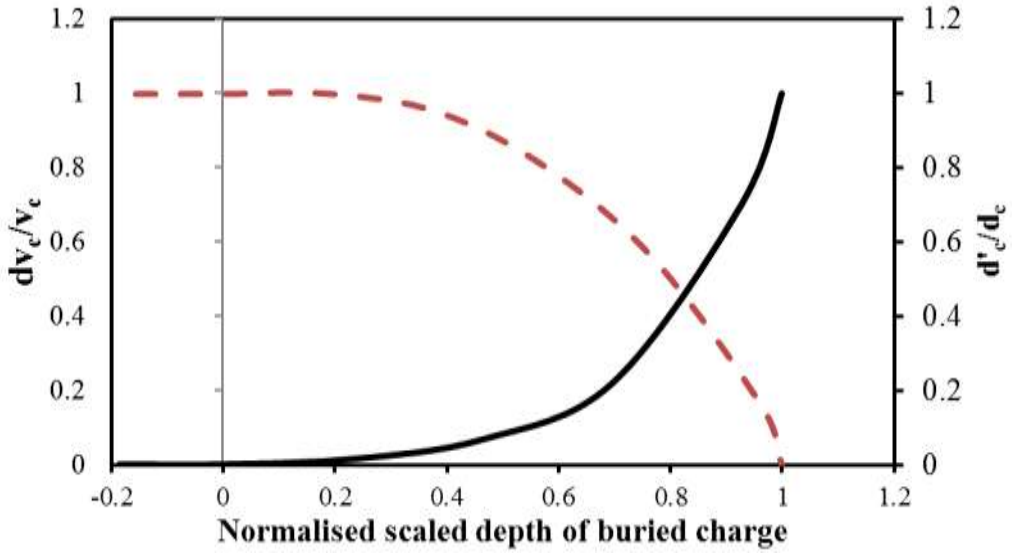

Figure 5.42 Plot of volume change in fall back material versus normalised scaled depth of buried charge

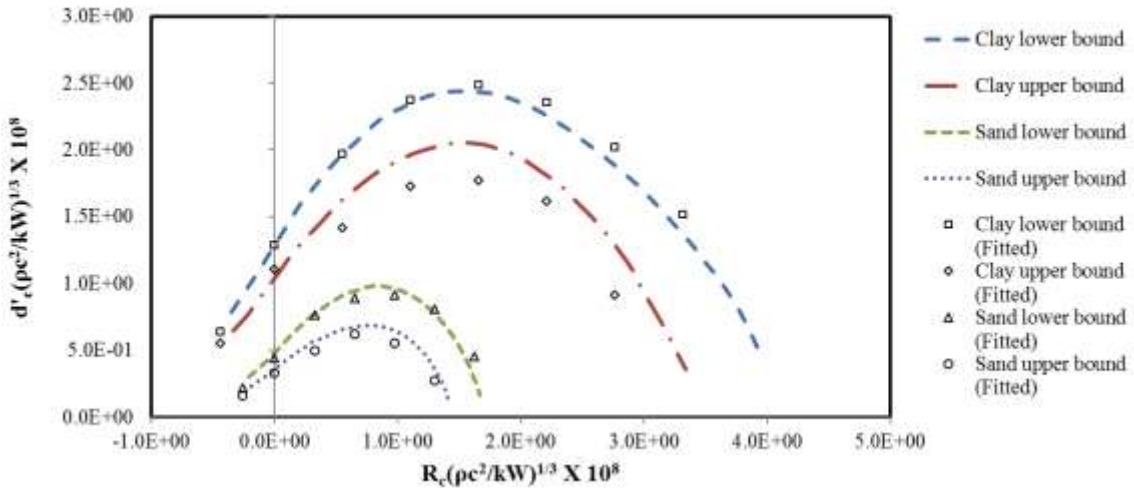

Figure 5.43 apparent crater depth versus scaled depth of buried charge

5.5 Small-scale field test simulation

As the small-scale field test cannot be simulated using a 2D axisymmetric FE model due to presence of the concrete structure, the problem was simulated using a 3D FE model. The configuration of this FE model consists of air (15m by 15m by 5m) and soil (15 m by 15 m by 10 m). A concrete structure of 0.45 m cube, buried at a depth of 1.4m below the ground surface, was surrounded by a layer of SRM which has a thickness of 0.1 m. A charge weight of 50 kg TNT, buried at a depth 1.4m, is simulated in the FE model. The FE model shown in Figure 5.44 was modelled in 3D using only a quadrant of 15 m cube. The finite element mesh consisted of 1,125,000 eight-noded solid elements with elements ranging in size starting with the smallest of 0.1m cube at the mid-section of the mesh and gradually increasing in size of 0.1m by 0.5m cuboid towards the top and bottom edge of the mesh. The nodes on the lateral boundaries of the model were constrained from lateral movements while the nodes on the bottom boundary were constrained from vertical movements. The P wave velocity, which is determined based on the travel time of the blast wave between the two RC structures, is estimated to be about 350 m/s. As explained previously, ALE

(Arbitrary-Lagrangian-Eulerian) formulation was used to perform automatic smoothing and re-zoning of the mesh throughout the simulation. The SRM barrier was simulated using MAT_005. The input properties of the SRM were as presented in Chapter 3 and are shown in Table 5.16. Table 5.17 shows comparison of field test and numerical modelling results for the corresponding sensors.

Table 5.16 Input properties for SRM

Mass density (kg/m^3)	793
Shear modulus (kPa)	8.0e2
*loading Bulk Modulus (kPa)	3.73e2
Unloading Bulk Modulus (kPa)	5.32e2
a_0 (kPa^2)	2.43e6
a_1 (kPa)	2.16e3
a_2	0.48
Pcut (kPa)	-3.9

Table 5.17 Figures and respective sensors

Figures	Sensors
5.46	P1-1
5.47	P2-7
5.48	P1-2
5.49	P2-6
5.50	A2-9
5.51	A2-10 (7m with SRM)
5.52	A1-4
5.53	A1-5 (12m w/o SRM)
5.54*	A1-3
5.55*	A1-5 (7m w/o SRM)
5.56*	A2-8
5.57*	A2-10 (12m with SRM)

* Simulated missing results

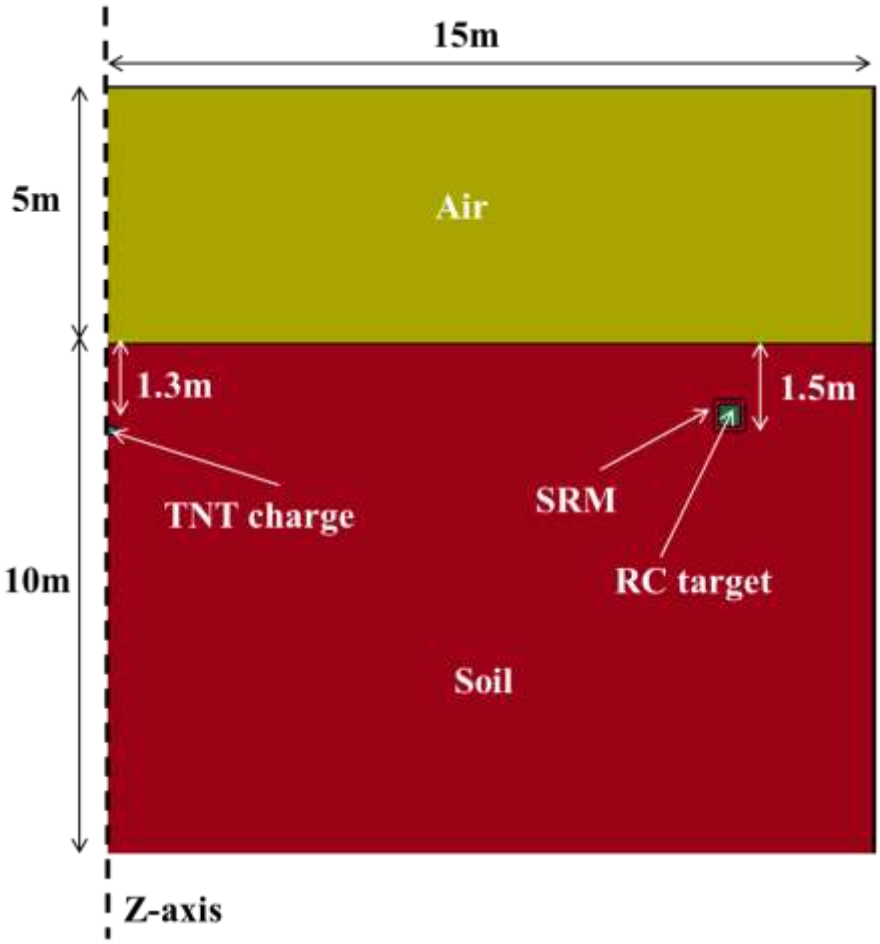

Figure 5.44 FE model for small-scale field test

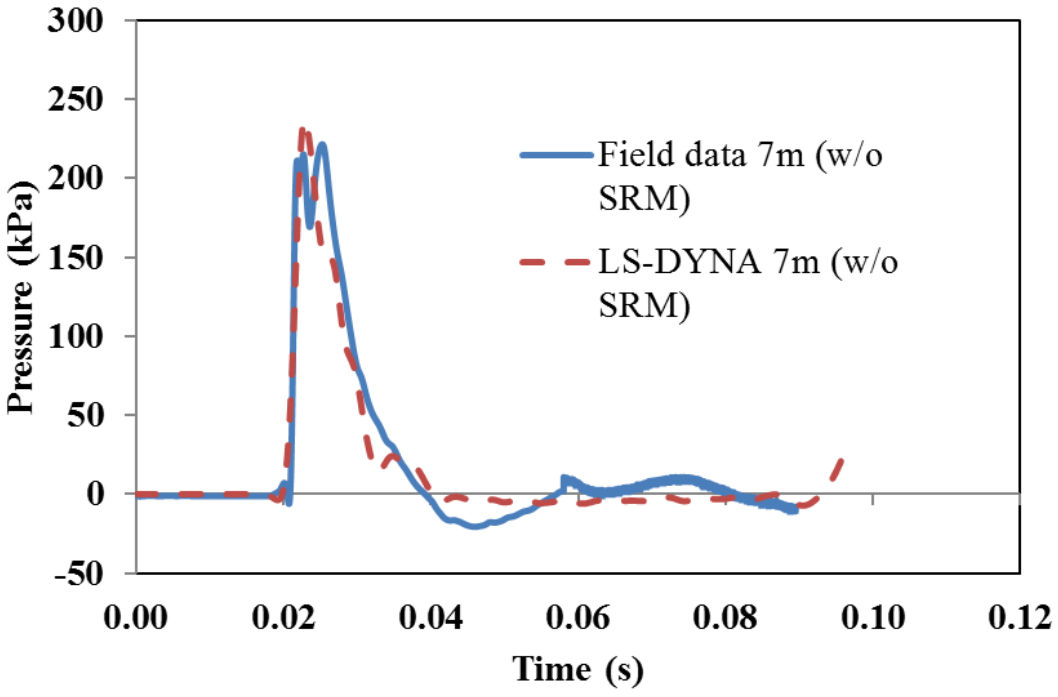

Figure 5.45 Pressure-time histories for P1-1

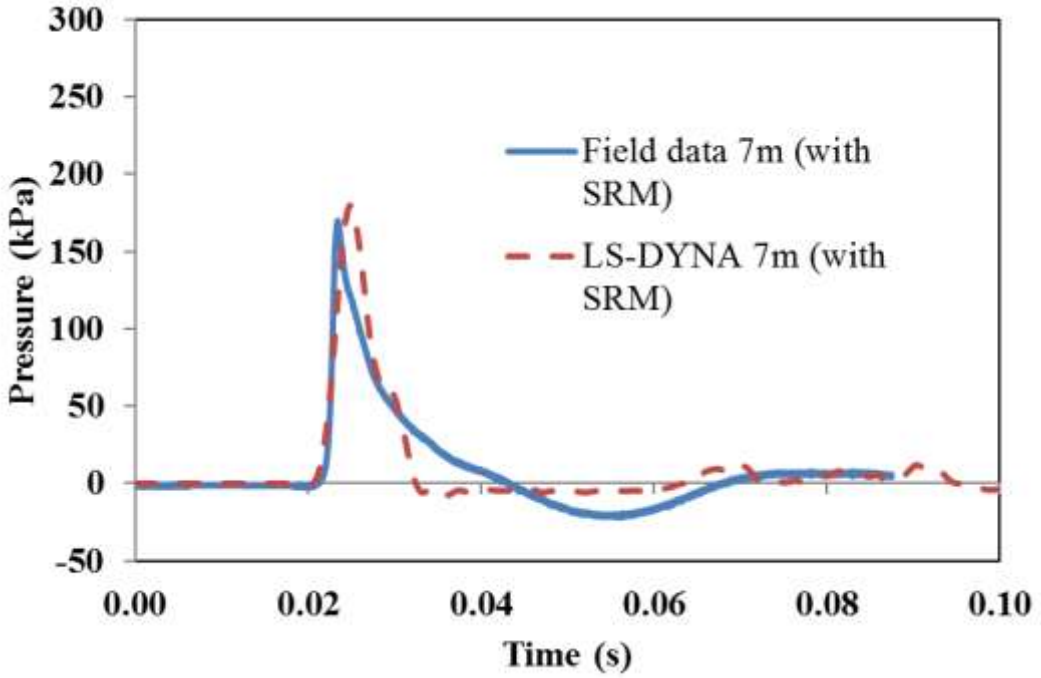

Figure 5.46 Pressure-time histories for P2-7

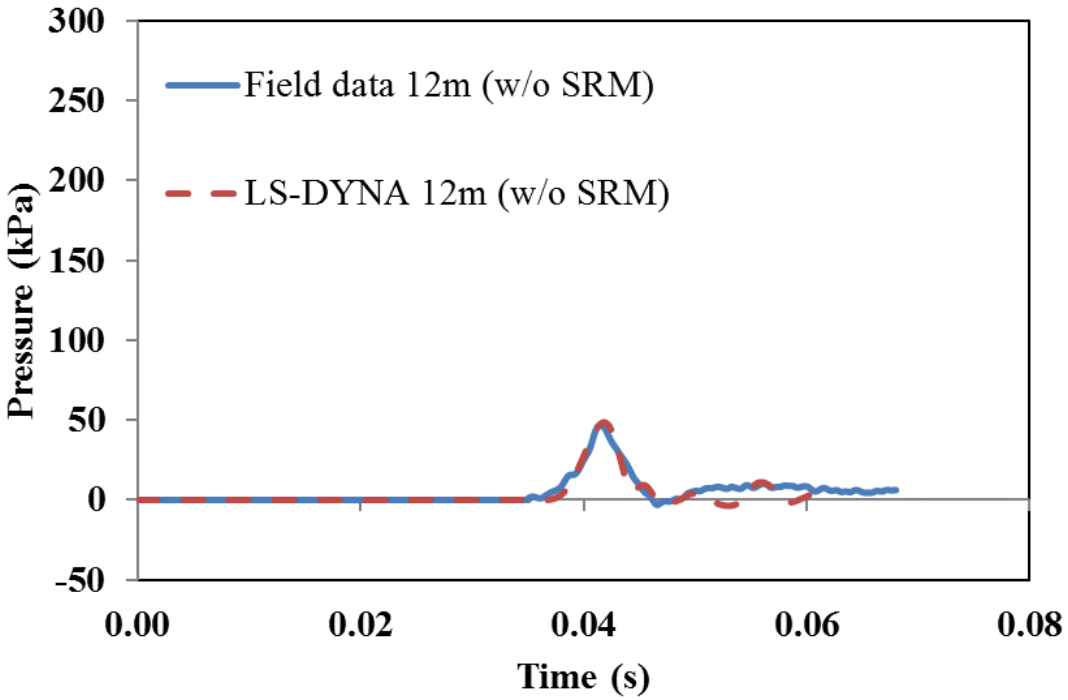

Figure 5.47 Pressure-time histories for P1-2

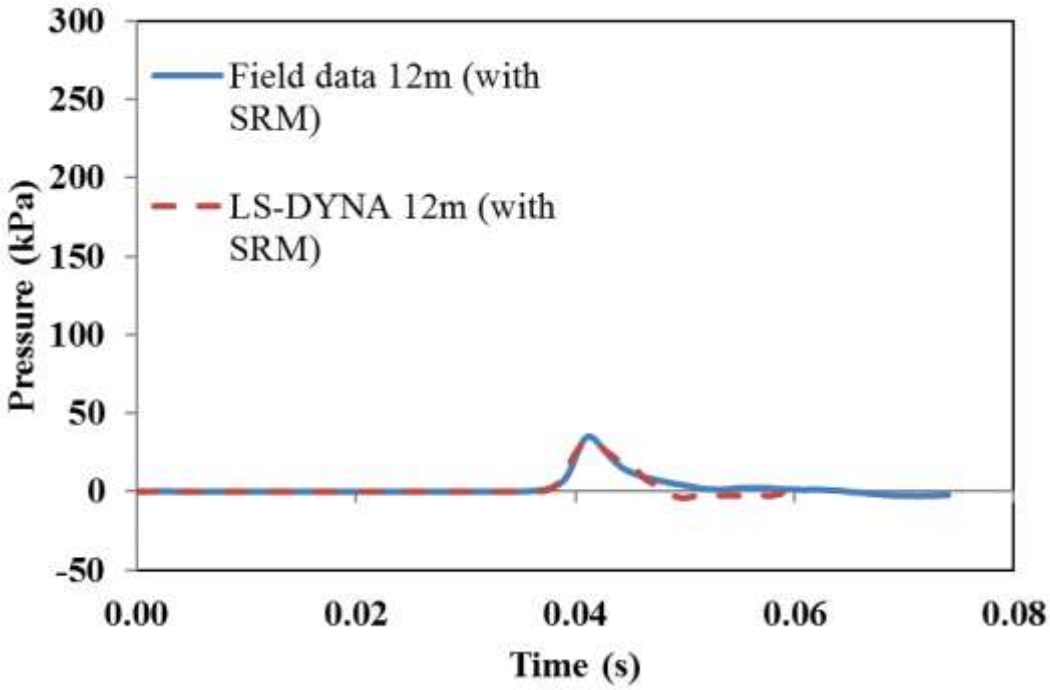

Figure 5.48 Pressure-time histories for P2-6

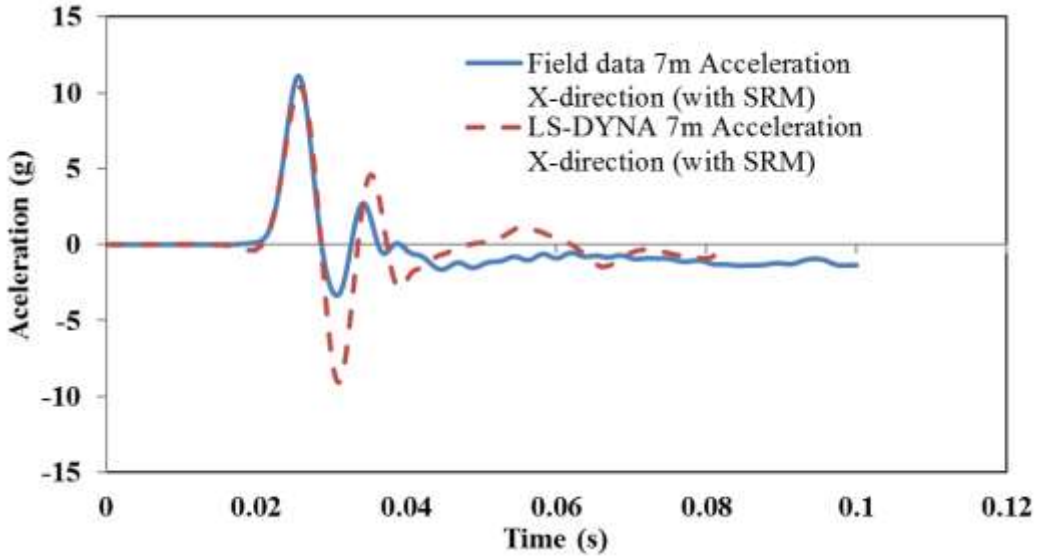

Figure 5.49 Acceleration-time histories for A2-9

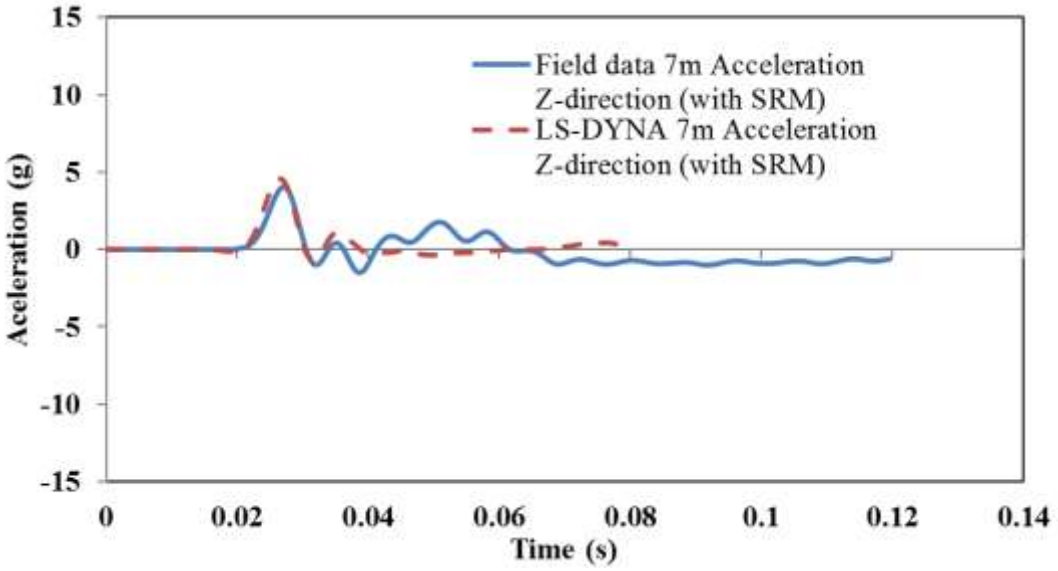

Figure 5.50 Acceleration-time histories for A2-10

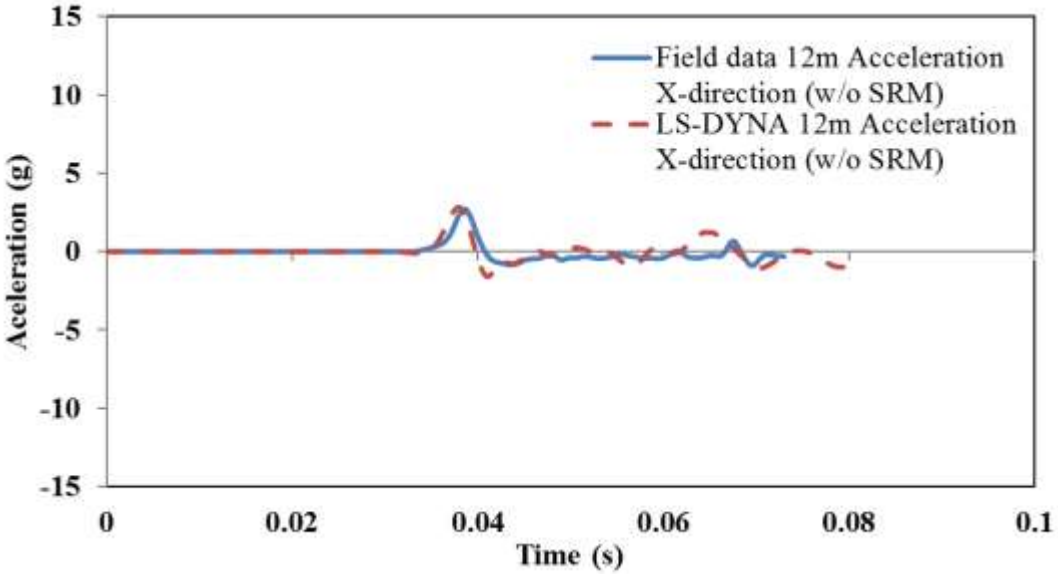

Figure 5.51 Acceleration-time histories for A1-4

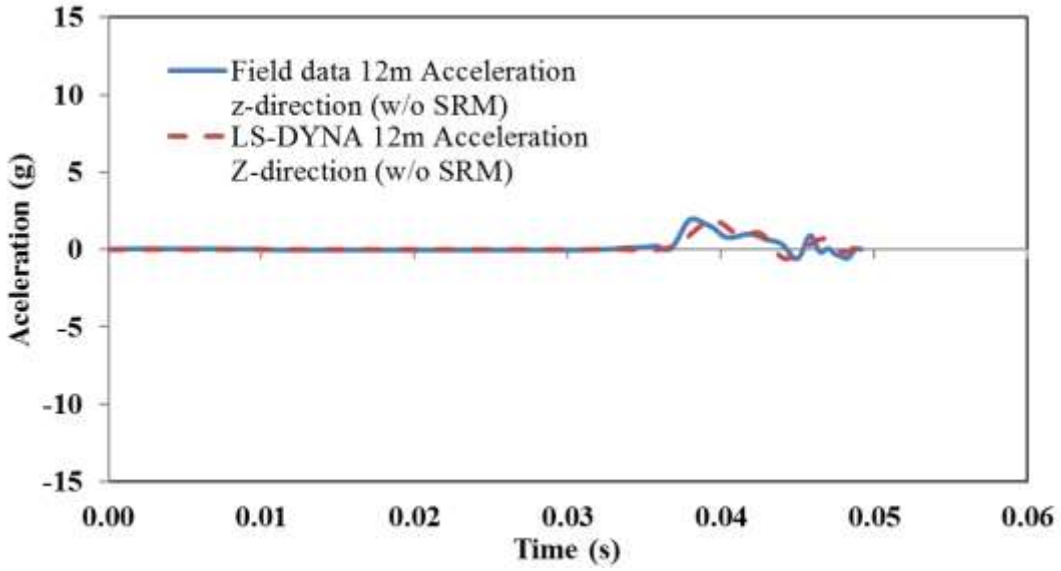

Figure 5.52 Acceleration-time histories for A1-5

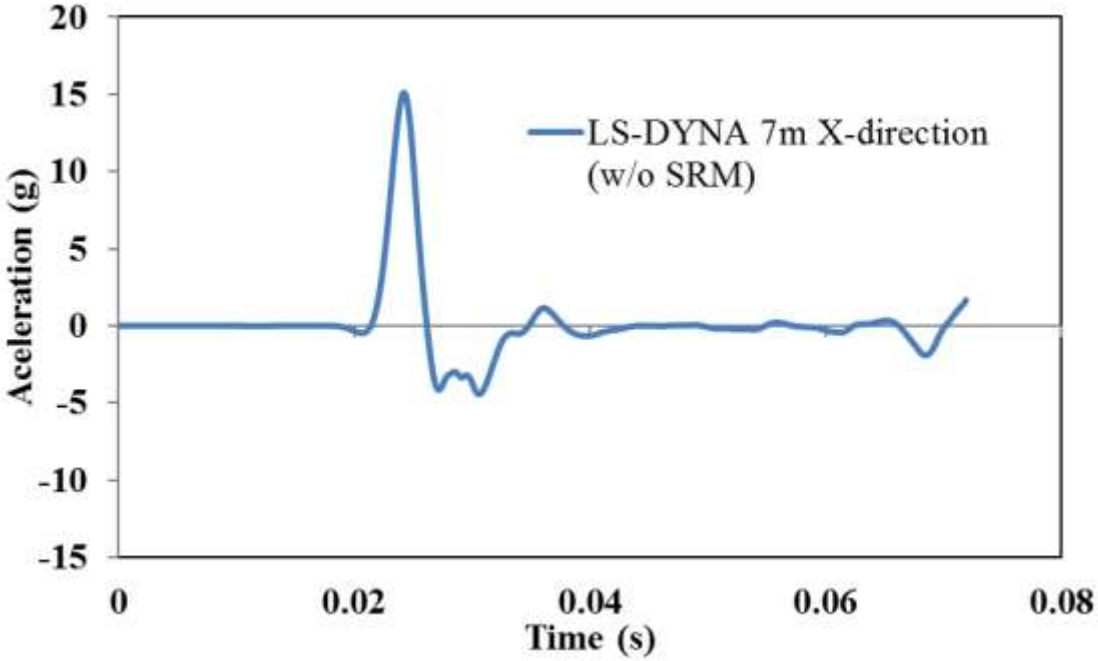

Figure 5.53 Acceleration-time histories for A1-3

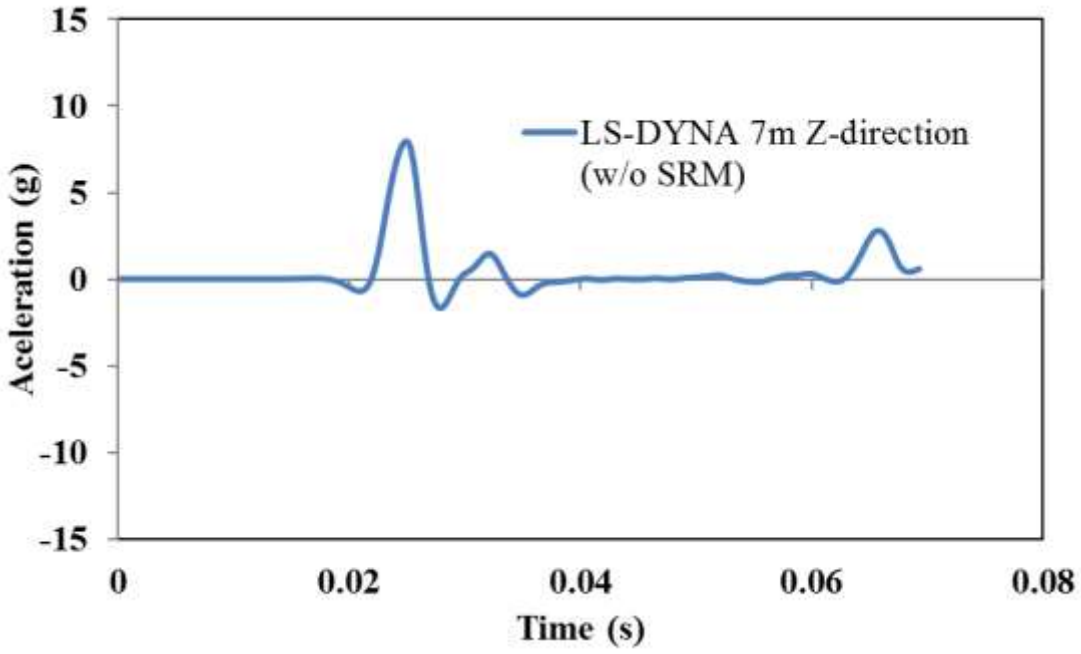

Figure 5.54 Acceleration-time histories for A1-5

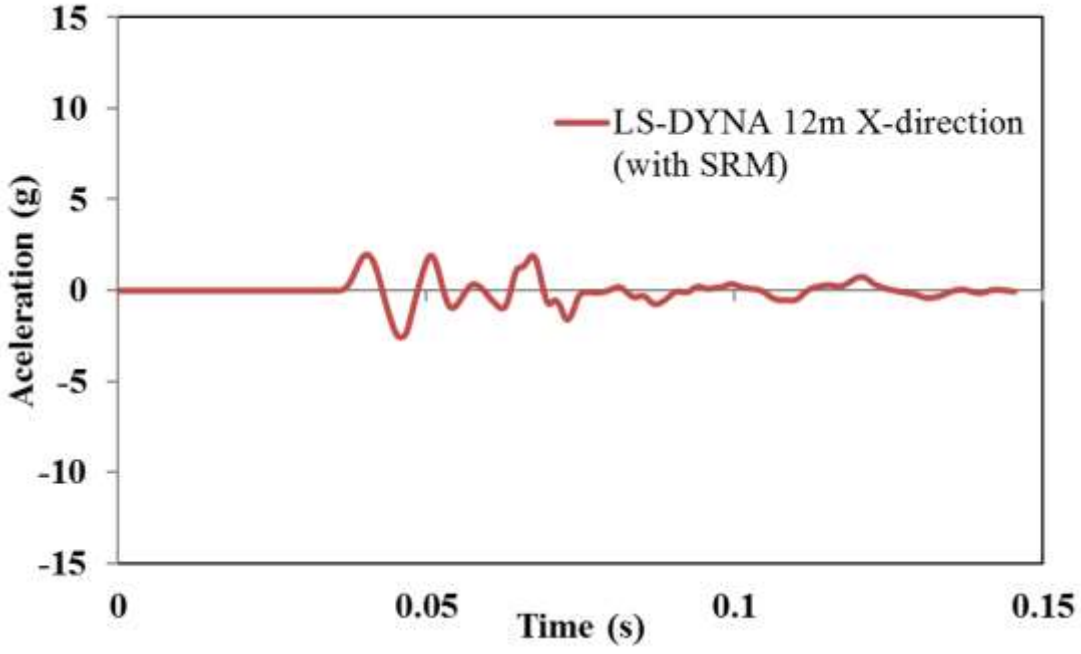

Figure 5.55 Acceleration-time histories for A2-8

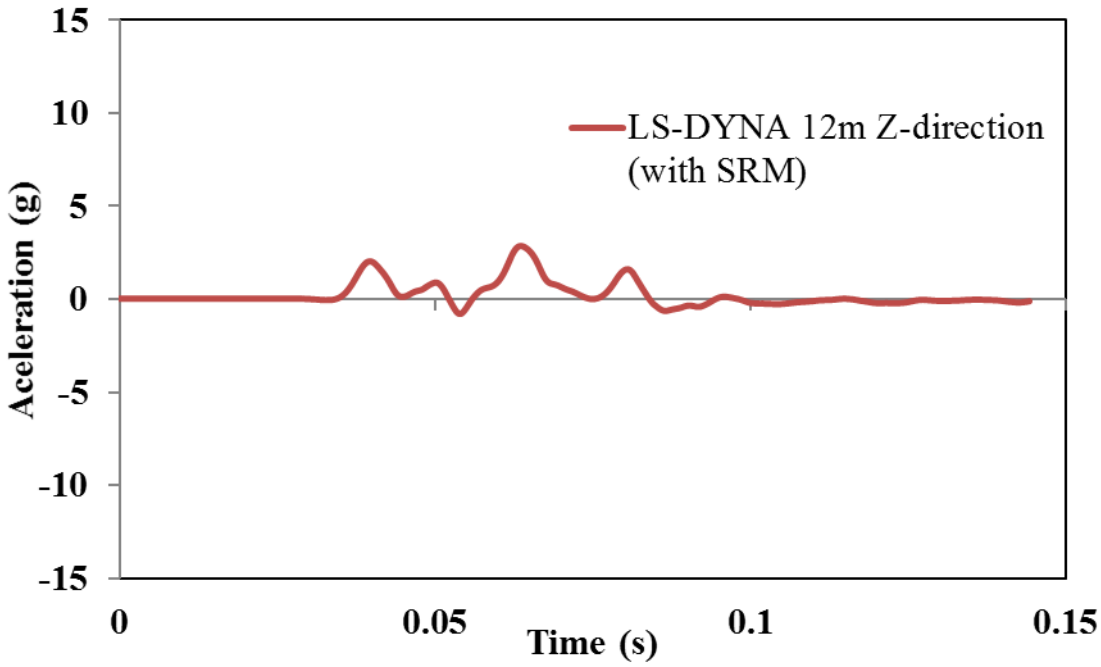

Figure 5.56 Acceleration-time histories for A2-10

Numerical results for pressure and acceleration-time histories from LS-DYNA showed a good match with field test data. This shows that the FE model is able to simulate the field tests reasonably well. The FE model can be further used to investigate effects of the density of the concrete structure relative to the density of soil. A total of three cases were simulated with concrete densities of 2400 kg/m^3, 1800 kg/m^3 and 1200 kg/m^3 positioned at 7m away from a buried charge of 50 kg TNT, 1.4m below ground level. The cases for concrete structure's density of 2400 kg/m^3, 1800 kg/m^3 and 1200 kg/m^3 are denoted as C2400, C1800 and C1200, respectively. For each of the case, two runs will be made (one with SRM and one without SRM). Table 5.18 shows the results obtained from the simulations. Figures 5.57 to 5.59 show the pressures-time history for each case.

A decrease in peak pressure is observed with decreasing concrete structure density. When comparing the reduction with and without SRM barrier (Table 5.18), the concrete structure with SRM barrier showed an increase in effectiveness. This observation is due to differences in material impedance between soil and concrete structure and inertial loading caused by the explosion. The concrete structure with higher density (heavier) will move less thus recording a higher peak pressure. On the other hand, concrete structure with lower density (lighter) will move more and thus records a lower peak pressure. This observation agrees with findings from Davis (1994) and Dongen and Weerheijm (1992).

From the observations above, it is suggested that while reducing the concrete structure's density results in further reduction in peak pressure recorded. However, reduction in density of the concrete structure has an implication on its structural strength. In light of this, the benefits of SRM for an actual of concrete structure may be higher than shown by the field tests which were conducted on a concrete block.

Table 5.18 Peak pressure and reduction from numerical runs

Cases	Density of RC structure (kg/m^3)	Peak pressure w/o SRM (kPa)	Peak pressure with SRM (kPa)	Reduction (%)
C2400	2400	234	170	28
C1800	1800	212	166	32
C1200	1200	207	160	33

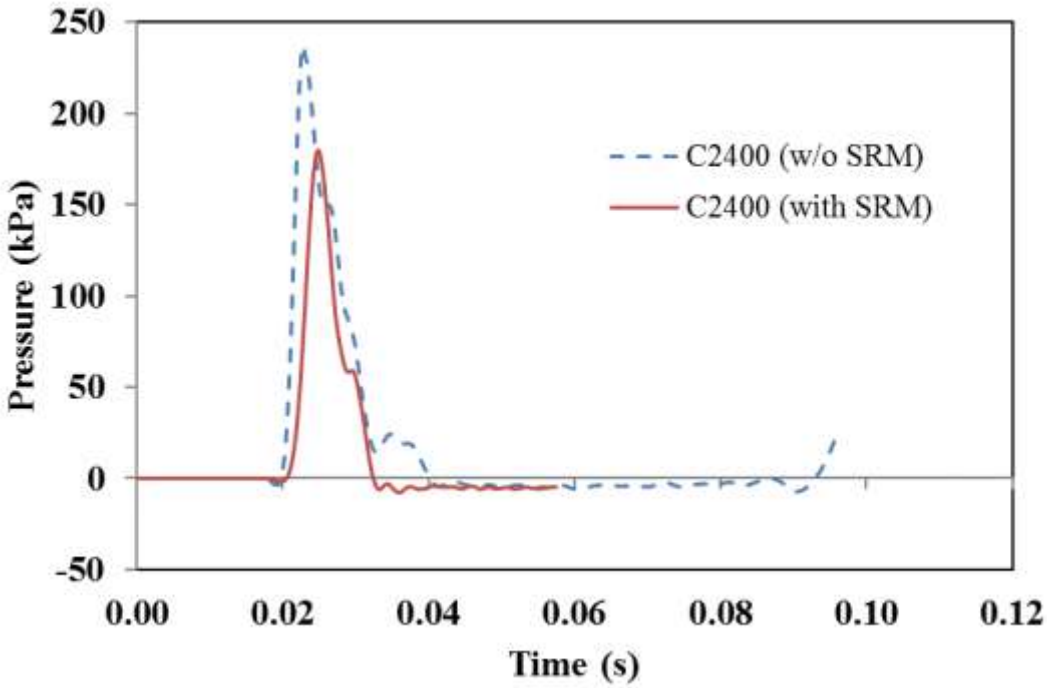

Figure 5.57 Pressure time-histories for C2400

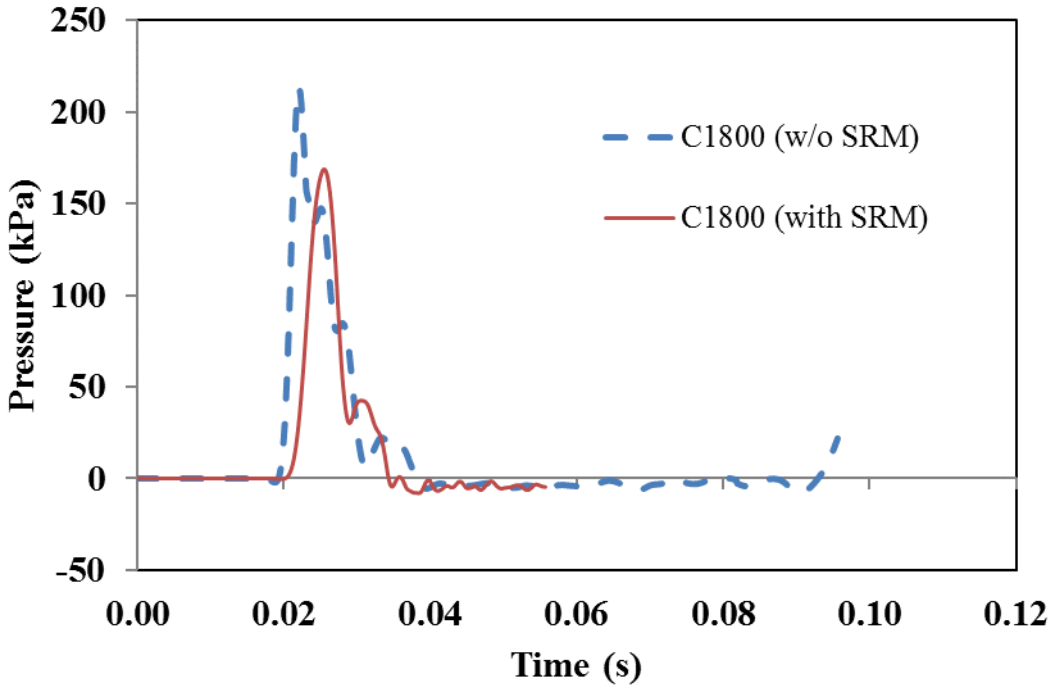

Figure 5.58 Pressure time-histories for C1800

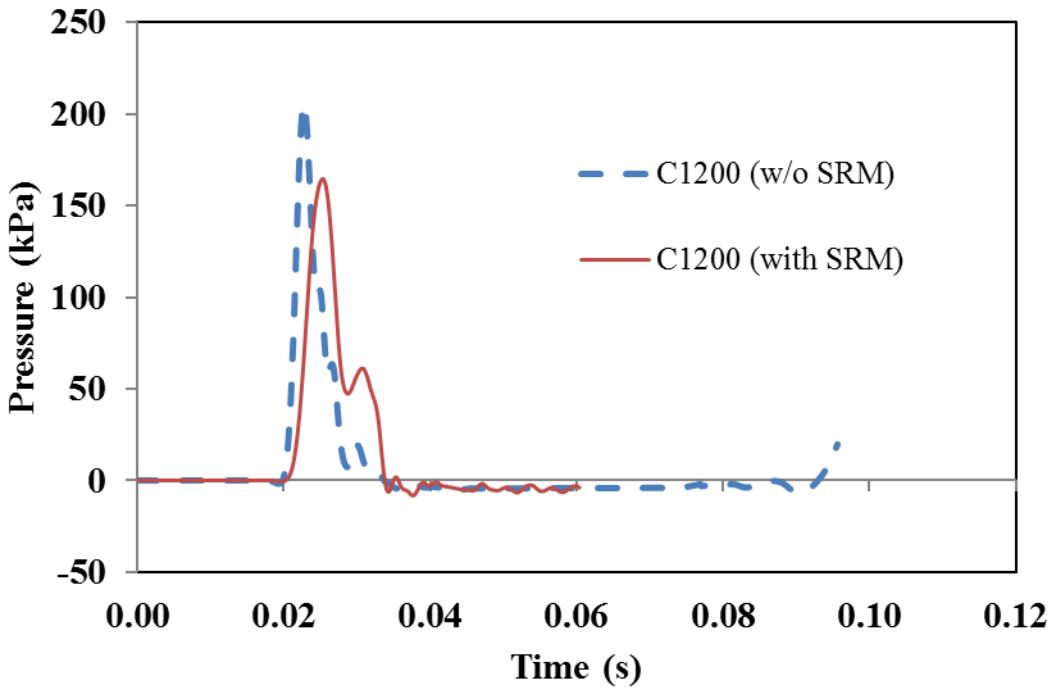

Figure 5.59 Pressure time-histories for C1200

5.6 Summary

Small-scale field tests to investigate the efficiency of SRM as seismic wave barrier in reducing ground shock from underground explosion were conducted. Two buried charges of 50 kg TNT were detonated. Pressure transducers and accelerometers were mounted on concrete structures to measure both peak pressure and accelerations for concrete structures with and without SRM. The small-scale field tests were complemented with numerical simulations using LS-DYNA. Prior to simulation of the field test, the finite element model in LS-DYNA was verified using the peak pressure and crater curves from TM5-855-1 (1986). The following conclusions can be drawn:

1. The field test peak pressures showed that SRM barrier has successfully reduced the peak pressure by 28% and 30% for targets located at 7m and

12m, respectively. These reductions were comparable to reductions found by other researchers (Wang et al. 2009) for geofoam barrier.

2. The peak pressure curves of different soil types in TM 5-855-1 (1986) can be replicated in LS-DYNA by changing the Poisson's ratio of the soil and with a fixed ratio of loading and unloading bulk modulus of 0.7. The Poisson's ratio was changed by varying the loading bulk modulus while keeping the shear modulus constant. All the soil types in TM 5-855-1 (1986) can be replicated using Poisson's ratio from 0.3 to 0.499.
3. Field test results in the more recent literature suggest that TM5-855-1 (1986) apparent crater diameter and depth curves are still valid. Finite element simulations performed in the present study shows that the apparent crater diameter can be obtained but not the depth.
4. By assuming that the 'true' crater from the finite element simulation can be approximated as a half ellipsoid, the volume of the fall back with the depth of buried charge can be estimated. Hence the apparent crater depth can be estimated. As the depth of buried charge increases, a camouflet is formed instead. A transition line can be plotted on to the TM5-855-1 (1986) crater curves plot showing the depth of buried charge where a camouflet is formed.
5. Numerical results for pressure and acceleration-time histories from LS-DYNA showed good match with the field test results. This shows that the FE model can simulate the field tests reasonably well. The effect of density ratio of concrete structure and soil was investigated. It is suggested that while reducing the concrete structure's density results in further reduction in peak pressure recorded. However, reduction in density of the concrete structure has an implication on its structural strength. In light of this, the benefits of SRM

for an actual of concrete structure may be higher than shown by the field tests which were conducted on a concrete block

Chapter 6 Conclusion and recommendations

6.1 Summary

Methods of reducing vibrations caused by surface wave and ground shock due to underground explosions are important to safeguard properties and human life especially in cities with high population density. The objective of this research is to study the responses of SRM as a seismic wave barrier to mitigate vibration and ground shock. Properties of the SRM were obtained from laboratory tests. Responses of SRM as a seismic wave barrier were investigated through field tests and numerical simulations. The first part of the research involves characterisation of the SRM using laboratory tests. Bender element tests and multi-stage triaxial compression tests were conducted. Effects such as effective confining pressure, rubber content and particle size ratio in SRM were investigated. Soil parameters such as V_p and V_s, damping ratio and friction angle were evaluated and compared with data in the literature. This study enhanced understanding on the behaviour of SRM with respect to confining pressure, rubber content and size ratio of sand and rubber particles. The second part of the research focuses on investigating the effectiveness of SRM barrier against surface wave using small-scale field tests. The small-scale field tests used two SRMs and an open trench as the seismic wave barrier. Numerical simulations of the field tests using LS-DYNA were performed; Parametric study on varying barrier dimensions and soil properties was performed and Ar contour plots were produced. Case studies from the literature were used to illustrate the use of the dimensionless Ar contour plots. The third part of this research investigated the use of SRM barrier to mitigate ground shock from buried explosions. Small-scale field tests were conducted involving two concrete structures (one with SRM barrier and one without SRM barrier) The field

tests were simulated in LS-DYNA. Before simulating the field tests, the finite element model in LS-DYNA was checked to endure that it could be simulate underground explosion correctly. The small-scale field tests were simulated successfully. In addition, the effect of density ratio between concrete structure and soil on the peak incident pressure was investigated by numerical simulations. The significant findings of this research are arranged according to the respective chapters and are presented below.

6.2 Conclusion

6.2.1 Characterisation of SRM

Through the use of bender element test and multi-stage shearing in a triaxial apparatus, soil parameters such as compression and shear wave velocities (V_p and V_s), small-strain shear modulus (G_{max}), damping ratio and friction angle were obtain. These parameters were found to be mainly affected by (a) rubber content present in the mix (b) effective confining pressure and (c) size ratio between sand and rubber particles. Wave velocities (V_p and V_s) and G_{max} decrease with increasing rubber content. With increasing rubber content, SRM shows rubber-like behaviour due to increase in rubber to rubber contact which resulted in lower wave velocity for all effective confining pressures. On the other hand, an increase in rubber content in SRM shows an increase in damping ratio. This is due to the high damping quality of rubber when compared to sand.

An increase in effective confining pressure will cause an increase in wave velocity (V_p and V_s) and G_{max}. This observation is due to sand and rubber particles being in better contact under a higher effective confining pressure. Similarly, damping ratio increases with increasing effective confining pressure. Damping in SRM is dependent

on the friction of the particle contacts as well as the deformation of particles (Brara et al. 2016). At high confining pressure, sand particles tend to restore contact by deforming rubber particles and rearrange. Thus reducing the interparticle friction leading to diminished frictional losses which explains the reduction of damping ratio with increasing confining pressure.

As size ratio increases, V_s and G_{max} generally decrease for all rubber contents. It is noted that V_s and G_{max} are determined by the stiffness of the inter-particle contact and the amount of small particle in the mixtures increases the coordination or particle contact area. This strongly suggests that V_s and G_{max} are governed by the smaller particles (Lee et al. 2009). It is observed that SRM with bigger rubber particles (sr0.25 and sr0.5) tend to have lower transitional volume fractions compare to SRM with smaller rubber particles (sr2, sr4 and sr8). For SRM with larger rubber particles, primary load carrying chain can be easily formed by the rubber particles before it is deformed and therefore has a lower transitional volume fractions (Lee et al. 2009).

A general decrease in damping ratio can be observed with decreasing rubber content for all size ratio. Damping ratios for all size ratios and rubber contents do not follow the empirical equation proposed by Anastasiadis et al. (2012). This is attributed to Anastasiadis et al. (2012) empirical equation being based only on the SRM tested. However, the empirical equation with modified parameters gave a good agreement with the damping ratios obtained in this study. An increase in rubber content leads to a decrease in friction angle which is due to increase in rubber-to-rubber contacts in SRM. An increase in size ratios leads to a decrease in friction angle. This observation is in good agreement with the data reported in the literature.

6.2.2 Trench barrier against surface wave

Small-scale field tests were carried out to investigate the effectiveness of open trench and SRM barriers in mitigating ground vibrations due to Rayleigh waves. To complement the field test results, the field tests were modelled using LS-DYNA with independently measured properties of soil and SRM. The FE model was also verified against data obtained from the literature. Parametric studies involving variations of barrier dimensions and impedance were carried out using LS-DYNA. Dimensionless Ar contour plots were developed from the parametric studies.

Open trench provides the best barrier effect, followed by R70 and R30. For the SRM barriers, the barrier effect is improved by increasing the rubber chip content of the SRM. The barrier becomes effective (Ar < 0.25) beyond D of 0.7 for both open trench and R70 barrier. The R30 barrier gives a minimum Ar value greater than 0.25 which shows that rubber chip content must be greater than 30% for the SRM barrier to be effective. The FE model was able to replicate the field test results for all the three types of barrier. FE modelling enabled a contour plot of Ar to be made. The Ar contour plot shows that amplification due to reflected waves is seen in front of the barrier and the barrier effect is only effective up to some distance behind the barrier.

A parametric study was performed using the FE model to develops dimensionless Ar contour plots. Results showed that the dimensionless Ar contour plots remain identical if normalised distance to source (R), normalised length (L) and depth of barrier (D) of barrier and impedance ratio (IR) are kept constant. Subsequently, useful dimensionless Ar contour plots with y/l as y-axis and x/d for x-axis can be used for preliminary implementation of seismic wave barrier for fixed R* and IR. The

dimensionless Ar contour plots can be use as a preliminary guide for the implementation of seismic wave barrier on site.

6.2.3 Trench barrier against shock wave

Small-scale field tests to investigate the efficiency of SRM as seismic wave barrier in reducing ground shock from underground explosion were conducted. The small-scale field tests were also simulated using LS-DYNA. Prior to simulation of the field test the finite element model was verified by replicating the peak pressure and crater curves from TM5-855-1 (1986).

The field test peak pressures show that SRM barrier has successfully reduced the peak pressure by 28% and 30% for targets located at 7m and 12 m, respectively. These reductions were comparable to reductions found by other researchers (Wang et al. 2009) for geofoam barrier against ground shock. From the numerical simulations, it was found that the peak pressure curves in TM 5-855-1 (1986) can be replicated by changing the Poisson's ratio of the soil while maintaining the ratio of loading and unloading bulk modulus. The Poisson's ratio was changed by varying the loading bulk modulus while keeping the shear modulus constant. All the soil types in TM 5-855-1 (1986) can be replicated using Poisson's ratio from 0.3 to 0.499.

Field test results in the more recent literature suggest that TM5-855-1 (1986) apparent crater diameter and depth curves are still valid. Finite element simulations performed in the present study show that the apparent crater diameter can be obtained but not the depth. By assuming that the finite element simulations give the 'true' crater, the crater can be well described as a half ellipsoid. Hence, the volume of the fall back with the depth of buried charge can be estimated. Using this plot the apparent crater depth can be estimated. As the depth of buried charge increases, a camouflet is formed instead.

Estimation of the diameter of camouflet was proposed and plotted on to the TM5-855-1 (1986) crater curves. These curves for different soil properties can be used to estimate depth of buried explosive for formation of camouflet as well as the size of the camouflet.

Numerical results for pressure and acceleration-time histories from LS-DYNA were shown to match with the field test data. This shows that the FE model can simulate the field tests reasonably well. It is suggested that while reducing the concrete structure's density results in further reduction in peak pressure recorded. However, reduction in density of the concrete structure has an implication on its structural strength. In light of this, the benefits of SRM for an actual of concrete structure may be higher than shown by the field tests which were conducted on a concrete block

6.3 Recommendations

The study on the use of SRM as a seismic wave barrier can be very extensive. Current study indicates that the rubber content of the SRM to be greater than 30% and the degree of saturation should be dry to be effective. However, due to time constraints and limited resources, some aspects of the research that deserve further studies were not researched. Given the results of this research, the following aspects are suggested for future research.

6.3.1 Characterisation of SRM

SRM can be tested using other dynamic laboratory tests such as resonant when, cyclic simple shear and cyclic triaxial tests. Further studies on factors that may change the properties of SRM should be investigated. Factors such as having a wider range in

size ratio between sand and rubber particles, dry density and degree of saturation should be investigated further

6.3.2 Seismic wave barrier against surface wave

The small-scale field tests were conducted with dry SRM. Hence, degree of saturation of the SRM which may affects its performance as a seismic wave barrier should be investigated. The dimensionless Ar contour plots can be further verified with monitoring of surface seismic wave projects with such seismic wave barrier. Vibrations with mixed frequency can be tested.

6.3.3 Trench barrier against shock wave

Additional readings should be taken from the field test to add to the limited data pool. SRM with different rubber content can be tested as seismic wave barrier against ground shock to find the balance between strength and mitigating properties. Similarly, effects such as differences in size ratio between rubber and sand particles and variation in degree of saturation which might potentially affect the mitigating effect of SRM as seismic wave barrier should be investigated.

References

Achenbach, J. (2012). Wave propagation in elastic solids (Vol. 16). Elsevier.

Ågårdh, L., & Laine, L. (1999). 3D FE-simulation of high-velocity fragment perforation of reinforced concrete slabs. International Journal of Impact Engineering, 22(9), 911-922.

Ahmad, S., & Al-Hussaini, T. M. (1991). Simplified design for vibration screening by open and in-filled trenches. Journal of geotechnical engineering, 117(1), 67-88.

Ahmed, I. (1993). Laboratory study on properties of rubber-soils. Report No. FHWA/IN/JHRP-93/4, School of Civil Engineering, Purdue University.

Allen, R. M., Kirkpatrick, D. J., Longbottom, A. W., Milne, A. M., & Bourne, N. K. (2004, July). Experimental and Numerical Study of Free-Field Blast Mitigation. In AIP Conference Proceedings (Vol. 706, No. 1, pp. 823-826). AIP.

Alzawi, A., & El Naggar, M. H. (2009). Vibration scattering using geofoam material as vibration wave barriers. In Proceedings of 62nd Canadian geotechnical conference, Halifax, NB, Canada (pp. 997-1004).

Alzawi, A., & El Naggar, M. H. (2011). Full scale experimental study on vibration scattering using open and in-filled (GeoFoam) wave barriers. Soil Dynamics and Earthquake Engineering, 31(3), 306-317.

Ambrosini, R. D., Luccioni, B. M., Danesi, R. F., Riera, J. D., & Rocha, M. M. (2002). Size of craters produced by explosive charges on or above the ground surface. Shock Waves, 12(1), 69-78.

Ambrosini, R. D., & Luccioni, B. M. (2006). Craters produced by explosions on the soil surface. Journal of applied mechanics, 73(6), 890-900.

Anand, S., Leong, E.C., & Cheong, H.K. (2001) Pressure amplification on buried structures due to transient dynamic loading, The Eighth East Asia-Pacific Conference on Structural Engineering & Construction, EASEC-8, Singapore.

Anand, S. (2007) Measurement and modelling of ground response due to dynamic loading, PhD Thesis, Nanyang Technological University, Singapore.

Anastasiadis, A., Pitilakis, K, and Senetakis, K. (2009) Dynamic shear modulus and damping ratio curves of sand/rubber mixtures. Proceedings of the earthquake geotechnical engineering satellite conference, XVIIth international conference on soil mechanics & geotechnical engineering, Alexandria, Egypt

Anastasiadis, A., Senetakis, K., & Pitilakis, K. (2012). Small-strain shear modulus and damping ratio of sand-rubber and gravel-rubber mixtures. Geotechnical and Geological Engineering, 30(2), 363-382.

Anastasiadis, A., Senetakis, K., Pitilakis, K., Gargala, C., & Karakasi, I. (2012). Dynamic behavior of sand/rubber mixtures. Part I: Effect of rubber content and duration of confinement on small-strain shear modulus and damping ratio. In Testing and Specification of Recycled Materials for Sustainable Geotechnical Construction. ASTM International

ASTM (2003), D2850-03: Standard Test Method for Unconsolidated-Undrained Triaxial CompressionTest on Cohesive Soils, ASTM International, West Conshohocken, PA, USA.

ASTM (2008), D2845–08 Standard test method for laboratory determination of pulse velocities and ultrasonic elastic constants of rock, ASTM International, West Conshohocken, PA, USA

ASTM (2011), D4767-11: Standard test method for consolidated undrained triaxial compression test for cohesive soils, ASTM International, West Conshohocken, PA, USA.

ASTM (2011), D7181-11: Method for consolidated drained triaxial compression test for soils. ASTM International, West Conshohocken, PA, USA.

ASTM (2014), D854-14: Standard Test Methods for Specific Gravity of Soil Solids by Water Pycnometer, ASTM International, West Conshohocken, PA, USA.

ASTM (2016), D4254-16: Standard Test Methods for Minimum Index Density and Unit Weight of Soils and Calculation of Relative Density, ASTM International, West Conshohocken, PA, USA.

ASTM D6913 (2017), D6913M-17: Standard Test Methods for Particle-Size Distribution (Gradation) of Soils Using Sieve Analysis, ASTM International, West Conshohocken, PA, USA.

Arulnathan, R., Boulanger, R. W., & Riemer, M. F. (1998). Analysis of bender element tests. Geotechnical Testing Journal, 21(2), 120–131.

Avilés, J., & Sánchez-Sesma, F. J. (1988). Foundation isolation from vibrations using piles as barriers. Journal of Engineering Mechanics, 114(11), 1854-1870.

Aung, A. M. W., & Leong, E. C. (2011). Finite-Element Modeling of Continuous Surface Waves Tests: Numerical Accuracy with respect to Domain Size. Journal of Geotechnical and Geoenvironmental Engineering, 137(12), 1294-1298.

Babuska, I., Ihlenburg, F., Strouboulis, T., & Gangaraj, S. K. (1997). A Posteriori Error Estimation for Finite Element Solutions of Helmholtz'Equation-Part II: Estimation of the Pollution Error. International Journal for Numerical Methods in Engineering, 40(21), 3883-3900.

Bałachowski, L., & Gotteland, P. (2007). Characteristics of tyre chips-sand mixtures from triaxial tests. Archives of Hydro-Engineering and Environmental Mechanics, 54(1), 25-36.

Bathe, K. J., & Noh, G. (2012). Insight into an implicit time integration scheme for structural dynamics. Computers & Structures, 98, 1-6.

Bathurst, R. J., Zarnani, S., & Gaskin, A. (2007). Shaking table testing of geofoam seismic buffers. Soil Dynamics and Earthquake Engineering, 27(4), 324-332.

Barkan, D.D. (1962) Dynamics of Bases and Foundations. McGraw Hill, New York.

Bergado, D. T., Youwai, S., & Rittirong, A. (2005). Strength and deformation characteristics of flat and cubical rubber tyre chip–sand mixtures. Geotechnique, 55(8), 603-606.

Beskos, D. E., Dasgupta, B., & Vardoulakis, I. G. (1986). Vibration isolation using open or filled trenches. Computational mechanics, 1(1), 43-63.

Brara, A., Brara, A., Daouadji, A., Bali, A., & Mostafa Daya, E. (2017). Dynamic properties of dense sand-rubber mixtures with small particles size ratio. European Journal of Environmental and Civil Engineering, 21(9), 1065-1079.

Bressette, T. (1984). Used Tire Material as an Alternate Permeable Aggregate (No. FHWA-CA-TL-84-07 Final Rpt.).

Brignoli, E. G., Gotti, M., & Stokoe, K. H. (1996). Measurement of shear waves in laboratory specimens by means of piezoelectric transducers. Geotechnical Testing Journal, 19(4), 384-397.

Britan, A., Liverts, M., Ben-Dor, G., Koehler, S. A., & Bennani, N. (2009). The effect of fine particles on the drainage and coarsening of foam. Colloids and Surfaces A: Physicochemical and Engineering Aspects, 344(1), 15-23.

Britan, A., Liverts, M., Shapiro, H., & Ben-Dor, G. (2012). Blast wave mitigation by a particulate foam barrier. Transport in porous media, 93(2), 283-292.

Britan, A., Zinovik, I. and Levin, V.A. (1992)b, Foam Destruction by Shock Waves, Fiz. Gorenia Vzriva 5, PP 108–116

Britan, A., Shapiro, H., Liverts, M., Ben-Dor, G., Chinnayya, A., & Hadjadj, A. (2013). Macro-mechanical modelling of blast wave mitigation in foams. Part I: review of available experiments and models. Shock Waves, 23(1), 5-23.

Bosscher, P. J., Edil, T. B., & Kuraoka, S. (1997). Design of highway embankments using tire chips. Journal of Geotechnical and Geoenvironmental Engineering, 123(4), 295-304.

BS5228-2:2009, (2008) Code of practice for noise and vibration control on construction and open sites – Part 2: Vibration, British Standard, BSI

Bull, J.W. & Woodford, C.H. (1998) Camouflets and their effects on runway supports, Computer and Structures, 69(6), 695-706.

Bulson, P. S. (2002). Explosive loading of engineering structures. CRC Press.

Busch, C. L., Aimone-Martin, C. T. & Tarefder, R.A., (2015) Experimental evaluation of cratering and ground vibration in clay soils subjected to explosive air blast loading, Journal of Testing and Evaluation, 43(2), 1-11.

Cabalar, A. F. (2011). Direct shear tests on waste tires–sand mixtures. Geotechnical and Geological Engineering, 29(4), 411-418.

Caicedo, B. (2007). Medida de Vibraciones Producidas Por Los Buses Alimentadores Del Sistema Transmilenio En la Ciudad De Bogotá. Reporte interno Universidad de los Andes.

Çelebi, E., Fırat, S., Beyhan, G., Çankaya, İ., Vural, İ., & Kırtel, O. (2009). Field experiments on wave propagation and vibration isolation by using wave barriers. Soil dynamics and earthquake engineering, 29(5), 824-833.

CEN (2007) Eurocode 3: 1992, Design of steel structures, chapter 5, piling, CEN.

Cetin, H., Fener, M., & Gunaydin, O. (2006). Geotechnical properties of tire-cohesive clayey soil mixtures as a fill material. Engineering geology, 88(1), 110-120.

Chadwick, P., Cox, A. D., & Hopkins, H. G. (1964). Mechanics of deep underground explosions. Philosophical Transactions of the Royal Society of London A: Mathematical, Physical and Engineering Sciences, 256(1070), 235-300.

Cheng, Z.Y. (2015). Properties of Soils using Laboratory Seismic Methods and Numerical Modelling, Ph.D Thesis, Nayang Technological University, Singapore

Cheng, Z.Y., & Leong, E. C. (2014b). A hybrid bender element–ultrasonic system for measurement of wave velocity in soils. Geotechnical Testing Journal, 37(3), 1-14.

Cheng, Z. Y., & Leong, E. C. (2014a). Effect of confining pressure and degree of saturation on damping ratios of sand. Unsaturated Soils: Research & Applications, 277.

Cheng, Z.Y., & Leong, E.C. (2015) Damping characteristics of sand-rubber chip mixtures as a seismic barrier. The 5th International Conference on Design & Analysis of Protective Structures (DAPS2015), Singapore.

Cheng, Z., & Leong, E. C. (2018). Determination of damping ratios for soils using bender element tests. Soil Dynamics and Earthquake Engineering, 111, 8-13.

Chin, F. K. (1970). Estimation of the ultimate load of piles from tests not carried to failure (pp. 83-91). Southeast Asian Society of Soil Engineering.

Chin, R. C. (1975). Dispersion and Gibbs phenomenon associated with difference approximations to initial boundary-value problems for hyperbolic equations. Journal of Computational Physics, 18(3), 233-247.

Christ, M., & Park, J. B. (2010). Laboratory determination of strength properties of frozen rubber–sand mixtures. Cold Regions Science and Technology, 60(2), 169-175.

Cole, R.H. (1965) Underwater explosions, New York: Dover Publications

Das, B. M. and Luo, Z. (2016) Principles of soil dynamics. Cengage Learning.

Davies, M. C. R. (1994, August). Dynamic soil structure interaction resulting from blast loading. In Centrifuge (Vol. 94, pp. 319-324). Balkema Rotterdam.

De, A., Morgante, A. N., & Zimmie, T. F. (2016). Numerical and physical modeling of geofoam barriers as protection against effects of surface blast on underground tunnels. Geotextiles and Geomembranes, 44(1), 1-12.

Diehl, T., Carroll, D., & Nagaraj, B. (2000). Applications of DSP to Explicit Dynamic FEA simulations of elastically-dominated impact problems. Shock and Vibration, 7(3), 167-177.

DIN 4150-3 (1999) Structural vibration – Part 3: Effects of vibration on structures, German Standards Association.

Dobratz, B. M. (1981). LLNL explosives handbook: properties of chemical explosives and explosives and explosive simulants (No. UCRL-52997). Lawrence Livermore National Lab., CA (USA).

Dolling, H. J. (1965). "Schwingungsisolierung von Bauwerken durch tiefe, auf geeignete Weise stabilisierte Schlitz" (Vibration isolation of buildings by means of deep, suitably stabilized trenches). VDI Bericht Nr. 88.

Drake, J. L., & Little Jr, C. D. (1983). Ground shock from penetrating conventional weapons. Army Engineer Waterways Experiment Station Vicksburgms.

Edil, T. B., & Bosscher, P. J. (1994). Engineering properties of tire chips and soil mixtures. Geotechnical testing journal, 17(4), 453-464.

El-Sohby, M. A., & Andrawes, K. Z. (1972). Deformation characteristics of granular materials under hydrostatic compression. Canadian Geotechnical Journal, 9(4), 338-350.xtures. Geotechnical testing journal, 17(4), 453-464.

Farnam, Y., Mahoutian, M., Mohammadi, S., & Shekarchi, M. (2008). Experimental and numerical studies of impact behavior of fiber lightweight aggregate concrete. In Structures Congress 2008: Crossing Borders (pp. 1-10).

Farnam, Y., Mohammadi, S., & Shekarchi, M. (2010). Experimental and numerical investigations of low velocity impact behavior of high-performance fiber-reinforced cement based composite. International Journal of Impact Engineering, 37(2), 220-229.

Feng, Z. Y., & Sutter, K. G. (2000). Dynamic properties of granulated rubber/sand mixtures. Geotechnical Testing Journal, 23(3), 338-344.

Fırat, S., Çelebi, E., Beyhan, G., Çankaya, İ., Kırtel, O., & Vural, İ. (2010). Field Experiments on Wave Propagation and Vibration Isolation by Using Wave Barriers. In Wave Propagation in Materials for Modern Applications. InTech.

Fiserova, D. (2006) Numerical analysis of buried explosions with emphasis on effect of soil properties on loading, PhD Thesis, Defence College of Management and Technology, Cranfield University, UK.

Fondaw, G. W. (1993). Mitigation of shock waves in a cylindrical tunnel by foam (No. AFIT/GNE/ENP/93M-2). AIR FORCE INST OF TECH WRIGHT-PATTERSONAFB OH.

Foose, G. J., Benson, C. H., & Bosscher, P. J. (1996). Sand reinforced with shredded waste tires. Journal of Geotechnical Engineering, 122(9), 760-767.

Fung, T. C. (2003). Numerical dissipation in time-step integration algorithms for structural dynamic analysis. Progress in Structural Engineering and Materials, 5(3), 167-180.

Gottlieb, J. J., Ritzel, D. V., & Miskew, I. A. (1981). Signal processing of shock-wave overpressure records (No. Dres-Memo-1021). Defence Research Establishment Syffieldralston (Alberta).

Groto, A. and Taniguchi, H. (2001) Effects of explosion energy and depth to the formation of blast wave and crater: field explosion experiment for the understanding of volcanic explosion, Geophysics Research Letters, 28(22), 428-435.

Hao, H. (2014). Measurement of plate compaction-induced ground vibrations, 23rd Australasian Conference on the Mechanics of Structures and Materials (ACMSM23), vol. II, Byron Bay, NSW, 9-12 December, Southern Cross University, Lismore.

Hao, Y., Hao, H., & Zhang, X. H. (2012). Numerical analysis of concrete material properties at high strain rate under direct tension. International Journal of Impact Engineering, 39(1), 51-62.

Hardin, B. O., & Richart Jr, F. E. (1963). Elastic wave velocities in granular soils. Journal of Soil Mechanics & Foundations Div, 89(Proc. Paper 3407)..

Haupt, W. A. (1981). Model tests on screening of surface waves. In Proceedings of the 10th international conference on soil mechanics and foundation engineering (Vol. 3, pp. 215-222).

Hazarika, H., Yasuhara, K., Karmokar, A., & Mitarai, Y. (2007, November). Shaking table test on liquefaction prevention using tire chips and sand mixture. In Proceedings

of the international workshop on scrap tire derived geomaterials—opportunities and challenges, Yokosuka, Japan (pp. 215-222).

Hendron Jr, A. J., & Auld, H. E. (1969, October). Effect of soil properties on the attenuation of airblast-induced ground motions. In pp 29-47 of Proceedings of International Symposium on Wave Propagation and Dynamic Properties of Earth Materials held on August 23--25, 1967 at Albuquerque, New Mexico. Triandafilidis, George E.(ed. Univ. of Illinois, Urbana.

Homae, T., Wakabayashi, K., Matsumura, T., & Nakayama, Y. (2007, December). Reduction of explosion damage using sand or water layer. In AIP Conference Proceedings (Vol. 955, No. 1, pp. 1289-1292). AIP.

Homae, T., Wakabayashi, K., Matsumura, T., & Nakayama, Y. (2008). Dependence of Blast Attenuation on Weight of Barrier Materials. In Materials Science Forum (Vol. 566, pp. 179-184). Trans Tech Publications.

Holmes, N., & Belytschko, T. (1976). Postprocessing of finite element transient response calculations by digital filters. Computers & Structures, 6(3), 211-216.

Horvath, J. S. (1994). Expanded polystyrene (EPS) geofoam: an introduction to material behavior. Geotextiles and Geomembranes, 13(4), 263-280.

Horvath, J. S. (1995). Geofoam geosynthetic. USA, Horvath Engineering

Huang, F., Wu, H., Jin, Q., & Zhang, Q. (2005). A numerical simulation on the perforation of reinforced concrete targets. International Journal of Impact Engineering, 32(1), 173-187.

Huang, N. E., Shen, Z., Long, S. R., Wu, M. C., Shih, H. H., Zheng, Q., & Liu, H. H. (1998, March). The empirical mode decomposition and the Hilbert spectrum for nonlinear and non-stationary time series analysis. In Proceedings of the Royal Society of London A: mathematical, physical and engineering sciences (Vol. 454, No. 1971, pp. 903-995). The Royal Society.

Hugoniot, H. (1887) Mémoire sur la propagation du mouvement dans les corps et spécialement dans les gaz parfaits. Gauthier-Villars.

Humphrey, D. N., & Manion, W. P. (1992). Properties of tire chips for lightweight fill. In Grouting, soil improvement and geosynthetics (pp. 1344-1355). ASCE.

Humphrey, D. N., Sandford, T. C., Cribbs, M. M., & Manion, W. P. (1993). Shear strength and compressibility of tire chips for use as retaining wall backfill. Transportation Research Record, (1422).

Idesman, A. V., Schmidt, M., & Foley, J. R. (2011). Accurate finite element modeling of linear elastodynamics problems with the reduced dispersion error. Computational Mechanics, 47(5), 555-572.

Idesman, A., Samajder, H., Aulisa, E., & Seshaiyer, P. (2009). Benchmark problems for wave propagation in elastic materials. Computational Mechanics, 43(6), 797-814.

Inglis, D., Macleod, G., Naesgaard, E., & Zergoun, M. (1996). Basement wall with seismic earth pressures and novel expanded polystyrene foam buffer layer. In Proceedings of the 10th Annual Symposium of the Vancouver Geotechnical Society, Vancouver, BC.

International Society of Explosive Engineers (ISEE) (2000) “Blaster Handbook”. 17th edition, published by ISEE, Cleveland, Ohio, USA, PP 724

Jovičić, V., Coop, M. R., & Simić, M. (1996). Objective criteria for determining G max from bender element tests. Geotechnique, 46(2), 357-362.

Kikkawa, N., Pender, M. J., Orense, R. P., & Matsushita, E. (2009). Behaviour of pumice sand during hydrostatic and Ko compression. In Proceedings of the 17th International Conference on Soil Mechanics and Geotechnical Engineering (pp. 812-815).

Kim, D. S., & Lee, J. S. (2000). Propagation and attenuation characteristics of various ground vibrations. Soil dynamics and Earthquake engineering, 19(2), 115-126.

Kim, H. K., & Santamarina, J. C. (2008). Sand–rubber mixtures (large rubber chips). Canadian Geotechnical Journal, 45(10), 1457-1466.

Kim, D. S., & Stokoe, K. H. (1994). Torsional motion monitoring system for small-strain (10− 5 to 10− 3%) soil testing. Geotechnical Testing Journal, 17(1), 17-26.

Kleinschmit, N. N. (2011). A shock tube technique for blast wave simulation and studies of flow structure interactions in shock tube blast experiments. PhD Thesis, University of Nebraska, Lincoln

Krieg, R. D. (1972). A simple constitutive description for cellular concrete. Albuquerque, NM: Sandia National Laboratories.

Kobielak, S., Krauthammer, T., & Walczak, A. (2007). Ground shock attenuation on a buried cylindrical structure by a barrier. Shock and Vibration, 14(5), 305-320.

Kuhl, D., & Crisfield, M. A. (1999). Energy-conserving and decaying algorithms in non-linear structural dynamics. International journal for numerical methods in engineering, 45(5), 569-599.

Kuznetsov, S. V. (2011). Seismic waves and seismic barriers. Acoustical Physics, 57(3), 420-426.

Lade, P. V., & Abelev, A. V. (2005). Characterization of cross-anisotropic soil deposits from isotropic compression tests. Soils and foundations, 45(5), 89-102.

Lampson, C.W. (1946) Effects of Impact and Explosions, Explosions in Earth, National Defence Reserach Centre, USA.

Lee, C., Truong, Q. H., Lee, W., & Lee, J. S. (2009). Characteristics of rubber-sand particle mixtures according to size ratio. Journal of materials in civil engineering, 22(4), 323-331.

Lee, J. H., Salgado, R., Bernal, A., & Lovell, C. W. (1999). Shredded tires and rubber-sand as lightweight backfill. Journal of geotechnical and geoenvironmental engineering, 125(2), 132-141.

Lee, J. S., & Santamarina, J. C. (2005). Bender elements: performance and signal interpretation. Journal of geotechnical and geoenvironmental engineering, 131(9), 1063-1070.

Leong, E. C., & Aung, A. M. W. (2013). Global Inversion of Surface Wave Dispersion Curves Based on Improved Weighted Average Velocity Method. Journal of Geotechnical and Geoenvironmental Engineering, 139(12), 2156-2169.

Leong, E.C., Anand, S., Cheong, H.K. & Lim, C.H. (2006) Re-examination of peak stress and scaled distance due to ground shock, International Journal of Impact Engineering, 34(9), 1487-1499.

Leong, E. C., Cahyadi, J., & Rahardjo, H. (2009). Measuring shear and compression wave velocities of soil using bender–extender elements. Canadian geotechnical journal, 46(7), 792-812.

Leong, E.C., Chew, J. H. & Anand, S. (2015) Modelling TM 5-855-1 Peak pressure plot using LS-DYNA, 5th International Conference Design and Analysis Of Protective Structure, Singapore.

Lin, V. W. J., Quek, S. T., Maalej, M., & Lee, S. C. (2010). Finite element model of functionally-graded cementitious panel under small projectile impact. International Journal of Protective Structures, 1(2), 271-297.

Liu, C. H., & Nagel, S. R. (1993). Sound Propagation in Granular Materials. In Phonon Scattering in Condensed Matter VII (pp. 244-248). Springer, Berlin, Heidelberg.

LSTC. (2006) LS-DYNA theory manual, Livermore Software Technology Corporation, California, USA.

Lings, M. L., & Greening, P. D. (2001). A novel bender/extender element for soil testing. Géotechnique, 51(8), 713-717.

Luna, R., & Jadi, H. (2000, December). Determination of dynamic soil properties using geophysical methods. In Proceedings of the first international conference on the application of geophysical and ndt methodologies to transportation facilities and infrastructure—geophysics (pp. 3-1).

Luo, H., Fang, X., & Ertas, B. (2009). Hilbert transform and its engineering applications. American Institute of Aeronautics and Astronautics Journal, 47(4), 923.

Massarsch, K. R. (2005). Vibration isolation using gas-filled cushions. In Soil dynamics symposium in honor of professor Richard D. Woods (pp. 1-20).

Maestas, J. T., Taylor, L. F., & Collis, J. M. (2014). Shock wave propagation along constant sloped ocean bottoms. The Journal of the Acoustical Society of America, 136(6), 2987-2997.

Masad, E., Taha, R., Ho, C., & Papagiannakis, T. (1996). Engineering properties of tire/soil mixtures as a lightweight fill material. Geotechnical Testing Jornal, 19(3), 293–304.

Marburg, S. (2002). Six boundary elements per wavelength: is that enough?. Journal of Computational Acoustics, 10(01), 25-51.

Marjanovic, J., & Germaine, J. T. (2013). Experimental study investigating the effects of setup conditions on bender element velocity results. Geotechnical Testing Journal, 36(2), 1-11.

Mavroulidou, M., Etan, O., & Suntharalingam, M. (2009, September). Mechanical Properties of Granulated Tyre Rubber Sand Mixture. In Proceeding of the 11th Internatio-nal Conference on Enviromental Science and Technology, China.

May, T. W., & Bolt, B. A. (1982). The effectiveness of trenches in reducing seismic motion. Earthquake Engineering & Structural Dynamics, 10(2), 195-210.

Miller, G. F., & Pursey, H. (1955, December). On the partition of energy between elastic waves in a semi-infinite solid. In Proceedings of the Royal Society of London a: mathematical, physical and engineering sciences (Vol. 233, No. 1192, pp. 55-69). The Royal Society.

Moorthy, T. N., Yaacob, M. H., Vicente, R., Mansor, M. T. & Nagah, S. (2015) A study into relationship between crater parameters and quantities of explosives in the scenes of IED explosions, Malaysian Journal of Forensic Sciences, 5(1), 17-25.

Muir Wood, D., & Kumar, G. V. (2000). Experimental observations of behaviour of heterogeneous soils. Mechanics of Cohesive-frictional Materials, 5(5), 373-398.

Murillo, C., Thorel, L., & Caicedo, B. (2009). Ground vibration isolation with geofoam barriers: Centrifuge modeling. Geotextiles and Geomembranes, 27(6), 423-434.

Nayak, G. C., & Zienkiewicz, O. C. (1972). Elasto-plastic stress analysis. A generalization for various constitutive relations including strain softening. International Journal for Numerical Methods in Engineering, 5(1), 113-135.

Nian, X., Yan, D., Zhao, H., Cheng, Y. & Wang, H. (2013) Investigation in craters formed by explosives with different burial depth in soil, Journal of Engineering, 1(3), 53-56.

Noh, G., & Bathe, K. J. (2013). An explicit time integration scheme for the analysis of wave propagations. Computers & structures, 129, 178-193.

Noh, G., Ham, S., & Bathe, K. J. (2013). Performance of an implicit time integration scheme in the analysis of wave propagations. Computers & Structures, 123, 93-105.

Pamukcu, S., & Akbulut, S. (2006). Thermoelastic enhancement of damping of sand using synthetic ground rubber. Journal of Geotechnical and Geoenvironmental Engineering, 132(4), 501-510.

Pankaj, Arif, M., & Kaushik, S. K. (2002). Mechanical Behavior of Ferrocement Composites: Numerical Simulation. Journal of Materials in Civil Engineering, 14(2), 156-163.

Peters, J. F., & Berney IV, E. S. (2009). Percolation threshold of sand-clay binary mixtures. Journal of geotechnical and geoenvironmental engineering, 136(2), 310-318.

Pichandi, S., Rana, S., Oliveira, D., & Fangueiro, R. (2013). Fibrous and composite materials for blast protection of structural elements—A state-of-the-art review. Journal of Reinforced Plastics and Composites, 32(19), 1477-1500.

Pitilakis, K., Karapetrou, S., & Tsagdi, K. (2015). Numerical investigation of the seismic response of RC buildings on soil replaced with rubber–sand mixtures. Soil Dynamics and Earthquake Engineering, 79, 237-252.

Prasad, B. B. (2011). Advanced Soil Dynamics and Earthquake Engineering. PHI Learning Pvt. Ltd..

Rahman, M. M., Cubrinovski, M., & Lo, S. R. (2012). Initial shear modulus of sandy soils and equivalent granular void ratio. Geomechanics and Geoengineering, 7(3), 219-226.

Rankine, W. M. (1870). On the thermodynamic theory of waves of finite longitudinal disturbance. Philosophical Transactions of the Royal Society of London, 277-288.

Richart, F. E. (1962). Foundation vibrations. Transactions of the American Society of Civil Engineers, 127(1), 863-897.

Richart, F. E., Hall, J. R., & Woods, R. D. (1970). Vibrations of soils and foundations.

Rio, J.F.M.E. (2006) Advances in Laboratory Geophysics Using Bender Elements, PhD thesis, University College London, England, United Kingdom.

Rocco, N. T. (2012). Characterization of expanded polystyrene (EPS) and cohesive soil mixtures, PhD thesis, Missouri University of Science and Technology. USA

Rossmanith, H. P., & Fourney, W. L. (1982). Fracture initiation and stress wave diffraction at cracked interfaces in layered media I. brittle/brittle transition. Rock Mechanics and Rock Engineering, 14(4), 209-233.

Sanchez-Salinero, I., Roesset, J.M. & Stokoe, K.H. (1986) Analytical Studies of Body Wave Propagation and Attenuation, Report GR 86-15, Civil Enginerring Department, University of Texas, Austin, United States.

Santamarina, J.C. & Fratta, D. (2005) Discrete Signals and Inverse Problems: An Introduction for Engineers and Scientists, John Wiley and Sons Ltd, West Sussex, England.

Santamarina, J.C.& Fam, M.A. (1997) Discussion on interpretation of bender element test (paper by Viggiani and Atkinson, 1995), Géotechnique, 47(4), 873–877.

Schimizze, B., Son, S. F., Goel, R., Vechart, A. P., & Young, L. (2013). An experimental and numerical study of blast induced shock wave mitigation in sandwich structures. Applied Acoustics, 74(1), 1-9.

Schmidt, R.M. and Housen, K.R. (1987) Some Recent Advance In The Scaling Of Impact And Explosion Cratering, International Journal Of Impact Engineering, 5(1-4), 543-560.

Schoutens, J.E. (1979) Nuclear Geoplosics Sourcebook. Volume IV. Part II. Empirical analysis of nuclear and high-explosive cratering and ejecta, General Electric Company- Tempo DASIAC, California, USA.

Senetakis, K., Anastasiadis, A., Trevlopoulos, K., & Pitilakis, K. (2009, June). Dynamic response of SDOF systems on soil replaced with sand/rubber mixture. In Proceedings of the ECOMAS Thematic Conference on Computation Methods in Structural Dynamics and Earthquake Engineering (pp. 22-24)

Senetakis, K., Anastasiadis, A., & Pitilakis, K. (2012). Dynamic properties of dry sand/rubber (SRM) and gravel/rubber (GRM) mixtures in a wide range of shearing strain amplitudes. Soil Dynamics and Earthquake Engineering, 33(1), 38-53.

Shehadeh, M., Shennawy, Y., & El-Gamal, H. (2015). Similitude and scaling of large structural elements: Case study. Alexandria Engineering Journal, 54(2), 147-154.

Singh, B., & Vinot, V. (2011). Influence of waste tire chips on strength characteristics of soils. Journal of Civil Engineering and Architecture, 5(9).

Simpson, D. C., & Evans, T. M. (2015). Behavioral thresholds in mixtures of sand and kaolinite clay. Journal of Geotechnical and Geoenvironmental Engineering, 142(2), 04015073.

Skews, B. W., Atkins, M. D., & Seitz, M. W. (1993). The impact of a shock wave on porous compressible foams. Journal of Fluid Mechanics, 253, 245-265.

Smith, P. D., & Hetherington, J. G. (1994). Blast and ballistic loading of structures. Digital Press.

Stokoe, K. H., Wright, S. G., Bay, J. A., & Roesset, J. M. (1994). Characterization of geotechnical sites by SASW method. Geophysical characterization of sites, 15-25.

Taiqieddin, S.A. (1982). The role of borehole pressure containment on surface ground vibration levels at close scaled distance, PhD Thesis, University of Missouri-Rolla.

Tedesco, J. W., McDougal, W. G., & Ross, C. A. (1999). Structural dynamics: theory and applications. Addison Wesley Longman.

Tsai, P. H., & Chang, T. S. (2009). Effects of open trench siding on vibration-screening effectiveness using the two-dimensional boundary element method. Soil Dynamics and Earthquake Engineering, 29(5), 865-873.

Tsang, H.H. (2008) Seismic isolation by rubber-soil mixtures for developing countries, Earthquake Engineering and Structural Dynamics, 37(2), 283–303.

Tsang, H. H., Lo, S. H., Xu, X., & Neaz Sheikh, M. (2012). Seismic isolation for low-to-medium-rise buildings using granulated rubber–soil mixtures: numerical study. Earthquake engineering & structural dynamics, 41(14), 2009-2024.

TM 5-855-1 (1986) Fundamentals of protective design for conventional weapons, Department of Army, Washington, DC, USA.

Turan, A., Hafez, D., & El Naggar, M. H. (2013). The performance of inclined secant micro-pile walls as active vibration barriers. Soil Dynamics and Earthquake Engineering, 55, 225-232.

Uchimura, T., Chi, N., Nirmalan, S., Sato, T., Meidani, M., & Towhata, I. (2007, November). Shaking table tests on effect of tire chips and sand mixture in increasing liquefaction resistance and mitigating uplift of pipe. In Proceedings, international workshop on scrap tire derived geomaterials—opportunities and challenges, Yokosuka, Japan (pp. 179-186).

Van der Eerden, F., & Van den Berg, F. (2010, January). The acoustic source strength of high-energy blast waves: combining measurements and a non-linear model. In Proceedings of 20 th International Congress on Acoustics.

Van Dongen, P., & Weerheijm, J. (1992). Interaction of Ground Shock with Soil Pressure Transducers. In Structures Under Shock and Impact II: Proceedings of the Second International Conference, held in Portsmouth, UK, 16th–18th June, 1992 (pp. 625-635). Thomas Telford Publishing.

Verdugo, R., & Ishihara, K. (1996). The steady state of sandy soils. Soils and foundations, 36(2), 81-91.

Viggiani, G., & Atkinson, J. H. (1995). Interpretation of bender element tests. In International Journal of Rock Mechanics and Mining Sciences and Geomechanics Abstracts, 8(32), 373A.

Viktorov, I. A. (1967) Rayleigh and Lamb Waves: Physical Theory and Applications: Translated from Russian. Plenum press.

Wang, J. (2001) Simulation of Landmine Explosion Using LS_DYNA3D software, Benchmark Work of Simulation of Explosion in Soil and Air, DSTO-TR-1168.

Wang, W., Chen, Y., Yang, G. & Liu, Y. (2016) Field tests and numerical simulations of blast-induced crater in wet sands, Chinese Journal of Rock Mechanics and Engineering, 35(1), 68-75.

Wang, Z. & Lu, Y. (2003) Numerical analysis on dynamic deformation mechanism of soil under blast loading, Soil Dynamic and Earthquake Engineering, 23(8), 705-714.

Wang, Z. L., Li, Y. C., & Wang, J. G. (2006). Numerical analysis of attenuation effect of EPS geofoam on stress-waves in civil defense engineering. Geotextiles and Geomembranes, 24(5), 265-273.

Wang, J. G., Sun, W., & Anand, S. (2009). Numerical investigation on active isolation of ground shock by soft porous layers. Journal of sound and vibration, 321(3), 492-50

Wang, Y. H., & Yan, W. M. (2006). Laboratory studies of two common saprolitic soils in Hong Kong. Journal of geotechnical and geoenvironmental engineering, 132(7), 923-930.

Westine, P. S. and Friesenhahn, G. J. (1983). Free-field ground shock pressures from buried detonations in saturated and unsaturated soils. Southwest Foundation for Research and Education, San Antonio, USA.

Wiącek, J., & Molenda, M. (2014). Effect of particle size distribution on micro-and macromechanical response of granular packings under compression. International Journal of Solids and Structures, 51(25), 4189-4195.

Wilson, S. D., & Sibley, E. A. (1962). Ground displacement from air blast loading. ASCE Proceedings Paprr, 3346.

Woods, R. D. (1968). Screening of surface waves in soils. American Society of Civil Engineer, Journal of Soil Mechanics and Foundation Division, 94(1).

Woods, R. D., Barnett, N. E., & Sagesser, R. (1974). Holography--a new tool for soil dynamics. Journal of Geotechnical and Geoenvironmental Engineering, 100(Proc. Paper 10949).

Wu, W. Y., Benda, C. C., & Cauley, R. F. (1997). Triaxial determination of shear strength of tire chips. Journal of Geotechnical and Geoenvironmental Engineering, 123(5), 479-482.

Xu, X. (2010). Earthquake Protection of Low-to-medium-rise Buildings using Rubber-soil Mixtures, Ph.D. Thesis, The University of Hong Kong

Xu, Z., Hao, H., & Li, H. N. (2012). Mesoscale modelling of fibre reinforced concrete material under compressive impact loading. Construction and Building Materials, 26(1), 274-288.

Youwai, S., & Bergado, D. T. (2003). Strength and deformation characteristics of shredded rubber tire sand mixtures. Canadian Geotechnical Journal, 40(2), 254-264.

Zhou, H., Zhao, Z., & Ma, G. (2012). Mitigating Ground Shocks with Cellular Solids. Journal of Engineering Mechanics, 139(10), 1362-1371.

Zarnani, S., & Bathurst, R. J. (2008). Numerical modeling of EPS seismic buffer shaking table tests. Geotextiles and Geomembranes, 26(5), 371-383.

Zornberg, J. G., Cabral, A. R., & Viratjandr, C. (2004). Behaviour of tire shred sand mixtures. Canadian Geotechnical Journal, 41(2), 227-241.

Appendix A

Collations of results for SRM

Sr0.25

Rubber content (%)	V_s (m/s)				V_p (m/s)		
	Effective confining Pressure (kPa)						
	50	**100**	**200**	**400**	**100**	**200**	**400**
0	187	222	257	315	428	512	625
30	160.00	180	237	280	420	505	605
50	130	138	188	220		437	570
70			150	180			508
100			66	73			461

Rubber content (%)	G_{max} (kPa)			
	Effective confining Pressure (kPa)			
	50	**100**	**200**	**400**
0	512.97	558.98	704.99	866.26
30	264.72	340.12	450.25	595.62
50	130.00	149.16	203.19	259.40
70			105.24	113.19
100			21.46	23.01

Rubber content (%)	ξs (%)		
	Effective confining Pressure (kPa)		
	100	**200**	**400**
0	4.54	2.49	3.32
30	5.74	5.74	5.34
50	6.26	6.03	5.80
70		7.98	7.81
100		11.58	12.06

Rubber content (%)	Friction angle (ϕ')
0	43
30	28
50	25
70	22
100	17

Sr0.5

Rubber content (%)	V_s (m/s)				V_p (m/s)		
	Effective confining Pressure (kPa)						
	50	**100**	**200**	**400**	**100**	**200**	**400**
0	187	222	257	315	428	512	625
30	159	175	230	270	419	500	600
50	119	133	171	202		425	562
70			145	187			500
100			66	73			461

Rubber content (%)	G_{max} (kPa)			
	Effective confining Pressure (kPa)			
	50	**100**	**200**	**400**
0	512.97	558.98	704.99	866.26
30	279.61	339.17	413.63	562.53
50	156.72	144.11	185.28	240.18
70			91.18	117.90
100			21.46	23.01

Rubber content (%)	ξs (%)		
	Effective confining Pressure (kPa)		
	100	**200**	**400**
0	4.54	2.49	3.32
30	5.22	5.97	5.40
50	7.23	6.76	5.83
70		9.31	8.45
100		12.05	12.75

Rubber content (%)	Friction angle (ϕ')
0	43
30	27
50	23
70	22
100	17

Sr2

Rubber content (%)	V_s (m/s)				V_p (m/s)		
	Effective confining Pressure (kPa)						
	50	**100**	**200**	**400**	**100**	**200**	**400**
0	187	222	257	315	428	512	625
30	141	170	216	260	400	461	600
50	130	131	170	202		400	545
70			130	170			461
100			66	73			

Rubber content (%)	G_{max} (kPa)			
	Effective confining Pressure (kPa)			
	50	**100**	**200**	**400**
0	512.97	558.98	704.99	866.26
30	233.28	314.35	420.52	545.99
50	140.50	191.59	253.74	327.78
70			95.38	106.90
100			21.46	23.01

Rubber content (%)	ξs (%)		
	Effective confining Pressure (kPa)		
	100	**200**	**400**
0	4.54	2.49	3.32
30	5.97	6.20	6.14
50	7.50	7.04	6.70
70		8.62	8.10
100		12.05	12.75

Rubber content (%)	Friction angle (ϕ')
0	43
30	25
50	22
70	21
100	17

Sr4

Rubber content (%)	V_s (m/s)				V_p (m/s)		
	Effective confining Pressure (kPa)						
	50	**100**	**200**	**400**	**100**	**200**	**400**
0	187	222	257	315	428	512	625
30	126	160	180	220	381	452	580
50	100	120	163	180		380	529
70			100	163			482
100			66	73			

Rubber content (%)	G_{max} (kPa)			
	Effective confining Pressure (kPa)			
	50	**100**	**200**	**400**
0	512.97	558.98	704.99	866.26
30	208.46	297.81	390.43	490.17
50	108.08	189.70	236.17	296.16
70			62.88	102.49
100			21.46	23.01

Rubber content (%)	ξs (%)		
	Effective confining Pressure (kPa)		
	100	**200**	**400**
0	4.54	2.49	3.32
30	6.66	8.04	6.26
50	9.71	9.65	9.42
70		10.68	10.34
100		11.58	12.06

Rubber content (%)	Friction angle (ϕ')
0	43
30	23
50	21
70	20
100	17

Sr8

Rubber content (%)	V_s (m/s)				V_p (m/s)		
	Effective confining Pressure (kPa)						
	50	**100**	**200**	**400**	**100**	**200**	**400**
0	187	222	257	315	428.	512	625
30	120	130	160	200	372	442	550
50	100	106	150	180		369	516
70			117	150			482
100			66	73			

Rubber content (%)	G_{max} (kPa)			
	Effective confining Pressure (kPa)			
	50	**100**	**200**	**400**
0	512.97	558.98	704.99	866.26
30	198.54	248.17	297.81	397.08
50	126.46	134.57	200.00	274.54
70			73.57	106.90
100			21.46	23.01

Rubber content (%)	ξs (%)		
	Effective confining Pressure (kPa)		
	100	**200**	**400**
0	4.54	2.49	3.32
30	7.52	8.27	7.64
50	10.51	10.05	9.82
70		10.86	11.72
100		12.05	12.75

Rubber content (%)	Friction angle (ϕ')
0	43
30	22
50	20
70	19
100	17

Appendix B

Small scale field test's data for surface vibrations

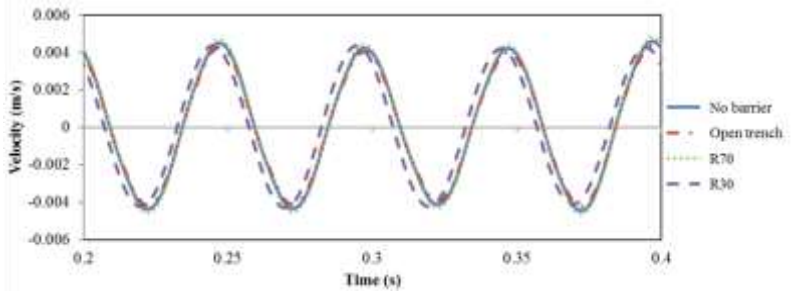

a) Geophone 1

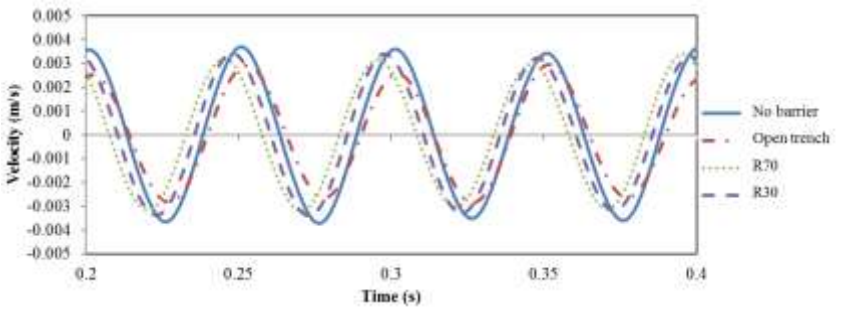

b) Geophone 2

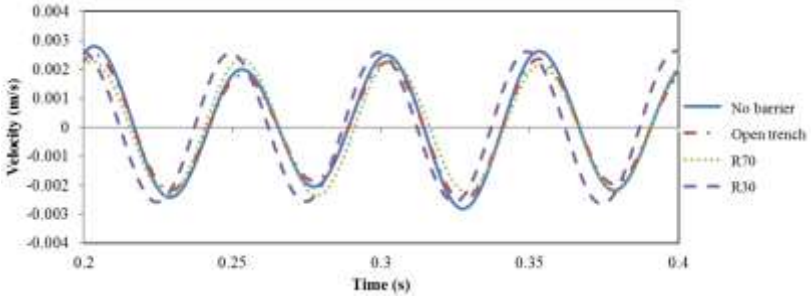

c) Geophone 3

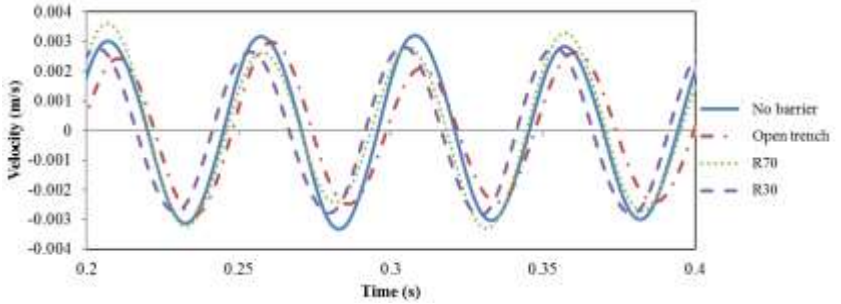

d) Geophone 4

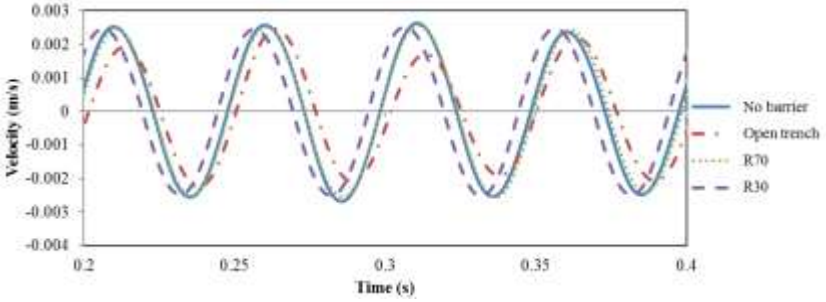

e) Geophone 5

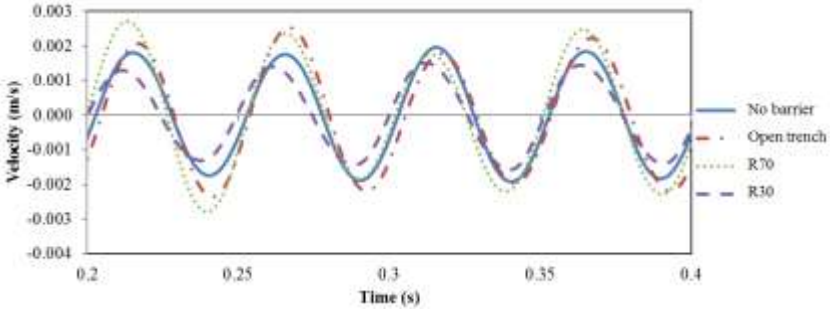

f) Geophone 6

Figure B-1 Geophones' signals for 20 Hz, line 1

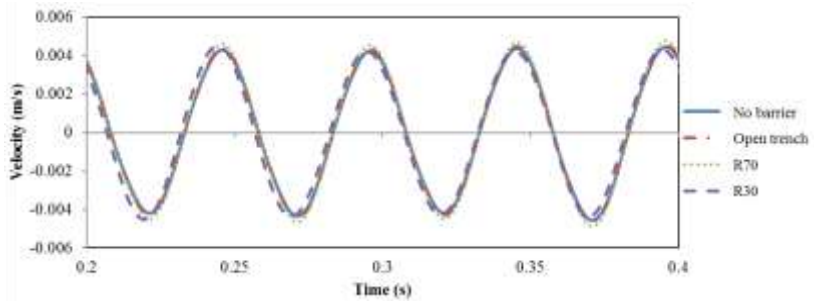

a) Geophone 1

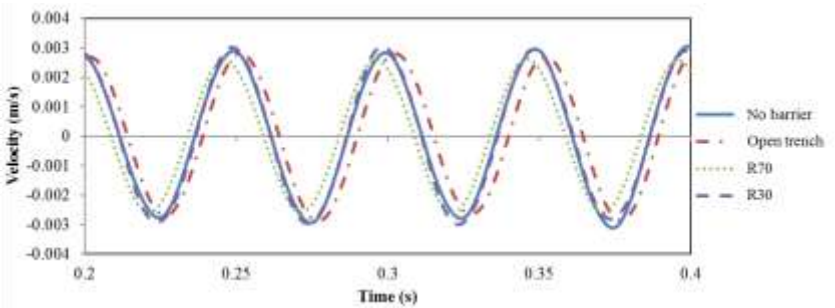

b) Geophone 2

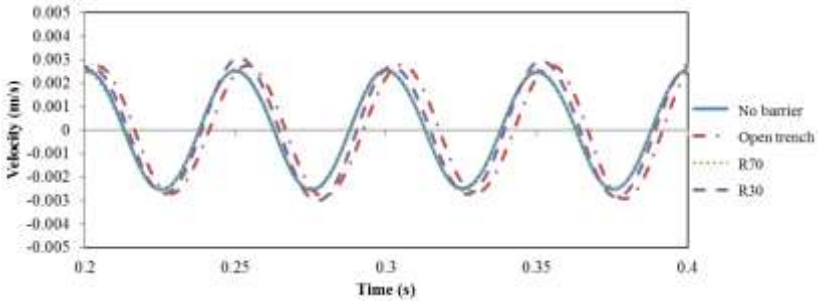

c) Geophone 3

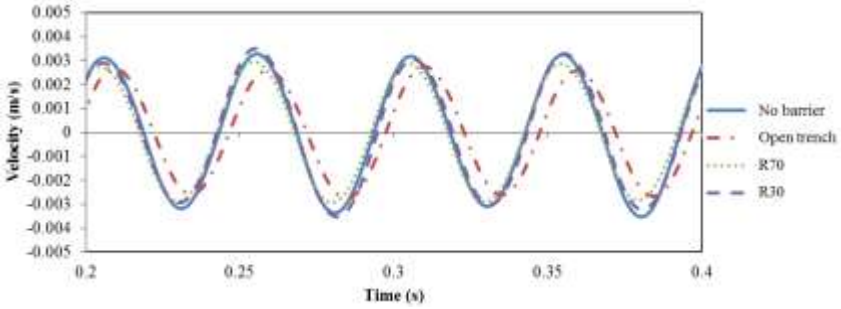

d) Geophone 4

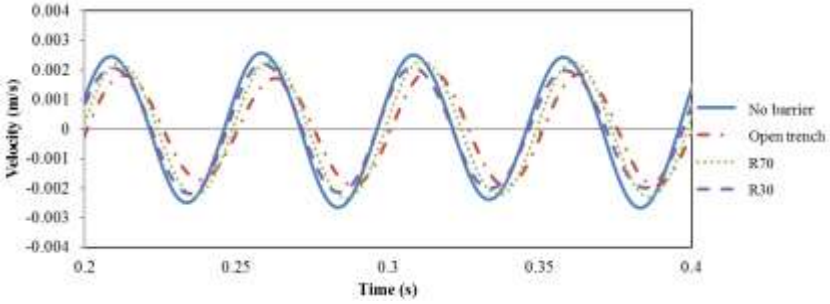

e) Geophone 5

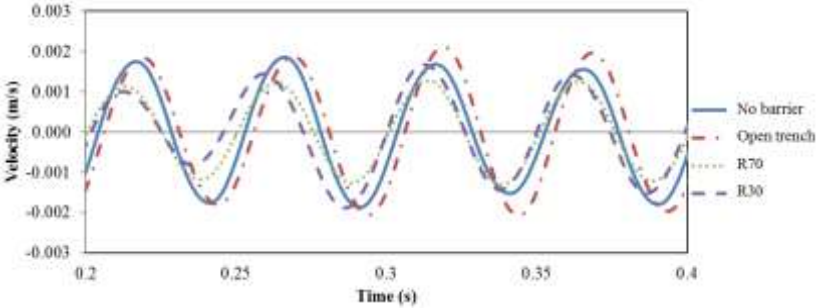

f) Geophone 6

Figure B-2 Geophones' signals for 20 Hz, line 2

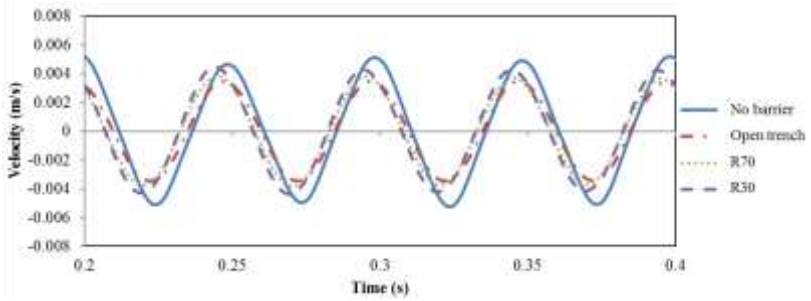

a) Geophone 1

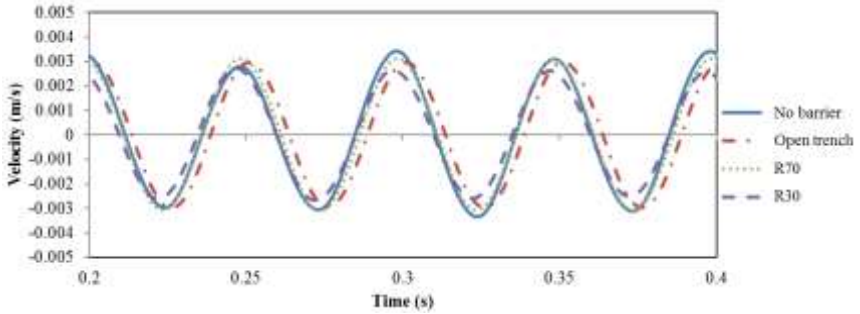

b) Geophone 2

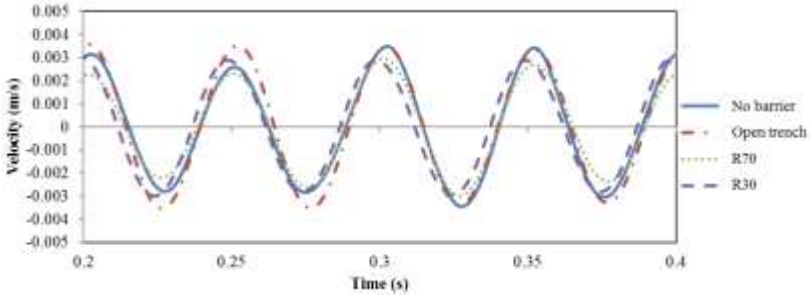

c) Geophone 3

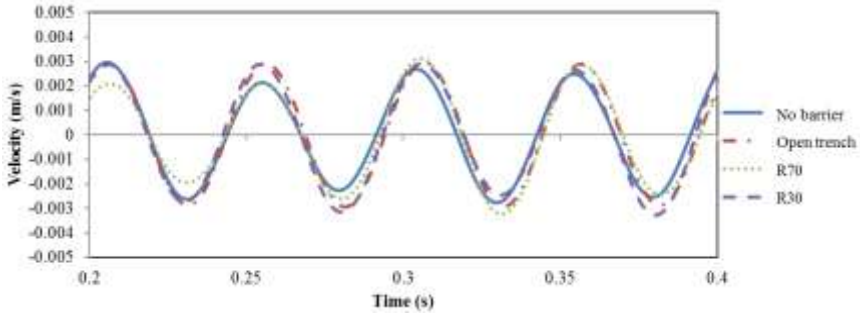

d) Geophone 4

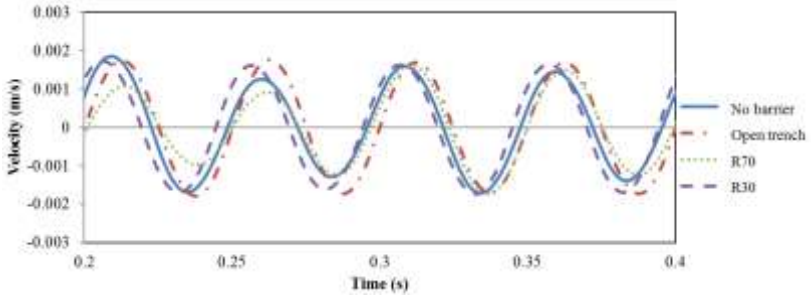

e) Geophone 5

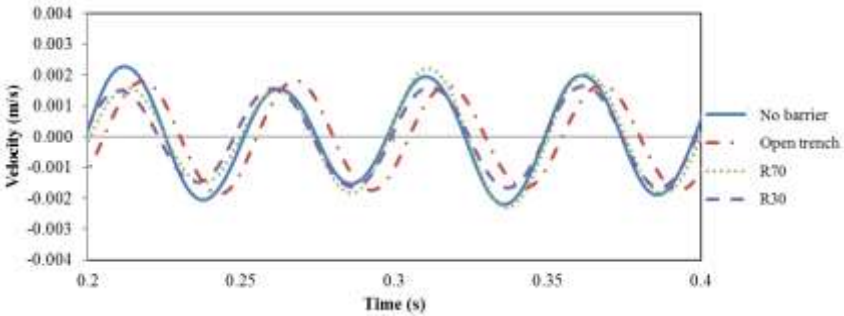

f) Geophone 6

Figure B-3 Geophones' signals for 20 Hz, line 3

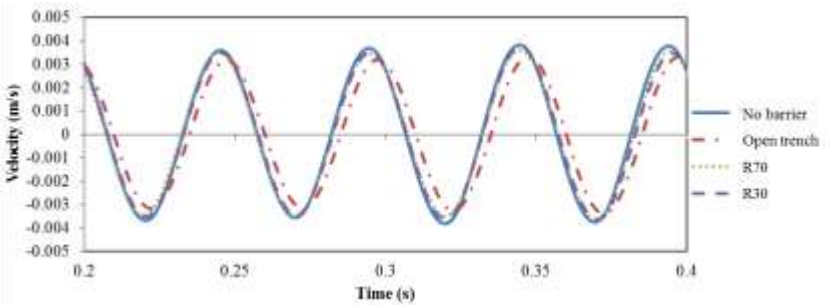

a) Geophone 1

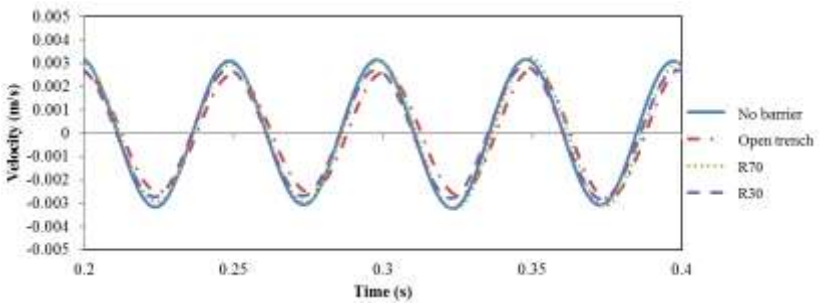

b) Geophone 2

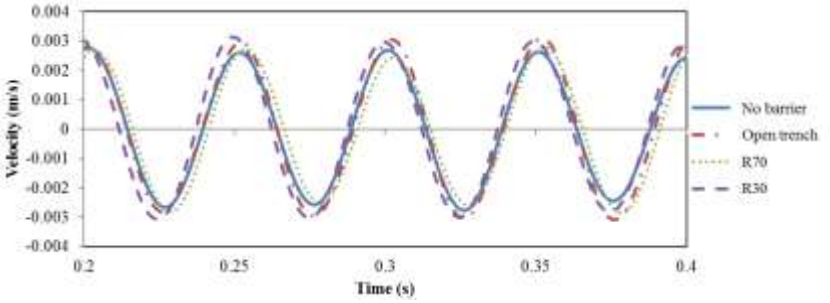

c) Geophone 3

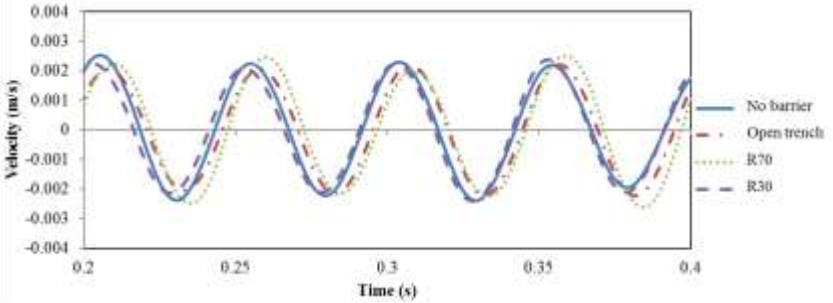

d) Geophone 4

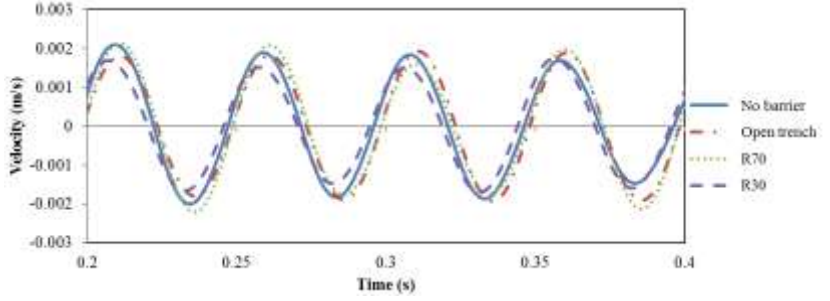

e) Geophone 5

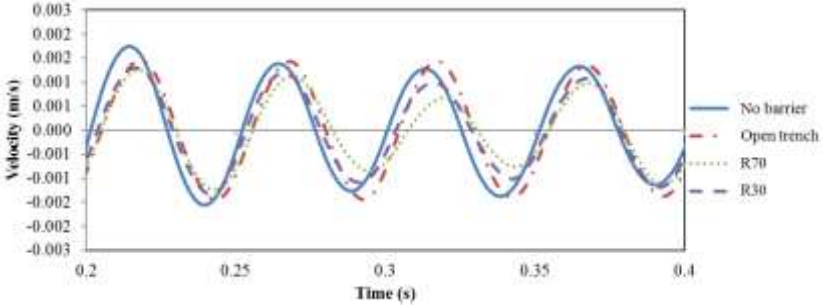

f) Geophone 6

Figure B-4 Geophones' signals for 20 Hz, line 4

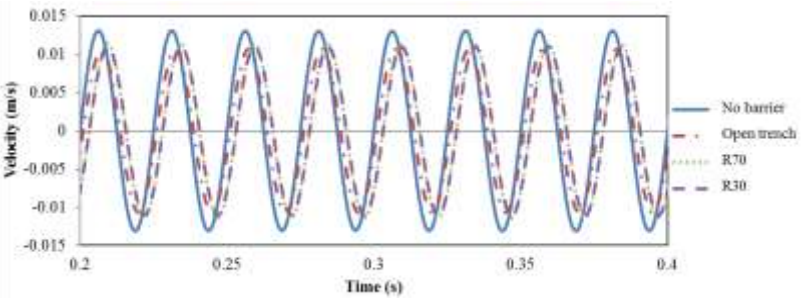

a) Geophone 1

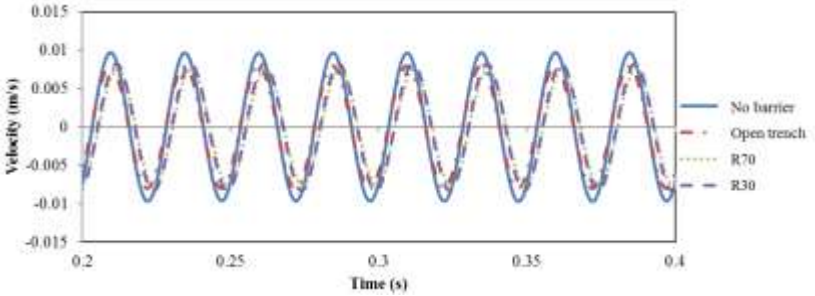

b) Geophone 2

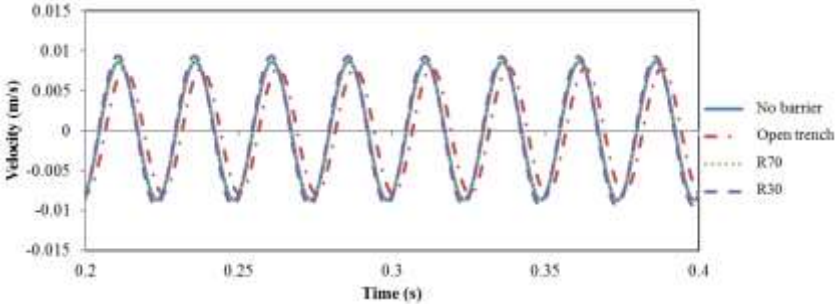

c) Geophone 3

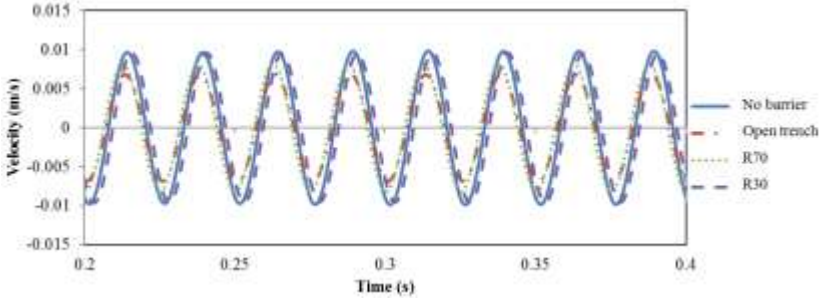

d) Geophone 4

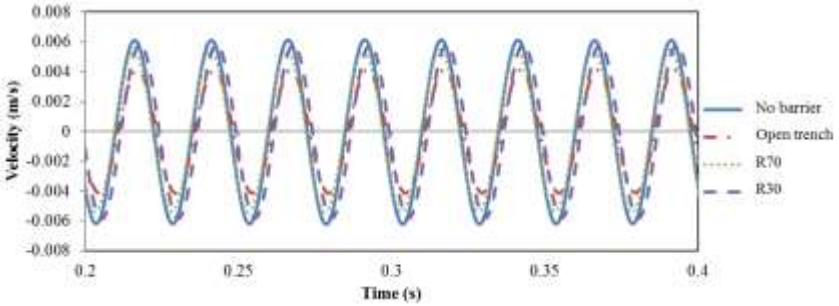

e) Geophone 5

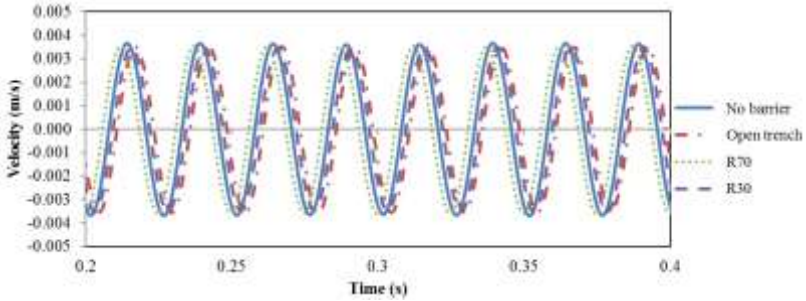

f) Geophone 6

Figure B-5 Geophones' signals for 40 Hz, line 1

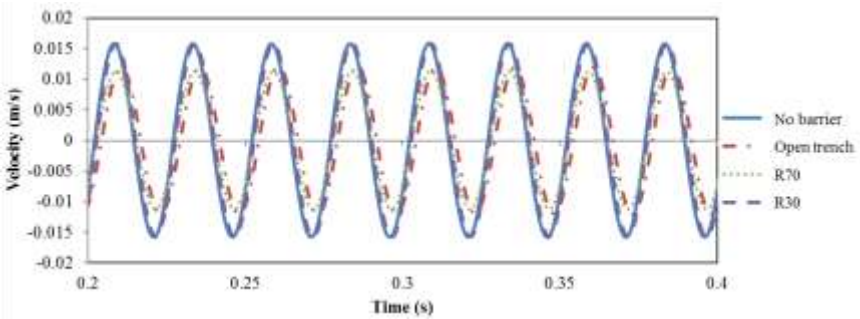

a) Geophone 1

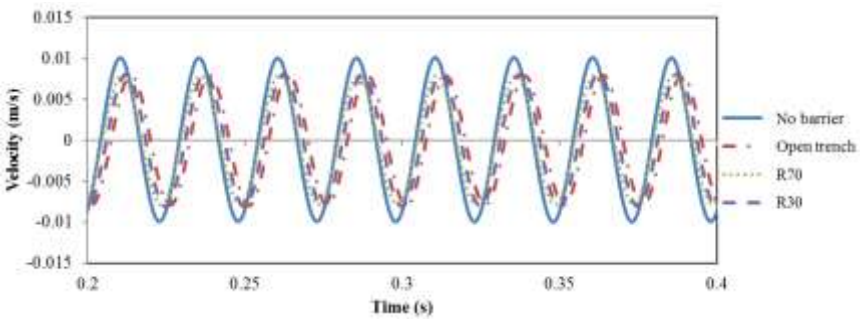

b) Geophone 2

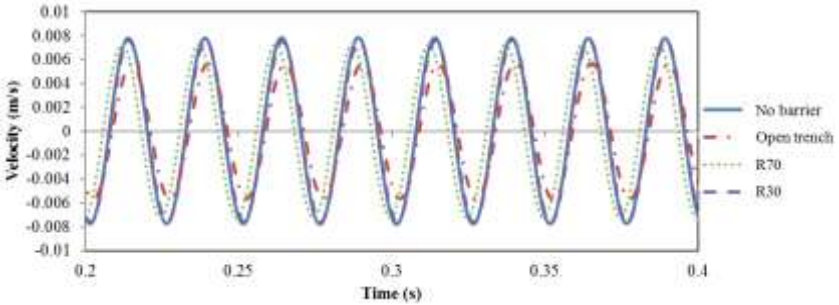

c) Geophone 3

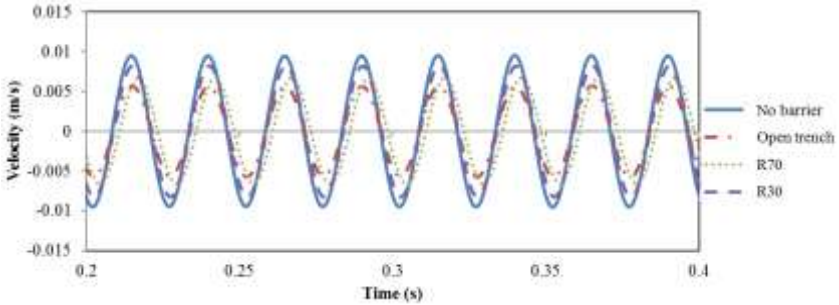

d) Geophone 4

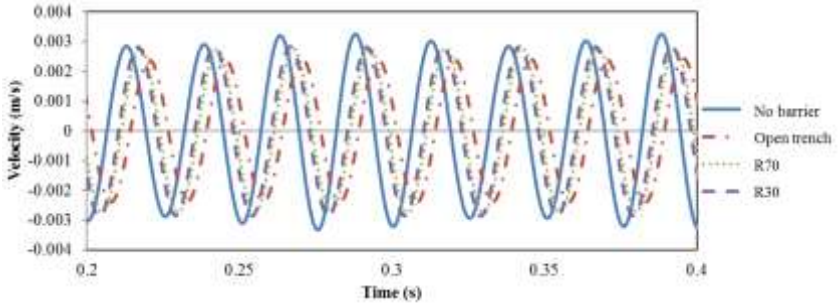

e) Geophone 5

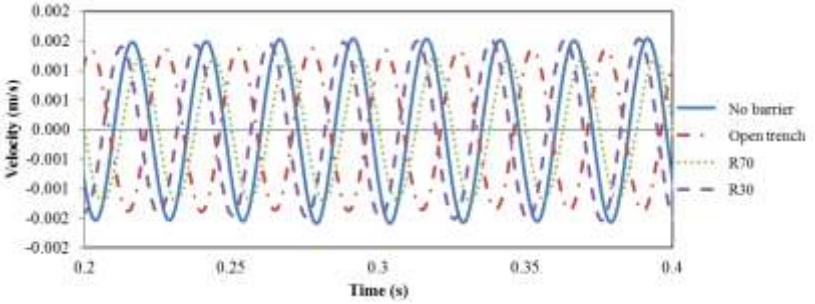

f) Geophone 6

Figure B-6 Geophones' signals for 40 Hz, line 2

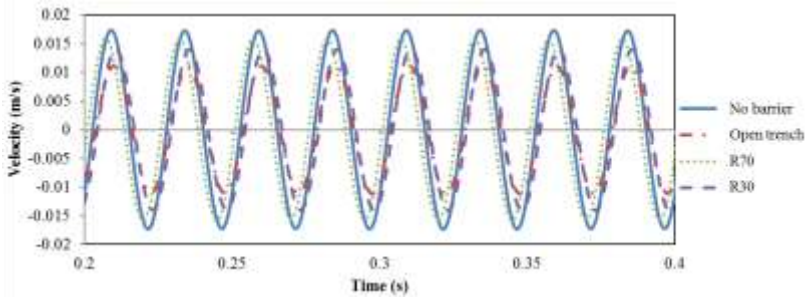

a) Geophone 1

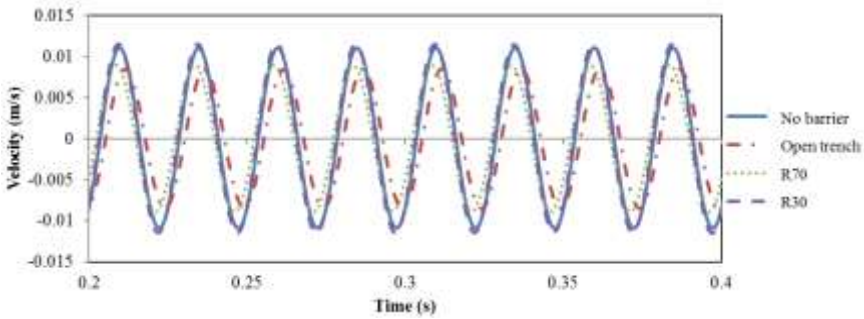

b) Geophone 2

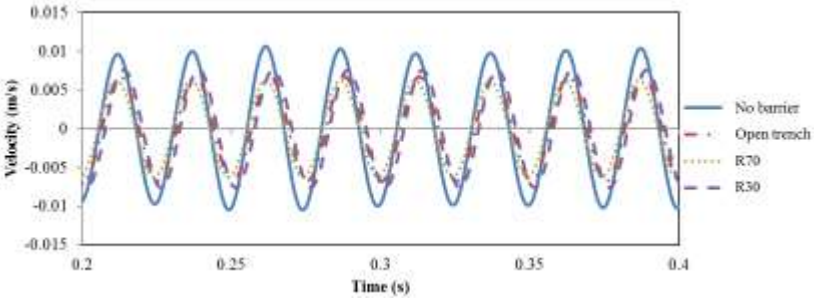

c) Geophone 3

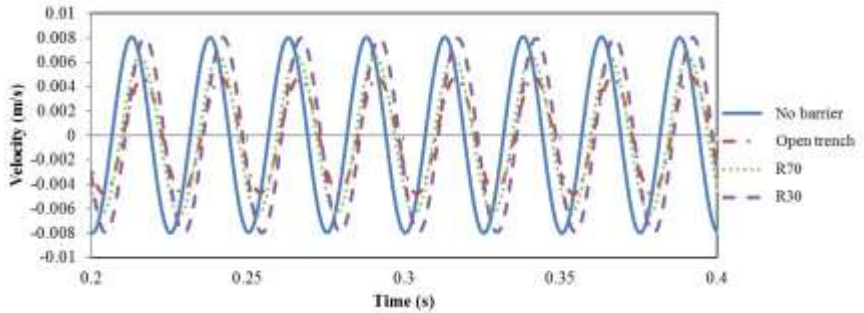

d) Geophone 4

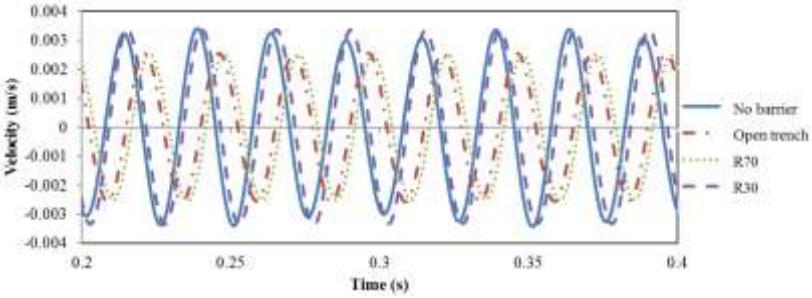

e) Geophone 5

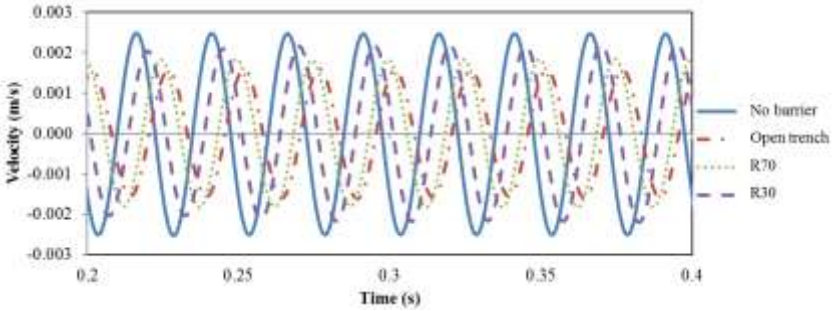

f) Geophone 6

Figure B-7 Geophones' signals for 40 Hz, line 3

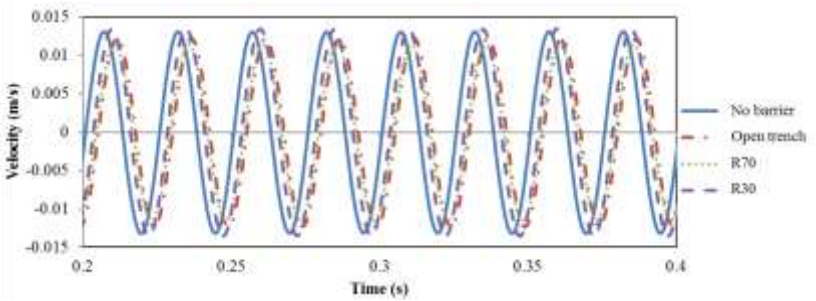

a) Geophone 1

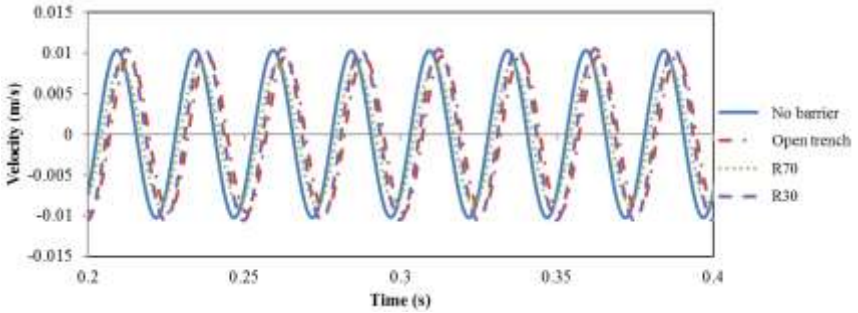

b) Geophone 2

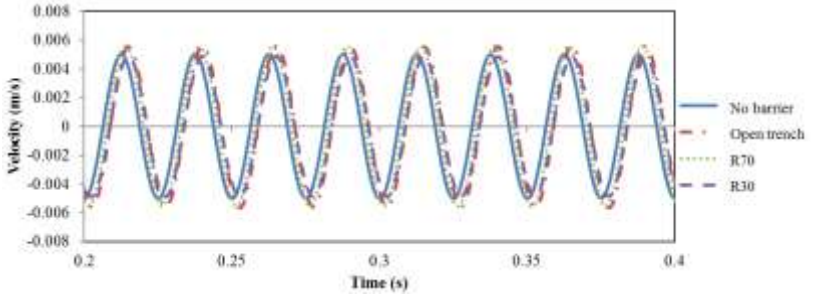

c) Geophone 3

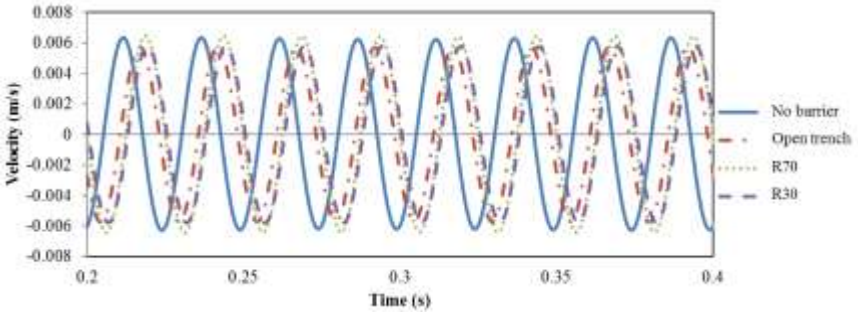

d) Geophone 4

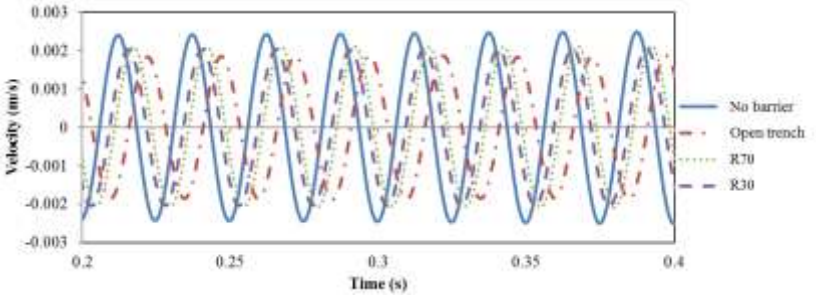

e) Geophone 5

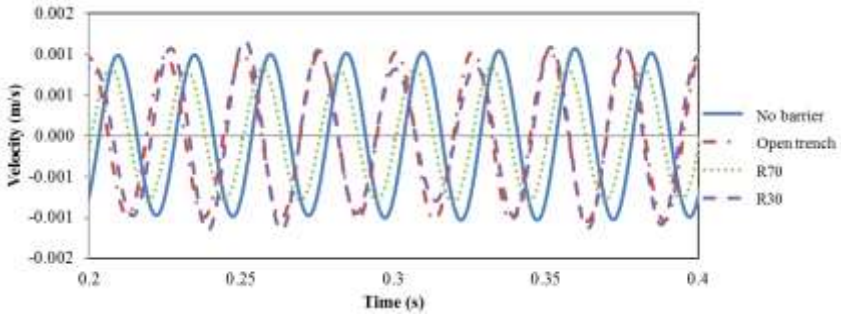

f) Geophone 6

Figure B-8 Geophones' signals for 40 Hz, line 4

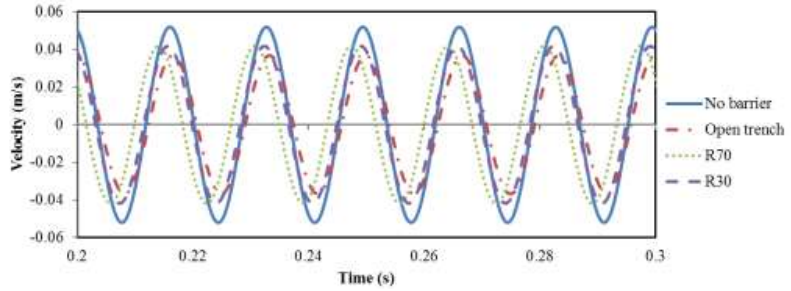

a) Geophone 1

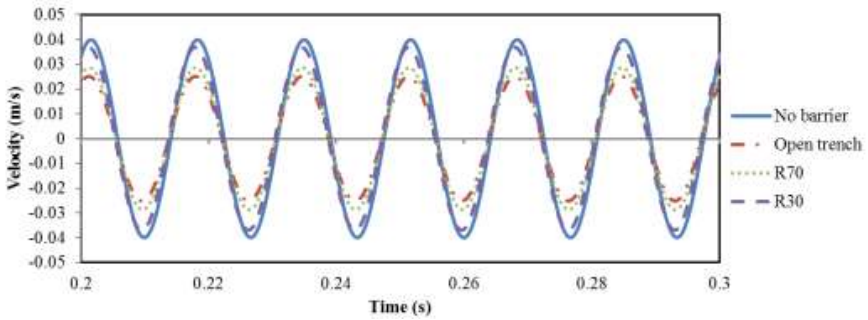

b) Geophone 2

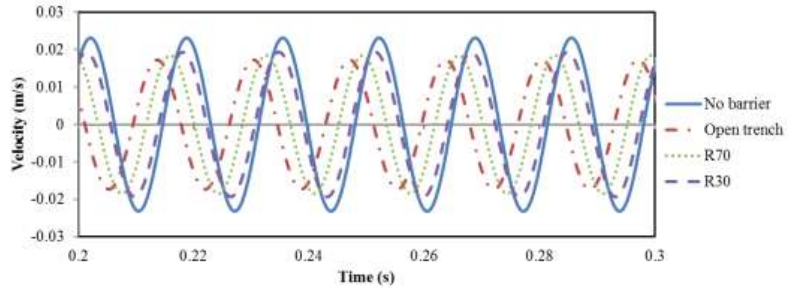

c) Geophone 3

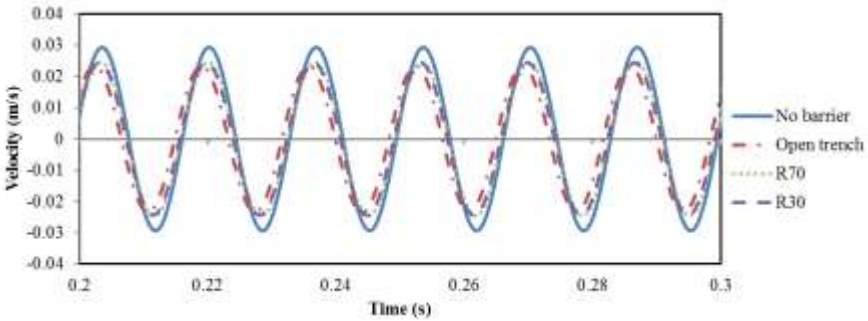

d) Geophone 4

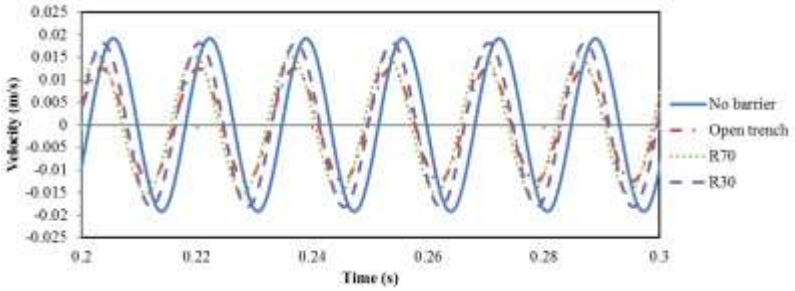

e) Geophone 5

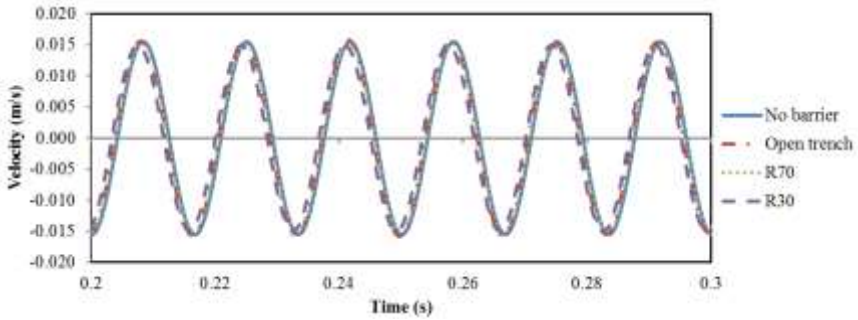

f) Geophone 6

Figure B-9 Geophones' signals for 60 Hz, line 1

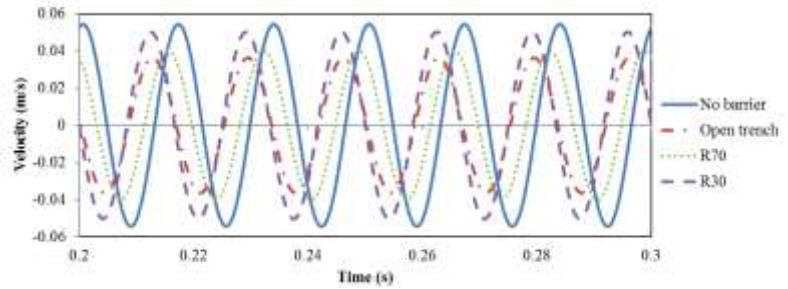

a) Geophone 1

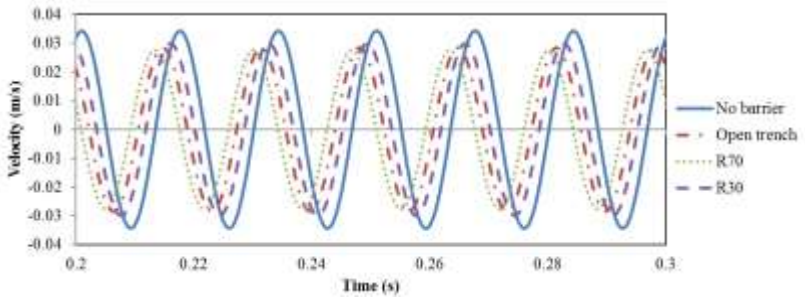

b) Geophone 2

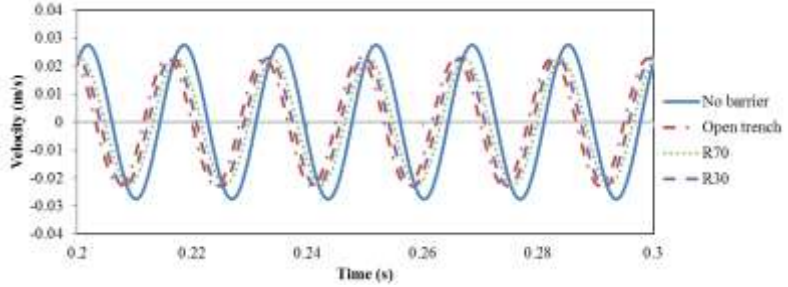

c) Geophone 3

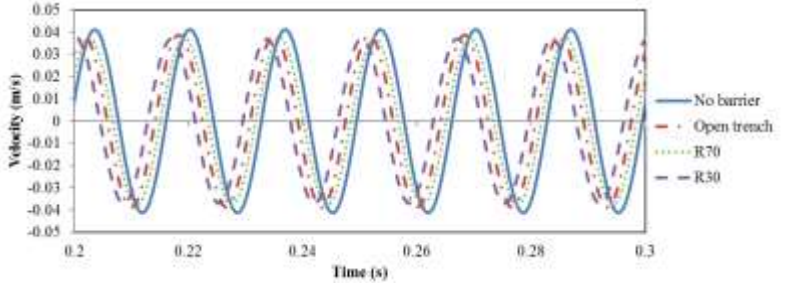

d) Geophone 4

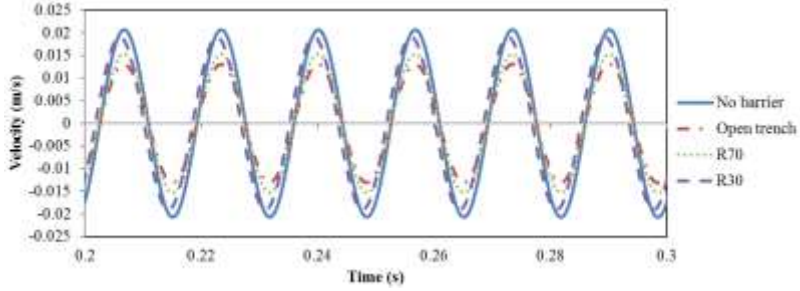

e) Geophone 5

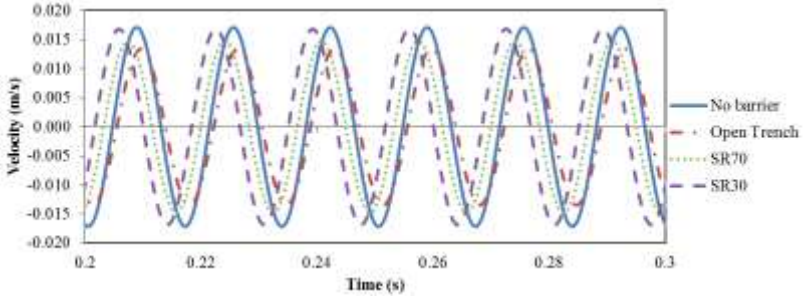

f) Geophone 6

Figure B-10 Geophones' signals for 60 Hz, line 2

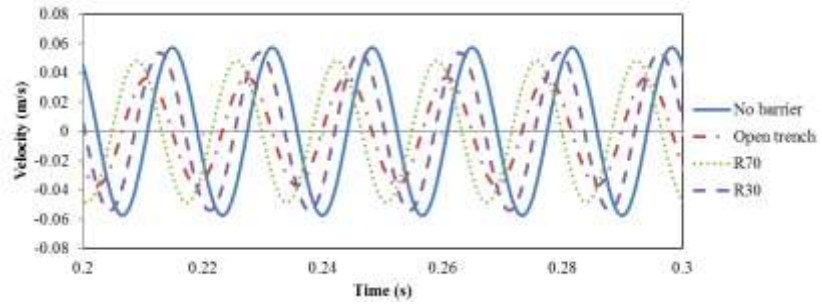

a) Geophone 1

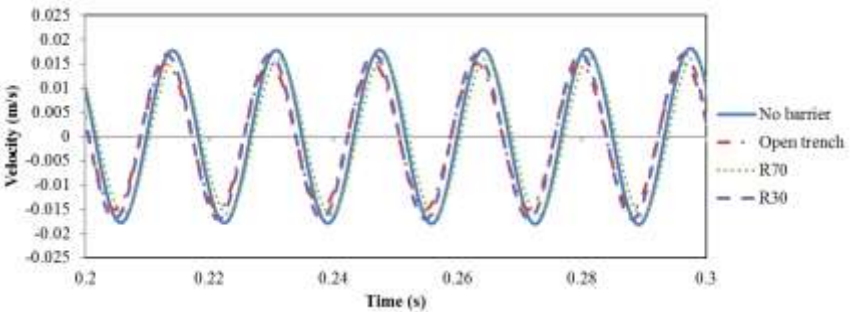

b) Geophone 2

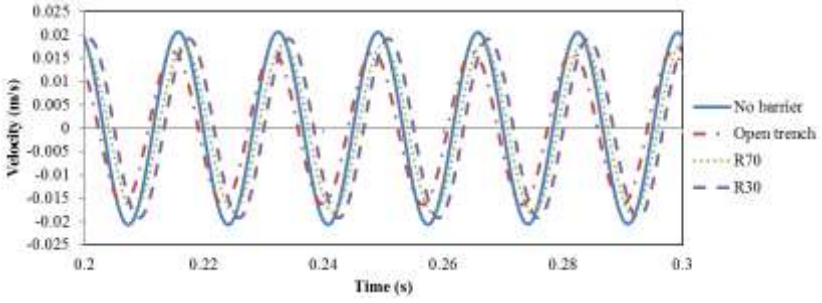

c) Geophone 3

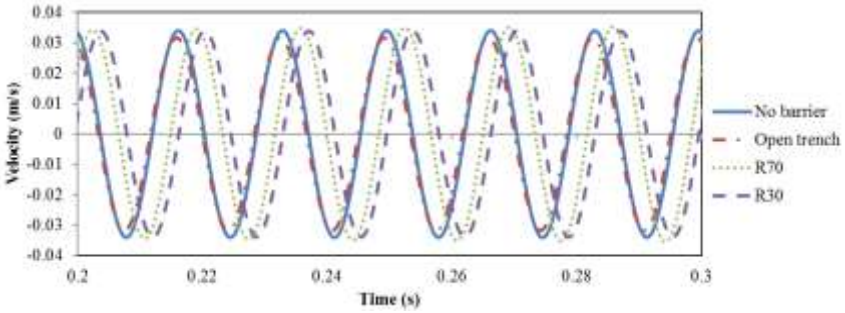

d) Geophone 4

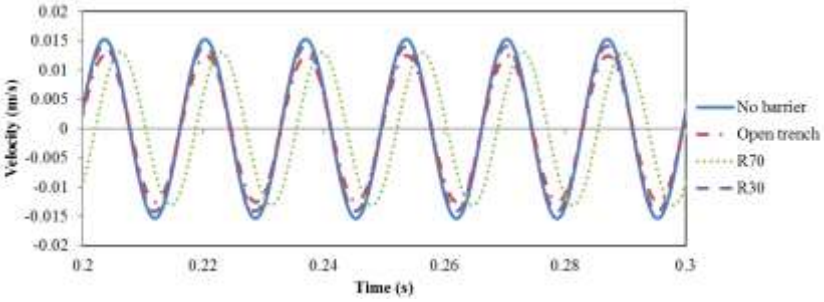

e) Geophone 5

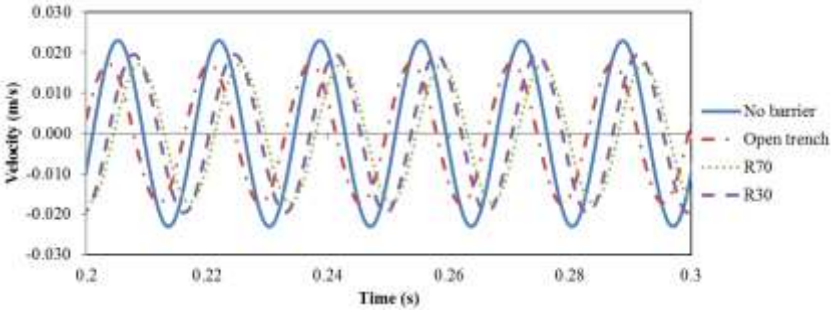

f) Geophone 6

Figure B-11 Geophones' signals for 60 Hz, line 3

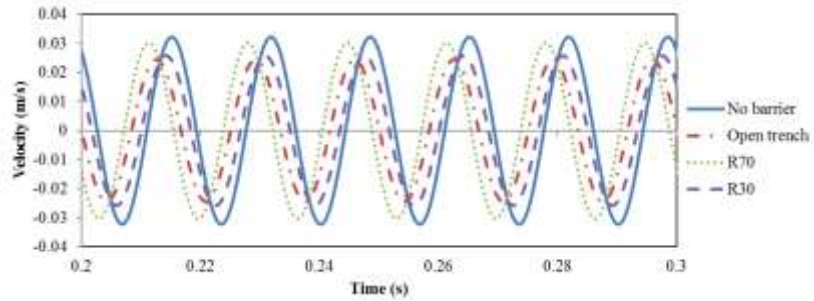

a) Geophone 1

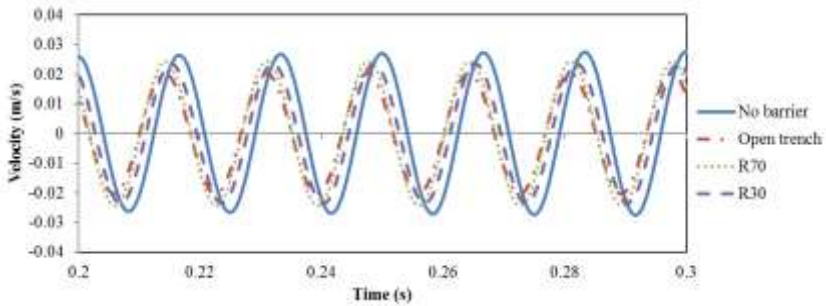

b) Geophone 2

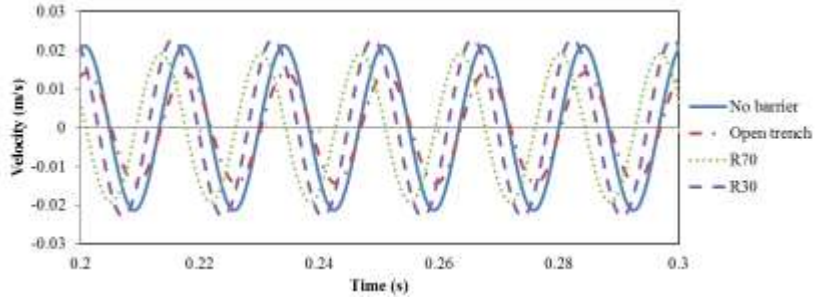

c) Geophone 3

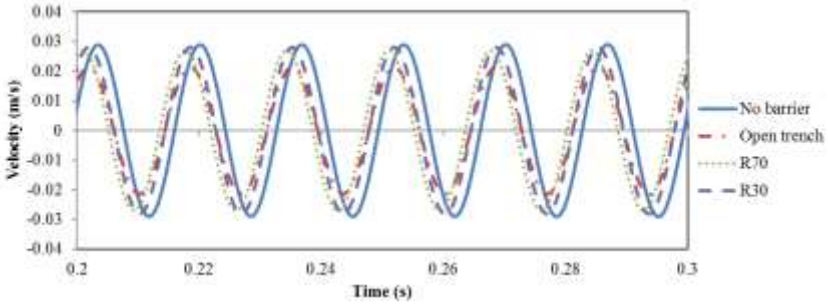

d) Geophone 4

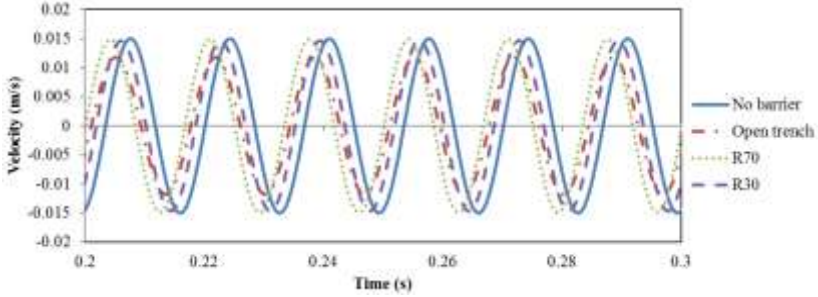

e) Geophone 5

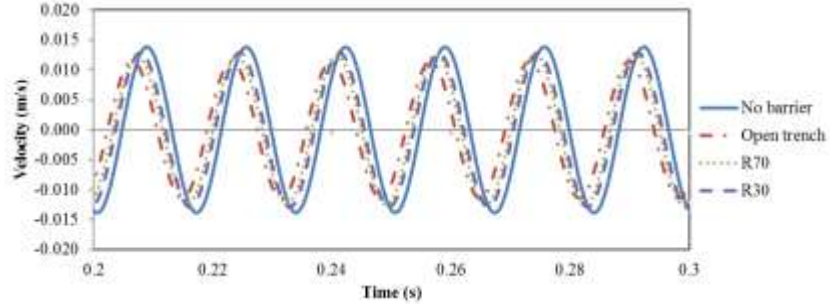

f) Geophone 6

Figure B-12 Geophones' signals for 60 Hz, line 4

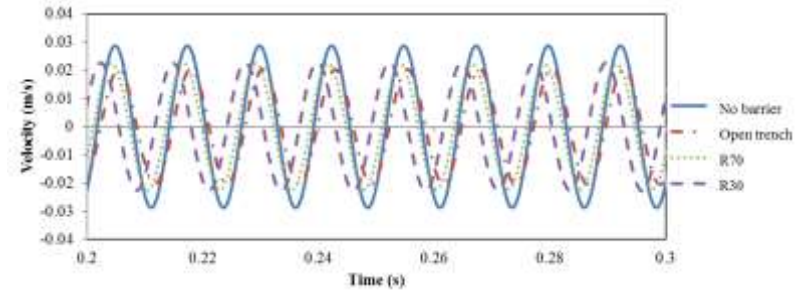

a) Geophone 1

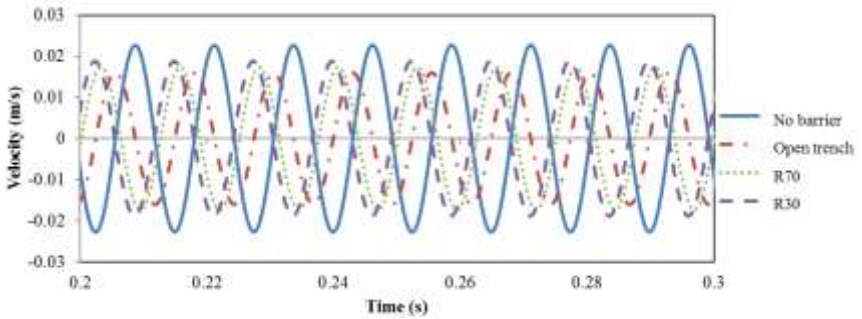

b) Geophone 2

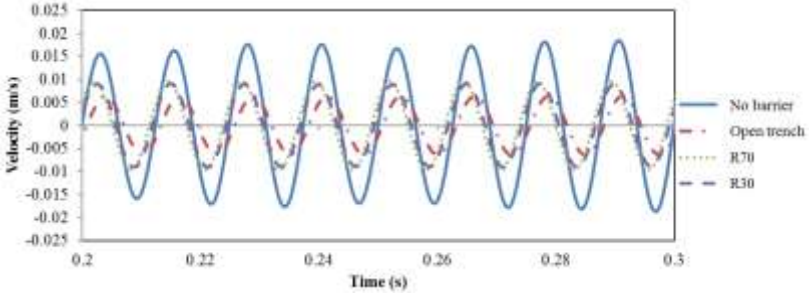

c) Geophone 3

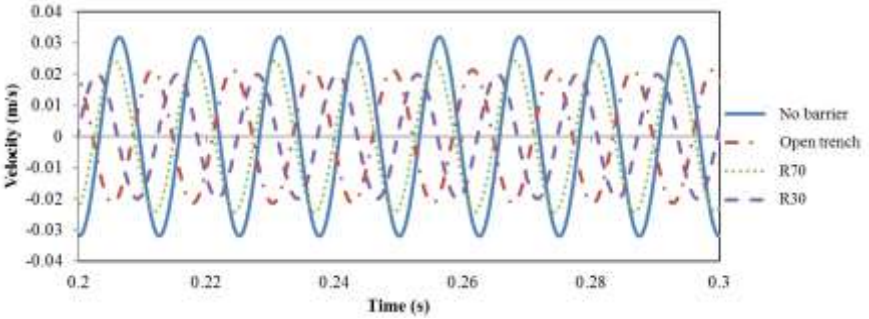

d) Geophone 4

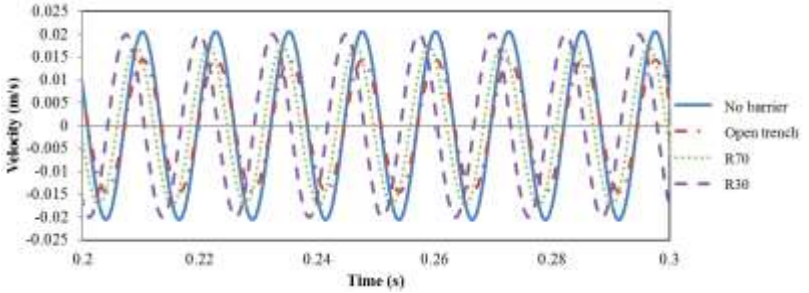

e) Geophone 5

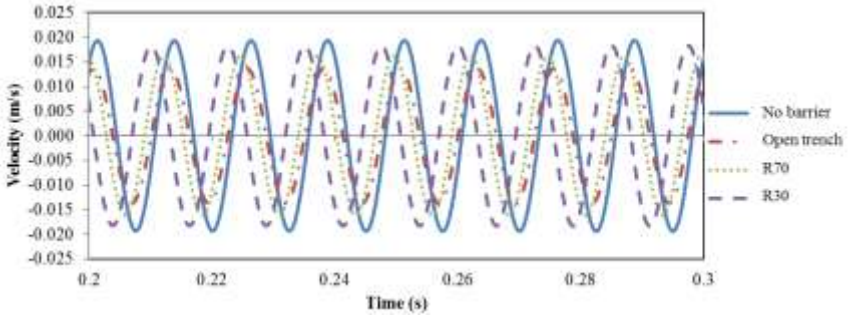

f) Geophone 6

Figure B-13 Geophones' signals for 80 Hz, line 1

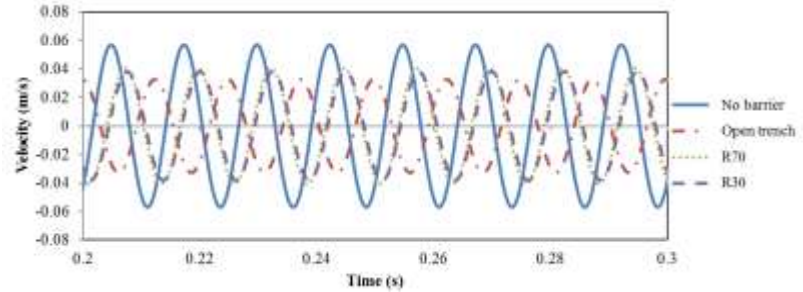

a) Geophone 1

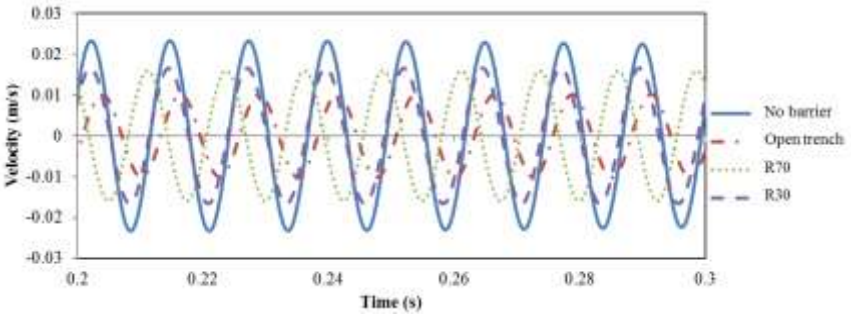

b) Geophone 2

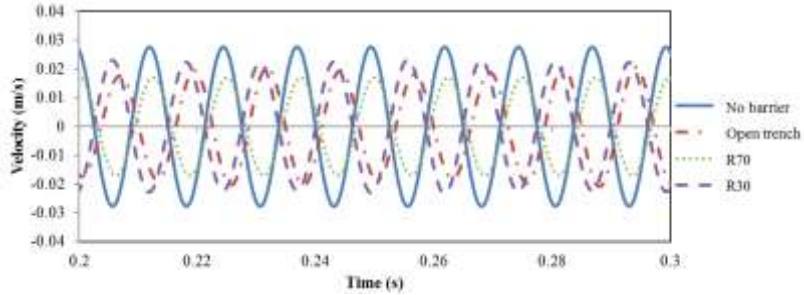

c) Geophone 3

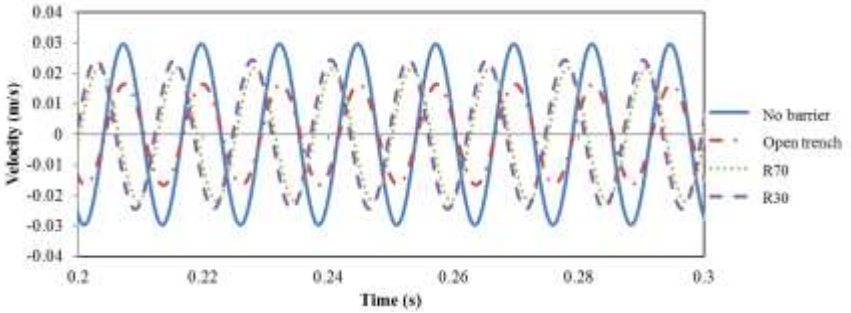

d) Geophone 4

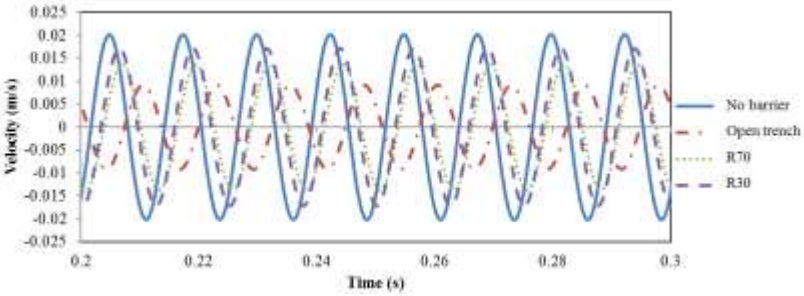

e) Geophone 5

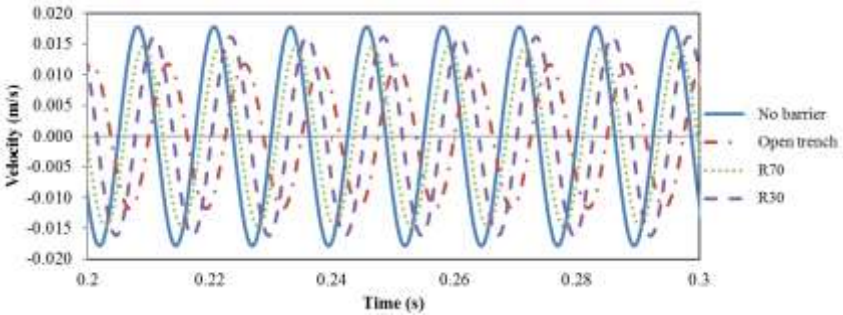

f) Geophone 6

Figure B-14 Geophones' signals for 80 Hz, line 2

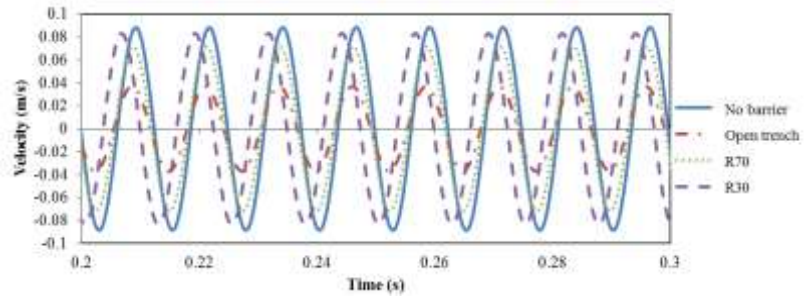

a) Geophone 1

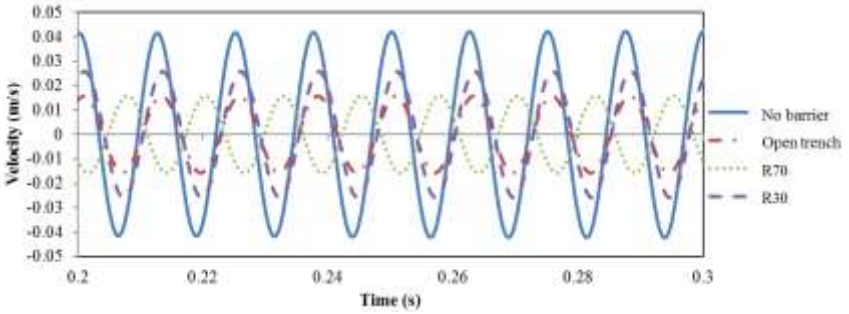

b) Geophone 2

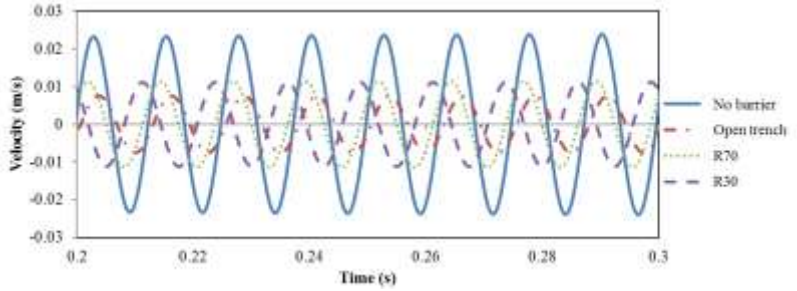

c) Geophone 3

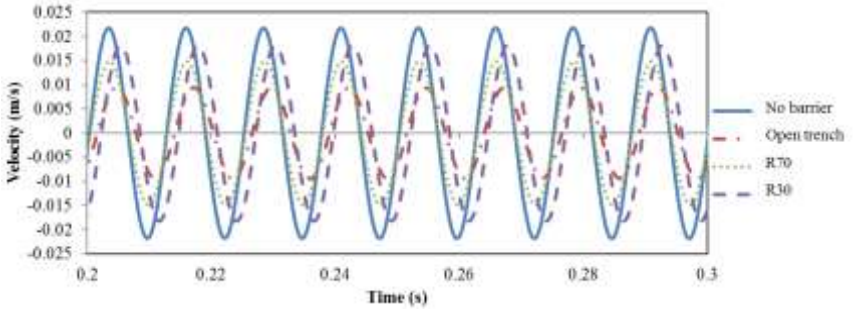

d) Geophone 4

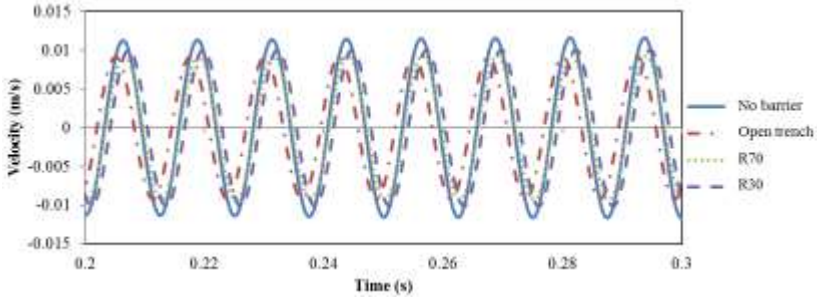

e) Geophone 5

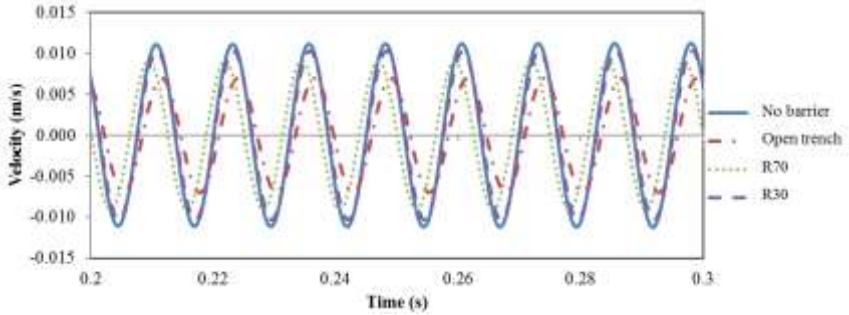

f) Geophone 6

Figure B-15 Geophones' signals for 80 Hz, line 3

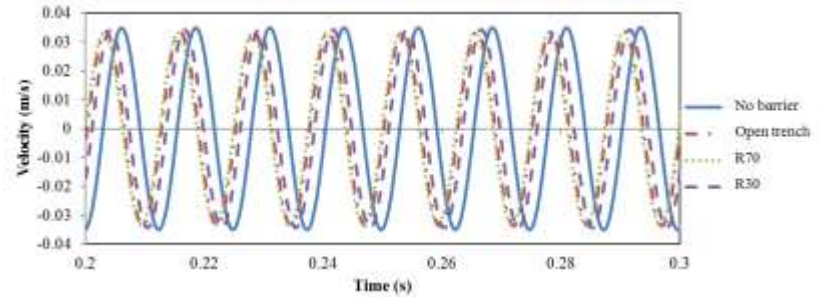

a) Geophone 1

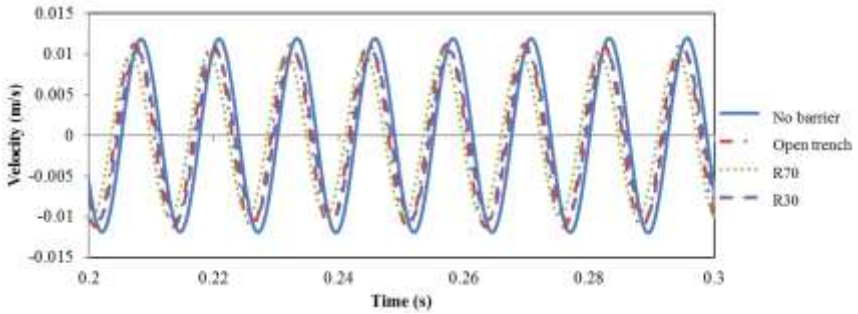

b) Geophone 2

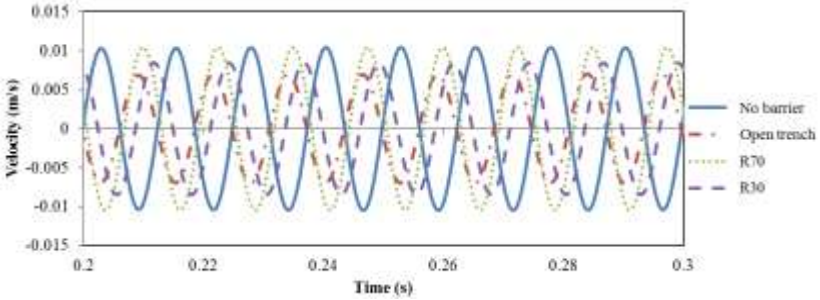

c) Geophone 3

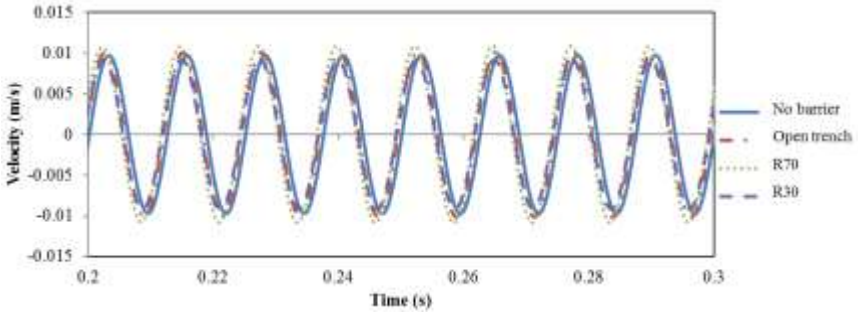

d) Geophone 4

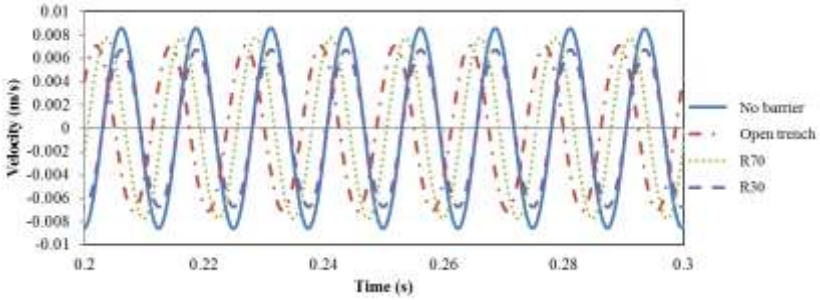

e) Geophone 5

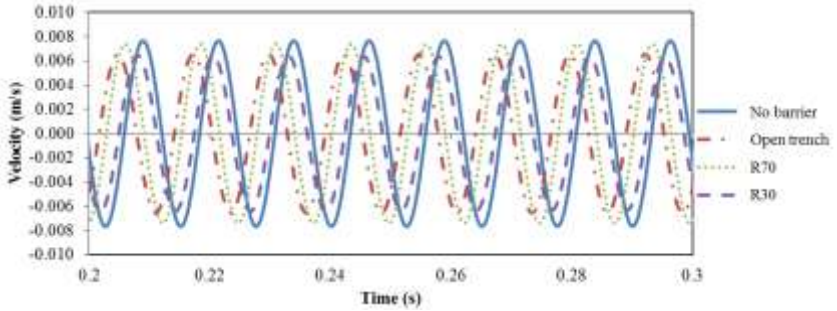

f) Geophone 6

Figure B-16 Geophones' signals for 80 Hz, line 4

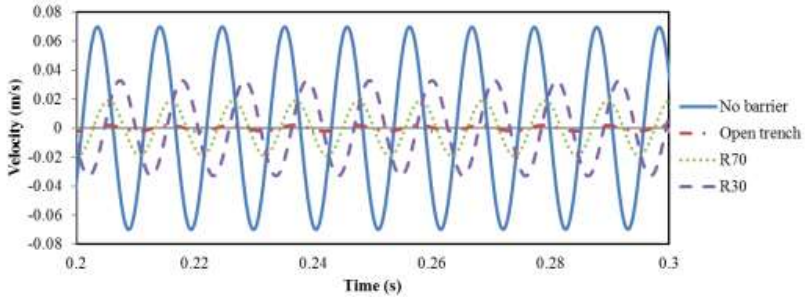

a) Geophone 1

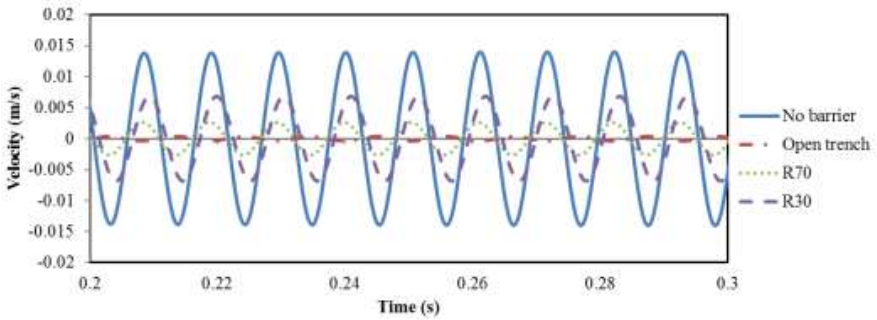

b) Geophone 2

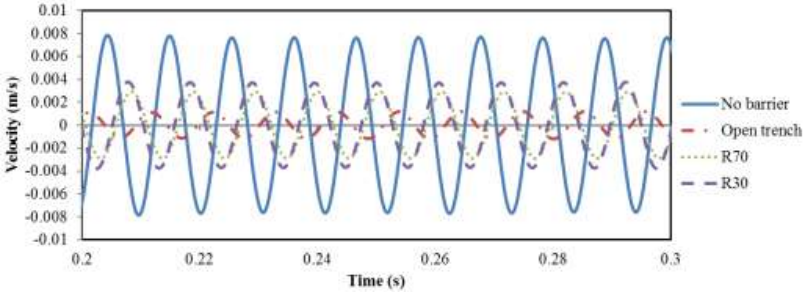

c) Geophone 3

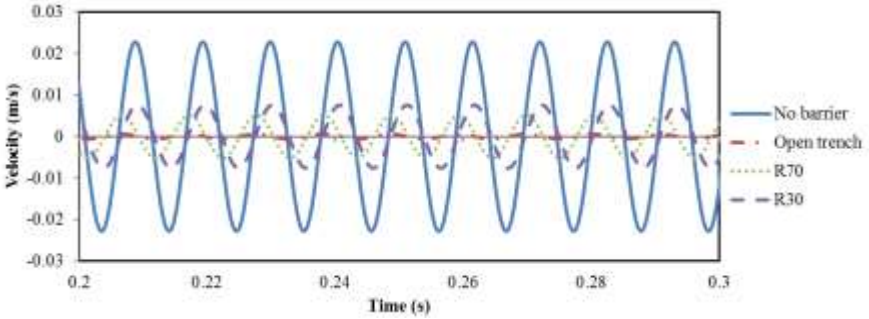

d) Geophone 4

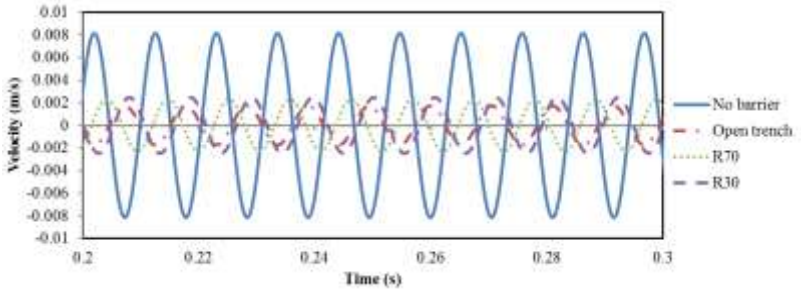

e) Geophone 5

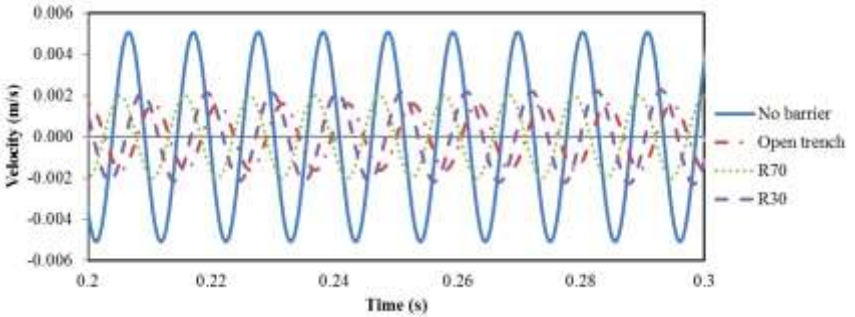

f) Geophone 6

Figure B-17 Geophones' signals for 95 Hz, line 1

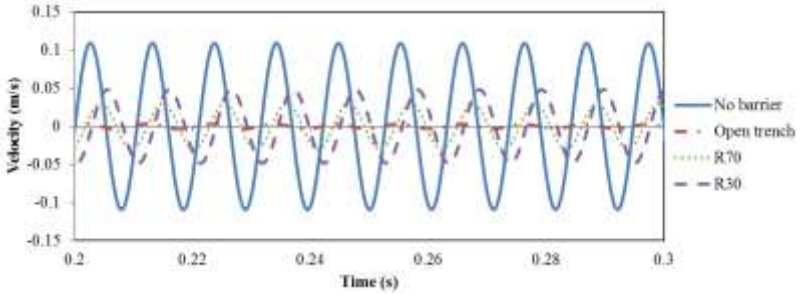

a) Geophone 1

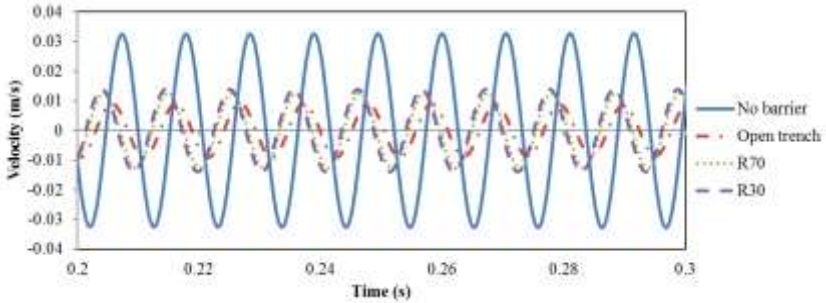

b) Geophone 2

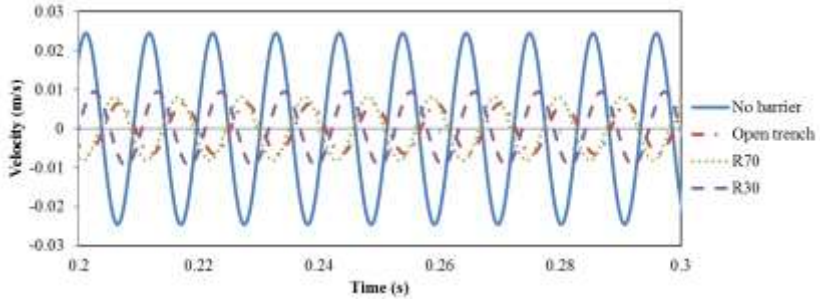

c) Geophone 3

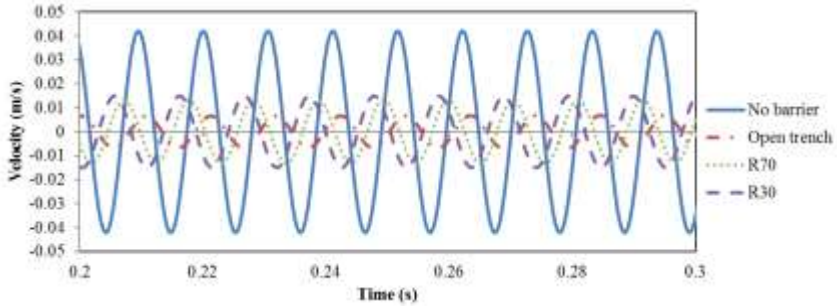

d) Geophone 4

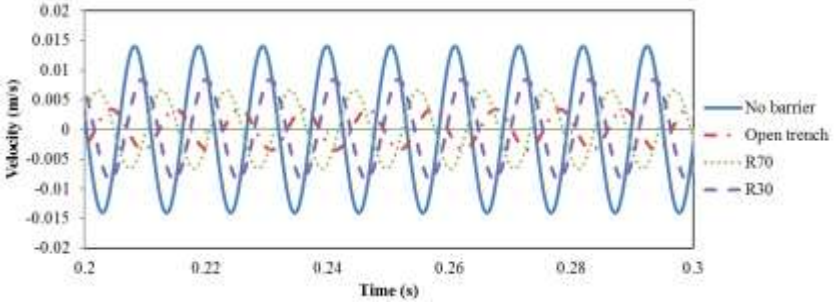

e) Geophone 5

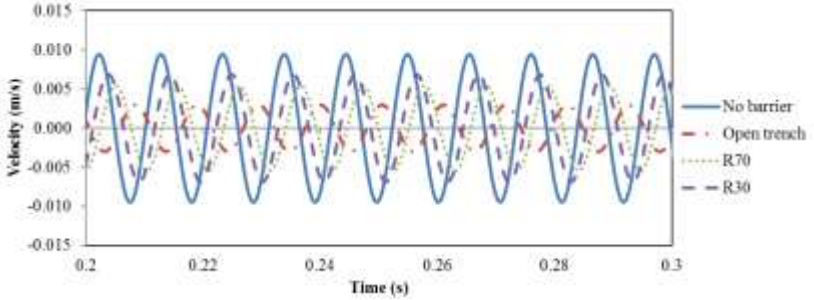

f) Geophone 6

Figure B-18 Geophones' signals for 95 Hz, line 2

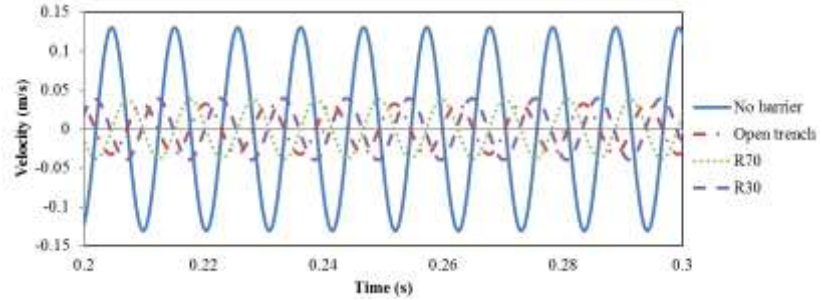

a) Geophone 1

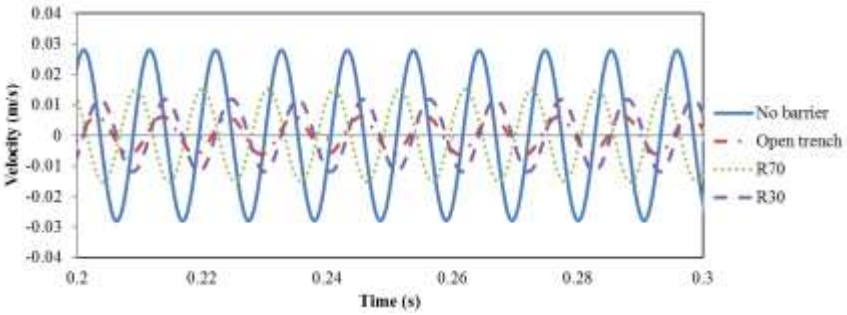

b) Geophone 2

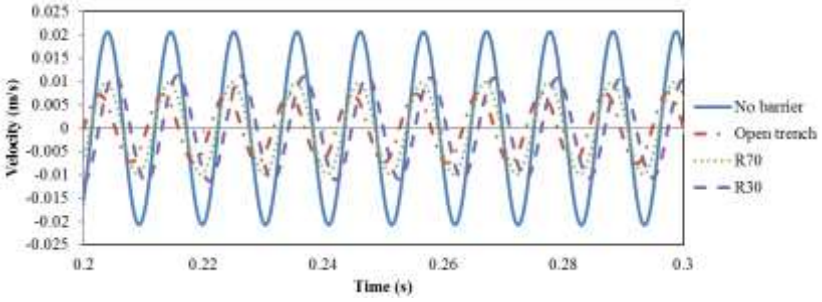

c) Geophone 3

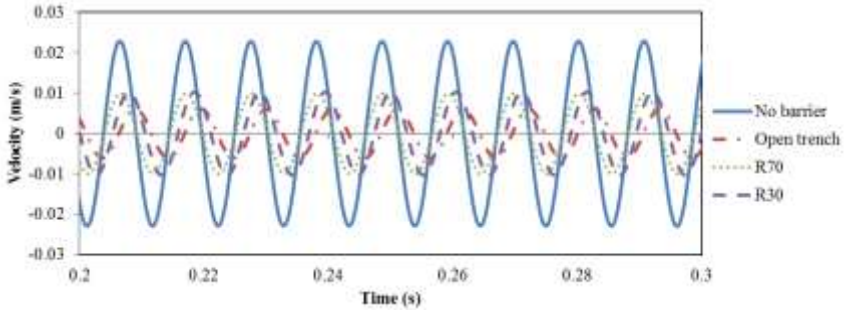

d) Geophone 4

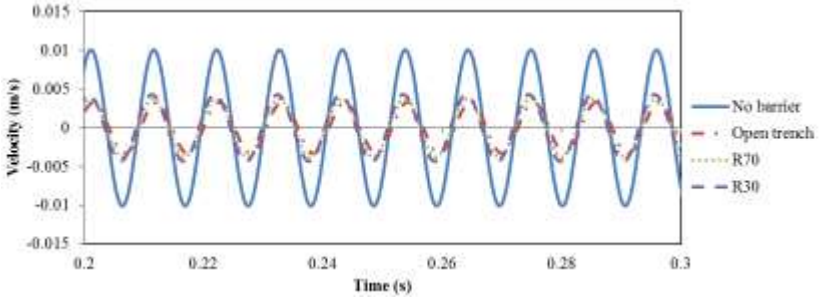

e) Geophone 5

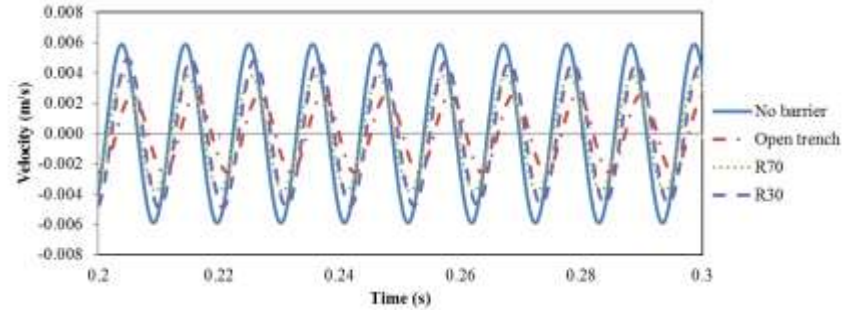

f) Geophone 6

Figure B-19 Geophones' signals for 95 Hz, line 3

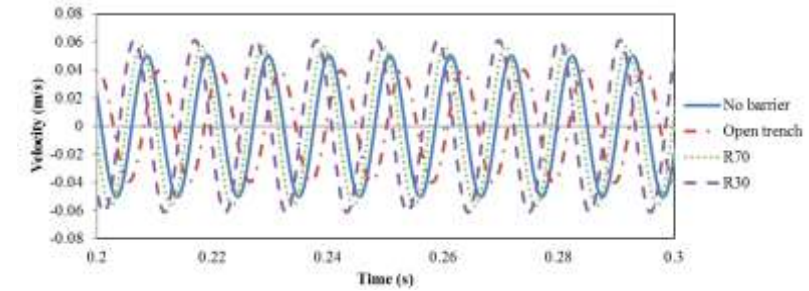

a) Geophone 1

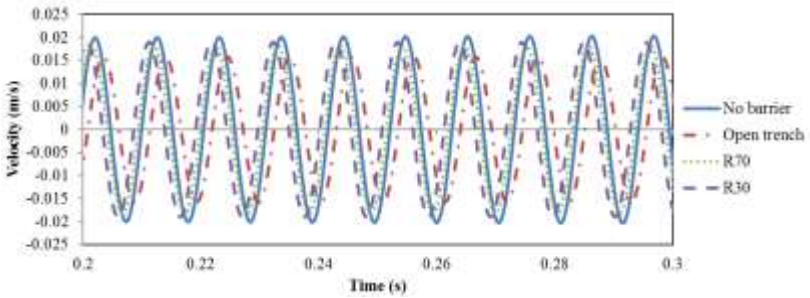

b) Geophone 2

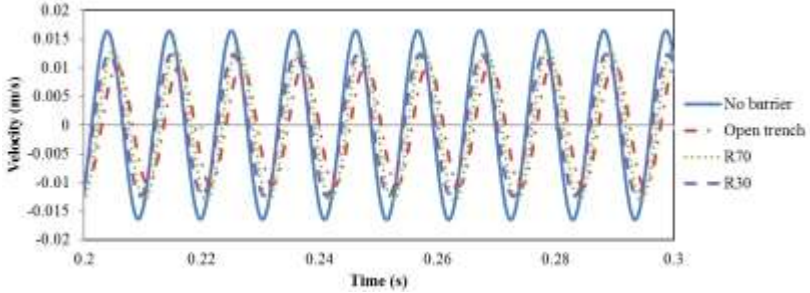

c) Geophone 3

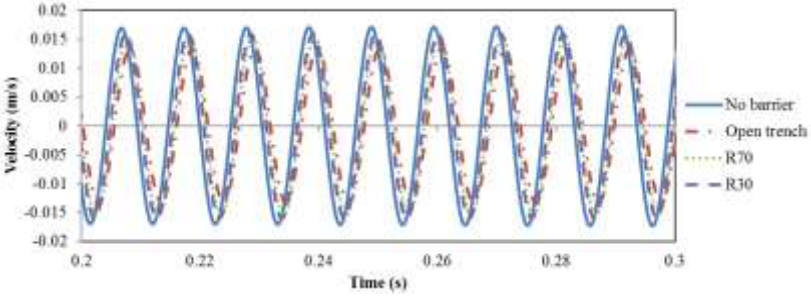

d) Geophone 4

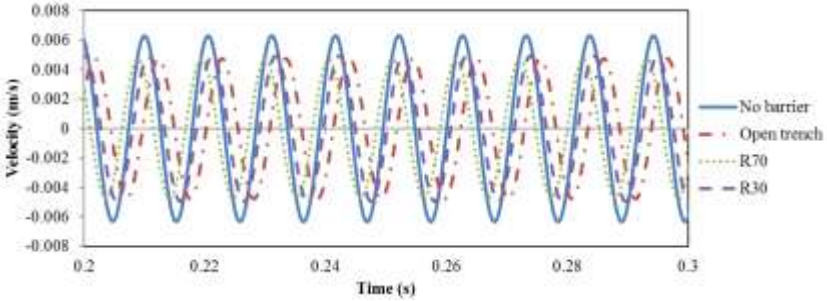

e) Geophone 5

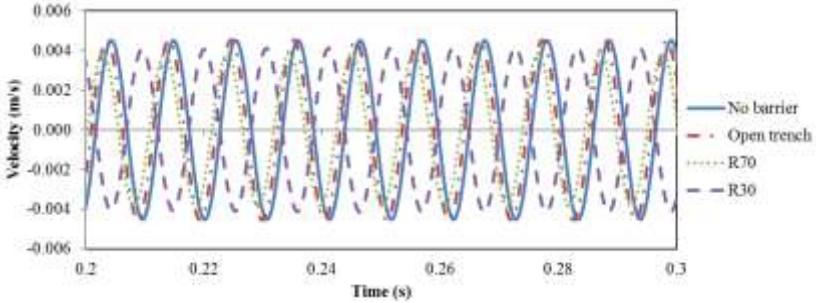

f) Geophone 6

Figure B-20 Geophones' signals for 95 Hz, line 4

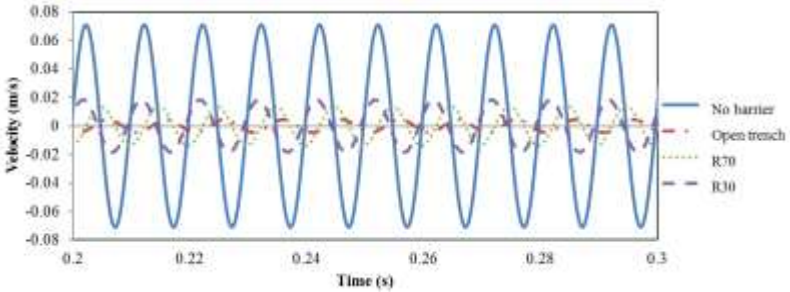

a) Geophone 1

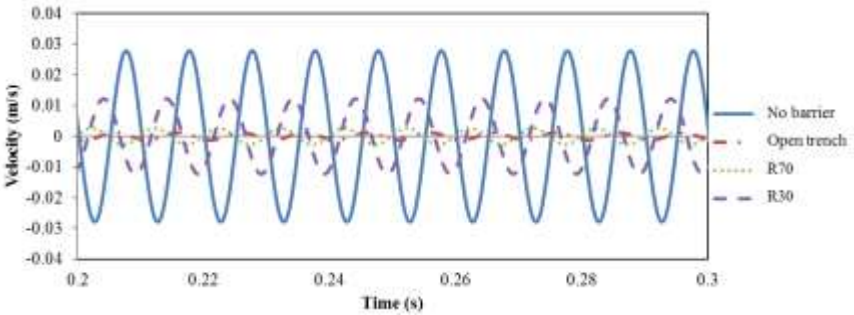

b) Geophone 2

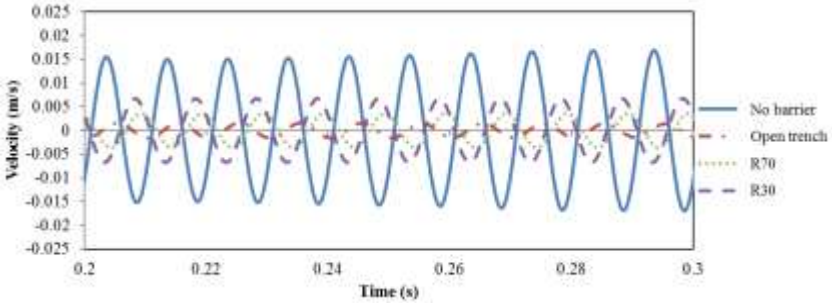

c) Geophone 3

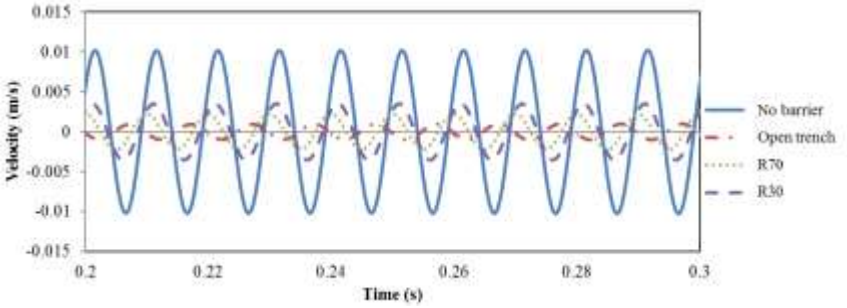

d) Geophone 4

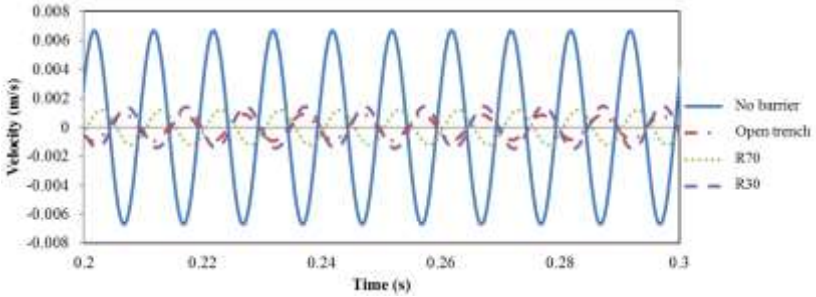

e) Geophone 5

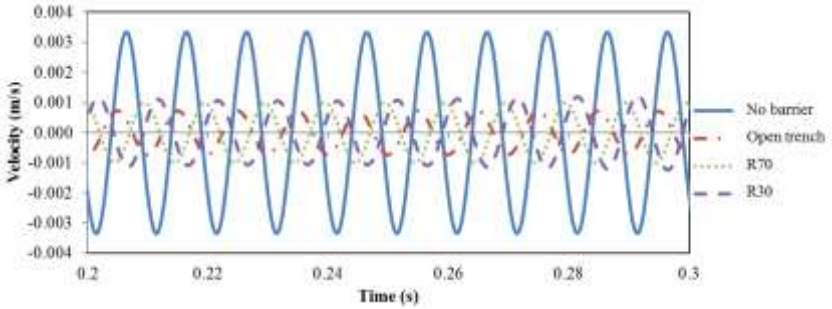

f) Geophone 6

Figure B-21 Geophones' signals for 100 Hz, line 1

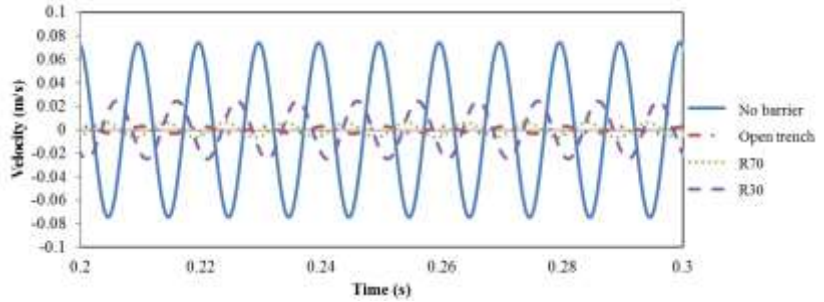

a) Geophone 1

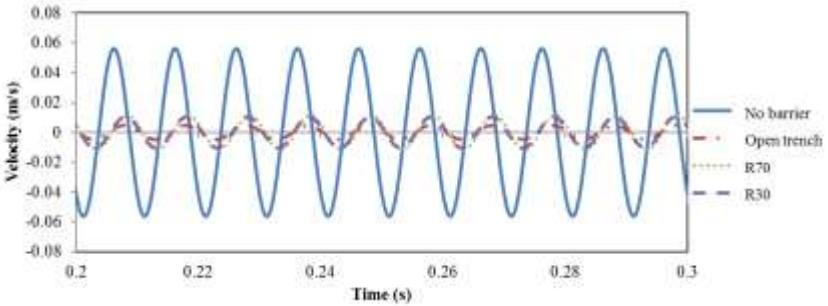

b) Geophone 2

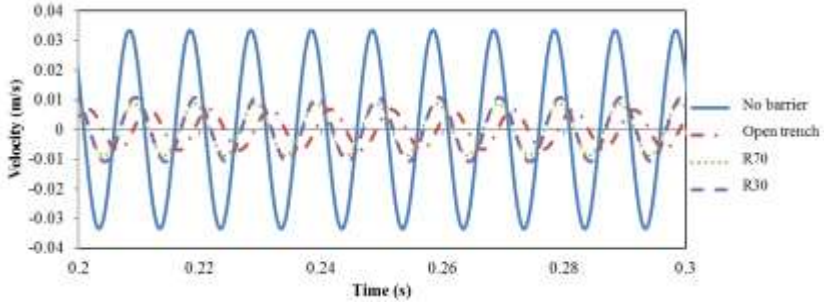

c) Geophone 3

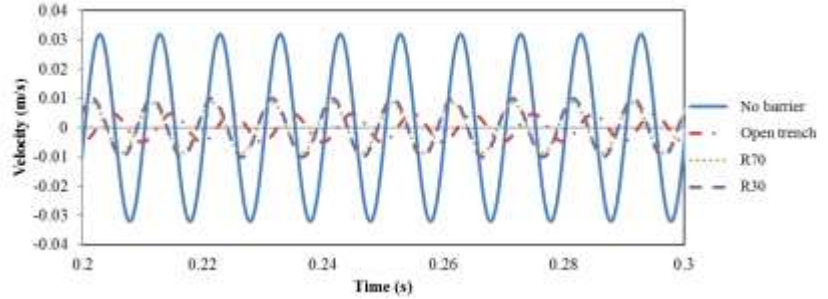

d) Geophone 4

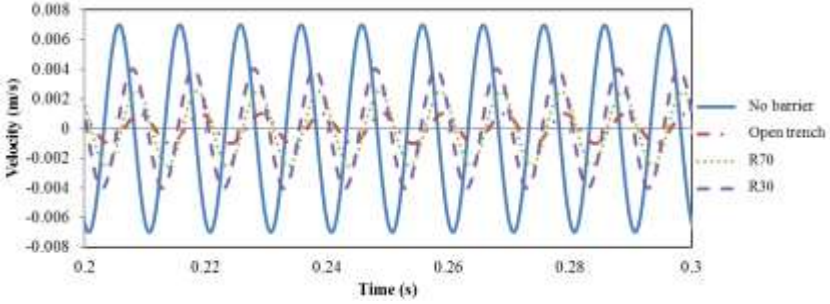

e) Geophone 5

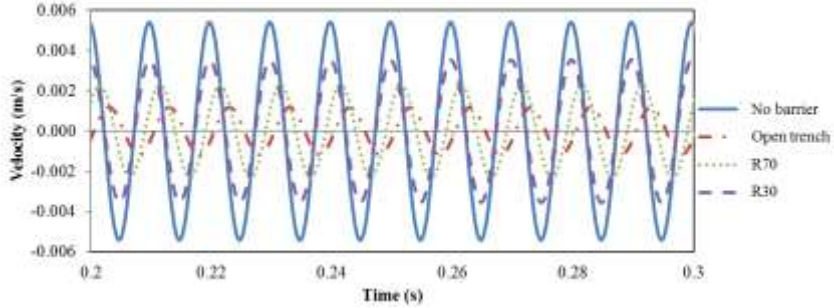

f) Geophone 6

Figure B-22 Geophones' signals for 100 Hz, line 2

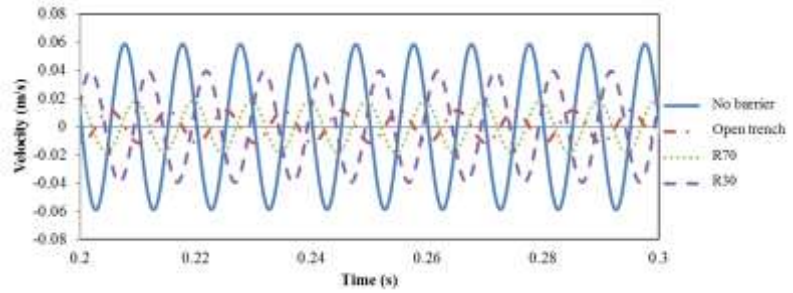

a) Geophone 1

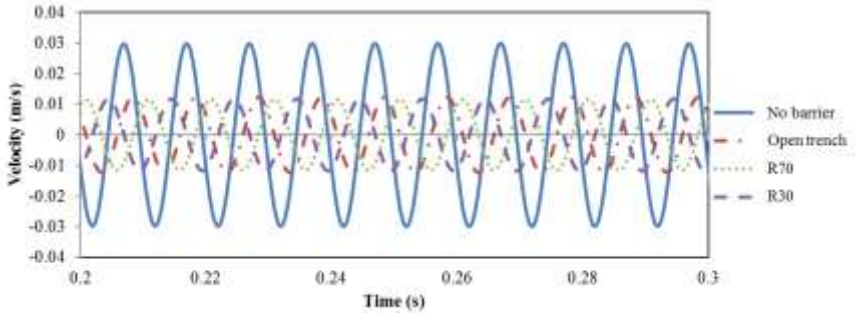

b) Geophone 2

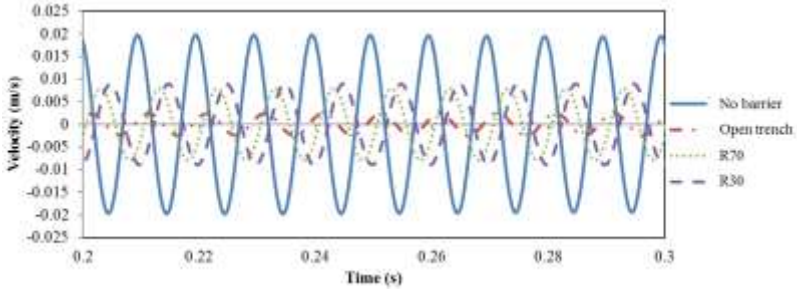

c) Geophone 3

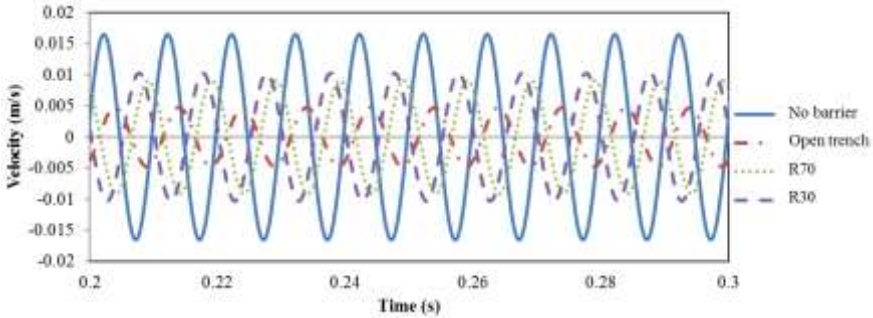

d) Geophone 4

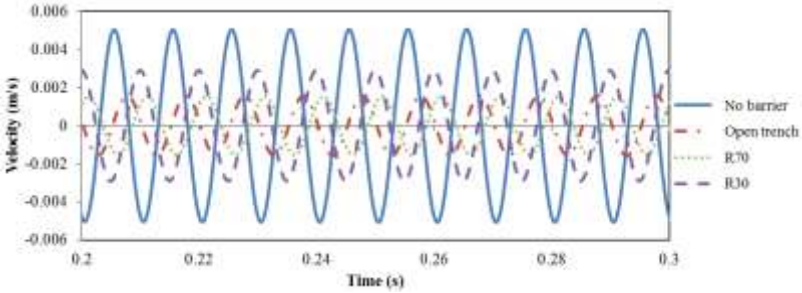

e) Geophone 5

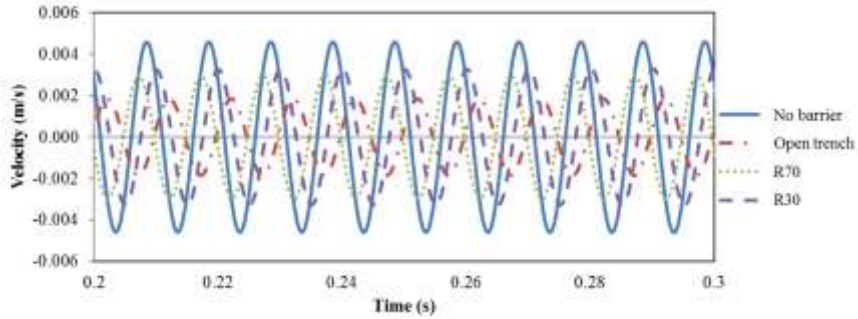

f) Geophone 6

Figure B-23 Geophones' signals for 100 Hz, line 3

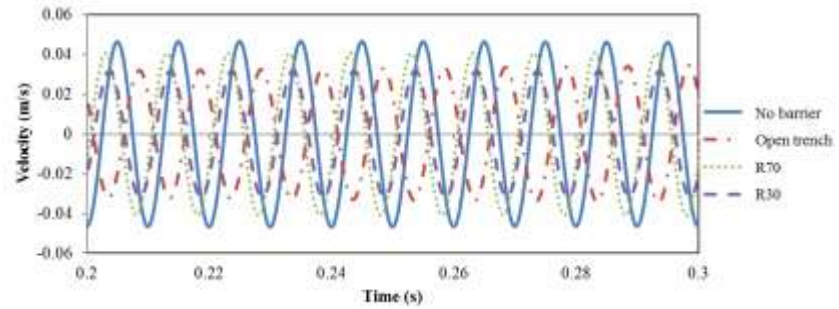

a) Geophone 1

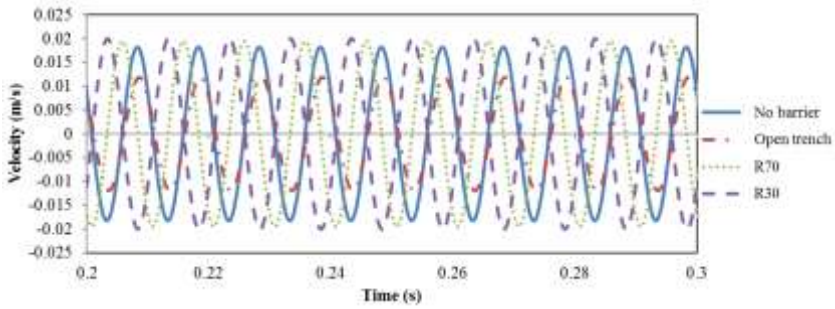

b) Geophone 2

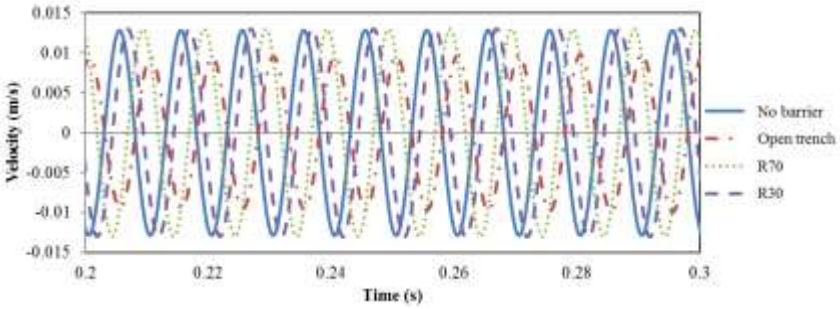

c) Geophone 3

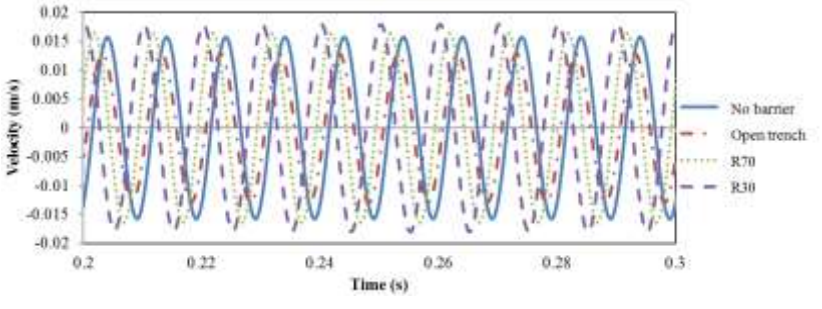

d) Geophone 4

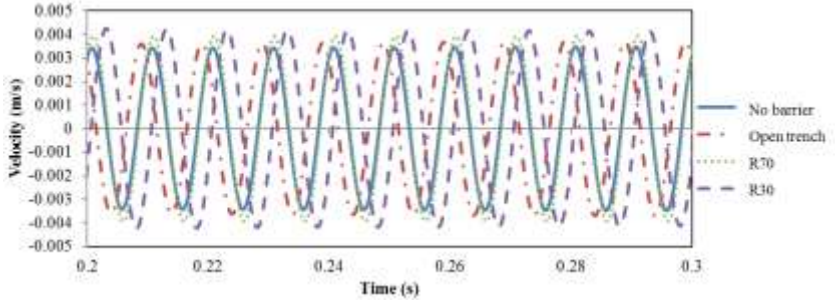

e) Geophone 5

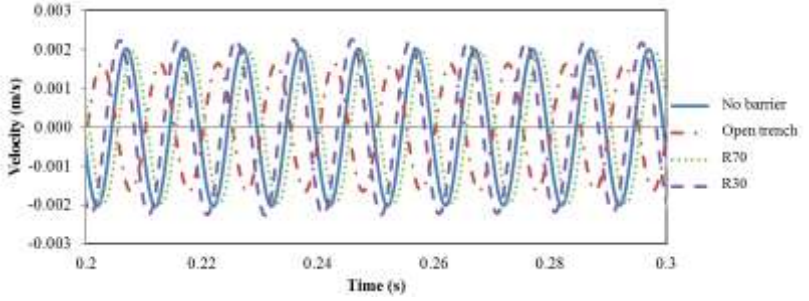

f) Geophone 6

Figure B-24 Geophones' signals for 100 Hz, line 4

Appendix C

2D free-field numerical results

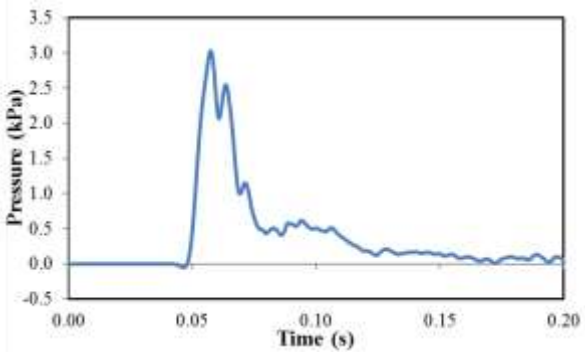

10m away from source

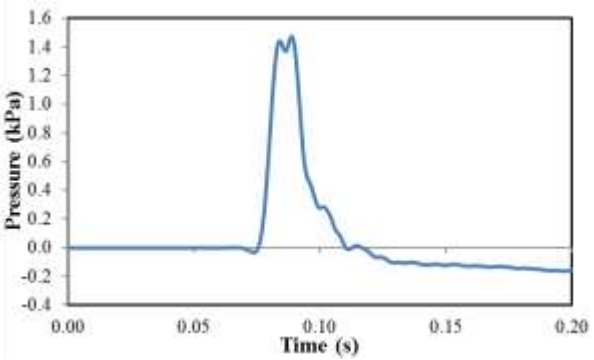

15m away from source

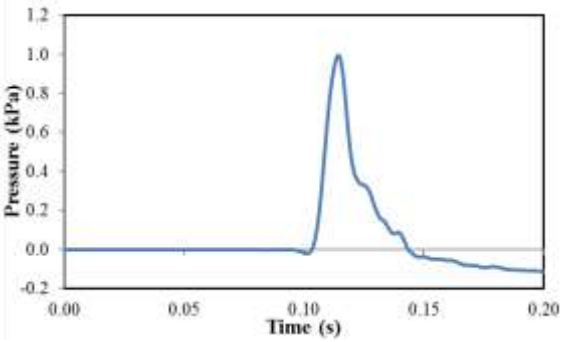

20m away from source

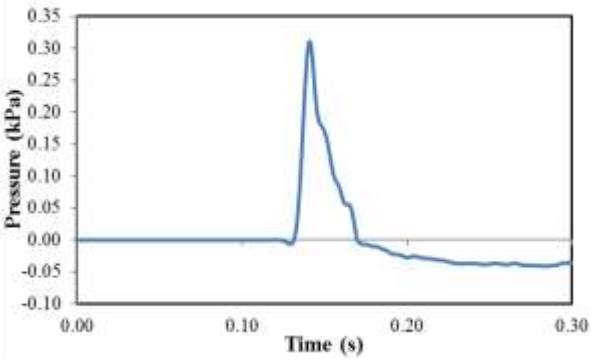

25m away from source

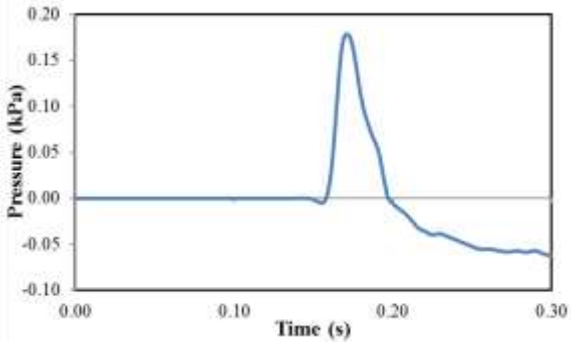

30m away from source

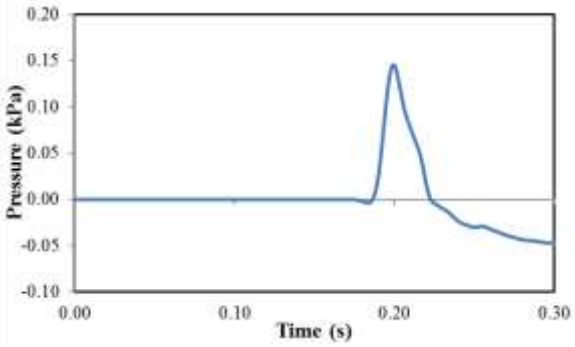

35m away from source

Figure C-1 Free-field peak pressure time history for Poisson's ratio 0.3

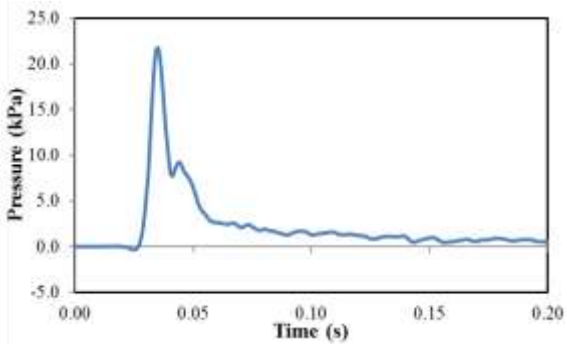

10m away from source

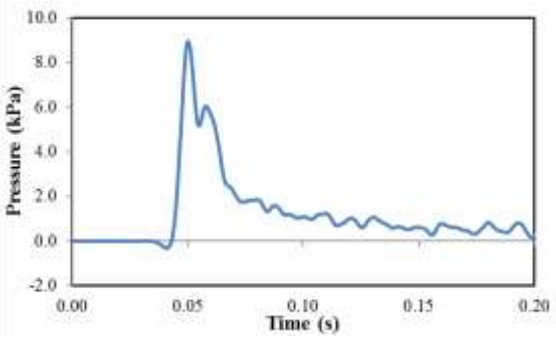

15m away from source

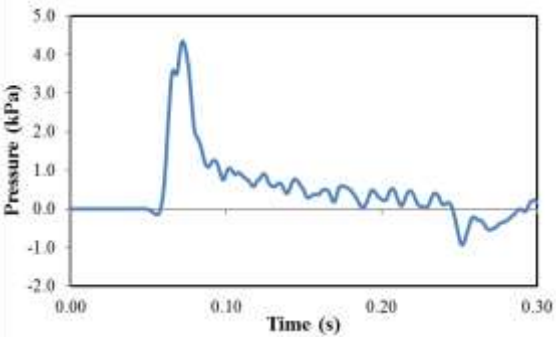

20m away from source

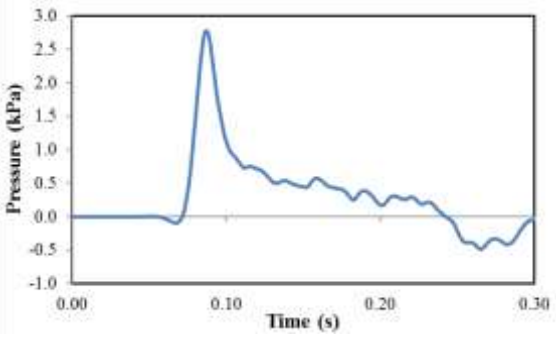

25m away from source

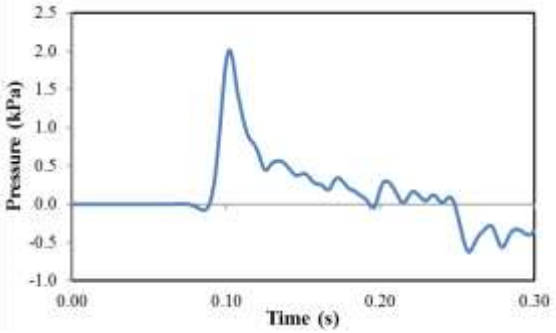

30m away from source

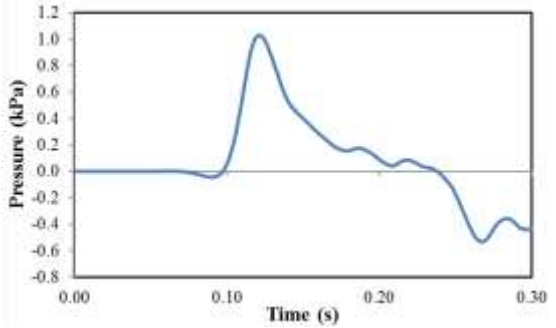

35m away from source

Figure C-2 Free-field peak pressure time history for Poisson's ratio 0.45

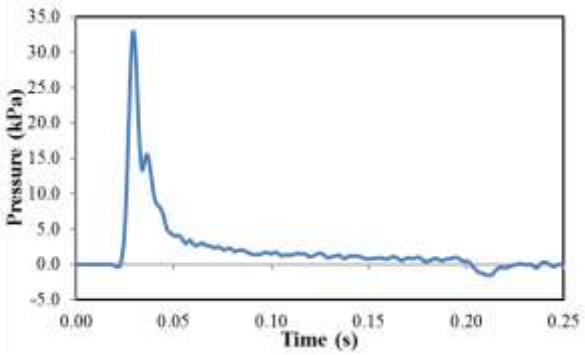

10m away from source

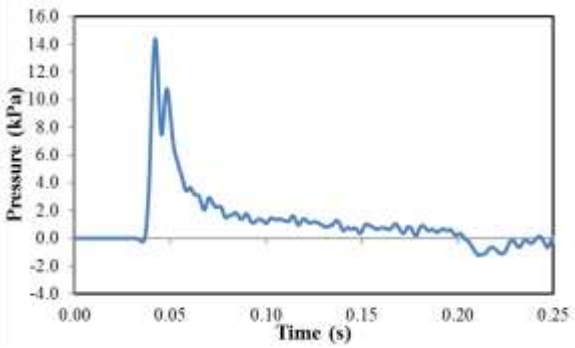

15m away from source

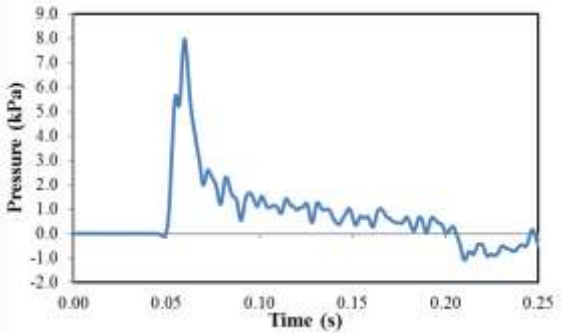

20m away from source

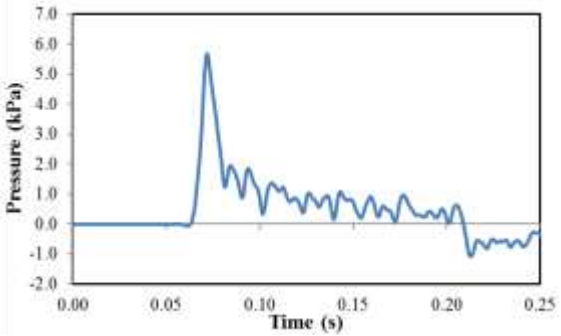

25m away from source

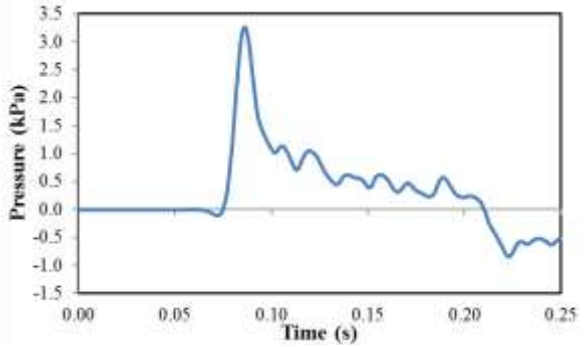

30m away from source

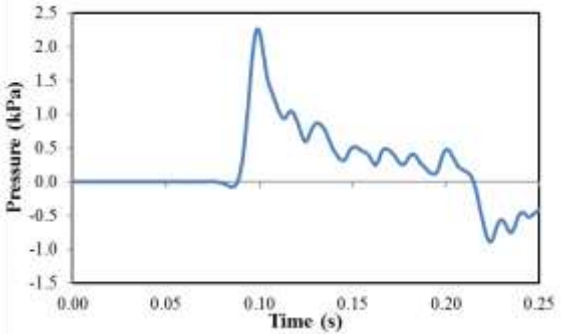

35m away from source

Figure C-3 Free-field peak pressure time history for Poisson's ratio 0.465

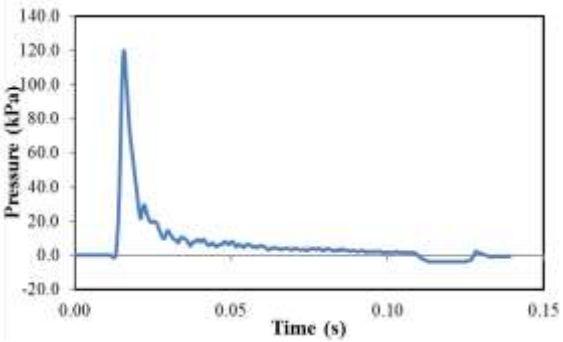

10m away from source

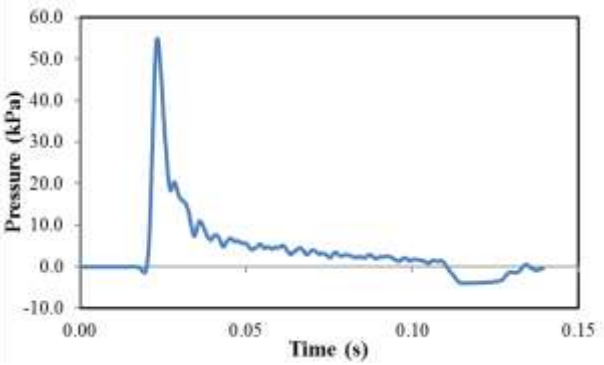

15m away from source

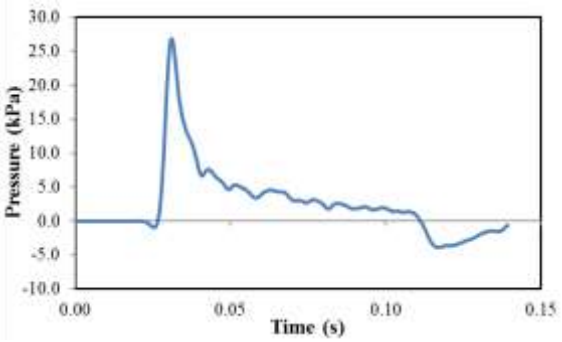

20m away from source

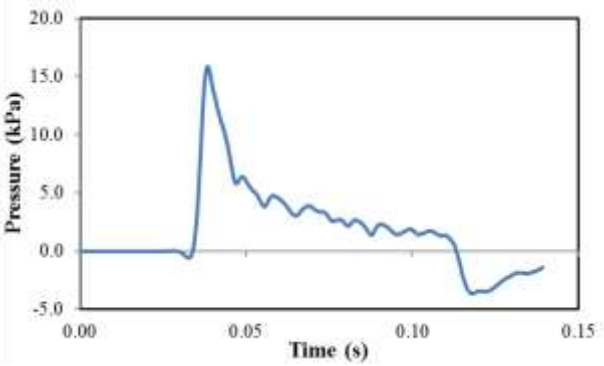

25m away from source

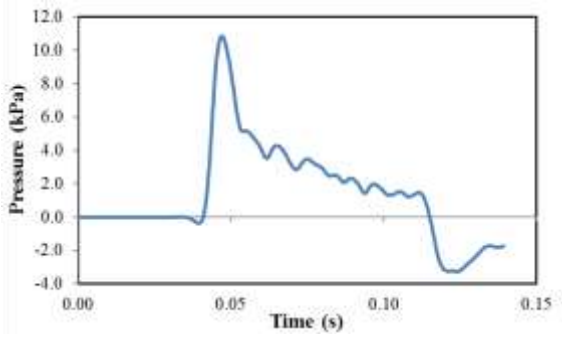

30m away from source

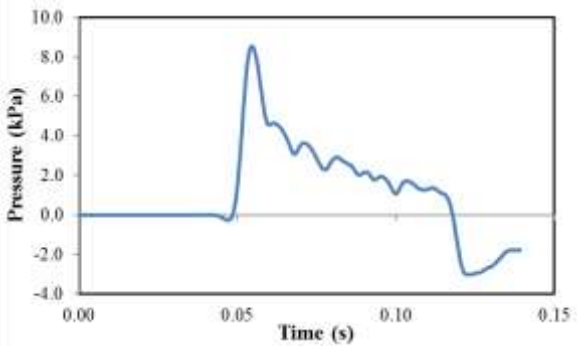

35m away from source

Figure C-4 Free-field peak pressure time history for Poisson's ratio 0.49

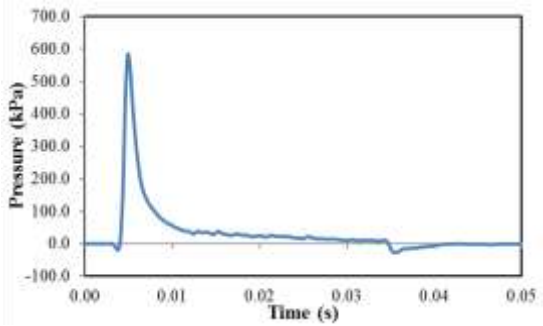

10m away from source

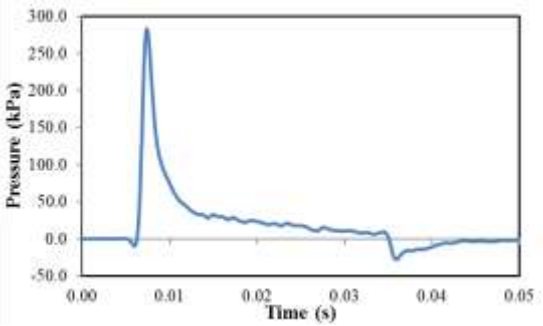

15m away from source

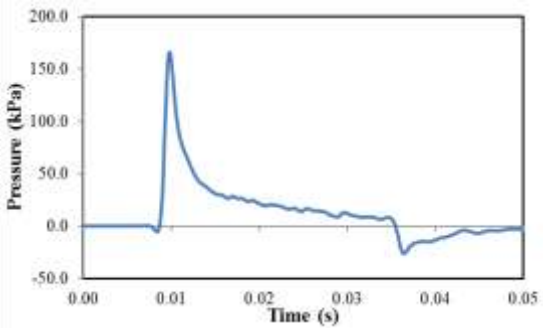

20m away from source

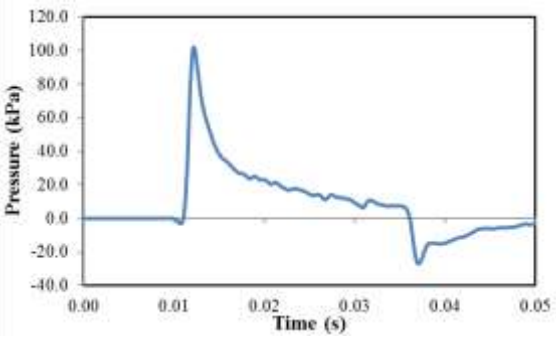

25m away from source

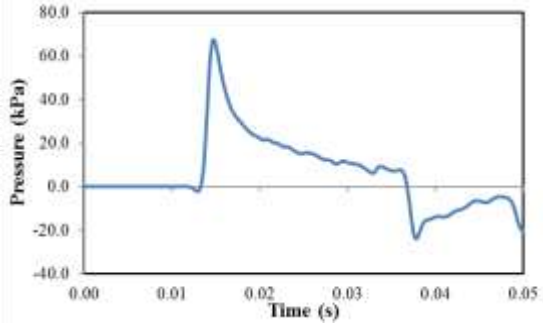

30m away from source

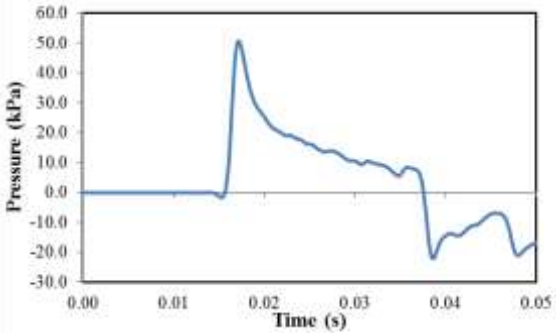

35m away from source

Figure C-5 Free-field peak pressure time history for Poisson's ratio 0.499